Title
Plasma-Material Interactions for Electric Propulsion and Plasma-Facing Components

Author
Thuppul, Anirudh

Publication Date
2022

Peer reviewed|Thesis/dissertation

UNIVERSITY OF CALIFORNIA
Los Angeles

Plasma-Material Interactions for Electric Propulsion and Plasma-Facing Components

A dissertation submitted in partial satisfaction
of the requirements for the degree
Doctor of Philosophy in Aerospace Engineering

by

Anirudh Thuppul

06/2022

ABSTRACT OF THE DISSERTATION

Plasma-Material Interactions for Electric Propulsion and Plasma-Facing Components

by

Anirudh Thuppul
Doctor of Philosophy in Aerospace Engineering
University of California, Los Angeles, 06/2022
Professor Richard E. Wirz, Chair

Quantifying lifetime and performance of electric propulsion devices is inherently challenging as device operations last on the order of thousands of hours. Physics-based approaches to capture the key mechanisms of particle or plasma-material interaction with components are required. The first limiting factor for electrospray thruster is propellant flux to and interaction with the grids, resulting in saturation and electrical failures. The process is primarily driven by impinging mass flux, as demonstrated by the first life model developed considering mass flux for evaluating lifetime of capillary droplet-mode electrospray thrusters. Mass flux was classically assumed gaussian in shape due to collisions and scattering processes, but novel measurements demonstrate that mass flux is super-gaussian in nature. The measurements provide novel insight on electrospray plume structure and how operating conditions affect their shape. The super-gaussian nature of the profile indicates the need to consider mass flux in addition to current for thruster performance and lifetime evaluation.

Plasma material interactions are also a challenge for lifetime and performance of components for electric propulsion and fusion applications. Ion bombardment and sputtering degrades boundary materials and contaminants contaminates the plasma, reducing performance, limiting device

lifetime, and increases component replacement costs. Plasma-infused volumetrically complex foams have been shown to persistently reduce sputtering-yield. In this work, experimental measurements of a foam under plasma exposure demonstrate the ability of the foam to partially-infused with plasma and provide insight on the plasma-infusion process dependence on plasma properties. PPI is shown to be the key design parameter to create VCMs for specific plasma properties and infusion behavior. Additionally, a novel sputtering model is developed to accurately describe the sputtering distributions and trapping mechanisms of VCMs of different materials and energies. The model demonstrates a key milestone in the development of VCMs to reduce sputtering yield up to 70%. The aspect ratio is shown to be the primary driver for sputtering behavior in the plasma-facing region and can be used tailor a VCM for a specific application independent of PPI, which can be tailored for specific plasma properties.

Additionally, the role of azimuthal instabilities in ExB systems on the PMI process is characterized. Characterization of the mode provides insight on the mode dependence on plasma properties, with implications for Hall thrusters, low-temperature plasma devices, and plasma-material interaction characterization of volumetrically-complex materials. Azimuthal instabilities must be accounted for as they are shown to be non-negligible in certain scenarios and significantly impact system dynamics via azimuthal velocity components.

The dissertation of Anirudh Thuppul is approved.

Daniel Eckhardt

Taylor Matlock

George Morales

Mitchell Spearrin

Ann Karagozian

Richard E. Wirz, Committee Chair

University of California, Los Angeles

06/2022

To meticulous planning and hard work... and if that fails, coffee

TABLE OF CONTENTS

List of Figures

List of Tables

ACKNOWLEDGMENTS

First, I would like to thank my advisor Professor Richard Wirz. Thank you for accepting me into your lab and and mentoring me throughout the last six years. Whether it was working on a new lab competency together such as electrospray propulsion, or age-old problems such as plasma probes and hollow cathodes, I have always appreciated the energy you have put into the work. I really appreciate the different perspectives you offered, and allowed me to pursue different ideas and lines of thought. All of that would have not been possible without your emphasis on creative time and space. Thank you for supporting throughout these years.

Next, I would like to thank Professor Ann Karagozian, Professor Mitchell Spearrin, Professor George Morales, Dr. Taylor Matlock, and Dr. Daniel Eckhardt for taking the time and energy to serve on my thesis committee. I am extremely grateful for all your advice and feedback throughout the process. The expertise you provide across multiple disciplines has been invaluable. Additionally, I would like to thank the following people for their for their technical support and advice: Dr. John Ziemer and Dr. Adam Collins on electrosprays, Dr. Christopher Dodson, Dr. Dima Osin, and Dr. Stephen Samples for plasma instabilities and diagnostics, and Dr. Gary Li, Dr. Pablo Guerrero, and Dr. Gary Wan for plasma-material interactions and hollow cathodes.

I want to acknowledge my funding sources, the National Aeronautics and Space Administration (NASA) Jet Propulsion Laboratory (JPL), the Air Force Research Laboratory (AFRL), the Air Force Office of Scientific Research (AFOSR), the United States Department of Energy (DOE), the Advanced Research Projects Agency - Energy (ARPA-E), the Aerospace Corporation, and the UCLA Mechanical & Aerospace Engineering Department.

I would also like to specifically acknowledge work in this dissertation that is the content of existing or in-preparation publications and the contributions of my collaborators and co-authors. Chapter 2 is a version of [2], Thuppul, A., Wright, P. L., Collins, A. L., Ziemer, J. K., & Wirz, R. E. (2020), “Lifetime considerations for electrospray thrusters", Aerospace, 7(8), 108. Richard Wirz was the PI. Peter Wright, Adam Collins, John Ziemer, and Richard Wirz all contributed to the tech-

nical content of the work, writing, editing, and reviewing. Chapter 3 is a version of [6], Thuppul, A., Collins, A. L., Wright, P. L., Uchizono, N. M., & Wirz, R. E. (2021), “Mass flux and current density distributions of electrospray plumes", Journal of Applied Physics, 130(10), 103301. Richard Wirz was the PI. Peter Wright, Adam Collins, Nolan Uchizono, and Richard Wirz all contributed to the technical content of the work, writing, editing, and reviewing. Chapter 4 is a version of a publication in-preparation, Thuppul A. & Wirz R.E. (2022) “Sputtering Behavior and Plasma Response of Plasma-Infused Volumetrically-Complex Materials” AIP Physics of Plasmas (in-preparation). Richard Wirz was the PI and also contributed to the technical content of the work, writing, editing, and reviewing. Chapter 5 is a version of a publication in-preparation, Thuppul A., Sabiston G., & Wirz R.E. (2022) “Sputtering Yield Reduction Model for Volumetrically-Complex Materials” AIP Applied Physics Letters (in-preparation). Richard Wirz was the PI. Graeme Sabiston and Richard Wirz all contributed to the technical content of the work, writing, editing, and reviewing.

I would like to thank my current and former lab members: Dr. Ben Dankongkakul, Dr. Marlene Patino, Dr. Christopher Dodson, Dr. Cesar Huerta, Dr. Gary Li, Dr. Stephen Samples, Dr. Nolan Uchizono, Peter Wright, Henry Huh, McKenna Davis, Angelica Ottaviano, Mary Konopliv, Nicolas Rongione, Patrick Crandall, Shehan Parmar, Richard Obenchain, and Blake Haist. Thank you all for always being an exciting and amazing group of people regardless of whether we are at work discussing technical content or enjoying life outside work by eating, backpacking, or adventuring. I would also like to thank the undergraduate students that I have had to pleasure of working with over the past years: John Hayes, Charvi Aggarval, Alvaro Pons Pelufo, Anna O’Conner, Oliver Fildes, Brittney Garcia, Jack Garvey, Anshul Gupta, Alyssa Boedigheimer, and Taiga Asanuma. Thank you all for the excellent work you all contributed and the enthusiasm you all brought to the work we did.

Thank you to my friends and family for constantly motivating and helping me over the past years. I am continuously inspired by each and every one of you. Thank you to my late grandfather, who got me interested in and taught me math, science, and sports from before I can even remember.

It's no surprise my interests and who I am today can still be largely described by those. Last but not least, thank you to my father, Padmanabhan Thuppul, my mother, Vijayalakshmi Thuppul, and my brother, Aathreya Thuppul. I would not be here without the sacrifices and risks you made to move to this country and provide me with the opportunities I have had throughout my childhood. Even though we have lived 2500 miles away the past 6 years, I have never felt alone thanks to your constant support and love. Thank you for everything!

VITA

2016 - 2022 PhD Candidate, Plasma & Space Propulsion Laboratory - *University of California, Los Angeles*

2018 Master of Science in Aerospace Engineering - *University of California, Los Angeles*

2017 - 2020 Teaching Assistant - *University of California, Los Angeles*

2019 Intern - *TAE Technologies*

2016 Bachelor of Science in Mechanical/Aerospace Engineering, Double Major in Astrophysics - *Rutgers University*

2014 - 2016 James J Slade Scholar, Applied Fluids Laboratory - *Rutgers University*

PUBLICATIONS

Thuppul A., Collins A.L., Wright P.L., Uchizono N.M., Wirz R.E. (2021) "Mass Flux and Current Density Distributions of Electrospray Plumes" *AIP Journal of Applied Physics* 130 (10), 103301.

Ottaviano A., Thuppul A., Hayes J., Dodson C., Li G.Z., Chen Z., Wirz R.E. (2021) "In-situ Microscopy for Ion-Induced Sputter Erosion of Featured Surfaces" *AIP Review of Scientific Instruments* 92 (7), 073701.

Uchizono N.M., Collins A.L., Thuppul A., Wright P.L., Eckhardt D.Q., Ziemer J., Wirz R.E.

(2020) “Emission Modes in Electrospray Thrusters Operating with high Conductivity Ionic Liquids” *MDPI Aerospace* 7 (10), 141.

Thuppul A., Wright P.L., Collins A.L., Ziemer J.K., Wirz R.E. (2020) “Lifetime Considerations for Electrospray Thruster” *MDPI Aerospace* 7 (8), 108.

Hansen T. E., Stern A., Thuppul A., Diez F.J. (2020) “Scalable Electro-Osmotic Thruster for Stealthy, Extreme Condition Underwater Propulsion” *ASME Journal of Offshore Mechanics and Arctic Engineering* 142 (1).

CHAPTER 1

Introduction and Motivation

In this chapter, the challenges and motivation for understanding and quantifying lifetimes for electric propulsion and plasma facing components are presented. Electrospray propulsion, plasma-facing components, and azimuthal E $\times$ B instabilities are introduced and contextualized in the scope of this dissertation. Finally, an overview of the remainder of this dissertation is provided.

1.1 Lifetime Estimation

Quantifying lifetime of components is a fundamental challenge in any field as it is critical to determining the performance and longevity of a given system. Understanding lifetime limiting mechanisms enables better design of components and systems to reduce cost and improve performance. This is especially true of plasma and charged-particle systems, such as electric propulsion or fusion, where extreme environments are encountered with multiple complex behaviors that evolve with time.

Although most spacecrafts do not use propulsion, demand for mission capabilities has produced significant interest and increased use of electric propulsion technologies. For example, of growing interest is the use of electric propulsion for orbit raising from low-earth orbit (LEO) to geo-synchronous orbit (GEO). As shown in Figure 1.1, this maneuver can be accomplished using chemical propulsion or electric propulsion. Chemical propulsion system typically produce thrust in the range of N -MN with specific impulses (I_{sp}) in the range of 300 s. This means the system will require high propellant mass fraction based on the rocket equation (equation 1.1), and achieve

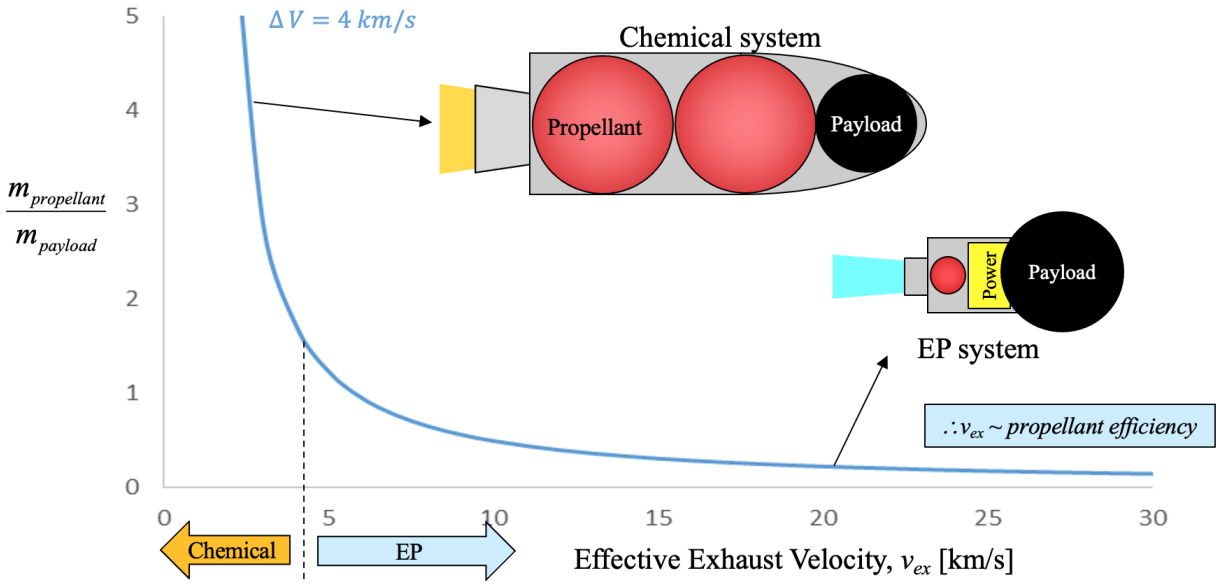

Figure 1.1: Propellant mass fraction as a function of exhaust velocity for a LEO-GEO mission example, adapted from Wirz [1].

the required mission impulse on the order of minutes (equation 1.2.

$$\frac{m_{prop}}{m_{pay}} = e^{\frac{\Delta V}{v_{ex}}} - 1 \tag{1.1}$$

$$MissionImpulse = \int Thrust * dt \tag{1.2}$$

Electric propulsion systems on the other hand produce much lower thrust on the order of mN, but at much higher Isp in the range of 300 - 10,000 s. As shown in Figure 1.1, this means an electric propulsion system can meet the required ΔV with much lower propellant mass. This makes the technology extremely attactive due to the significant reduction in launch costs associated with the reduces mass. The catch, however, is that the mission impulse for the electric propulsion system is on the order of months. This means the system must operate reliably for months on orbit, therefore requiring a firm understanding of device lifetime.

Ground testing of propulsion systems for months is inefficient and often impractical. For exam-

ple, the LISA mission requires operation of an electrospray thruster for 40,000 hours [13], which cannot be tested for. Physics-based lifetime estimation is needed to accurately determine lifetime and performance of these devices.

1.2 Electrospray Propulsion

Electrospray thrusters are a subset of electric propulsion technology where charged species are electrostatically accelerated from a liquid meniscus (often referred to as a Taylor Cone) to produce thrust. As shown in Figure 1.2, the Taylor cone is produced from an applied electric field balanced out by the surface tension of the propellant. Electrospray thrusters typically use either ionic liquids or liquid metals as propellant. Ionic liquid propellants are of particular interest due to their negligible vapor pressure and high conductivity near room temperature. Electrospray thrusters are often classified by their emitter geometry: capillary, porous bulk, or externally-wetted. Generally, specific impulse increases from capillary to porous bulk to externally-wetted, however the thrust-power ratio decreases. Electrospray thrusters offer advantages such as high thrust precision and a wide specific impulse range, but have yet to demonstrate lifetimes that are attractive for many space missions [14]. Improving thruster lifetime has been noted as a key area of high specific impulse electrospray development by NASA [15]. Efforts investigating thruster performance and lifetime of Field Emission Electric Propulsion (FEEP) devices established trends associated with emitter-extractor separation and electrode impingement current [16, 17, 18]. The efforts identified geometric considerations crucial to reducing impingement current on the extractor electrodes, which was a key consideration for lifetime of the thruster.

The first successful in-space demonstration of electrospray propulsion technology was the Colloid MicroNewton Thruster (CMNT). The CMNT was developed by Busek Co., Inc and NASA Jet Propulsion Laboratory (JPL) for the European Space Agency (ESA) Laser Interferometer Space Antenna (LISA) Pathfinder mission as a technology demonstration of high thrust precision (100 nN) and low thrust-noise capability [19, 20, 21]. A representative geometry of what the cap-

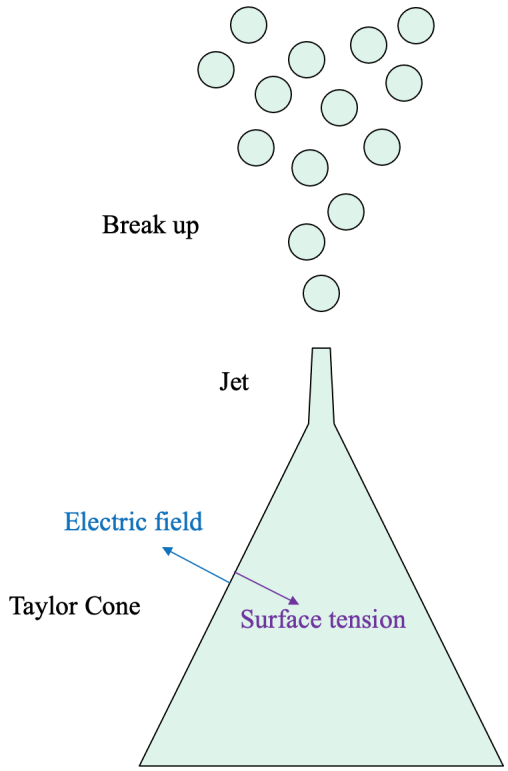

Figure 1.2: Illustration of the electrospray mechanism where a cone-jet forms from the balance of surface tension and electric traction, resulting in a stream of ion and/or droplets that produce a plume.

illary emitter system looks like is shown in Figure 1.3, and discussed in more detail in Chapter 2. The demonstration was successful in establishing the CMNT's thrust performance and precision, with 7 of 8 thrusters operating in flight for over 2,400 hours using 1-Ethyl-3-methylimidazolium Bis(trifluoromethylsulfonyl)imide (EMI-Im) as propellant [13]. Results from the LISA-Pathfinder mission represent 1 datum for thruster lifetime and 7 instances where the thruster lifetime is only known to be greater than the total operational time; how much greater is unknown. These results do not provide a sufficient understanding of the mechanisms responsible for thruster failure, nor an understanding sufficient for accurate estimation of thruster lifetime. Multi-year missions, such as the ESA LISA mission, require operational lifetimes on the order of 40,000 hours [22], and hence require an understanding of the failure modes in electrospray devices.

The motivation for this work is to bridge the gap in understanding of droplet-mode electrospray

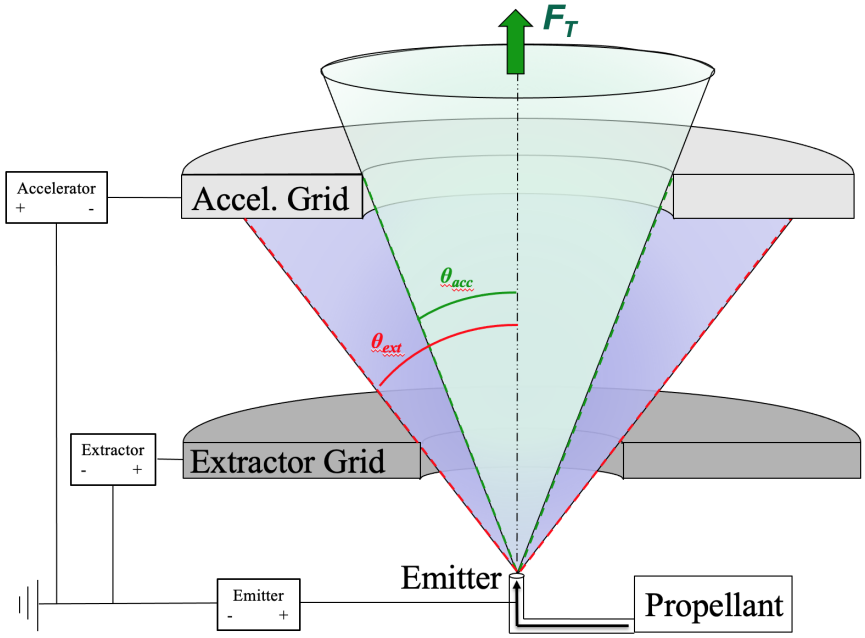

Figure 1.3: Electrospray emitter and electrode geometry with line of sight plumes, adapted from [2].

thruster lifetime for mission applications. It has been proposed that overspray leading to grid (also referred to as electrode) impingement is the primary failure mechanism [23, 24], resulting in eventual saturation of the porous accelerator grid as shown in Figure 1.3. The objective of this work is to identify and understand the effects of design and operating conditions on electrospray thruster lifetime. Physics-based approaches will be used to capture key life and performance mechanisms via development of an analytical life model and experimental measurements of electrospray profiles as detailed in Chapters 2 and 3.

1.3 Plasma Facing Components

While electrospray propulsion uses ionic liquids, more common systems such as Hall effect thrusters and ion thrusters create a plasma discharge from which the ions are accelerated for thrust. Hall thrusters, shown in Figure 1.4, use a cross field configuration with a magnetic field to confine electrons and ionize gas. The plasma ions are then accelerated by the axial electric field to produce

thrust. The consequences of this configuration is explained in more detail in Section 1.4.

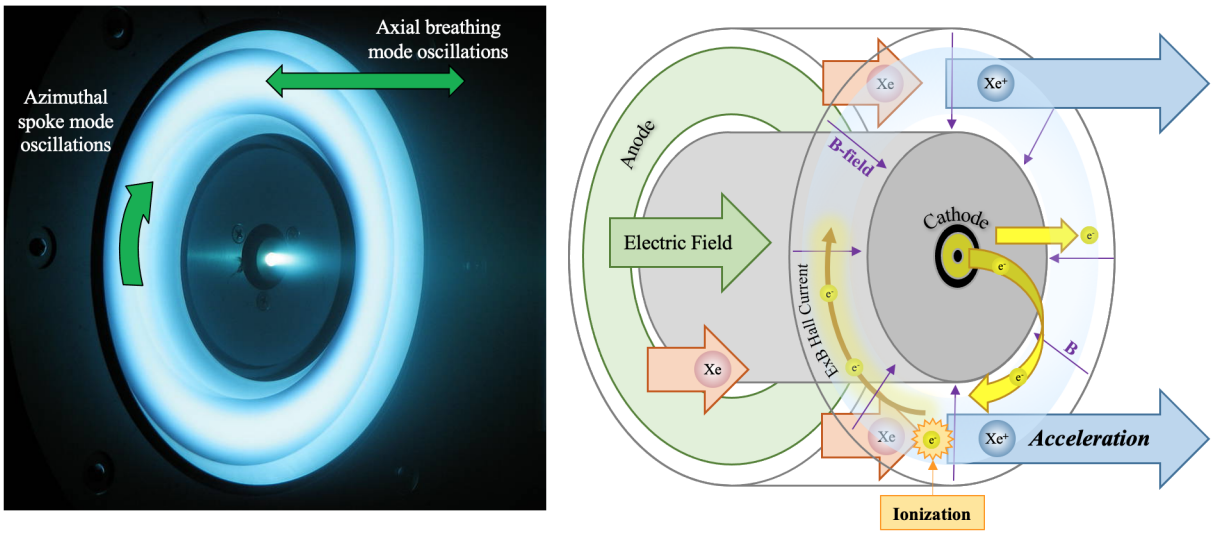

Figure 1.4: From [3], (Left) A magnetically-shielded NASA Hall thruster with key oscillatory dynamics indicated, and (Right) illustration of the Hall thruster processes.

One of the primary challenges with Hall thrusters is sputtering erosion of the ceramic walls in the channel, which produces ridges after 100s of hours of operation and eventually exposes the magnetic circuitry. Magnetically shielded Hall thrusters use field geometry to reduce energy of ions hitting the channels, but suffer from sputtering erosion of pole pieces.

Beyond traditional electric propulsion systems, higher power systems such as magnetoplasmadynamic (MPD) thusters show promising potential for mission requirements but are limiting by severe lifetime limitations at the plasma conditions they experience. A key component that suffers from erosion in MPDs and high power Hall Thrusters are cathodes. Electric propulsion systems typically use hollow cathodes as plasma sources, which suffer from evaporative and sputtering erosion limiting lifetime. Understanding the sputtering behavior and improving material choices can increase electric propulsion technology lifetime and performance.

Another field of interest where the lifetime and sputtering mechanisms of plasma-facing surfaces are critical is nuclear fusion. Fusion is a revolutionary technology that has the promise to deliver unlimited clean energy by fusing nuclei to release energy. This process requires enormous

amounts of energy, resulting in extremely energetic particles that can cause significant sputtering, thermal loads, and neutron damage of plasma-facing surfaces [25]. An additional challenge for fusion is the high quality of plasma required to achieve fusion. Impurities and secondary electrons emitted from the plasma-material interaction contaminate the plasma and reduce performance. Additionally, sputtering erosion limits the lifetime of electrodes and plasma-facing components, increasing cost of operation and development. Limiting sputtering and increasing plasma-favorability of plasma-facing materials is significant interest and on-going work in the fusion field.

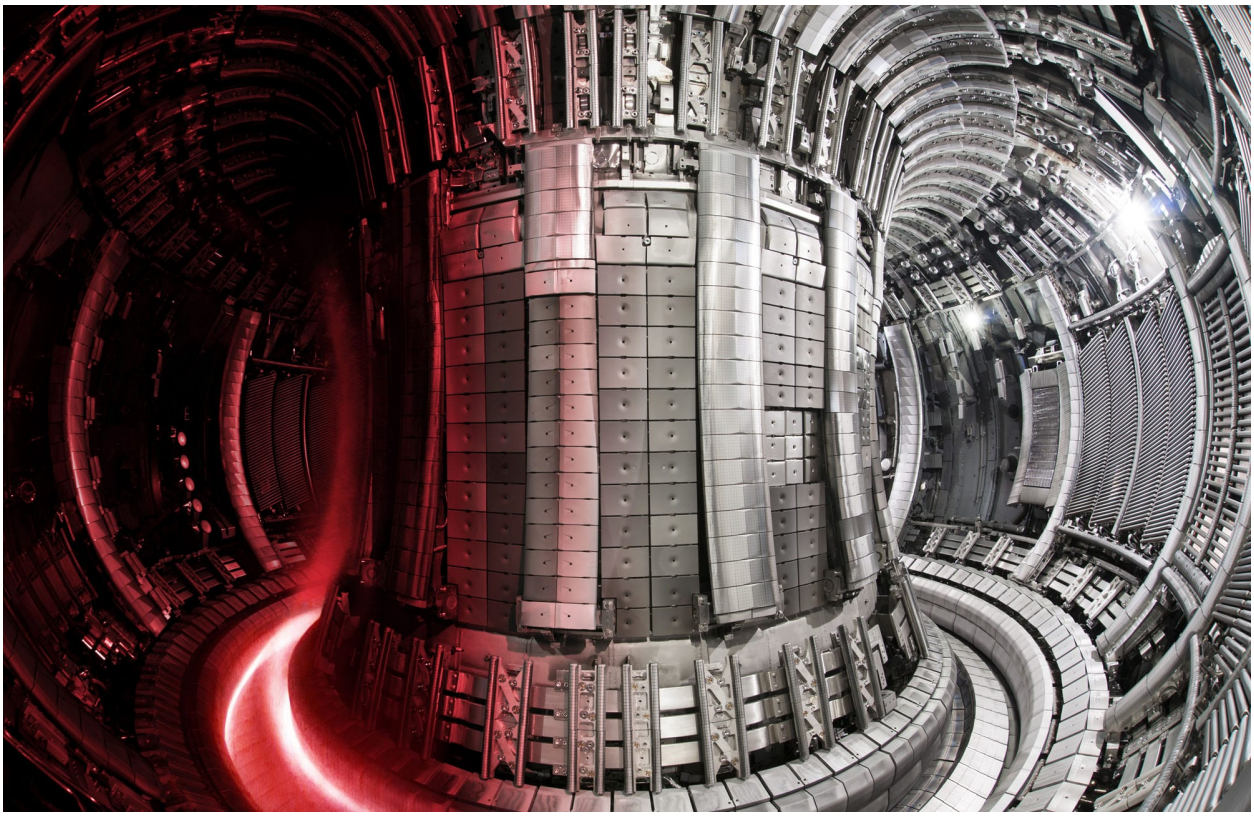

Figure 1.5: The Joint European Torus (JET) reactor with plasma during operation.

Reducing sputtering has been a topic of interest for electric propulsion and fusion applications. Misco-architectured surfaces have been demonstrated to initially reduce sputtering yield but tend toward that of a flat surface with erosion [26]. Recent work by Li and Wirz [9] has shown volumetrically-complex materials (VCMs), such as foams, exhibit persistent sputter reduction to

featured surfaces. They demonstrated that aluminum foams exposed to argon plasmas can reduce sputtering by 50% at 300 eV. This is enabled by a new regime, plasma-infusion, where the plasma can penetrate into the 3-dimensional structure of the VCM. The regime and theory is discussed in more detail in Section 4.1. On-going work is currently investigating the infusion and sputtering behavior to design improved VCM electrodes and plasma-facing components that are plasma-favorable.

These efforts are the contents of Chapters 4 and 5. As shown in Figure 1.6, lifetime of PFCs requires additional complexity in the form of multiple different mechanisms in comparison to electrosprays. However, a similar approach can be used by conducting critical experiments of plasma-infused and plasma-facing volumetrically-complex materials to characterize material sputtering and plasma response. The objective is to determine the impact of critical plasma and material parameters on plasma-material interaction for VCMs.

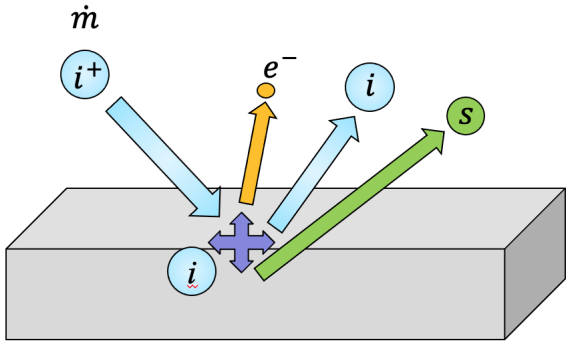

Figure 1.6: Lifetime of plasma-facing components is adds additional complexity due to multiple mechanisms that occur resulting in species implantation, sputtering, and secondary electron emission.

1.4 E x B Instabilities

Plasma discharges are used for a wide range of applications, such as space propulsion, materials processing, nuclear fusion, and electronics. The ionized nature of a plasma poses a challenge in

confining it for any application. The mean free path of the electrons is often long (on the scale of the system or larger). The result is that electrons will be lost to the electric field (from cathode to anode) and the plasma cannot be maintained. For a direct current discharge, an external magnetic field applied perpendicular to the electric field can confine the electrons, as demonstrated in Figure 1.4. The magnetic field traps electrons along the field lines, increasing the electron residence time by imposing a barrier against the electron transport towards the anode.

The configuration described above is commonly known as an E×B configuration. The configuration is common to a variety of devices such as Hall effect thrusters (HETs), magnetrons, and Penning-type discharges. However, a consequence of the E×B configuration is that the ionized species experience a drift in the cross-product direction, known as an E×B drift. Therefore, the cross-product direction cannot terminate on a surface as the electrons would be lost as a consequence. The consequence is that the geometry must be cylindrical such that the E×B drift is in the azimuthal direction and does not terminate on a surface (known as a Hall current). However, the E×B configuration tends to develop instabilities.

The development of instabilities leading to anomalous transport is a concern for numerous applications that rely on the magnetic field for effective electron confinement. Though the existence of the instabilities has been well documented, accurate descriptions of them and their role in facilitating electron transport is still unclear and largely empirical [27]. The anomalous transport and heating has generally been attributed to turbulence. However, that is a broad general explanation, with open questions still remaining regarding what drives turbulence is varying systems of interest. A feature of turbulent systems is the occurrence of long-wavelength coherent (or "self-organized") structures whose role in system dynamics is topic of significant interest in the broader field of turbulence. These coherent structures are a common feature in numerous E×B configuration devices that are inherently prone to turbulent behavior. This includes Penning-type discharges, magnetrons, dielectric barrier discharges, Hall effect thrusters, and various laboratory devices. For example, the formation of coherent azimuthal structures in a magnetron is shown below in Figure 1.7, and a concern for the role it plays in anomalous transport and plasma behavior in plasma

processing and thin film deposition.

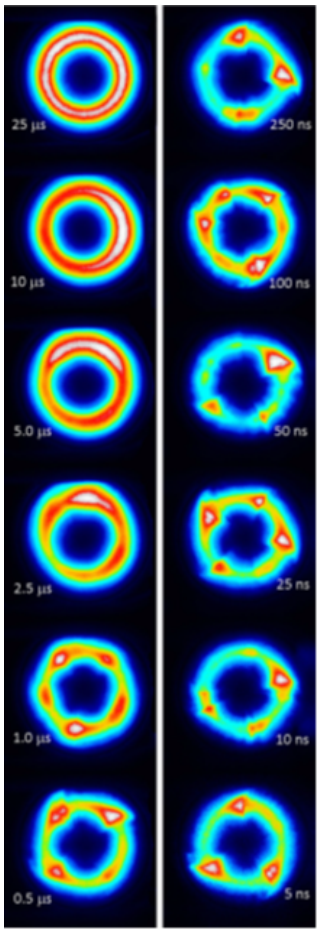

Figure 1.7: Formation of coherent azimuthal oscillating structures in a magnetron, taken from [4].

The focus of this effort is on Hall thruster and Penning-type laboratory discharge applications that produce low-frequency oscillations and coherent structures. Anomalous transport and heating are an issue for both devices, affecting lifetime and performance. Hall thrusters use a radial magnetic field to confine electrons to ionize neutral gas and an axial electric field to accelerate the ions to generate thrust. This results in a E$\times$B drift in the azimuthal direction, leading to a cylindrical design for discharge channels that allow the drift to close on itself. Hall thruster discharges contain a variety of modes and instabilities, but low frequency modes are of particular interest as the fall in the frequency band associated with ion dynamics and are therefore significant for ion thrust. The two modes are aptly referred to as spoke mode and breathing mode due to their respective

behaviors, as indicated in Figure 1.4. The breathing mode occurs in the axial direction, usually on the order of 80 kHz, and has significant effects on the discharge behavior (significant enough to kill the discharge at times) [28, 29]. The spoke mode occurs in the azimuthal direction, at lower frequencies on the order of 20-30 kHz, and is pictured below in Figure 1.8 [30].

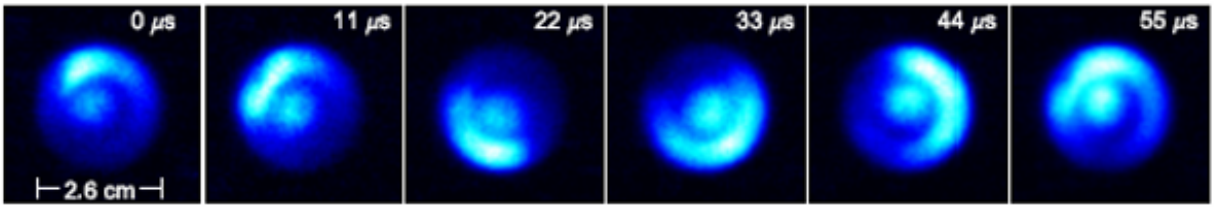

Figure 1.8: Rotating structure (spoke mode) in the discharge channel of a hall effect thruster, taken from [5].

The spoke mode is of particular interest to the problem of anomalous electron transport, the coherent structure has been shown conduct 50% of total radial current and affect thrust and performance [30]. Additionally, the spoke mode can couple with the breathing mode, further driving the instability and causing turbulent axial behavior [29, 31]. Despite the long observed presence of the modes and their impact, the fundamental nature and mechanisms that cause the spoke mode are not yet clearly understood. This impacts predicting performance and lifetime of these thrusters, as the modes cannot be self-consistently modelled and captured. Further complicating the matter are facility effects, where the operation and performance of thrusters on ground versus in-flight varies due to background effects. The growing requirements of space propulsion applications has led to a greater need to understand the role of facility effects, and ultimately, accurately model and predict in-flight thruster performance and lifetime.

The complex dynamical nature of Hall thrusters and the complexities of facility effects motivates the use of a simpler, canonical plasma discharge with similar plasma conditions to investigate the fundamental nature of these low-frequency azimuthal modes. This effort used the Plasma interactions (Pi) facility at UCLA to investigate the nature of a low frequency azimuthal instability believed to be modified Simon Hoh type instability. The facility is used to study and character-

ize advanced materials for plasma boundary applications, but the presence of spoke-like density oscillations can affect studies by causing erosion patterns [32]. Understanding the nature of the low frequency azimuthal mode, specifically the ion motion that is significant to its behavior and its coherent versus turbulent nature, will provide insight on the impact it has on experiments in the facility as well as generally inform the impact it has on other devices, such as the spoke mode in Hall thrusters.

Low-frequency instabilities in the cross field direction of weakly-ionized plasmas were first investigated by Simon and Hoh in the early 1960s [10, 33]. Both concurrently investigated low frequency instabilities in magnetized, partially-ionized cross-field configuration plasmas from an analytical standpoint considering different geometries and demonstrated an $m = 1$ mode that becomes unstable when the electric field and density gradient amplify each other. A more detailed discussion of their findings and their theory is presented in Chapter 6. The occurrence of a Simon-Hoh like instability in an unmagnetized ion scenario was first shown by Sakawa et al. in 1992 [34]. The large ion orbit was thought to contribute to the charge separation that developed the azimuthal fluctuating potential necessary for the instability. The ion motion was noted to be a significant factor in the transition from coherent to turbulent mode, and was further investigated in a follow-up effort [35].

Since the publications of Simon and Hoh, numerous explorations of instabilities in the E×B devices have conducted and, as a result, are tough to comprehensively review and present. Advances in computation modeling and experimental capabilities further support the large quantity of literature available. As such, the critical literature relevant to low-frequency azimuthal oscillations in partially-ionized direct current plasma discharges with unmagnetized ions and their impact on electron transport and turbulence in Hall Effect thrusters and Penning-type discharges are prioritized.

A combination of fluid and kinetic models have been used to investigate anomalous electron transport [36, 37, 38, 39, 40, 41, 11, 29]. A 2013 effort investigating the role of boundary conditions in the direction parallel to the magnetic field has shown that E×B electron drift can drive the

saturation of streaming instabilities leading to strong turbulence [42]. A 2D PIC model of magnetron discharges with spokes shows the occurrence of electron-cyclotron drift instability due to resonant coupling between Bernstein modes and ion acoustic waves that lead to increased cross-field electron transport [27]. A 2017 effort used a fluid model to investigate the role of coupling between ion acoustic mode and E$\times$B electron drift on turbulent transport and coherent structures [43]. A later effort using PIC simulations showed large amplitude coherent modes at electron cyclotron drift resonance and the cascade to low frequency modes [44]. Additionally, nonlinear fluid models have shown that azimuthal drift modes drive axial instabilities, thus driving the instability growth and turbulence [31].

Experimental efforts have used a variety of techniques to investigate the topic. Previous efforts at UCLA conducted by Matlock, Dodson, Goebel, and Wirz have identified a modified Simon Hoh like instability in the Plasma interactions (Pi) facility [45, 46]. The mode has been characterized as a low frequency potential and density oscillations that have been experimentally resolved and shown to contribute to significant anomalous electron transport to the walls and boundaries [47, 12]. Understanding the behavior of this mode is important in characterizing the plasma-material interaction and plasma response of VCMs. They have been shown to cause erosion patterns on the surface of materials [32], as well as sheath instabilities [27, 42] and ionization effects [27] that could impact the infusion and sputtering behavior and analysis. As described in Section 6.4, the angle of incidence caused by the mode can affect the sputtering behavior of the material. The objective of Chapter 6 is to characterize the mode to better understand the impact on ion motion and the PMI process.

1.5 Dissertation Overview

The remainder of this dissertation is organized as follows. Chapter 2 is adapted from a journal paper [2] detailing a novel analytical model evaluating lifetime limiting mechanisms for electrospray thrusters. Chapter 3 is adapted from a journal paper [6] performing the first mass-flux measure-

ments of an electrospray plume and detailing insights on plume physics, lifetime, and performance. Chapter 4 details unique experimental investigation of plasma infusion of volumetrically-complex materials, focusing on measurements of sputtering behavior and plasma response. Chapter 5 details an analytical model for determining sputtering profiles and yields of foams and insights on design for plasma-facing component applications. Chapter 6 then details the characterization of a low-frequency azimuthal mode in the Pi facility for the role it plays in the plasma-material interaction experiments and fundamental nature of the mode. Chapter 7 finally summaries the key conclusions of the dissertation and future work. Additionally, appendices are used to provide extra details and insights on topics that may be of interest to certain readers.

CHAPTER 2

Electrospray Life Estimation

This chapter describes lifetime estimation techniques for electrospray propulsion. The content has been adapted from a journal paper [2] and a conference proceeding [48]. The objective was to develop a framework for designing long-lifetime electrospray thrusters and to guide experiments that seek to evaluate thruster lifetime. Lifetime limiting mechanisms are identified, characterized, and examined to understand and predict thruster lifetime.

2.1 Lifetime Limiting Mechanisms

Electrospray thruster lifetime depends on numerous design parameters and multi-tier life mechanisms, as outlined in Figure 2.1. Considerations for thruster design may be separated into three categories: operation and control, geometry, and material and propellant selection. Operation and control encompasses static and dynamic operation parameters such as applied potentials, emitted flow rate, emitted current, thrust command variations, and startup and shutdown transients. The physical design parameters of the thruster, such as spacing between electrodes or thickness of the grids, are captured in the geometry, while the chemical and thermal response considerations are encompassed by material and propellant selection.

The ultimate failure mechanism for electrospray thrusters is shorting and Power Processing Unit (PPU) Failure, which can result from a variety of first and second tier mechanisms, as shown in Figure 2.1. The primary first-tier mechanism implicated in electrospray failure is overspray, which is defined as any emission that directly impinges on the grids. The impinging flux is de-

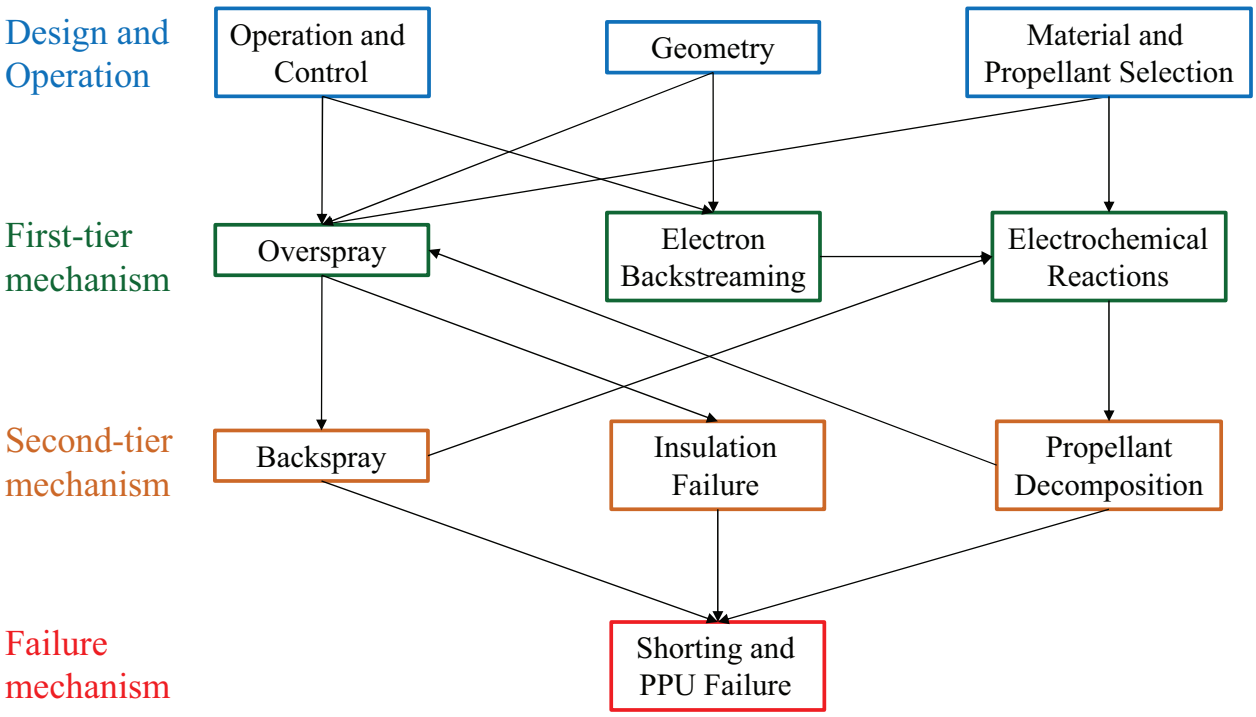

Figure 2.1: Hierarchical failure tree for electrospray life describing different failure modes and paths, from [2].

pendent on static and transient emission properties related to operation and control of the thruster, such as emitter voltage, emitted flow rate, varying thrust commands, or startup and shutdown operations. As shown in Figure 1.3, the geometry of the electrodes determines the minimum line of sight half-angle that will result in grid impingement. Additionally, misalignment of the electrodes can result in increased flux to the grids. A detailed approach for characterizing overspray based on electrode geometry and misalignment is described section 2.2. Propellant accumulation on the grids from overspray, coupled with sufficiently strong electric fields, can lead to emission of the opposite polarity back to the emitter, known as backspray. Further, insulation failure can occur due to propellant wetting of the insulator materials, resulting in electrode shorting. These two scenarios can be treated as second-tier mechanisms since they result from the first-tier mechanism of overspray. To delay the onset of backspray, porous grids can be used to absorb the impinging

propellant [49]. Since grid saturation leads to backspray, the wicking rate and absorption capability/capacity of porous grids must be carefully considered. For example, pore size has been shown to have a strong effect on the emission from porous emitters [50] and is expected to have the same influence on backspray from porous grids.

In addition to propellant accumulation from overspray, other considerations can contribute to reduced lifetime. Flux of electrons towards the emitter due to the positive potential of the emitter, known as electron backstreaming (EBS), can induce electrochemical reactions in the propellant that can result in emitter damage and propellant decomposition near the emission site [51]. Chemical reactions due to the electric double layer can also contribute to propellant decomposition [52, 53], leading to growth of undesirable byproducts on, or near, the emission surface. The propellant decomposition causes variations in fluid properties that affect the emission behavior, and therefore can lead to increased overspray. The accelerator grid is typically used to shield against EBS, which requires careful selection of operating voltage and geometry for successful implementation. Additionally, startup and operational transients can induce periods of unsteady emission that produce increased overspray emission [54, 55].

2.2 Life Model Approach

2.2.1 Overspray

While many lifetime-limiting mechanisms exist, the primary concern for the electrospray thruster is overspray to the grids. Such overspray will coat the grids and can lead to shorting of the high potential electrodes. If porous grids are utilized, then the time to failure can be estimated as the time needed for overspray to effectively fill the grids. As detailed in Figure 2.2, grid impingement (fluxes 2 and 3 in Figure 2.2) can be categorized via two mechanisms that lead to propellant flux to the extractor and accelerator grids. The primary mechanism is direct overspray (indicated by fluxes 4 and 5 in Figure 2.2), from the emission site, where the plume expansion begins, to the extractor and accelerator grids. The secondary mechanism is radial expansion of the plume due to

repulsion and fragmentation of emitted charged species [56, 57] and electric field divergence, with the resulting increase in radial motion in the emitter-accelerator region causing propellant flux to the grids (indicated by 6 and 7 in Figure 2.2). Propellant accumulation on the grids due to these two mechanisms coupled with a sufficiently strong electric field may lead to backspray (indicated by 8 and 9 in Figure 2.2).

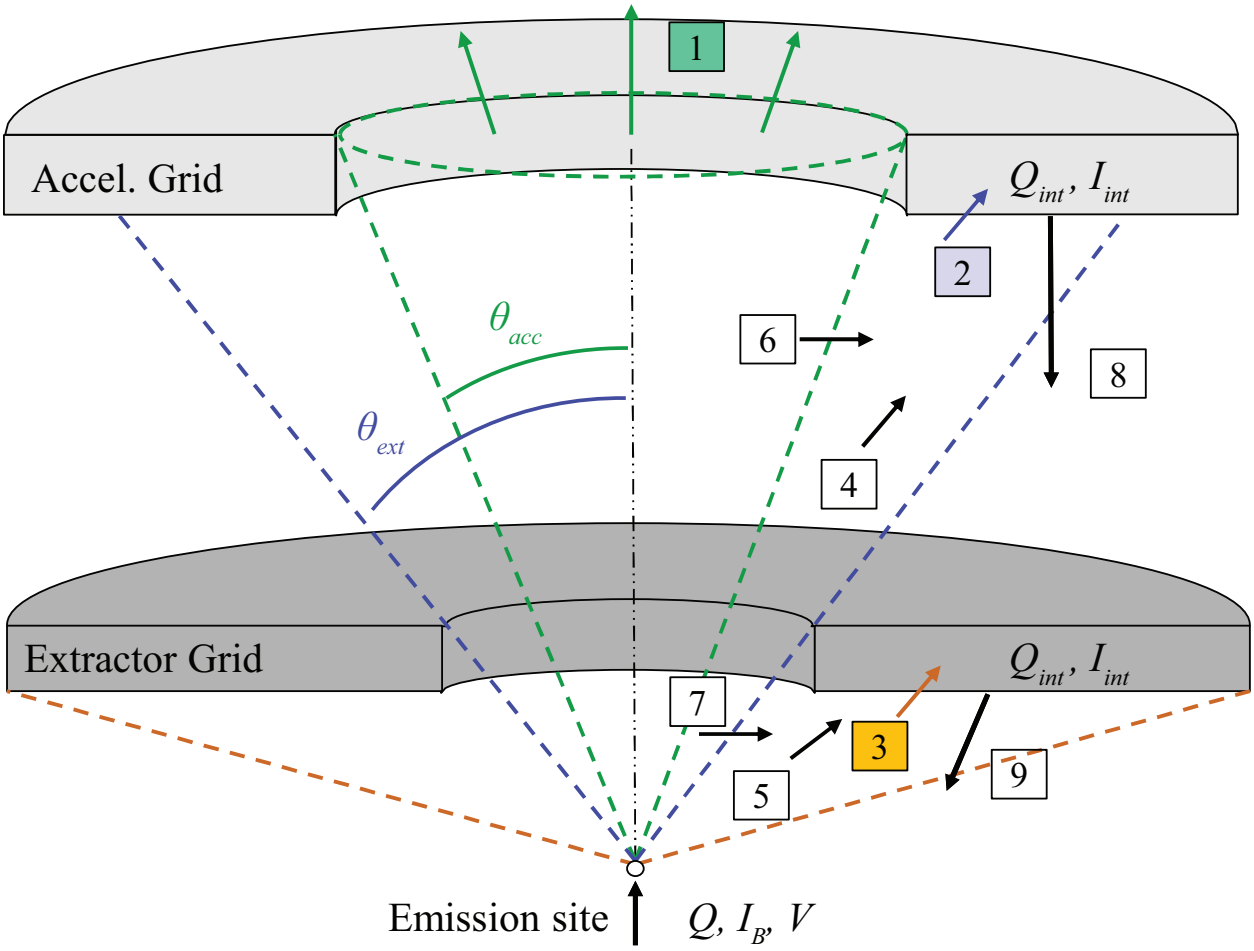

Figure 2.2: Emission from an electrospray that passes through the accelerator grid produces thrust (1). Additional non-thrust emission pathways exist that lead to lifetime reduction (numbered). From [2].

Recent electrospray modeling efforts have sought to use molecular dynamics (MD) simulations to understand the behavior of electrosprays through simulation of the forces on each molecule. While MD provides useful results concerning the emission of ions from an electrified meniscus,

high fidelity with experimental results has not been explicitly shown for cone-jet emission; for this reason we do not use results from MD simulations to inform this effort yet. The current state of the art suggests that MD simulation is a valuable tool for predicting emission of ions and small clusters but does not adequately represent the cone-jet structure for droplet mode electrospray emission [58, 59, 60, 61, 62].

While ion emission may influence the lifetime of electrospray devices, the majority of emission from the Taylor cone in cone-jet emission mode is in the form of droplets. Thus, any simulation technique must capture the behavior of the large, heavy droplets that dominate the plume. Simulating the emission process through MD would require modeling the cone-jet structure and hundreds of droplets. Through evaluation of the characteristic radius of the jet emerging from the Taylor cone, each droplet is estimated to contain on the order of 1000 EMI-Im molecules for the thruster in the presented effort [63]. Modeling droplet emission from a cone-jet structure requires including several orders of magnitude more molecules in a simulation than in a single droplet; the state of the art is currently modeling up to tens of thousands of molecules [58, 59, 60, 61, 62]. Predicting electrospray behavior on the scale of the jet and droplets requires orders of magnitude increase in the capabilities for simulating large numbers of molecules. It is for this reason that the presented effort has focused on well-established empirical relations for the emission in cone-jet mode and experimental results for the distribution of droplets in the plume.

While plume expansion exists and its role in reducing thruster lifetime has been identified, in this study the effects are considered negligible. Plume expansion is neglected due to the electrospray emission occurring in vacuum rather than in atmosphere. Emission in atmosphere has the effect of decelerating emitted droplets, increasing the space charge density and thus the repulsion between droplets [64]. Without drag in vacuum, any initial spread in the plume causes the repulsion experienced by nearby droplets to decrease rapidly. This likely results in plumes largely without expansion after only a few jet diameters [57], or on the order of 20 nm for the thruster of interest of this study. Furthermore, variations in the velocity and specific charge of emitted droplets may cause intermittent expansion events in the plume [54]. These events are only considered as

part of this study insofar as they contribute to a Gaussian-like distribution of charge in the plume. Numerical simulation of the plume as a collection of charged particles is sought as a means of understanding how local droplet interactions may lead to plume expansion [65, 66].

Gamero-Castaño showed that current density profiles of capillary electrospray emission can be described using Gaussian-like distributions for EMI-Im [67]. Current density profile measurements of the CMNT reported in [68] also exhibit Gaussian-like distributions and indicate that any current beyond $\sim 25^{\circ}$ half-angle is minimal. However, current density profiles and mass flux profiles can deviate from each other as there is no expectation or requirement that charge-mass ratio be uniform throughout the beam [7]. For example, lower charge-mass ratio droplets at high angles can result in significant mass flux while representing negligible current to the grids. So while current collected by the grids can be an indicator of high impingement, mass flux is the specific mechanism that leads to grid saturation, which can result in backspray and/or insulator wetting. Therefore, minimizing *mass flux*, rather than current, to the grids is the principal factor in increasing the lifetime of electrospray thrusters. Further, even with an extremely small mass flux, grid saturation can occur over long operation time.

In lieu of direct mass flux measurements, mass flux can be estimated from the current density through empirically determined scaling laws and experimentally determined constants. De La Mora [69, 70] has previously shown that in cone-jet operating mode, emitted current can be empirically related to emitted flow rate as described in Equation 2.1:

$$I_B = C_1 Q^{\frac{1}{2}}, \tag{2.1}$$

where I_B is the emitted beam current, C_1 is the flow rate coefficient, and Q is the volumetric flow rate.

The relationship between current and flow rate can be used to estimate thrust based on momentum conservation. The beam current is determined from the commanded thrust, T_{com}, and emitter voltage, V, as shown in Equation 2.2:

$$T_{com} = C_2 I_B{}^{\frac{3}{2}} (V - V_{TC})^{\frac{1}{2}}, \tag{2.2}$$

V_{TC} is the potential drop across the Taylor cone. The thrust coefficient $C_2 \propto \sqrt{\varepsilon\rho/\gamma\kappa}$, takes the nominal value $0.0319\,\mu\mathrm{N}\cdot\mu\mathrm{A}^{-\frac{3}{2}}\cdot\mathrm{V}^{-\frac{1}{2}}$ [71], where ε is relative permittivity, ρ is mass density, γ is surface tension, and κ is conductivity. The analysis for determining the thrust and flow rate relations can be repeated for ion emission mode, yielding a relation similar to Equation 2.2 [72].

Mass flux, $\dot{\boldsymbol{M}}$, and current density, $\boldsymbol{J}$, functions are now defined in spherical polar coordinates with the origin at the emitter tip, then taken to be azimuthally symmetric, and spherically expanding. The mass flux and current density are only dependant on the polar angle, θ, given by Equations 2.3 and 2.4,

$$\dot{\boldsymbol{M}} = \dot{m}(\theta)\hat{\boldsymbol{r}}, \tag{2.3}$$

$$\boldsymbol{J} = j(\theta)\hat{\boldsymbol{r}}, \tag{2.4}$$

where $\dot{m}(\theta)$ and $j(\theta)$ define the mass flux and current density angular distribution profiles per steradian respectively.

In the general case, $\dot{m}(\theta)$ and $j(\theta)$ are defined by arbitrary functions $f(\theta)$ and $g(\theta)$, which are scaled via F_{full} and G_{full} in Equations 2.5 and 2.6 to match the input flow rate and current.

$$\dot{m}(\theta) = \frac{Q\rho}{F_{full}} f(\theta), \text{ where } F_{full} = \int_0^{\pi} 2\pi \sin\theta f(\theta) \mathrm{d}\theta. \tag{2.5}$$

$$j(\theta) = \frac{I_B}{G_{full}} g(\theta), \text{ where } G_{full} = \int_0^{\pi} 2\pi \sin\theta g(\theta) \mathrm{d}\theta. \tag{2.6}$$

The exit velocity distribution, $v_{exit}(\theta)$, is determined from the charge and mass distributions together,

$$v_{exit}(\theta) = \sqrt{2\frac{j(\theta)}{\dot{m}(\theta)}V_B} = \sqrt{2V_B\frac{I_B F_{full}}{Q\rho G_{full}}}\sqrt{\frac{g(\theta)}{f(\theta)}}, \tag{2.7}$$

(where $V_B = V - V_{TC}$), which is then combined with the mass flux to create a thrust element $\mathrm{d}T$ that can be integrated over the half-space to calculate the total thrust, T_{calc}, described in Equation 2.9:

$$\mathrm{d}T(\theta) = \dot{m}(\theta)v(\theta)\cos\theta; \tag{2.8}$$

$$\begin{aligned} T_{calc} &= \int_0^{\frac{\pi}{2}} \dot{m}(\theta)v_{exit}(\theta)\cos\theta 2\pi\sin\theta \mathrm{d}\theta \\ &= \pi\sqrt{\frac{2V_B I_B Q\rho}{G_{full}F_{full}}}\int_0^{\frac{\pi}{2}} \sqrt{f(\theta)g(\theta)}\sin(2\theta)\mathrm{d}\theta. \end{aligned} \tag{2.9}$$

For a given $f(\theta)$ or $g(\theta)$, $g(\theta)$ or $f(\theta)$ respectively are parameterized and iterated until T_{com} of Equation 2.2 and T_{calc} of Equation 2.9 are within a specified range, providing fully-defined estimates of the mass flux and current density distributions commensurate with empirical relations.

It is assumed that the flux to the extractor grid is many orders of magnitude smaller than the flux to the accelerator grid for geometries where the accelerator grid line of sight (θ_{acc}) is smaller than the extractor grid line of sight (θ_{ext}). The failure of the accelerator grid is therefore the primary lifetime concern; the onset of backspray is now defined as the time at which the accelerator grid saturates, t_{sat}, and is treated as the end-of-life criterion. t_{sat} is calculated via Equation 2.10,

$$t_{sat} = \frac{\rho \forbidden{V}_{crit}}{\dot{m}_{loss}}, \tag{2.10}$$

where $\forbidden{V}_{crit}$ is the critical accumulated propellant volume at which the accelerator grid is saturated, and $\dot{m}_{loss}$, is the rate of mass impingement on the accelerator grid, calculated as in Equation 2.11,

$$\dot{m}_{loss} = 2\pi \int_{\theta_{acc}}^{\frac{\pi}{2}} \dot{m}(\theta) \sin\theta \mathrm{d}\theta \tag{2.11}$$

$\forall_{crit}$ is a tunable parameter which is a fraction of the open volume of the porous grid. In the present study $\forall_{crit}$ is nominally taken to be the open volume of the porous grid, but future analysis can be further-informed by experiments that demonstrate the fill-fraction at which backspray occurs.

The algorithm for determining the time to grid saturation, t_{sat}, is outlined in Figure 2.3. Note that no restriction has been placed on the functional form of $f(\theta)$ and $g(\theta)$ beyond it being finite within the half-space.

2.2.2 Electron Back-streaming

Due to large grid apertures and the large positive potential at the emitter, electron back-streaming (EBS) from downstream of the thruster towards the emitter is likely. Similar to ion thrusters, a negative voltage applied on the accelerator grid creates a potential barrier to minimize the back-streaming electron current [73]. An analytical process similar to that performed by Wirz *et al.* for the NSTAR thruster [73] is carried out for various geometries. The electron density is assumed to be equal to the charge density downstream of the accelerator grid as specified by charge neutralization requirements.

An estimate of the space charge density, q_{sc}, is analytically determined by dividing $j(\theta)$ (Equation 2.6) by $v_{exit}(\theta)$ (Equation 2.7), at a spherical radius from the plume origin, r_{sph}, resulting in Equation 2.12,

$$q_{sc}(r_{sph}, \theta) = \frac{1}{r_{sph}^2} \sqrt{\frac{I_B Q \rho f(\theta) g(\theta)}{2 V_B F_{full} G_{full}}}. \tag{2.12}$$

q_{sc} is calculated to be $\sim 1 \times 10^{-10}\,\mathrm{C \cdot sr^{-1}}$ on-axis for nominal operating conditions if a Gaussian plume profile is assumed.

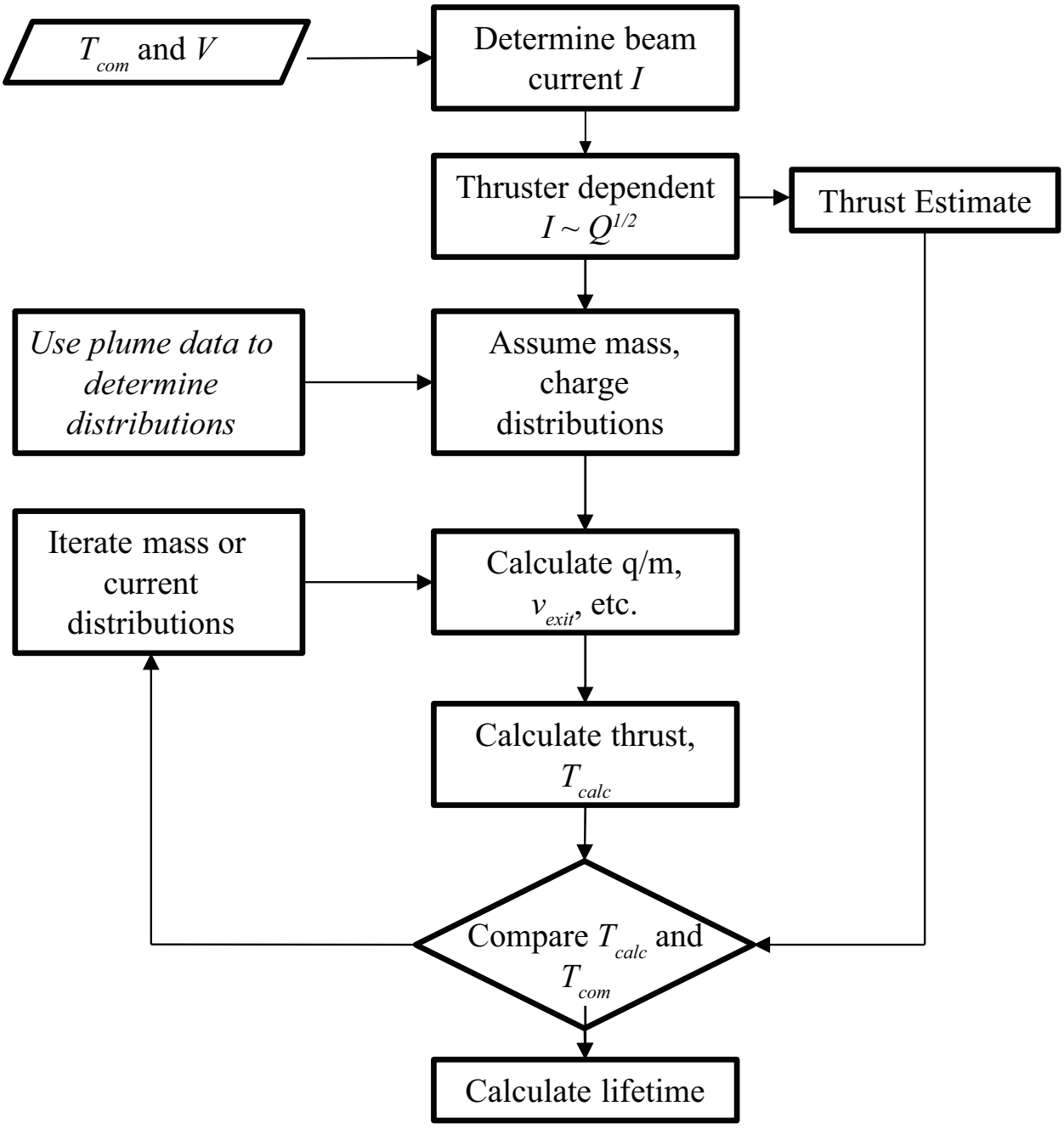

Figure 2.3: Description of grid impingement life model detailing required inputs and iterative process employed to determine lifetime estimate, from [2].

The minimum potential along the axial path defines the potential barrier that retards electron back-streaming, as shown in Figure 2.4. The potential is a superposition of the applied field and space charge contribution. As shown in Equation 2.13,

$$V_{sc} = \frac{1}{2\varepsilon_0}\sqrt{\frac{I_B Q \rho}{2V_B}}\sqrt{\frac{1}{G_{full}F_{full}}}\int_0^{\theta_{acc}}\int_0^{r_{neut}}\frac{\sqrt{f(\theta)g(\theta)}\sin\theta}{\sqrt{h_{sp}^2 + r_{sph}^2 - 2r_{sph}h_{sp}\cos\theta}}\mathrm{d}r_{sph}\mathrm{d}\theta, \tag{2.13}$$

where h_{sp} is the emitter-accelerator spacing, the space charge potential on axis at the accelerator (V_{sc}) is calculated by summing the contribution of the charges in the plume, integrating out to a neutralization distance (r_{neut}) of 1000 times the spacing between the emitter and accelerator electrode (considered to be beyond the distance at which the plume would be neutralized by external sources.). The resulting space charge potential is on the order of 2 V, which is more than an order-of-magnitude smaller than the minimum potential in the barrier and is thus ignored in further analysis.

For the purposes of lifetime estimation philosophy and obtaining a tractable analytical form, a Maxwellian distribution of electrons is assumed downstream of the thruster. This has been shown to be the case for ion thrusters [73] and provides a reasonable estimation for worst-case scenarios for electrospray thrusters, especially when experimental data to guide this process are not currently available. Alternative electron distributions, e.g. Druyvesteyn, are possible and are the subject of future research efforts. For the present effort, the effects of bulk electron energy on electron backstreaming were estimated by varying the temperature of a Maxwellian electron distribution function as done by Wirz *et al.* [73] The portion of the Maxwellian electron distribution function with enough energy to overcome the potential barrier and stream into the thruster can be described by Boltzmann's relation relating density to the exponential of local potential and distribution temperature. This one-sided electron flux to the emitter as a function of the radius from the centerline, $\Gamma_e(r)$, is dependent on the temperature of the electrons, T_e, the magnitude of the potential barrier along the axial path as a function of the radius from the centerline in cylindrical coordinates, $\phi_m(r)$,

the local electron number density, n_e, and mean thermal speed, $\bar{c}$, as shown in Equation 2.14:

$$\Gamma_e(r) = \frac{n_e \bar{c}}{4} \exp\left(\frac{\phi_m(r)}{T_e}\right). \tag{2.14}$$

Integrating the flux from the centerline to the grid radius, r_{max}, and assuming azimuthal symmetry leads to the electron back-streaming current (J_{EBS}) shown in Equation 2.15:

$$J_{EBS} = 2\pi e \int_0^{r_{max}} r\Gamma_e(r)\,\mathrm{d}r. \tag{2.15}$$

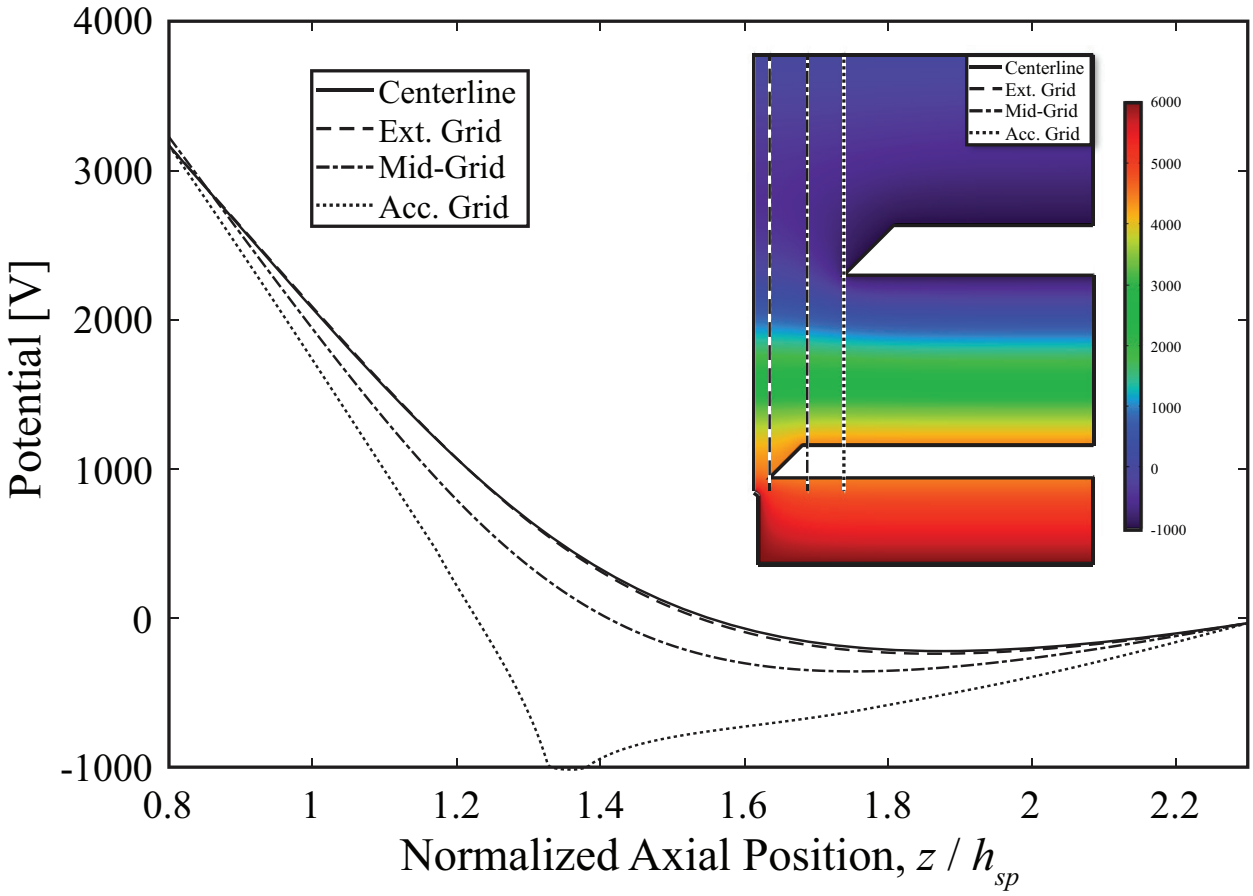

Figure 2.4: Electric potential along various axial lines showing the potential well that retards back-streaming electrons. Inset: Electric potential for nominal geometry with varying axial lines indicated. From [2].

This approach is utilized to determine the EBS current for a specific geometry. The implications of varying geometric parameters and bias voltages are discussed in the following section.

2.3 Plume and Geometry Implications

2.3.1 Life Estimation

Experimental data from CMNT ground testing [68] is used as the base current profile to inform the model. As the measured data are restricted to a half angle of 20°, the values at larger half angles, crucial to determining grid impingement flux, are extrapolated by fitting Gaussian distributions to the data, shown in Figure 2.5a). The current density profile, $g(\theta)$, is therefore set to a Gaussian distribution, parameterized by a width σ_q, and the mass flux function, $f(\theta)$, is assumed to be Gaussian parameterized by width σ_m. Iterating σ_m to satisfy equations 2.1, 2.2, and 2.9 yields two solutions for the mass flux distribution, where one width (σ_m) is larger than σ_q and one smaller. Further analysis assumes the $\sigma_m > \sigma_q$ case, as it provides a worse-case lifetime calculation (see Figure 2.5b), and has been preliminarily observed in simultaneously-measured mass flux and current density distributions of an electrospray plume [7].

To estimate the uncertainty in grid saturation time of this device, a full-scale error of 7.5% for the experimental dataset is assumed, which additionally encompasses a range of similarly-measured plume profiles [74, 75, 76, 77, 67, 7, 78]. Gaussian distribution fits based on the least squares method are determined for the best, nominal, and worst-case scenarios of the estimated spread of the current profile data. The resulting beam current profiles, described by the standard deviation of the Gaussian profile, σ_q, are indicated in Figure 2.5a). At large angles, the assumed error results in uncertainty in current flux that exceeds the nominal values by over an order of magnitude, highlighting how data in the large half-angle regions, especially mass flux, can greatly improve understanding of beam profiles associated with this emission mode and lifetime of electrospray devices.

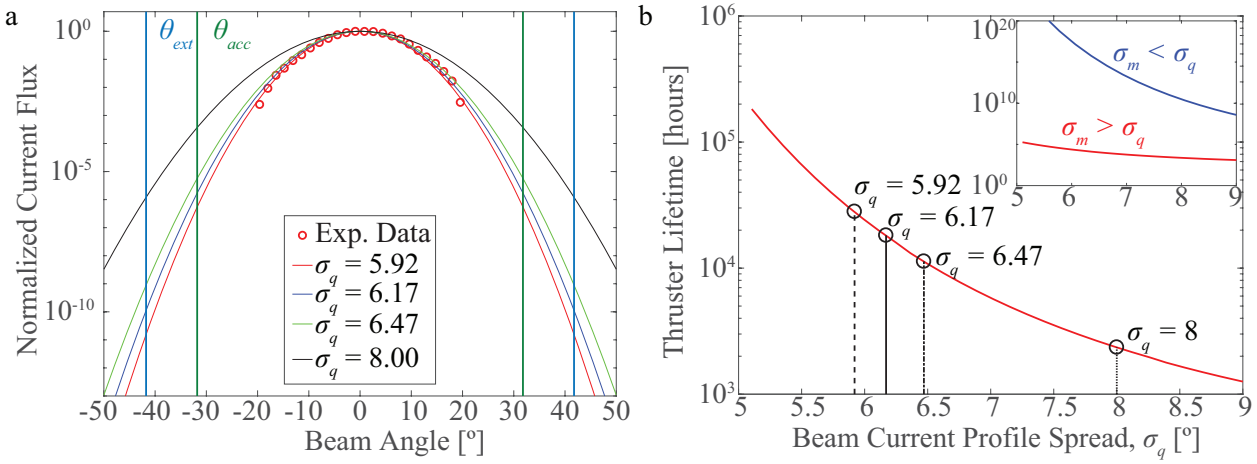

Figure 2.5: a) A range of Gaussian fits to CMNT current profile data assuming 7.5% full-scale error and a normal fit indicating a current profile outside full-scale error but within uncertainty in the high-angle region. θ_{acc} in the given case is 32°. b) Life model predictions for thruster lifetime as a function of current profile standard deviation with data fits from a) indicated. Inset shows the lifetime calculation for both values of σ_m that satisfy Equation 2.9. From [2].

The impact of beam current profile on accelerator grid saturation time is shown in Figure 2.5b) to provide a comparison to experimental data. As the beam current profile grows in width (increased σ_q), the mass flux width σ_m also grows, leading to increased impingement. The model indicates an expected lifetime of approximately 18,000 hours for the nominal fit to the CMNT data (assuming a constant thrust command of 10 μN), with a range of 11,000 - 28,000 hours for worst to best case scenarios. The broader beam current profile, described by a standard deviation of 8.00°, demonstrates the reduction in lifetime poor emission behavior can cause.

While it is tempting to work only with Gaussian distributions for $f(\theta)$ and $g(\theta)$, there is no requirement that the plume take such a form. Indeed, examples of non-Gaussian mass flux and current density have been reported [6, 7, 67, 76]. The origins and implications of non-Gaussian plumes will be considered in a further publication, and further analysis in this paper will assume Gaussian plume profiles as described in Equation 2.16:

$$f(\theta) = \exp\left(-\frac{\theta^2}{2\sigma_m^2}\right). \tag{2.16}$$

The time to saturate the accelerator grid is dependent on a variety of factors such as the accelerator grid aperture, the applied electric field, the spacing between emitter and accelerator grid, and the open volume of the porous material, generally characterized by θ_{acc} and V_{crit}. The accelerator grid aperture and spacing between emitter and the accelerator grid can be collectively represented using θ_{acc}. Assuming the effects of plume expansion to be negligible, the impact of varying accelerator grid aperture and emitter-accelerator grid spacing is illustrated in Figure 2.6 using curves of constant geometric factors. Changes to geometry that do not affect beam profile, such as minor changes to θ_{acc} or varying the porosity or open volume of the porous grid, result in vertical translation between curves. Changes to beam profile, such as varying operational setpoints or applied electric field, cause shifts along the curve for a specified geometry.

It is evident that the best method for improving lifetime is better beam confinement, but geometry alterations to increase θ_{acc} can provide the desired lifetimes as well. While methods of improving beam confinement were not part of this effort, an analysis of accelerator grid geometry was performed to determine the implication of different approaches to θ_{acc} changes. As shown in Figure 2.7, a nominal geometry with $\theta_{acc} = 32^\circ$ is assumed. Alternate geometries with larger θ_{acc} were then generated by increasing the accelerator grid radius, decreasing the spacing between the accelerator grid and emitter, and a combination of both changes. The geometry of the extractor in relation to the emitter is held constant in all cases. The applied potential on the extractor and emitter are significantly larger than the potential on the accelerator grid as detailed in [13]. Therefore, small changes to the accelerator grid geometry do not substantially influence the field near the emitter and consequently the emission behavior. As a result, small changes to θ_{acc} are assumed not to affect emission behavior. As shown in Figure 2.8, relatively small changes to θ_{acc} yield a significant gain in grid saturation time. Decreasing the grid spacing and increasing grid aperture both increase grid saturation time similarly due to a nearly equivalent effect on θ_{acc}. Although neither change alone produces the desired lifetime, the combination of changes creates a geometry

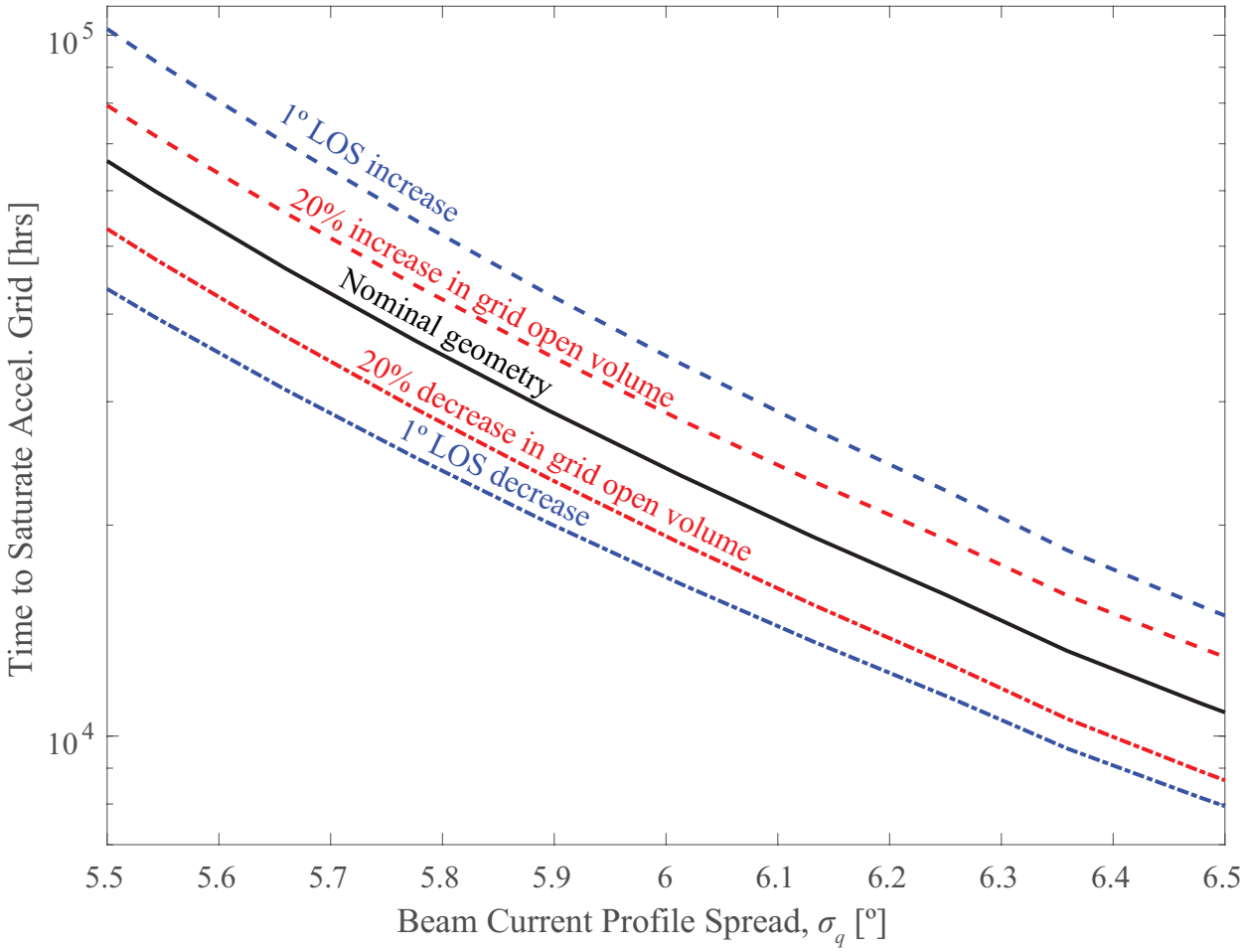

Figure 2.6: The effects of geometry changes, porous grid capacity, and beam shape (indicated by standard deviation) on accelerator grid saturation time, from [2].

with a much larger θ_{acc} and resulting lifetime.

Large changes to grid spacing or aperture can impact parameters that contribute to lifetime considerations. For example, increasing the accelerator grid aperture radius decreases the volume of porous grid between emitters (septum). Decreasing the volume of porous material decreases the volume of propellant that can be accumulated before saturation and backspray occur ($\forall_{crit}$). In order to maintain the open volume in the septum, the emitters need to be shifted further apart, introducing potential design challenges. Decreasing grid spacing is not a simple solution either as it will increase the electric field magnitude downstream of the extractor grid. The rise in electric

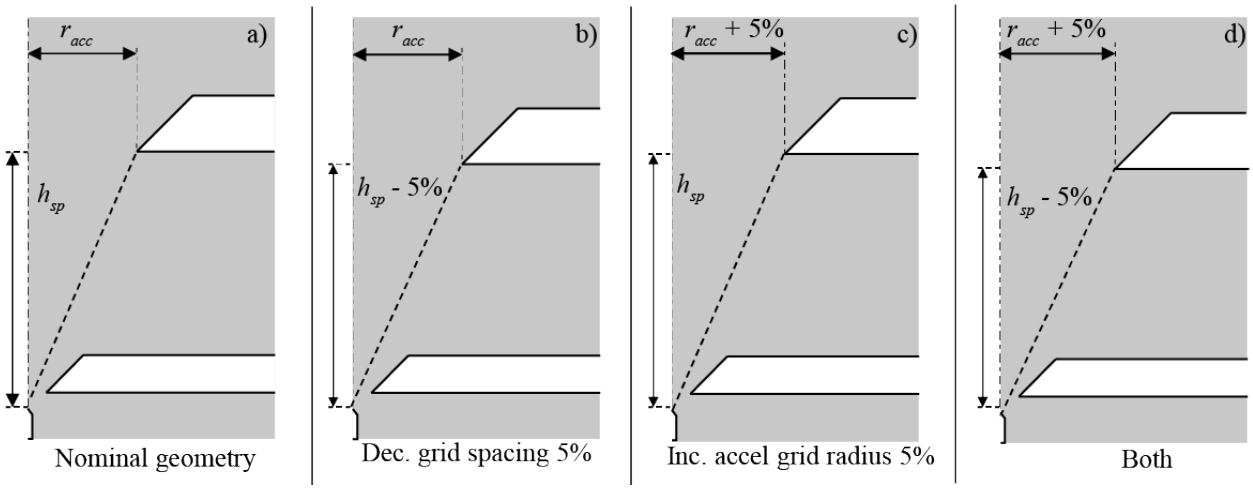

Figure 2.7: Varying accelerator grid geometries demonstrating methods to increase θ_{acc}. Extractor grid geometry is held constant in all configurations to ensure emission behavior is not affected. From [2].

field may expedite the onset of backspray emission. Additionally, changes to the electric field downstream of the emission region can lead to increased plume divergence [79] and increased fragmentation of droplets, both of which may result in increased mass flow to the grids.

2.3.1.1 Misalignment and Tolerances

The significance of minuscule mass flux to the porous grids causes even small misalignments to have a substantial impact on lifetime. To estimate this effect, the overspray estimation approach was adapted to calculate intercepted flux in 3D, while maintaining the assumption that minor changes to accelerator geometry have negligible impact on the plume characteristics. These assumptions approximate the case where the emitter is concentric with the extractor aperture but not necessarily concentric with the accelerator aperture. In this case, the θ_{ext} is constant while θ_{acc} is a function of the azimuthal angle around the emitter. Thus, a lateral offset in alignment of the emitter to the accelerator aperture decreases the line of sight angle in the direction of the offset while increasing the line of sight angle in the direction opposite to the offset. These two cases represent the extremes of θ_{acc} with all other azimuthal angles having an intermediate value

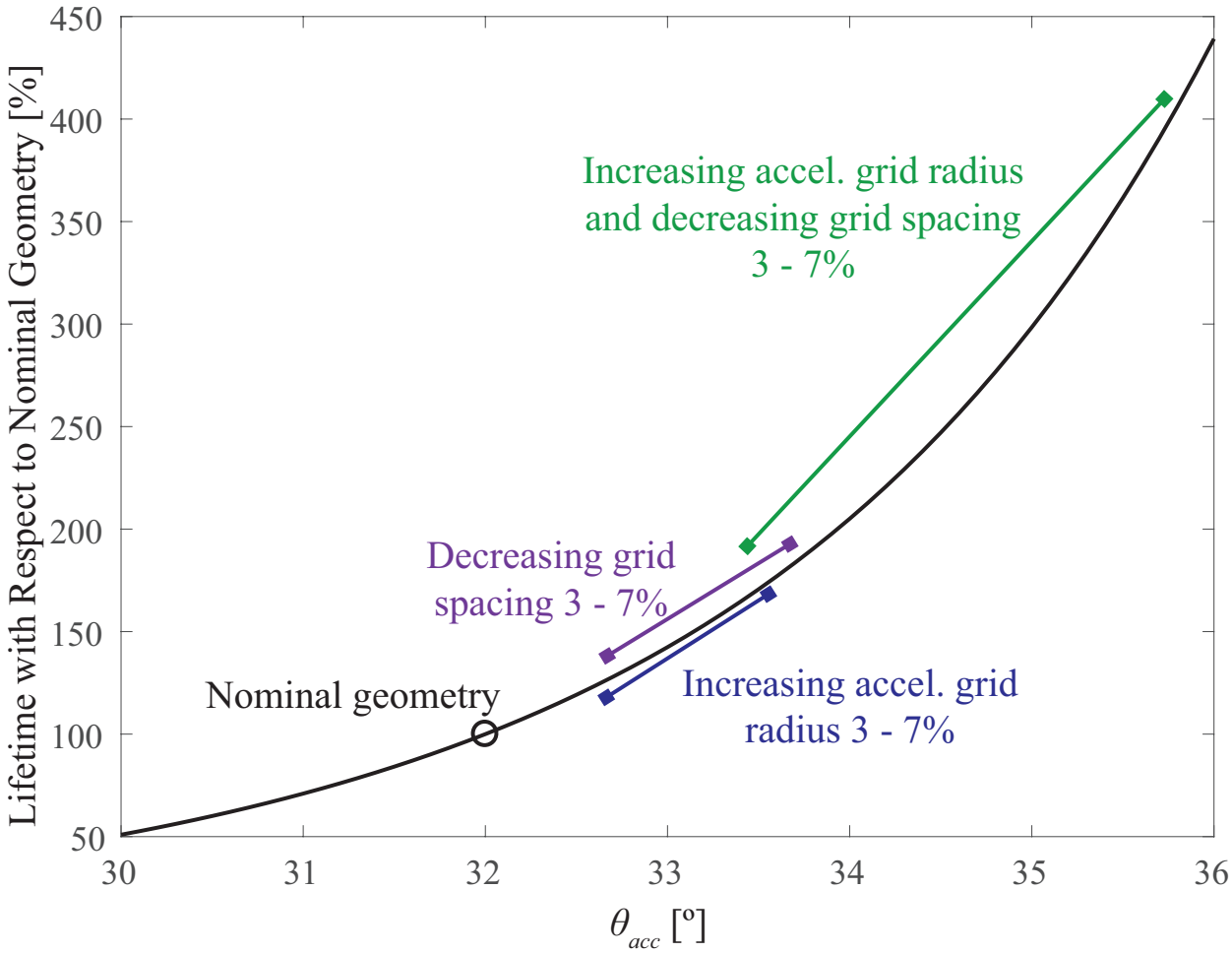

Figure 2.8: The effect of changing accelerator grid aperture radius and spacing between accelerator and extractor grids on time to saturate the accelerator grid, from [2].

of θ_{acc}. The overspray to the accelerator grid is estimated by calculating the overspray flow rate per azimuthal angle and integrating about the emitter axis. The decrease in lifetime with any lateral offset is a consequence of the non-linear decrease in flux with polar angle: a small decrease in θ_{acc} causes a large increase in the overspray flow rate. To transition from a single emitter to a multi emitter lifetime estimation, the overspray flow rate into the accelerator grid from each emitter is summed. The time required to fill the grid is the total volume in the grid divided by the total flow rate into the grid from all emitters together. As shown in Figure 2.9, accelerator misalignment can significantly reduce lifetime. For example, in a thruster containing 9 emitters, introducing a 4%

offset in the accelerator grid aperture from the emitter axis for just two emitters can reduce thruster lifetime by 5%, while introducing this offset for all nine accelerator apertures can result in a 25% reduction of lifetime.

After investigating the reduction in accelerator grid saturation time due to accelerator misalignment, the expected degree of misalignment in an electrospray thruster was estimated using tolerance stackups. Multiple tolerances and misalignments were evaluated to determine the potential impacts on lifetime of thrusters with designs similar to the CMNT. For this analysis, dimensional variations are assumed to be independent of design tolerances [80]. The central accelerator aperture was assumed to be manually aligned to the central emitter, resulting in a degree of misalignment. The individual emitters all possess an inherent misalignment with respect to the mounting structure from the mounting process. The accelerator grid manufacturing process determines positioning tolerance with respect to the mounting holes on the thruster and can result in an offset with respect to all emitters. Additionally, the mounting hole clearance can introduce a rotational offset. Each of these tolerances are considered together in order to determine the maximum resulting misalignment for each emitter in the thruster head.

The accelerator aperture alignment, mounting hole positioning, and mounting hole clearance were all assumed to have a 3.1% non-dimensional tolerance. The emitter position tolerance was approximated as 7.7%. For the purpose of establishing a distribution of misalignments, it was assumed that the features contributing to misalignment were produced by a process by which 95% of resulting features would be within the design tolerance. A single Gaussian distribution was used to approximate the stack-up of all the tolerances. This resulted in a maximum misalignment of 3.1% for the center aperture and 7.5% for the side and corner apertures due to stack-up of offsets. Assuming a realistic distribution of misalignment leads to an approximate 20.8% lifetime reduction. Assuming worst case, where each aperture is at maximum misalignment, a 46.9% lifetime reduction is possible. The manufacturing, alignment, and handling process of these devices is crucial to ensuring long lifetimes.

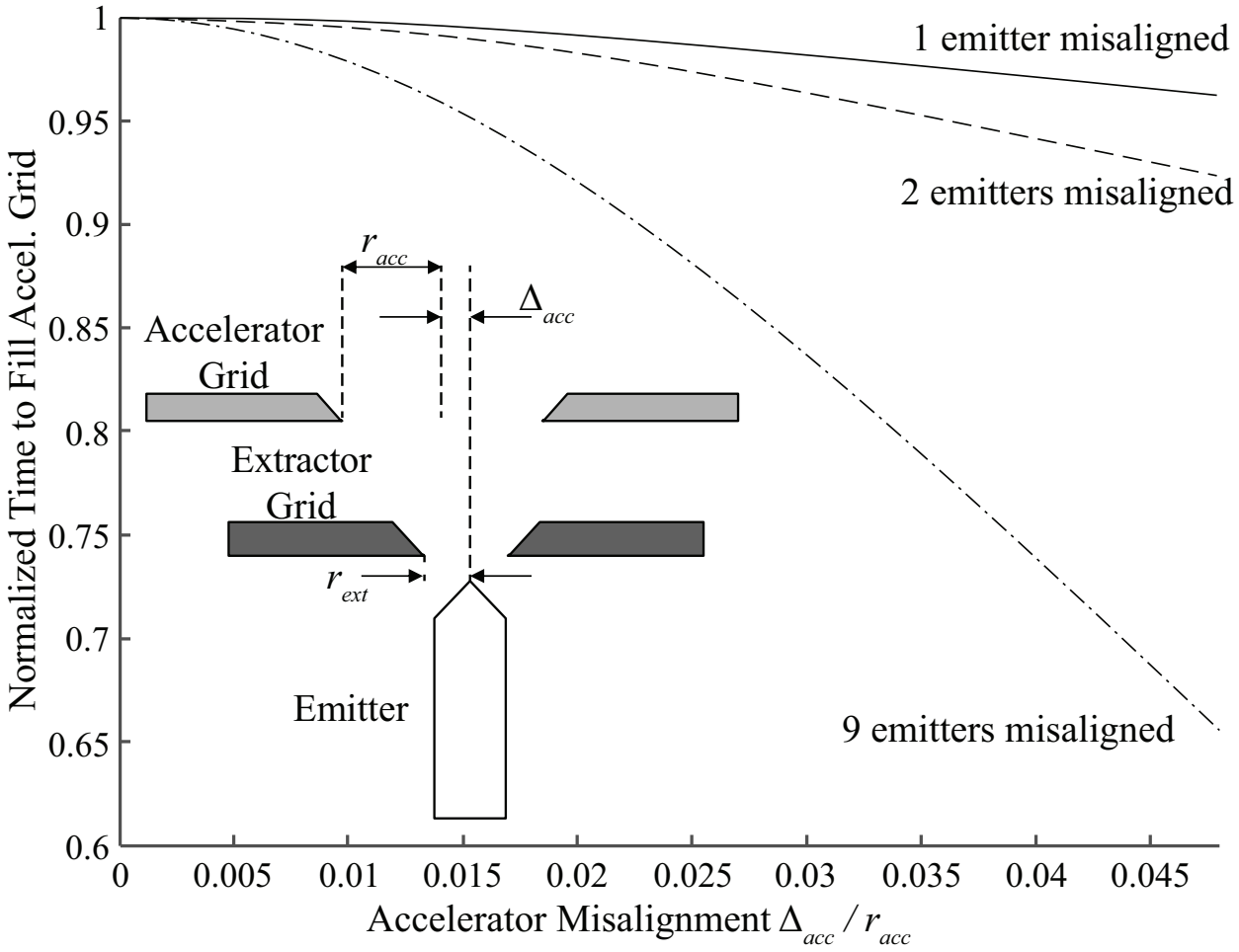

Figure 2.9: Misalignment can result in accelerator grid aperture offset from emitter centerline; the impact of accelerator aperture misalignment on accelerator grid fill time is shown. From [2].

2.4 Electron Back-streaming Effects

Emission properties and beam profile are dependent on propellant properties, specifically near the emitter tip. Chemical reactions due to electron back-streaming can impact propellant properties. The negative potential bias of the accelerator grid serves as a barrier against EBS. Figure 2.10 shows the current density and minimum potential as a function of distance from the centerline for geometries described in Figure 2.7, as computed using Equations 2.15 and 2.14 respectively. Similar to the EBS behavior in ion thrusters, the majority of electron flux is along the centerline

of emission axis. A strong radial gradient in minimum potential is effective in reducing back-streaming current. Increasing the grid aperture size increases the minimum potential in comparison to a smaller aperture size.

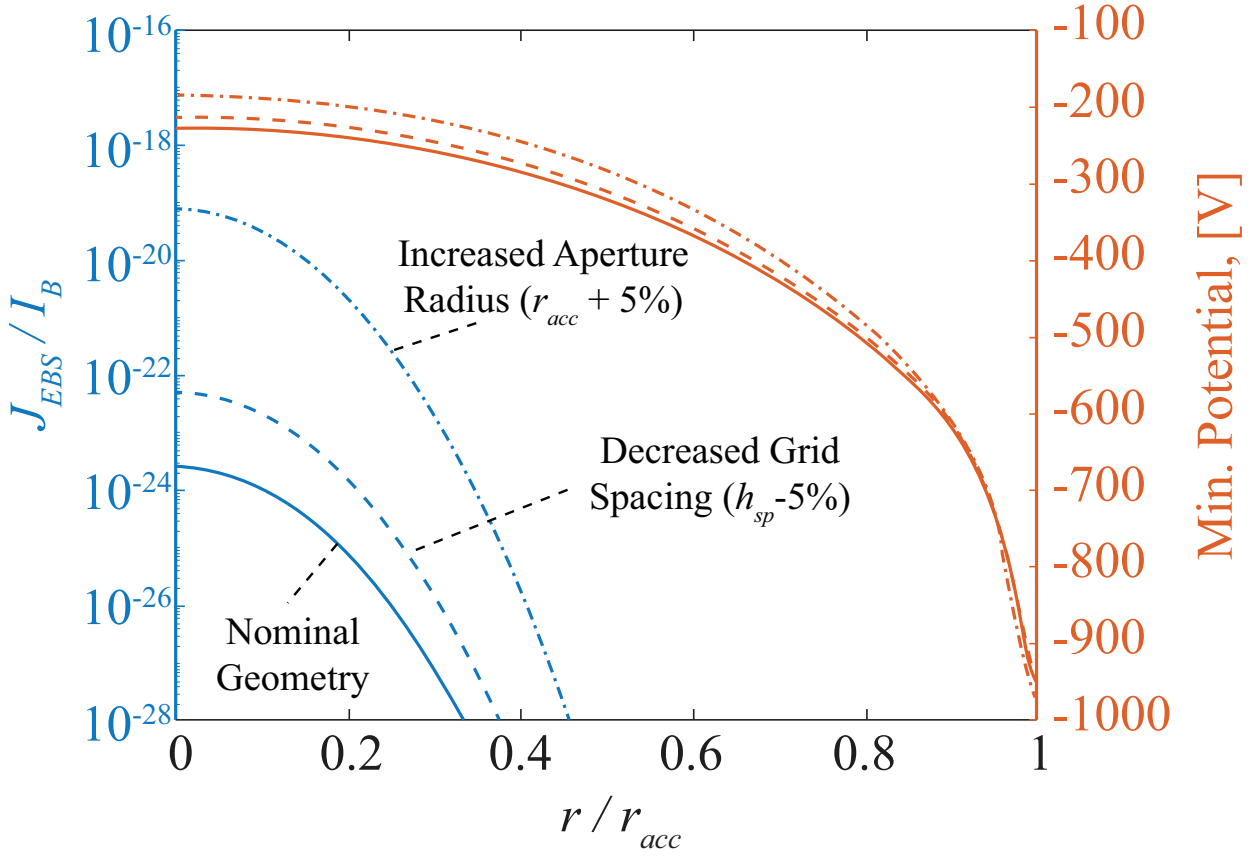

Figure 2.10: Radial profiles of back-streaming current density and minimum potential for varying geometries. The majority of flux occurs through a small region near the centerline. From [2].

A more detailed explanation of the effects of increasing aperture radius is seen in Figure 2.11a). Increasing the aperture size produces a smaller minimum potential, which serves as the barrier against electron flux. As expected from Equation 2.14, the back-streaming current density increases non-linearly with increasing accelerator grid aperture. Figure 2.11b) illustrates the impact of changing grid spacing on EBS flux. Decreasing grid spacing causes the emitter and extractor potential to dominate and effectively penetrate further downstream, increasing the minimum po-

tential. As a result, the back-streaming current increases with decreasing grid spacing. As seen in Figure 2.10, and by comparing Figure 2.11a) and 2.11b), increasing aperture radius is the larger concern for EBS effects because the current fraction increases at a larger rate than in comparison to the result of changing grid spacing.

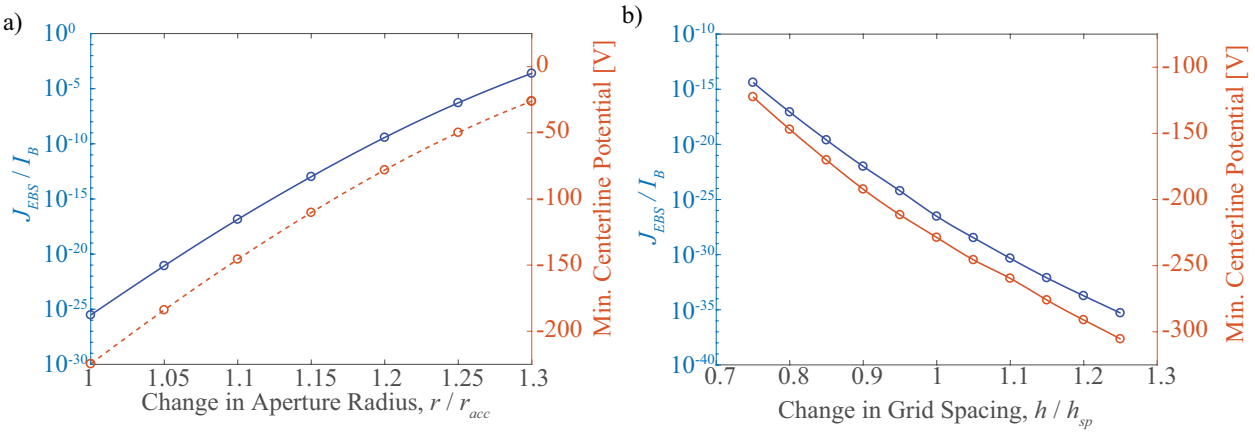

Figure 2.11: EBS current fraction and minimum centerline potential for varying a) grid spacing, and b) aperture radius, normalized by nominal geometry conditions. From [2].

Figure 2.12 shows the back-streaming current for varying bias voltages. Lower grid bias voltages leave the thruster susceptible to EBS in high electron temperature conditions. A strong accelerator grid bias ensures EBS current is negligible over the range of electron temperatures and reduces the impact of hotter electrons.

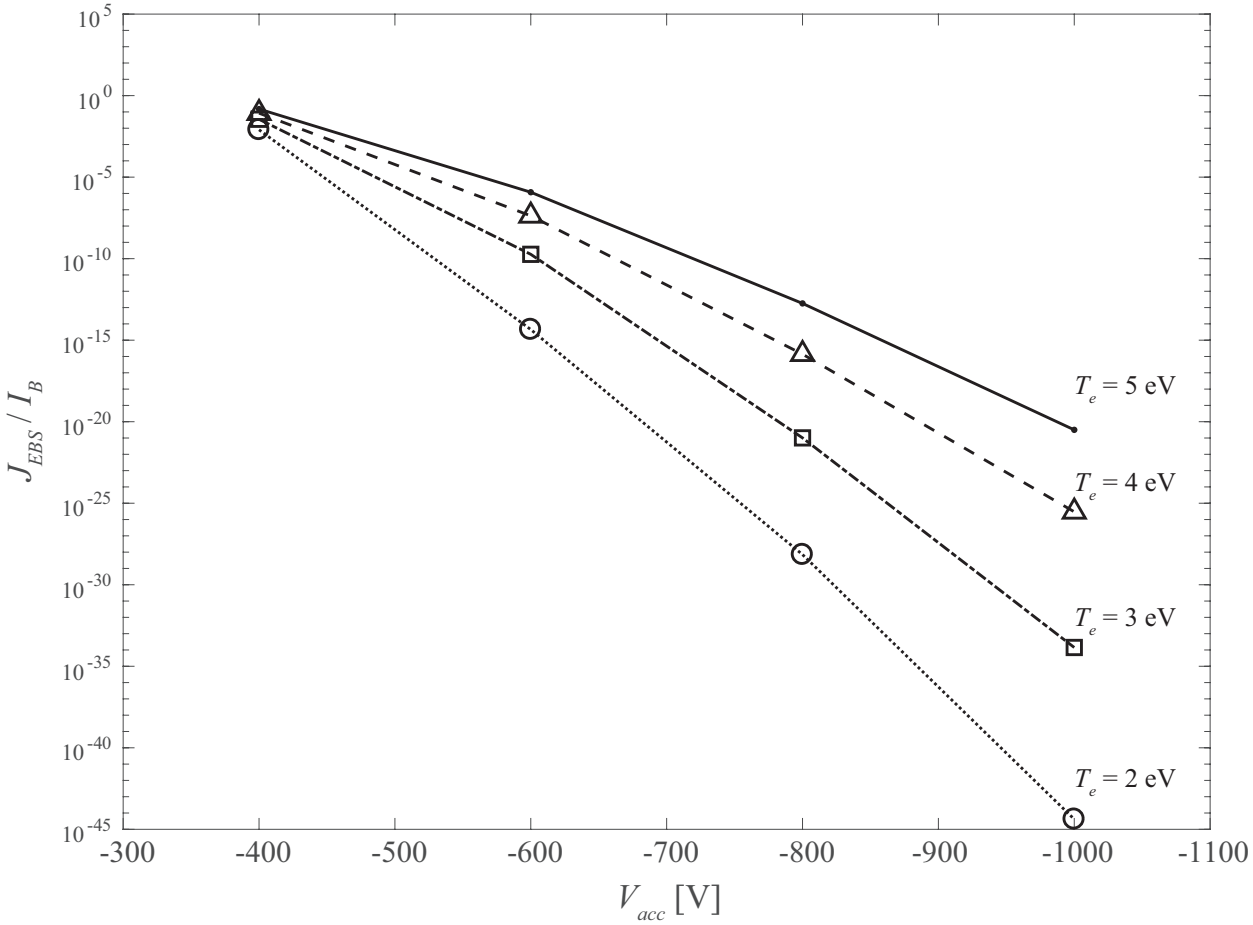

Figure 2.12: Electron backstreaming current fraction as a function accelerator grid bias voltage for varying electron temperatures, from [2].

2.5 Lifetime Model Takeaways

The impact of lifetime liming mechanisms in electrospray thrusters were quantified and evaluated. Overspray leading to grid impingement was treated as the primary failure mode, resulting in saturation of the porous accelerator grid. Grid geometry changes that increase line of sight angle without significantly affecting emission behavior are shown to considerably increase lifetime. In the context of potentially affecting electric field and beam profiles, accelerator grid aperture enlargement is shown to be more attractive than decreasing grid spacing. The significance of misalignment and tolerances on lifetime is presented. Emitter misalignment is shown to reduce lifetime signifi-

cantly. Additionally, tolerance stack-ups from conservative estimates of manufacturing tolerances and misalignments are shown to reduce lifetime by approximately 20%, with worst-case scenario of nearly 50%.

Electron backstreaming analysis shows that increasing aperture radius produces a significant increase in backstreaming current compared to changing grid spacing. However, reasonably high accelerator grid bias voltages can minimize backstreaming current to negligible amounts for a wide range of geometries and electron temperatures. To optimize an emitter geometry for long operational lifetime, the effect of accelerator grid geometry on EBS and overspray accumulation must be considered together. The results show that in general, grid geometry changes that decrease accelerator grid impingement also increase EBS current, and vice versa. Balancing these effects represents a unique optimization problem to meet thruster requirements.

Fitting Gaussian distributions to existing current profiles yields high uncertainty in the wide half-angle regions, resulting in a broad range of lifetime predictions. Therefore, mass flux profiles of the beam are needed to better estimate accumulation at the grids, and are presented in Chapter 3.

CHAPTER 3

Electrospray Plume Profiles

This chapter focuses on experimental measurements of electrospray plumes to investigate assumptions and mechanisms crucial to lifetime and performance. The content has been adapted from a journal paper [6] and a conference proceeding [7].

As detailed in chapter 2, the primary concern for electrospray lifetime is overspray. Addressing overspray as a failure mechanism requires a rigorous understanding of the plume profiles, specifically the mass flux and current density impinging the grids at wide angles. While electrospray plume current density profiles for devices operated in droplet-mode using EMI-Im propellant have been previously measured [68], the existing data are not resolved to high angles that are of significance for lifetime investigation efforts. Using data-fitting techniques on these measurements to extrapolate the properties at high angles has proved challenging as uncertainty overwhelms the data fit values beyond the range of the experimental data [2]. The objective of this chapter is obtaining and analyzing charge- and mass- flux measurements of an ionic liquid electrospray plume to investigate implications on thruster performance and lifetime.

3.1 Electrospray Facility and Experiment

The Highly Optimizable Apparatus for Groundbreaking Investigations of Electrosprays (HOAGIE) facility at UCLA PSPL was developed to investigate various aspects of electrospray emission. The primary objectives of the facility are to provide critical data for electrospray performance and lifetime estimation, and validate computational models [1]. This study utilizes HOAGIE for

experimental electrospray plume characterization to measure mass flux and current density profiles resolved to high angles. A schematic of the HOAGIE system configuration with the diagnostics suite employed in this study is shown in Fig. 3.1.

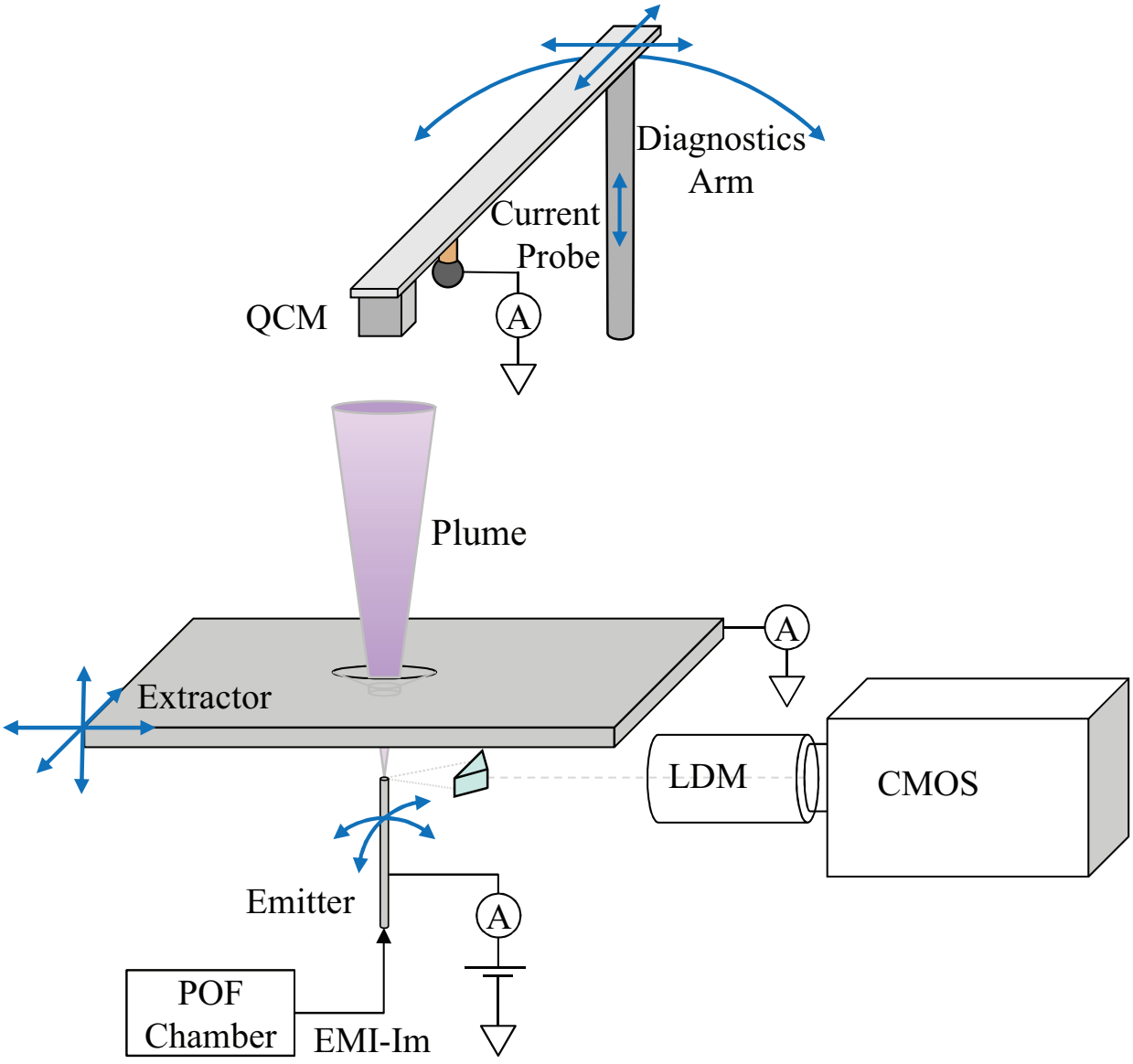

Figure 3.1: HOAGIE electrospray system with relevant diagnostic systems indicated. Arrows indicate actuated motion capabilities for diagnostics and alignment, from [6].

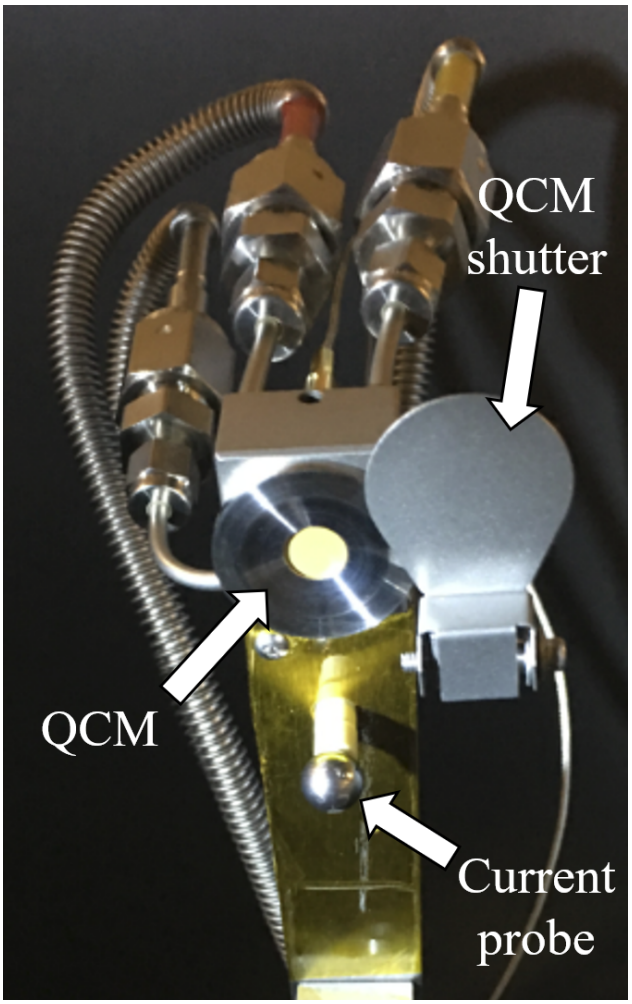

Figure 3.2: Diagnostics mount with QCM and current probe indicated, from [6].

The system consists of a platinum capillary emitter and a stainless steel extractor plate, with part dimensions matching that of the Space Technology 7 - Disturbance Reduction System (ST7-DRS) [13]. High voltage is applied to the emitter while the extractor plate is held at ground, resulting in an electric potential difference on the order of kV that produces electrospray emission. A pressure-over-fluid (POF) feed system is used to flow degassed EMI-Im propellant to an emitter in vacuum. The POF chamber is equipped with a high-precision pressure transducer (7.5 PSIA full scale, 0.01% full scale accuracy) and two mass flow controllers (MFCs) connected to vacuum and nitrogen pressurization lines, respectively, that enable precision flow rate control. The hydraulic resistance of the emitter line is measured before the experiment, and the flow rate is calculated in

real time from the pressure in the POF chamber. The MFC control algorithm results in a roughly 100 Pa variation in driving pressure, with a frequency of roughly 3 Hz, although these oscillations were not observed to have an effect on emission current. Measuring the height of the emitter above the POF reservoir to within 1 cm corresponds to an uncertainty in hydrostatic pressure of ± 75 Pa. Voltage has been shown to promote flow through a capillary emitter[81] by reducing the pressure at the emission site[82]; whether or not this effect should be taken into account when estimating flow rate introduces an uncertainty in pressure of ± 120 Pa based on estimating the electric pressure at the emission surface [83]. Taking the quadratic mean of the two dominant sources of uncertainty in driving pressure, electric pressure and hydrostatic pressure, and dividing by emitter hydraulic resistance yields a $\pm 25\,\mathrm{pLs}^{-1}$ uncertainty in flow rate. An emission current monitor is used for high-voltage emission current measurements with nA-resolution at a 10 kHz sampling rate. The emission current can be related to the flow rate by Eq. 3.1 for droplet-mode electrospray emission, where I is the emission current, C_1 is the device-specific flow rate coefficient, and Q is the volumetric flow rate [84].

$$I = C_1 Q^{\frac{1}{2}} \tag{3.1}$$

A spherical current probe is mounted on the diagnostics mount, as shown in Fig. 3.2, and is connected to a current monitor. The monitor can measure the extractor or probe current with nA-resolution at a 10 kHz sampling rate. All current measurements presented in this paper have a record length of 1 s, with uncertainty on the measurements determined from the 10,000 datapoints collected over that record length. Longer record lengths were conducted to ensure that no larger timescale effects were unaccounted for. A water-cooled quartz crystal microbalance (QCM) with a shutter is also mounted on the diagnostics mount, as shown in Fig. 3.2, to measure mass flux. The frequency response of the gold-coated quartz crystal is measured over a sampling period of 60 s to 300 s based on the spatial location of the QCM to ensure enough sampling to measure the anticipated mass flux while minimizing the exposure of the crystal to prevent saturation beyond which the measurements become unreliable. The slope of the measured response is used with

Eq. 3.2, also known as the Sauerbrey Equation, to determine the mass flux to a resolution on the order of $1\,\mathrm{pg\,cm^{-2}\,s^{-1}}$. Here, $\frac{dm}{dt}$ is the mass flux, ρ_q is the density of the quartz crystal, μ_q is the shear modulus of the quartz crystal, f_0 is the initial resonant frequency, and $\frac{df}{dt}$ is the rate of change of the measured frequency. Uncertainty on the mass flux measurements is determined from propagating the root mean square (rms) on the fit to the raw frequency data in determining the slope. More details on the QCM and measurement details are presented in Appendix A.

$$\frac{dm}{dt} = -\frac{\sqrt{\rho_q \mu_q}}{2 f_0^2} \frac{df}{dt} \tag{3.2}$$

The diagnostics mount is height-adjustable and actuated with two perpendicular translation stages that allow the probes to move in a user-selectable horizontal plane across the electrospray plume for current density and mass flux mapping. Additionally, the diagnostics are mounted on a rotation stage for angular plume sweeps about a horizontal rotation axis aligned with the tip of the emitter. A long-distance microscope (LDM), with stereoscopic optics enabling multiple lines of sight simultaneously, observes the electrospray emission region *in-situ* to ensure nominal emission conditions and to identify operating setpoints that produce off-axis emission. Additional details about the HOAGIE facility, diagnostics, and complementary efforts can be found in Wirz et al. [1].

3.2 Plume Measurements

In order to characterize the electrospray emission response of this system, voltage sweeps were conducted to determine the start-up voltage and operational stability range. The resulting I-V curve is shown in Fig. 3.3 with arrows labeled 1, 2, and 3 to indicate the chronology of the sweep. The voltage sweep was conducted at a flow rate of 480 $pl\ s^{-1}$. The emitter voltage was set initially to 1200 V and then ramped up in 50 V increments with a 10 s duration at each voltage setpoint. Extractor current was recorded at each setpoint in the sweep. No emission was observed until 1550 V, which agrees with the estimation of start-up voltage required for emission for this geometry. As the emitter voltage is further increased incrementally up until 2000 V, the emitter current increases

as expected for low flow rate electrospray systems [81]. As the voltage is swept back down from 2000 V to 1200 V in identical increments, the emitter current decreases as expected. The hysteresis effect of emission continuing below 1550 V is due to the existence of a stable cone-jet which allows for emission to continue below the start-up voltage threshold.

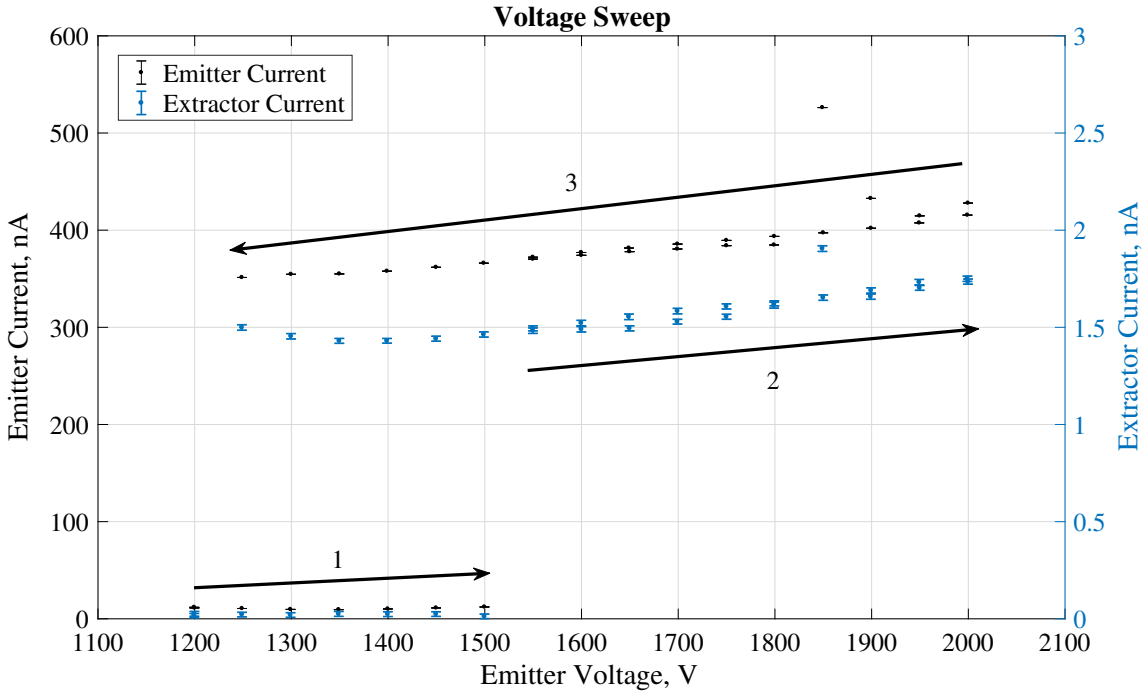

Figure 3.3: Emitter current versus emitter bias shown along with impinging extractor current for each voltage setpoint. Arrows labeled 1, 2, and 3 indicate the order at which the emitter voltage was swept to highlight the hysteresis. From [7]

Extractor current measurements show that the extractor current increases with increasing emitter voltage as expected since the emitted current is increasing. The elevated extractor current at the high and low voltage region is likely due to the onset of off-axis and/or unstable emission events. Visual evidence of off-axis emission that occurred at higher extraction voltages is shown in Fig. 3.4, and additionally reported by Uchizono et al. [85] where the repeatability of the phenomena was demonstrated.

In addition to voltage sweeps, flow rate sweeps were performed to characterize the system and determine the device-specific flow rate coefficient. The sweep was conducted at a fixed extraction

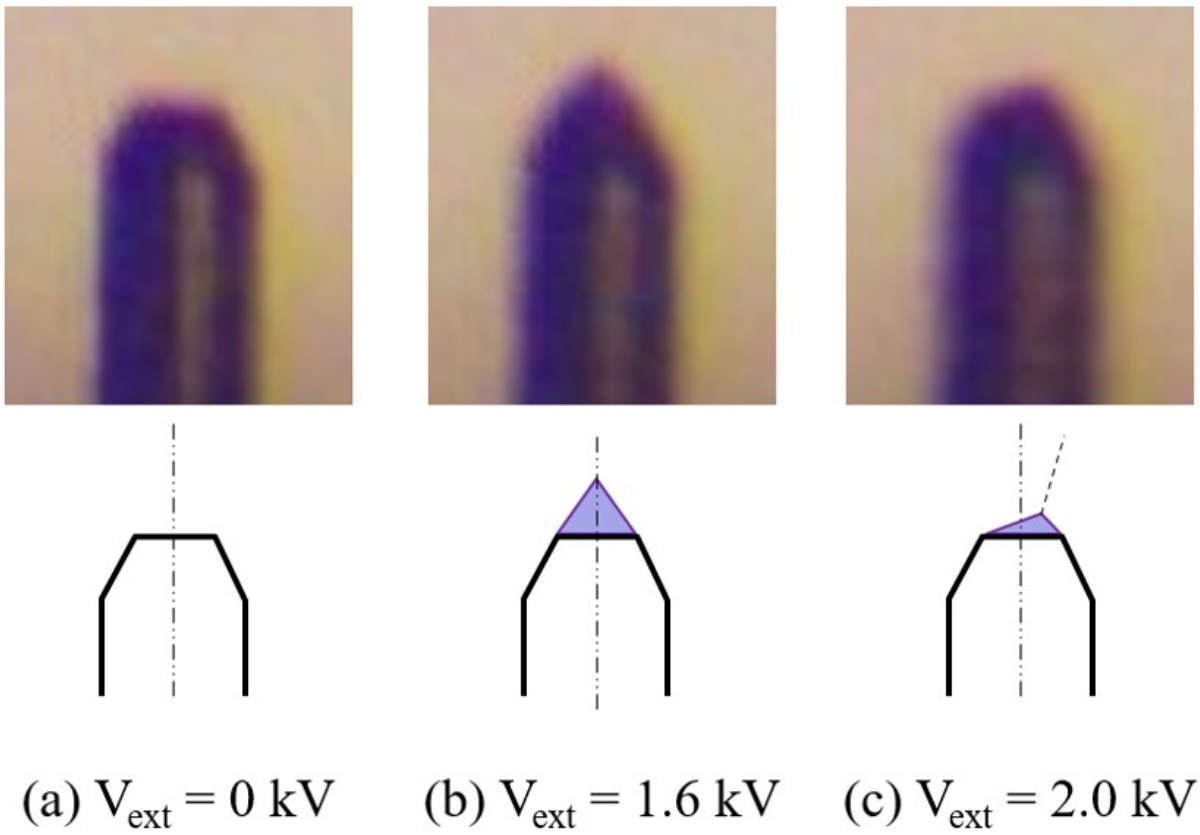

Figure 3.4: Microscopy of emission site (a) without flow, (b) during nominal extraction voltage (1.6 kV) and flow rate showing paraxial cone shape, (c) high voltage (2 kV) at nominal flow rate showing off-axis cone shape. From [6].

voltage of 1.6 kV. The flow rate was initially set to 220 pL s^{-1} and increased in 50 pL s^{-1} increments. An *I*-*Q* sweep result is shown in Fig. 3.5, and is repeatable across multiple experiments.

A fit of Eq. 3.1 to the data indicates that the system exhibits the expected emission current response. The flow rate coefficient (C_1) was determined to be 509 nAs$^{\frac{1}{2}}$/nL$^{\frac{1}{2}}$ for this system, which allows for conversion between emission current and flow rate for analysis and modeling efforts. Note that the value of C_1 represents updated analysis from that presented by Thuppul et al. [7], whereby a $\sim$6 kPa gravity-driven pressure head in the system is now corrected for. Converting our value for C_1 to SI units yields 0.509 As$^{1/2}$m$^{-3/2}$. Comparing this value to those published in literature shows reasonable agreement. Ziemer[21] presented an analogous colloid performance

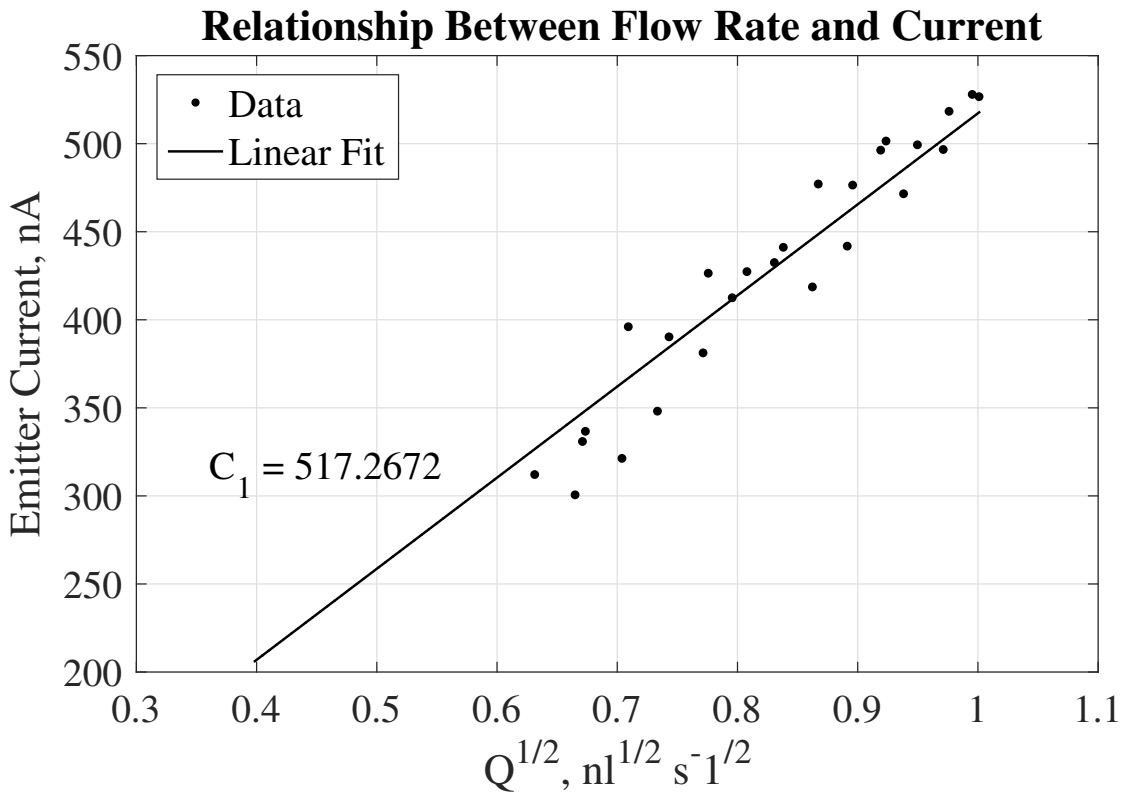

Figure 3.5: Emitter current flow rate relationship exhibits expected behavior for capillary emission. From [7].

parameter α, which can be converted to a C_1 coefficient of 0.354 $\mathrm{As}^{1/2}\mathrm{m}^{-3/2}$ for their experiment. Regression of experimental results presented by Gamero-Castaño[64] indicate a C_1 coefficient of 0.485 $\mathrm{As}^{1/2}\mathrm{m}^{-3/2}$. The validity of the C_1 coefficient determined in this effort is supported by 5 % agreement with experimental results from Gamero-Castaño[67].

A 2D map of the plume current was measured by conducting a planar sweep of the diagnostics probe across the electrospray plume. The diagnostics arm was positioned 5.125" above the emitter tip for the sweep where emitter current and probe current measurements were obtained. A contour map of the resulting plume profile is shown in fig. 3.6. Uncertainty on the measurements were less than 1% and is not shown in the figure. The contour indicates that the plume is axisymmetric and provides the location of the centerline along which angular sweeps were conducted.

Angular sweeps of the diagnostics mount were conducted at the centerline determined from the

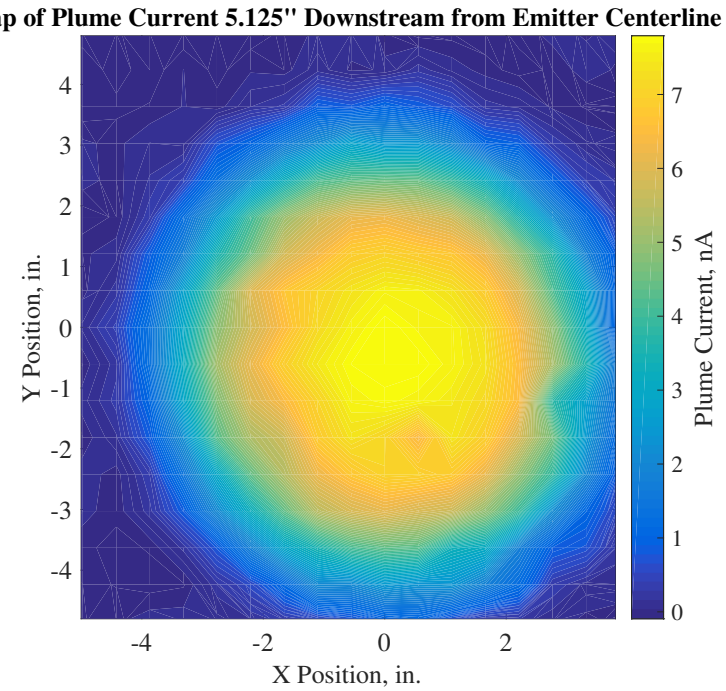

Figure 3.6: 2D profile of current 5.125" downstream from emitter, from [7].

2D plume contour to measure the plume current density and mass flux profiles. The angular sweeps were conducted for varying extraction voltages and flow rates with the QCM and current probe sweeping through the expected center of the plume. The current profiles are shown in Fig. 3.7(a) and 3.7(b) for varying extraction voltages and flow rates respectively. All current density profiles have a Gaussian-like shape, but are not truly Gaussian. As the emitter bias voltage is increased, the peak of the current profiles increases sightly and the plume profiles becomes narrower. A sharp change in the profile width occurs at 1.8 kV due to off-axis emission as mentioned previously and further demonstrated with the mass profiles. The uncertainty of the measurements is computed by averaging a sample of 10,000 datapoints acquired over a 1 second interval. Variation in the emitter current during the acquisition are neglected from the uncertainty estimation as they were determined to be negligible. In general, the measurements reported in this study show good agreement with other published measurements of current density profiles of ionic liquid electrospray devices [86, 67].

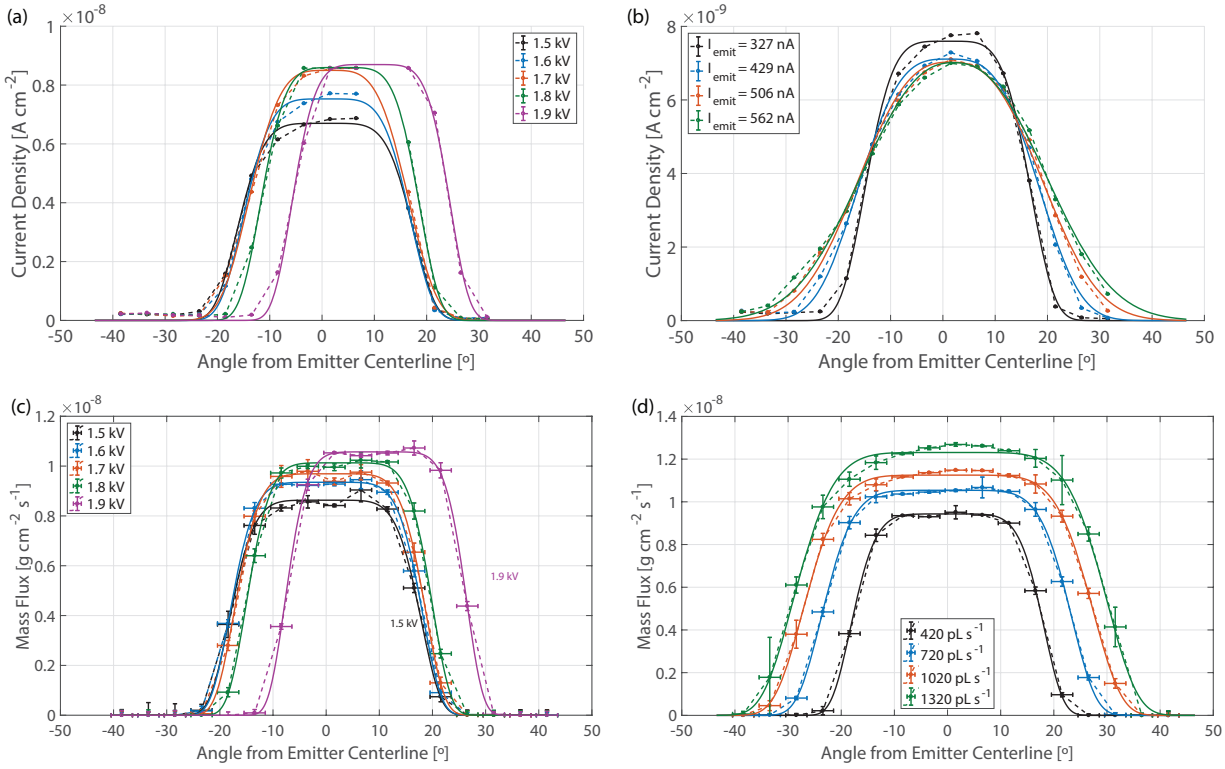

Figure 3.7: Current density as a function of half angle for varying a) extraction voltage (fixed flow rate of 420 pL s^{-1}) and b) flow rate (constant voltage of 1.6 kV). Mass flux as a function of half angle for varying c) extraction voltage (fixed flow rate of 420 pL s^{-1}) and d) flow rate (constant voltage of 1.6 kV). All profiles shown with Super-Gaussian fits, and are originally from [6]. The trends of these fits with voltage and flow rate are shown in Fig. 3.9.

The mass flux profiles are shown in Fig. 3.7(c) & 3.7(d) for varying extraction voltages and flow rates respectively. It is evident from the measurements that the mass flux profiles are not Gaussian. Instead, the profiles are extremely broad near the center with sharper-than-Gaussian decay. More critically, the shape of the mass flux profiles differs notably from that of the current density profiles, highlighting the significance of these measurements for thruster performance and lifetime efforts. As the flow rate is increased, the peak magnitude of the mass flux profiles increases and the profiles grow wider. The broadening of the profiles decreases with increasing flow rate. Uncertainty in the position of the QCM represented in Fig. 3.7 is a result of the sensor size having a cross-section of 4°. The decay in the mass flux profile is larger than 4°, indicating that this decay is adequately resolved by the QCM. Fig. 3.7(c) shows that varying the extraction voltage voltage from 1.5 kV to 1.7 kV has no significant impact on the profiles. At 1.8 kV, the emission begins to move off-axis, as shown previously in the voltage sweep and current density profiles. The off-axis emission becomes more apparent at 1.9 kV where the plume shifted by $\sim$9°.

3.3 Plume Profile Discussion

The total volume flux captured by the measurements was calculated by performing surface integrations of the measured profiles in spherical coordinates. The integrated volume flux is shown in Fig. 3.8 as a function of the flow rate. A linear fit applied to the calculated values shows that there is a 93 % agreement of the integrated volume flux with the measured flow rate. The 7 % offset is well within the uncertainty arising from the value of propellant density used in calculating the volume flux, the flow rate measurement, and neglected propellant sprayed at higher half angles. These calculations indicate the QCM measurements are accurately capturing and resolving the mass flux in the electrospray plume.

A convolution analysis was performed to ensure that the flat top plume shape was not an artifact of the finite-sized QCM sensor response. The measured plume profile, $\Gamma(\theta)$, is a convolution of the “true", unperturbed plume profile, $g(\theta)$, the QCM sensor response, $f(\theta)$, and an experimental

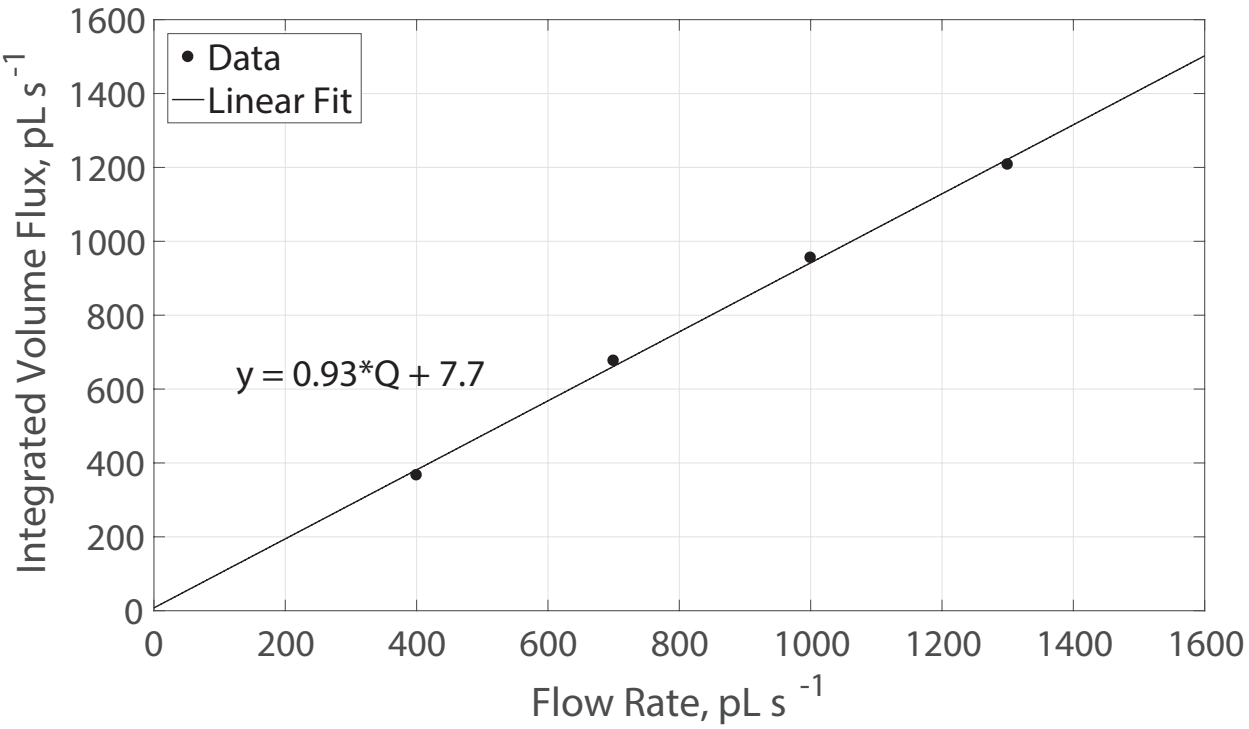

Figure 3.8: Volume flux determined from mass flux profiles vs. flow rate. 93 % agreement is found, which is well within experimental uncertainty, showing that the QCM mass flux measurements are accurately capturing the total emitted propellant. From [7].

windowing function $W(\theta)$. The “true" plume profile can in principle be determined via a Fourier transform and the convolution theorem as shown in eq. 3.3.

$$g(\theta) \;=\; F^{-1}\left(\frac{F(\frac{\Gamma(\theta))}{W(\theta)})}{F(f(\theta))}\right) \tag{3.3}$$

Using the measured mass flux profile, a rectangular windowing function, and assuming the QCM sensor response to be an elliptic function, the “true" plume profile cannot be a Gaussian plume. The unperturbed plume profile must be some type of distribution with a flat top, indicating that the measured profile shape is not due to sensor response and does in fact represent the shape of the mass flux profile.

Given the non-Gaussian nature of the observed plume profiles, the mass flux and current density data can be parameterized with a Super-Gaussian form, per equation 3.4:

$$p(\theta) = A \cdot \exp\left\{-\left(\frac{(\theta-\theta_t)^2}{2\sigma^2}\right)^n\right\} \tag{3.4}$$

The Super-Gaussian form allows convenient description of the plume width (σ), magnitude (A), and sharpness (n) of the decay at high angles, with θ_t capturing any tilt of the plume away from the central axis; note that equation 3.4 reduces to a Gaussian description for $n = 1$. Super-Gaussian fits to the mass flux and current density profiles are shown in figure 3.7. The parameterization allows clearer description of the key features of the plume, plotted in figure 3.9. With confidence in the mass flux measurements, the observed mass flux and current density trends are considered in the context of established high conductivity electrospray understanding.

It has been shown [87] that plume species from a high-conductivity electrospray can originate from both the cone-jet break up and the expulsion of charged species by "over-charged" particles downstream of the jet. Therefore, the resulting population of plume species can originate from multiple sources, with different break up mechanisms leading to different relationships between particle charge and mass. Distributions in the charge and mass of such particles, coupled with neg-

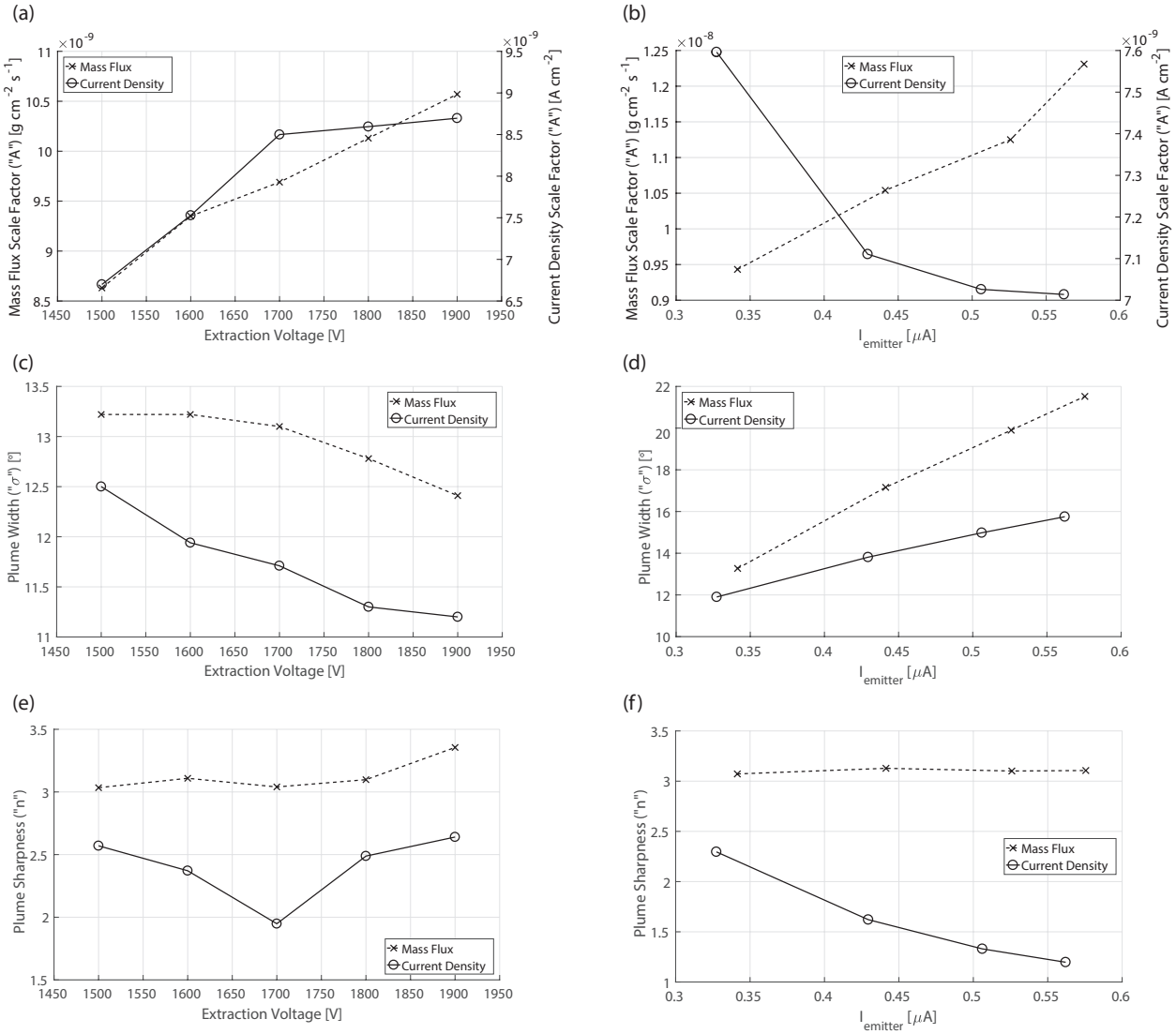

Figure 3.9: Super-Gaussian fit parameters for trends, per equation 3.4, from [6]. Mass flux and current density show similar response to changing extraction voltage, but different response to changing flow rates.

ative velocity gradients, cause Coulombic interactions between particles and perturbations in their motions near the jet break-up region (also described as the interaction region) [88, 89, 90]. The applied electric field accelerates radial motion toward the extractor as species propagate downstream. Accordingly, a substantially polydisperse plume is anticipated for the plumes reported herein.

The plume measurements are the sum of different distributions of plume species with a wide range of specific charge, including neutral species. If ion evaporation and Coulomb explosion downstream of jet break up are considered substantial contributors to plume species, one may anticipate that the higher specific charge species generated in such events would have a wider distribution than the larger droplets directly created from cone-jet break up [87].

As such, the reported plume measurements are the result of species extraction, interaction (Coulombic and fissive), and acceleration [1]. It is expected that changing the flow rate at a fixed voltage (figure 3.9b, d, f) changes the population of emitted species (i.e. relative population of species of different specific charges), whereas changing the voltage at fixed flow rate (figure 3.9a, c, e) will not substantially change the population of emitted species but change their trajectories downstream of the interaction region. [91, 92, 87] Also, as discussed later, increased voltage can lead to substantial tilt.

It is evident from figure 3.9 that the behavior of charge and mass in the plume differ, so it is inaccurate to solely use measurements of current density to estimate mass flux, thrust, and device lifetime. Indeed, with its increased sharpness (n) the mass flux presents a more sustained value across the center of the plume than the current density does. A more uniform thrust profile results, as well as a substantial reduction in mass flux at high angles than would be assumed had the current density been used as the profile [2, 93]. A one-to-one correspondence between mass flux and current density would necessitate a uniform specific charge across the plume: the discrepancy between the plume profiles indicates polydispersity, as expected for EMI-Im electrospray devices operating under these conditions.

As shown in figure 3.9, increasing voltage increases the mass flux and current density scale (A) and tightens both the both mass flux and current density width (σ); however, current density

tightens more substantially. For the same set of generated plume species, the trajectories of higher specific charge droplets will more closely follow the electric field lines than heavier, lower specific charge species. These results suggest that as the voltage is increased and the field lines concentrate toward the center of the plume, proportionately more high specific charge species are maintained near the center or the plume, manifesting as a tighter distribution of charge than mass.

As flow rate is increased, the mass flux profile grows similarly in scale and width, thus retaining its sharpness (n). A growing plume of this kind would indicate that extra mass is being volumetrically added to all species in the plume. However, the current density behavior with flow rate is quite different: with increasing flow rate (and hence the extraction current) the extra current is distributed more toward the high-angle regions of the plume. This can be seen by the scale reducing, the width slightly increasing, and the kurtosis increasing (i.e. the tails of the distribution are increasing). At higher flow rates, it is anticipated that emitted droplets are generally larger with smaller specific charge [87], and are therefore less susceptible to ion evaporation and fission. The presence of larger, more-stable droplets reduces the probability, and hence frequency, of high specific-charge generating events. With fewer high-specific-charge species generated that are more responsive to the accelerating field, proportionately more charge and mass results at higher angles. This suggests that the mass flux widens because heavier primary species are less responsive to the accelerating field, so traject further from the center; the charge density has higher kurtosis because there are fewer high-specific-charge species responding to the accelerating field, leaving much of the charge on heavier droplets that can maintain wider trajectories.

The measurements and discussion of plume structure presented in this manuscript are generally consistent with those reported in literature [89, 90, 94, 87], while providing insight into the phenomena responsible for these behavior via direct measurement of both charge and mass plume properties.

In addition to the Super-Gaussian parameterization of the plume shape, tilt (θ_t) is also observed as a function of voltage, with minimal tilt emerging as a result of flow rate changes (in agreement with that observed by Uchizono et al. [85]). As shown in figure 3.10, the plume deviates from

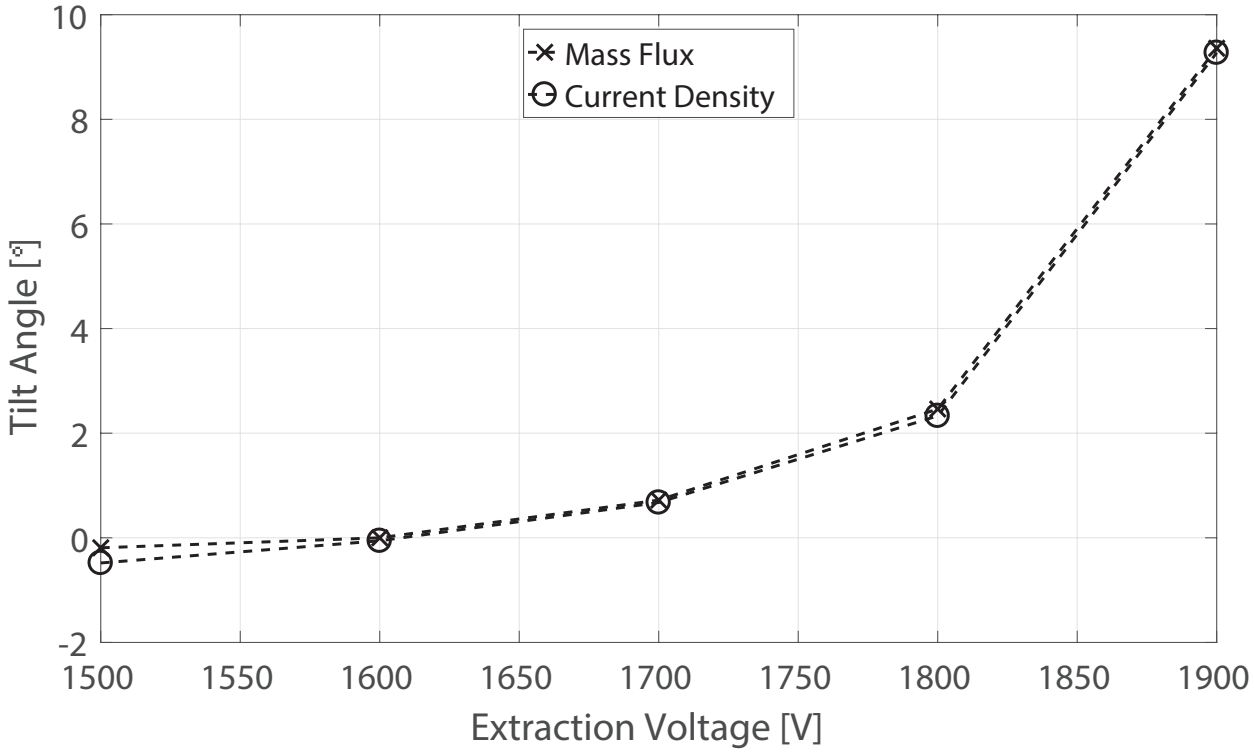

Figure 3.10: Mass flux and current density plume tilt with voltage, from [6].

the emitter-axis and potentially out of the measurement plane once the voltage increases above $\sim$1.8 kV. Almost 10° of plume tilt was observed in the measurement plane at 1.9 kV, and there was little deviation in the tilt between the mass flux and current density; deviation of the current density tilt from the mass flux tilt might manifest in the presence of an accelerator grid. While tilt has been observed in the cone-jet itself (figure 3.4 and Uchizono et al. [85]), it would seem the tilt also propagates into the plume.

Cone tilt shown in figure 3.4 represents the projection of the polar tilt angle into the object plane of the LDM. Uchizono et al. [85] use the orthogonality of the plume measurement plane and the LDM object plane to reconstruct the polar and azimuthal tilt angles, finding that the cone both tilts and rotates with increasing emitter bias voltage. The observed tilting phenomenon is highly repeatable and has been observed when using different emitters of identical geometry, even after several realignments of the emitter and extractor.

The cause of "tilted emission" is important in the context of electrospray thruster design, yet not fully understood. The formation of a conical meniscus represents an equilibrium between capillary fluid force and electric traction force of the applied bias. Electrical Bond number is a dimensionless number that relates the electric force to capillary force, and is given by

$$Bo_e = \frac{\varepsilon_0 \phi^2}{\gamma D_o}, \tag{3.5}$$

where ε_0 is vacuum permittivity, ϕ is emitter bias potential, γ is surface tension, and D_o is the capillary's outer diameter. Steady cone-jet emission occurs at a Bo_e of order unity, and increases with ϕ^2. The variation in observed tilting response indicates that effects of manufacturing defects, surface contamination, and imperceptible misalignment between the emitter and extractor may become non-negligible as Bo_e increases. Small perturbations in the electric field may draw the conical meniscus in a direction that satisfies a more stable equilibrium. At voltages below the start-up voltage, the meniscus takes on an elongated, ogival shape, and only occurs in the downward progression of the voltage sweep. The cause of tilt in the low-voltage regime may possibly be explained by interplay between the electric and gravity forces, since the electric force is relatively weak.

The results of this study have implications on the performance and lifetime of electrospray thrusters. The thrust profile of an electrospray device is dependent on the specific charge and mass flux profile. The measurements in this study indicate Super-Gaussian mass flux profiles, which result in more uniform thrust profiles for electrospray thrusters than previously anticipated. The differences between the current density and mass flux profiles, especially in response to varying flow rate, further signify the importance of mass flux measurements for accurate lifetime estimation of electrospray thrusters [2]. The measurements in this study show low steady-state mass flux in the high angle regions at nominal thruster operating setpoints. Lifetime modeling efforts based on these measurements indicate that oversprayed mass flux at these operating conditions do not pose significant challenges to the lifetime of electrospray thrusters [93]. This suggests that

transient events and off-nominal operating conditions are likely the lead contributors to lifetime reduction [93, 85, 95]. Plume *and* cone jet tilt away from nominal operating conditions have not been previously reported for electrospray thruster geometries. A tilted plume deviates the thrust vector from the expected axis, reducing effective thrust. Tilt may also be problematic for lifetime: while mass flux at high angles is impinging on the grids, by moving the plume over, the peak of the distribution is no longer going through the aperture as designed, and the flux to the grid increases substantially, likely reducing lifetime.

3.4 Plume Profile Takeaways

Mass flux and current density profiles for an EMI-Im capillary electrospray show that mass flux and current density profiles are considerably different in shape and width. These profiles also exhibit different shape changes across different operating conditions. Therefore, current profiles alone should not be used for predicting thruster lifetime and performance, but rather accurate knowledge of the mass flux must be employed. The current density profiles consistently exhibit order $n \sim 1.5 - 2.5$ Super-Gaussian profiles from high to low flow rates, respectively. In contrast, mass flux profiles consistently exhibit order $n \sim 3$ Super-Gaussian form. Increasing flow rate causes both current density and mass flux profiles to increase in width, but critically, the mass flux grows while maintaining its shape whereas the current density profiles exhibit considerable increase in kurtosis, i.e. profiles with proportionally more current at higher angles. Increasing the extraction voltage does not considerably change the mass flux and current density profiles, but leads to off-axis emission, as previously observed. A consistent tilt onset occurs when operating above or below a critical emitter bias voltage of 1.6 kV to 1.7 kV for the presented emitter geometry; for untilted emission, it is recommended to operate with the critical voltage range for a given electrospray system. For a polydisperse electrospray, the *shape* and *response* of the mass flux and current density profiles can be substantially different across operating conditions, which must be considered for accurate electrospray thruster lifetime and performance assessments.

CHAPTER 4

Plasma Interactions with Volumetrically-Complex Materials

This chapter covers plasma-material interactions (PMI) with volumetrically-complex surfaces. The concept of volumetrically-complex surfaces is introduced along with the phenomena of plasma-infusion. Details of plasma infusion and theory are then presented to inform the subsequent analysis of experimental data. The Pi facility where PMI experiments are conducted is then described along with relevant details on diagnostics and techniques used. Experimental measurements and analysis of different PPI foams under plasma exposure are then presented and analyzed to draw conclusions on the sputtering behavior and plasma-favorability of VCMs.

4.1 Plasma Infusion Background and Theory

Volumetrically-complex materials (VCMs) offer a unique capability in allowing the plasma or incident particle beam to penetrate into a 3-dimensional structure rather than interact in 2-dimensions. As discussed in Section 1.3, this capability is of interest to plasma-facing components or electrodes that must endure extreme conditions while maintaining plasma-favorability. An example of VCMs of specific interest to this work are foams.

An example of a VCM eroding under plasma exposure is shown below in Figure 4.1. The images are obtained in-situ using a long-distance microscope coupled with focus variation to produce a composite image from all elements of the 3-dimensional material and a corresponding height map [8]. Investigation of the evolution of the surface seems to indicate that the ligaments erode in multiple directions (evidenced best by the thin ligament in the bottom left).

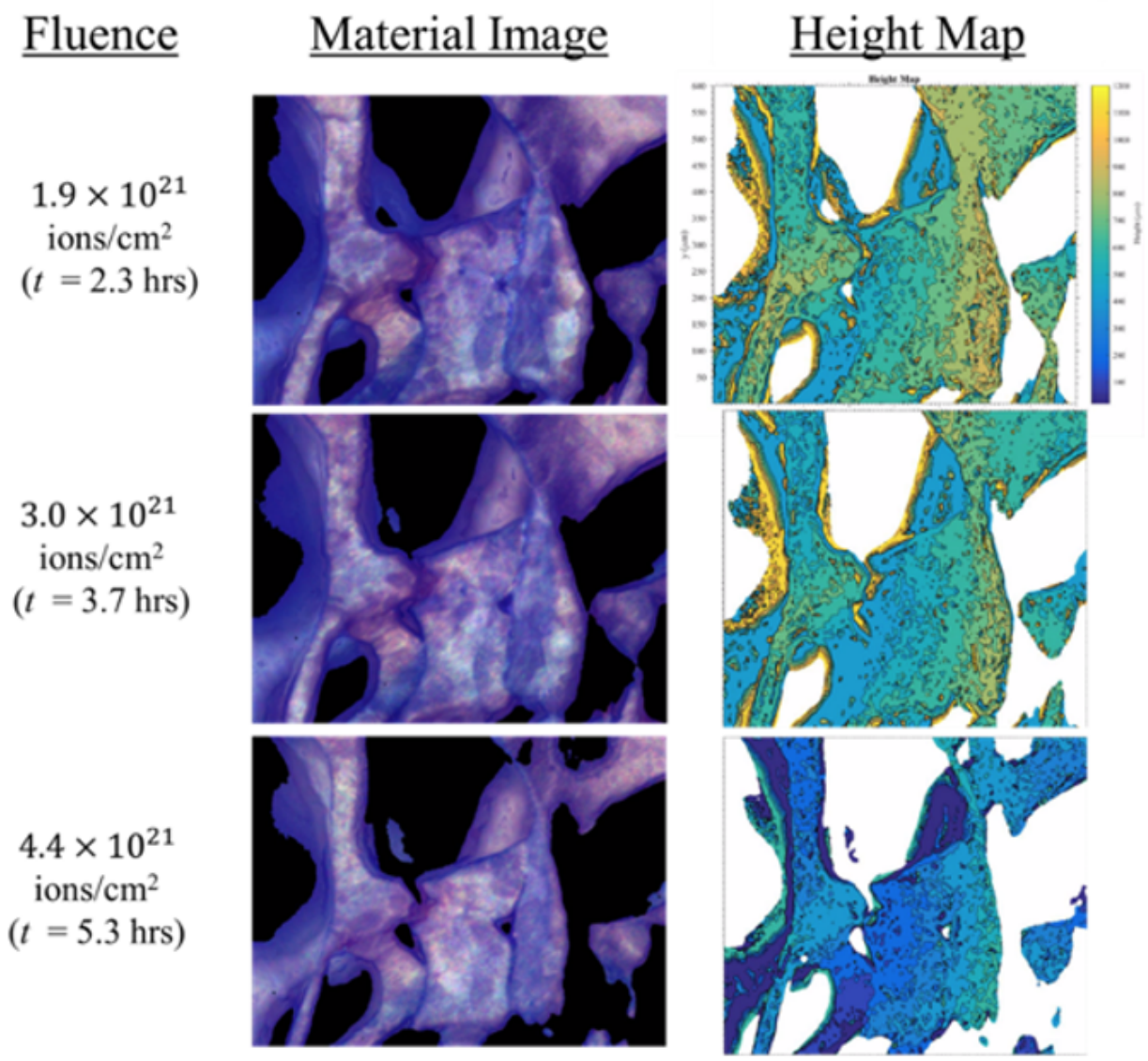

Figure 4.1: LDM imaging of a foam under argon plasma exposure with (Left) composite image sequence and (Right) height maps using focus variation profilometry to measure erosion in-situ. Adapted from [8].

This penetration of the foam by the plasma leading to unexpected erosion behavior was investigated by Li and Wirz [9, 96]. The regime is referred to as plasma infusion. As shown in Figure 4.2, when in the plasma-infused regime, the sheath forms normal to the local surface of the ligament rather than the surface plane of the whole foam itself. This results in normal surface incidence of

incident species hitting the ligament surface. The contrasting regime is plasma-facing, where the sheath is formed normal to the surface plane of the material, and therefore incident with varying angles on the ligament surfaces.

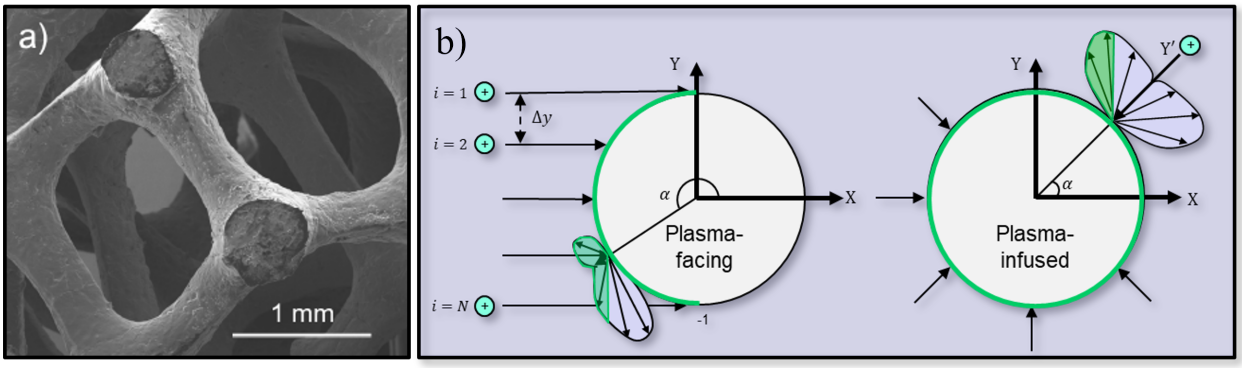

Figure 4.2: Key geometric parameters and plasma regimes for VCMs from Li and Wirz [9]. (Left) SEM image of a foam indicating key geometric features pore size (D) and ligament size (d). (Right) Angle of incidence of plasma ions sputtering ligament surface for plasma-facing and plasma-infused ligament scenarios.

The size of the pores of the foam is critical to the infusion of the plasma. As shown in Figure 4.2, two primary length scales in the definition of the foam geometry are pore diameter, D, and ligament diameter, d. These two scales are often linked together by the defining parameters for foams, PPI (pores-per-inch), as shown in equation 4.1. The ratio of pore size to ligament size is known as the aspect ratio, equation 4.2.

$$PPI = \frac{0.0254}{D+d} \tag{4.1}$$

$$AR = \frac{D}{d} \tag{4.2}$$

When a plasma makes contact with a surface, it forms a sheath to balance out charge conservation. An example of an ion sheath is shown in Figure 4.3. In the bulk plasma, quasi-neutrality is maintained. However, due to the strong negative bias of the material surface, ions stream toward to the surface and shield it out over a distance, L_s. Within the sheath itself, ion dominate over

electrons and accelerate toward the surface due to the potential drop. Typically, the energy gained is assumed to be the potential drop across the sheath, but collisions can limit that as discussed later in this section.

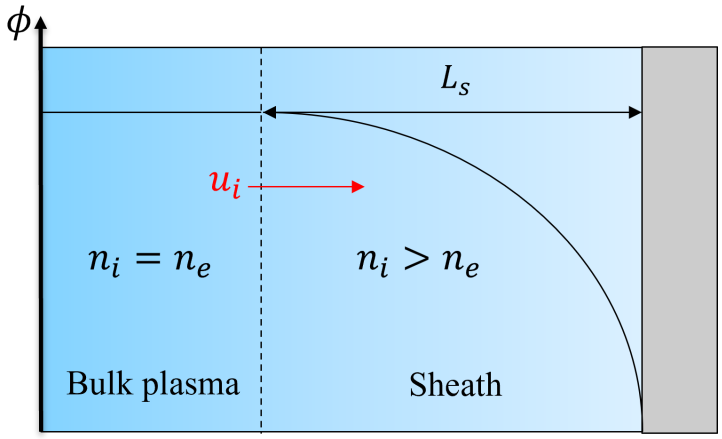

Figure 4.3: Ion sheath between the bulk plasma and a negatively biased surface. The sheath length, L_s, is scaled based on the Child-Langmuir Law, with bulk plasma ions accelerated into the material surface.

In order for the plasma to infuse into the foam, the sheath that forms along the surface must be smaller than the radius of the pore. Plasma sheaths can be complex based on different theories and corrections. In this analysis, two types of sheaths are considered. The first is a Debye Sheath (or Debye Shielding), which occurs in the case of a floating sample and are typically a few Debye Lengths. The Debye length is defined in equation 4.3 where λ_D is Debye length, ε_0 is free-space permittivity, k_B is the Boltzmann constant, T_e is electron temperature, n_e is electron density (plasma density if quasi-neutral), and e is electron charge.

$$\lambda_D = \sqrt{\frac{\varepsilon_0 k_B T_e}{n_e e^2}} \tag{4.3}$$

The second type of sheath is a Child-Langmuir sheath, which forms on a biased surface. The Child-Langmuir sheath length, L_s, is described by equation 4.4 where $\Delta\phi_s$ is the potential drop of

the sheath.

$$L_s = \frac{\sqrt{2}}{3}\lambda_D \left(\frac{2e\Delta\phi_s}{k_B T_e}\right)^{3/4} \tag{4.4}$$

The plasma infusion can then be described by the infusion parameter [9], ξ, which is the ratio of the pore diameter to the sheath length as shown in equation 4.5. If $\xi >> 1$ the VCM is plasma-infused, and if $\xi << 1$ the VCM is plasma facing.

$$\xi = \frac{D}{L_s} = D\left(\frac{18en_e^2 k_B T_e}{\varepsilon_0^2 \Delta\phi^3}\right)^{1/4} \tag{4.5}$$

It is important to note that both sheath lengths depend purely on plasma properties and nothing on material geometry. The infusion parameter, as a result, becomes a scaling between plasma and material with each term independent of each other. Figure 4.4 shows scaling of the infusion parameter with respect to PPIs, sample bias, and densities of relevance to the experiments discussed in this work and potential applications. Generally, as density increases, the sheath size decreases and therefore the plasma will infuse further for a given PPI or sample bias. As PPI increases, the pore diameter decreases and therefore the infusion parameter decreases. Similarly, as sample bias increases, the sheath length increases and so the infusion decreases. For the experiments presented in this work, the infusion parameter tends to be in the 0.1 - 10 range. This will be referred to as partially-infused as the density drops beyond the first or second foam layer and becomes plasma facing.

The sputtering behavior of a surface is strongly dependent on the energy of the incident particle and angle of incidence. As alluded to earlier in the section, typically the energy of the incident ion is assumed to be the energy gained from the potential drop of the sheath (approximately the bias voltage). However, a collisional sheath will cause the ions to lose some energy and reduce the impact energy. The collisionality, defined by number of collisions (αd) in equation 4.6, is the ratio of the sheath length to the mean free path of the ions.

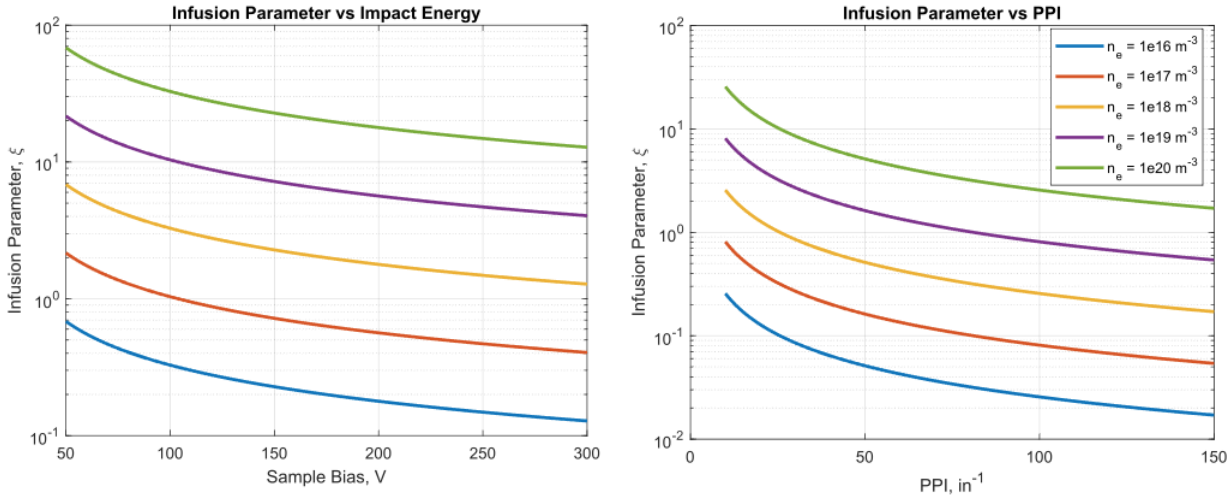

Figure 4.4: Infusion parameter as a function of (Left) sample bias and (Right) foam PPI for varying plasma densities assuming 6 eV electron temperature. The parameter space indicates the versatility of VCM design to tailor to specific application needs and the different regimes encountered in this work.

$$\alpha d = \frac{L_s}{\lambda_{mfp}} \tag{4.6}$$

Based on this, collisional sheath models [97] have been developed to describe the energy fraction of incident particles, equation 4.7.

$$\varepsilon = \frac{\zeta_w}{\zeta_{max}} = \frac{1+\alpha d}{1+\frac{13}{7}\alpha d + \frac{6}{5}(\alpha d)^2} \tag{4.7}$$

The effect of accounting for collisionality is shown in Figure 4.5. The mean free path of the ions is assumed to be the bulk plasma value from [46], which is likely an over-estimate since the sheaths are ion dominated. Figure 4.5 shows that impact energy is reduced at lower densities and therefore can affect measurement assumptions in these experiments. This is due to effect of sheath size increasing with decreasing density. One caveat however, is that the mean free path would also vary with density but is not accounted for in this analysis. That would likely counteract the sheath size increasing to an extent and produce a less significant energy fraction effect that descibed in

Figure 4.5.

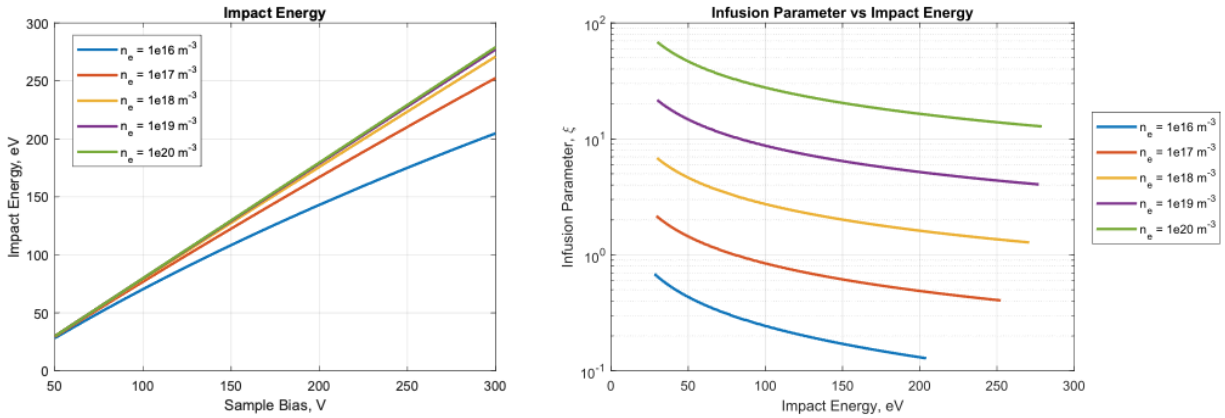

Figure 4.5: (Left) impact energy reduction of a plasma ion on material surface due to collisional losses. (Right) Infusion parameter as a function of impacting energy when accounting for the collisional loss on sample bias for varying densities.

The sheath sizes and types are significant to understanding the infusion process. Figure 4.6 shows a 10 PPI aluminum foam under xenon plasma exposure in the Pi facility. The facility is described in detail in Section 4.2, but the only significant detail to note here is that an axial magnetic field exists confining electrons.

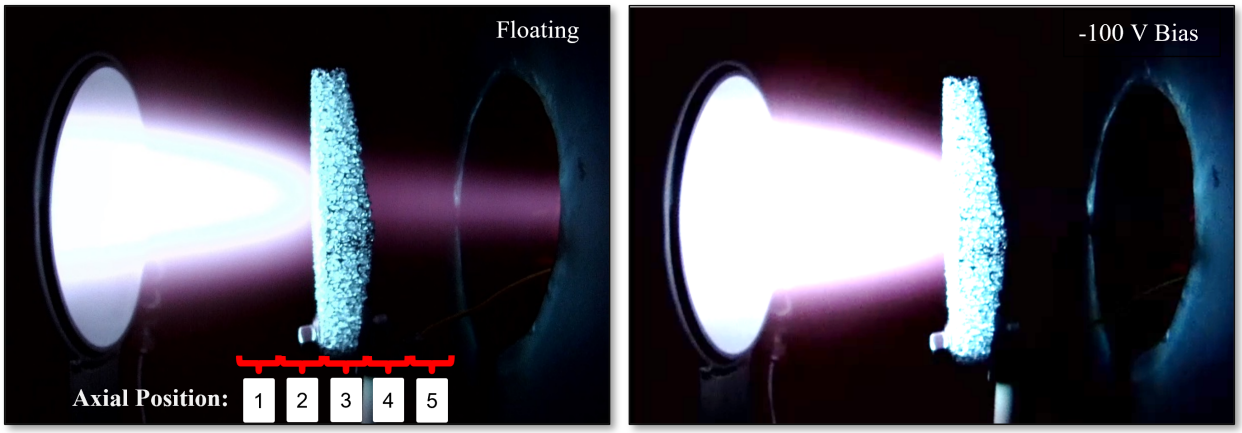

Figure 4.6: 10 PPI aluminum foam exposed to xenon plasma imaged for plasma infusion with axial positions of spectrometer optics indicated. (Left) Foam floating (no current collection) at -50 V with plasma species streaming through foam and (Right) foam biased to -100 V with no plasma species behind foam.

The purpose of the experiment was to demonstrate plasma infusion and provide some insight on the process. Table 4.1 describes the different setpoint conditions for the optical emission spectroscopy measurements shown in Figure 4.7. A 484.4 nm line is used for ionized xenon (XeII) and 672.8 nm line for neutral xenon (XeI) based on a collisonal-radiative model(CRM) by Konopliv et al. [98, 99]. Figure 4.6 shows setpoint 2 on the left and setpoint 3 on the right.

Setpoint	Discharge	Chamber Magnet	Sample Bias
1	65 A	O A	Floating
2	65 A	4 A	Floating
3	65 A	4 A	-100 V
4	65 A	4 A	-150 V

Table 4.1: Setpoints for plasma infusion study of a 10 PPI aluminum foam.

When the foam is floating (-45 V), some of the plasma species can pass through it. A Debye sheath forms at the foam ligament surfaces balancing ion and electron currents. The glow behind the foam is likely due to a combination of plasma infusion and magnetized electrons streaming through the foam. Spectroscopy measurements in Figure 4.7 show neutral xenon only at setpoint 2.

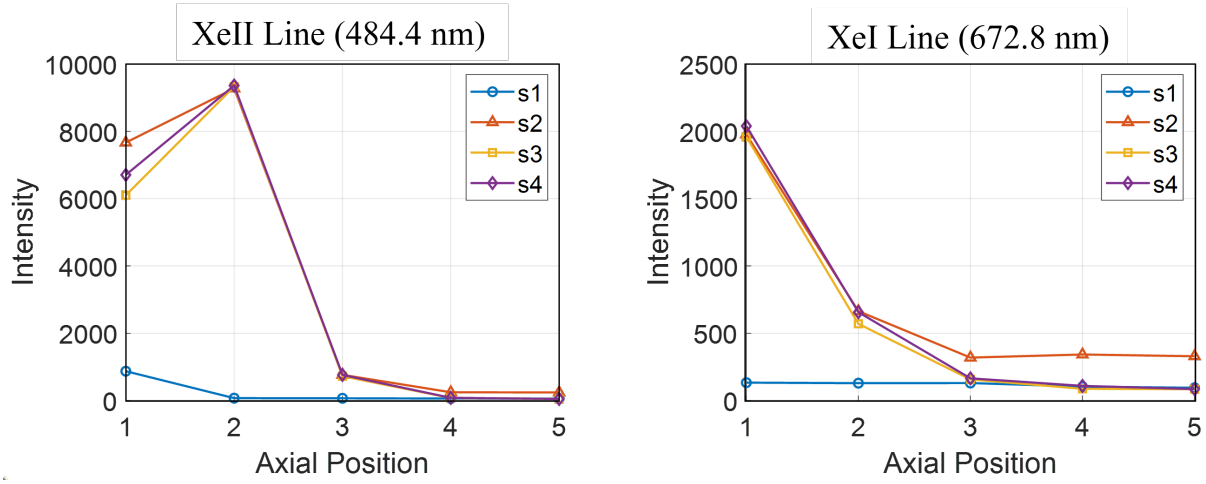

Figure 4.7: Optical emission spectra of (Left) ionized xenon and (Right) neutral xenon at different axial position in relation to foam sample at different experiment setpoints demonstrating plasma infusion of a VCM.

When the foam is biased weakly to -50 V, the Child-Langmuir sheath length is roughly $4\lambda_D$. This is essentially a transition point as the bias is increased further, the sample begins collecting ion current and sheath repelling elections, with nothing visible behind the foam. This demonstrates the ability of a foam, a type of VCM, to plasma-infuse.

4.2 Plasma Interactions Facility and Experiments

4.2.1 Pi Facility

The Plasma interactions (Pi) facility at UCLA was developed for investigating and testing advanced material candidates for electric propulsion, pulsed power, and fusion applications [46, 26]. The facility is a roughly 2 m diameter by 3 m long vacuum chamber with dual cryopumps with a combined pumping speed of 5000 L/s. An image of the Pi facility with a xenon plasma discharge is shown in Figure 4.8, followed by a drawing of the facility and key components in Figure 4.9. Neutral gas (xenon or argon) is flowed in thru a 250 A LaB_6 hollow cathode on one end of the chamber that is coupled to a 6 cm diameter by 30 cm long cylindrical copper anode. Gas is also injected downstream of the cathode keeper face before the anode to damp out instabilities. The cathode is placed coaxially inside a copper tube wound with magnet coil (cathode magnet) to confine electrons for ionization and guide the plasma. More information on the hollow cathode, including design upgrades and contamination issues, can be found in Appendix B. The anode is also wound with magnet coil (anode magnet) to confine the plasma and guide it axially. Both the cathode and anode float relative to the chamber.

The plasma from this source region is then guided downstream to the target by two 10 cm diameter by 30 cm long copper solenoids at chamber ground potential. Magnet coils are also wound around the chamber guides (chamber magnets) to confine the plasma and guide it downstream. The chamber magnets serve to decouple the source region from the target region, essentially preventing sputterants from making their way back to the cathode. The plasma column is then cusp down using a solenoid located behind the target (sample magnet) to focus the column onto the

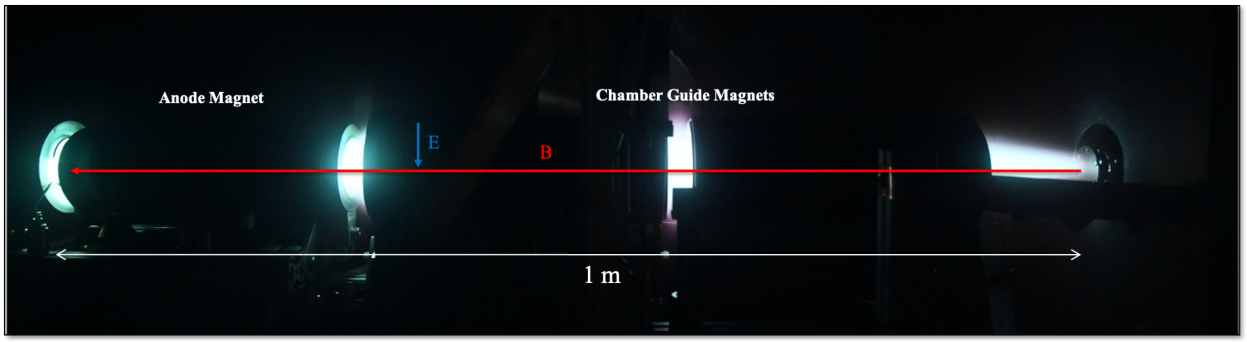

Figure 4.8: Image of the Pi facility plasma discharge configuration with a xenon Plasma.

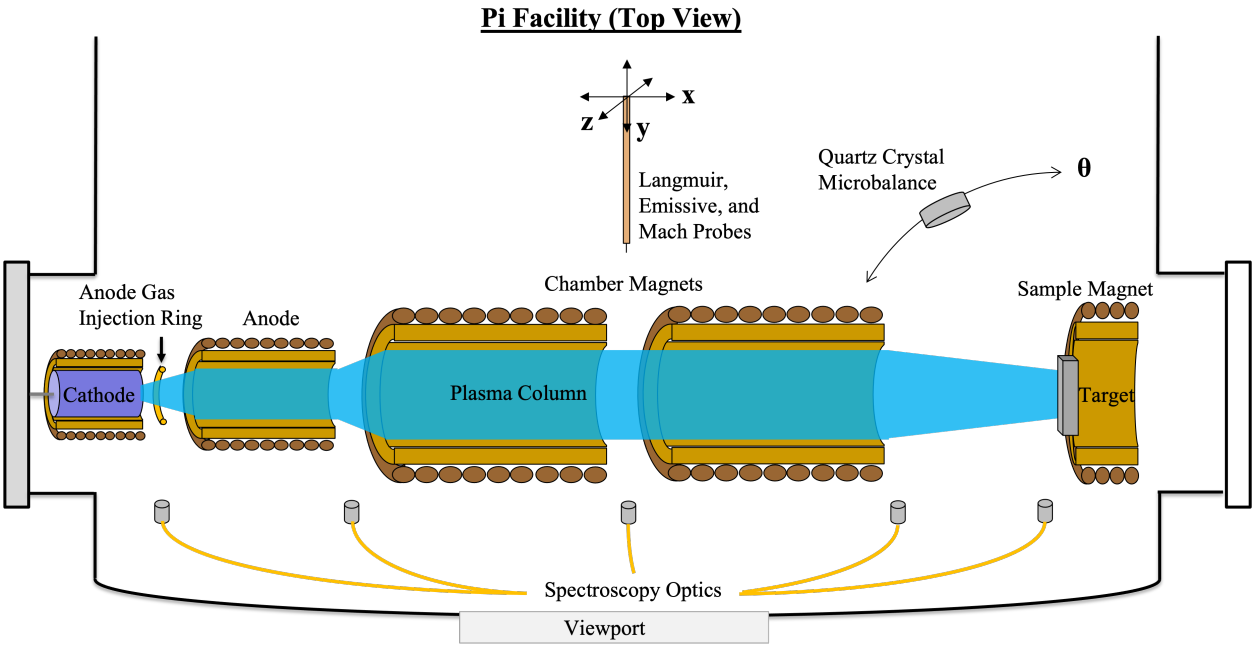

Figure 4.9: Diagram of the Pi facility configuration for the experiments discussed in this work with relevant diagnostics indicated.

target for plasma-material interaction experiments. The choice of target material and bias conditions will affect the plasma behavior, specifically the low-frequency oscillation [42]. This creates a parameter space too large to explore for this effort. To reduce the variable space, all experiments related to this work are conducted with a flat 5 cm diameter Molybdenum disc that is allowed to float (typically -30 to -50 V).

The solenoid magnets in general generate an axial magnetic field pointing towards the sample.

The potential structure of the plasma column, as shown in Figure 4.10 and Section 6.2, generates an inward electric field in the radial direction. Thus, the system is an E×B configuration. The electric field is discussed more in 6.2 with the plasma potential measurements. The remainder of the current section focuses on the magnetic field.

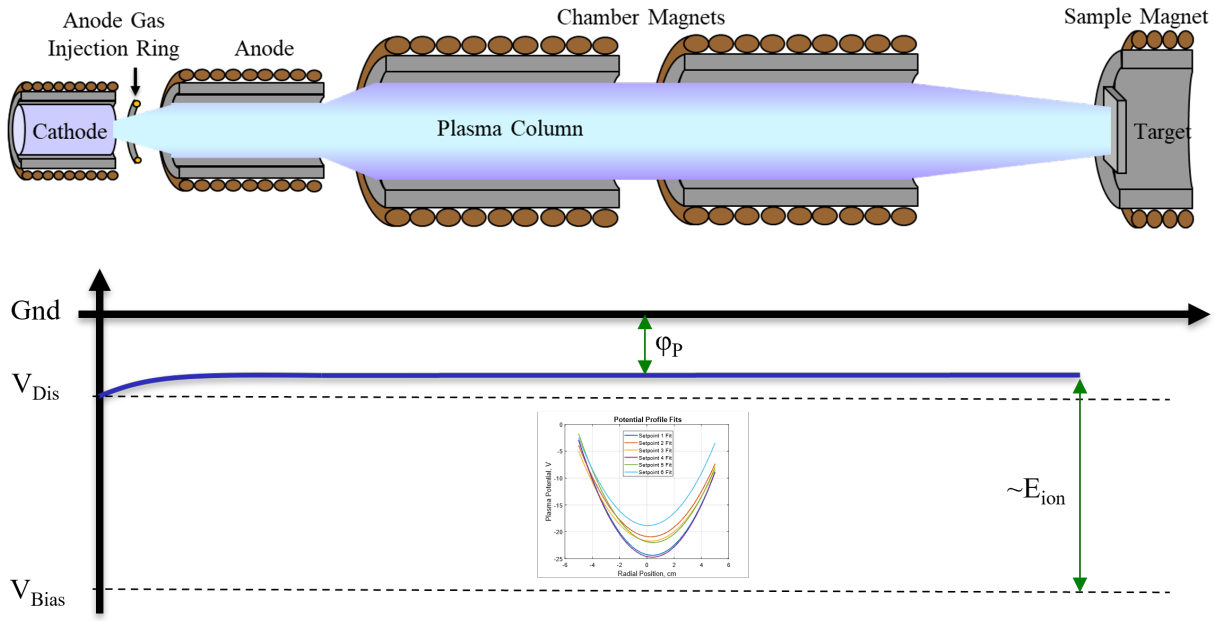

Figure 4.10: Illustration of the column center plasma potential axially in the Pi facility. The potential increases going away from the cathode until the sample where the strong negative bias attracts ion bombardment of E_{ion}.

4.2.2 Magnetic Field

The magnetic fields for the Pi facility were simulated in [45] using the Maxwell Software during the design and initial characterization of the facility. The field inside the solenoids were uniform as expected, with a decrease in intensity at the edges due to the gap between magnets. A outward-bowing of the field lines in the gap was apparent and is also observed experimentally and visually. This bowing is generally considered negligible, but worth further consideration for precise measurements in those regions.

A Lakeview gaussmeter was used to experimentally validate the magnetic field model using

measurements made in the gaps between the magnets. The purpose was to have experimental measurements of the magnetic field in the measurement plan for analysis purposes and also validate the model by comparing the predicted and measured values, thus enabling knowledge of the magnetic field in regions that cannot be measured. The probe was calibrated and zero'd before being mounted on a linear motion stage that moved the probe down vertically thru the gap downstream of the anode magnet and between the chamber magnets. The measurements were conducted at a few different operating setpoints representative of typical system operation and conditions that Langmuir probing was performed, and is tabulated in Table 4.2.

Setpoint	Cathode Magnet I_{CM}	Anode Magnet I_{AM}	Chamber Magnet I_{ChM}
1	0 A	25 A	4 A
2	14 A	19 A	4 A
3	7 A	22 A	4 A
4	7 A	22 A	7 A

Table 4.2: Setpoints for experimental mapping of Pi magnetic field structure.

The measured magnetic field profiles are shown in Figure 4.11. As anticipated, the profiles are parabolic with peaks in the center and a radial drop-off. The peak magnitude varies from 70 - 100 G in the anode magnet gap and 25-45 G in the chamber magnet gap. These anode magnet gap measurements show good agreement with the model values from [45], allowing us to use the model for magnetic field strength for regions in the anode and other operating setpoints. The measured profiles are still essential for informing the magnetic field encountered during measurements and interpreting the collected data and any probe theory considerations. Additionally, analysis of the individual vector components of the measured values indicates a radial component towards the edges as expected due to the field lines bowing outward.

4.2.3 Diagnostics

The facility has a wide variety of intrusive and non-intrusive diagnostic capabilities described elsewhere [46, 26]. The diagnostics can be mounted on a 3-axis motorized stage system designed

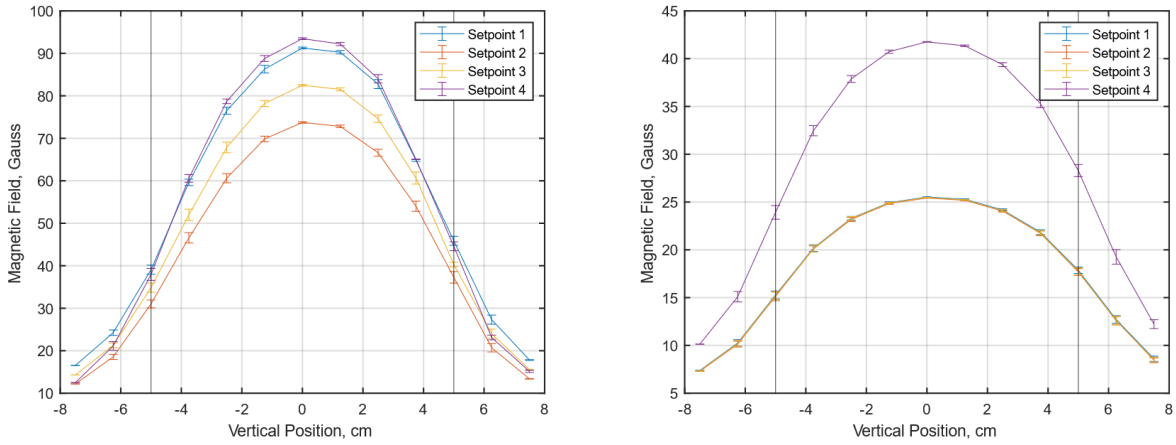

Figure 4.11: Experimentally measured profiles of magnetic field downstream of anode (left) and in-between chamber magnets (right) in Pi at varying magnet current setpoints. Vertical lines indicate boundary of chamber magnet solenoid wall

to access the gaps between the solenoids to characterize the plasma. In this effort, the stage is equipped with a Langmuir probe further discussed in Section 6.2. The configurations of any other diagnostics used in this work are described in the context of their own sections.

The steady-state plasma properties, namely density, plasma potential, and electron temperature, are commonly obtained using Langmuir probing. The technique inserts a cylindrical or spherical electrode into the plasma and measures the current response as the electrode bias voltage is varied. The generated current-voltage response curve (IV curve) can be used along with plasma sheath and probe theory to determine the plasma properties. Details of these theories is a larger topic of discussion and thus, is just summarized here. The simplest is a thin-sheath approximation, where the plasma is treated as steady-state, cold, unmagnetized, drift-free, collisionless, and thermalized. As these assumptions are almost always violated, advanced theories exist to account for the variances [100]. Applied in this effort are orbit motion limited theory, which accounts for large sheaths where the finite ion temperature and orbit motion, and Laframboise (BRL), which accounts for a sheath varying due to the bias voltage. The details of these theories and their algorithmic implementation can be found in [101, 100]. More details are presented in Appendix C on the Langmuir probing analysis process for these data.

A cylindrical Langmuir probe made of 0.016 in diameter tungsten wire protruding 4.5 mm from a single-bore alumina tube is used to measure the steady-state properties. The alumina tube is wrapped with copper tape connected to chamber ground for shielding and is inserted inside another alumina tube for improved rigidity. The probe is biased using a Kepco BOP-200 power supply and swept from -90 to 25 V using a ramp waveform with 10% symmetry and 50 Hz frequency. A 7.5 kΩ sense resistor is placed in-line between the power supply and probe with the voltage drop across the resister measured using a 10 MHz differential probe. A Tektronix oscilliscope sampling at 250 kS/s for 300 kS is used to measure the voltage of the power supply and differential probe response (from which the probe current is determined). The Langmuir probe is mounted to the transnational stage, as shown in Figure 4.9, and swept in an 11 x 11 datapoint grid in the yz-plane gap between the chamber magnet solenoids. A LabVIEW VI is used to trigger the oscilliscope measurement at each datapoint.

The design of the emissive probe is mostly similar to that of Langmuir probes, with a tungsten filament extending out of a alumina tube. The filament is heated up by a current passed from a floating power supply. As the tip of the probe is heated, it emits electrons and floats to a potential. As the emitted electron current increases, the plasma sheath surrounding the probe saturates until no higher an electron current can be emitted [102]. At this saturation point, the probe floats to within an electron temperature of the plasma potential. The local plasma potential can thus be estimated by monitoring the probe floating voltage and measuring the electron temperature, as seen in equation 4.8.

$$\widetilde{\phi}_{pl} = \widetilde{V}_f + \frac{T_e}{e}\frac{\widetilde{n}_e}{n_e} \tag{4.8}$$

Both probes are mounted on the three-axis stage and swept hourly in a 2-dimensional plane from 1-10 cm from the sample surface. The emissive probe potential is used to guide and feed the Langmuir probe fits to better converge on density values using the appropriate probe theory.

Sputtering yield is measured using a QCM swept angularly 30 cm from the surface of the sam-

ple from 90 degrees to 30 degrees in 5 degree increments on an hourly basis. The QCM is placed far enough away to provide a point-source estimation of the sample [46, 26] while also reducing any interference on the measurement from the plasma. The fundamental frequency method is used with a dwell time of 60 s to determine the sputtering yields with considerations on background and noise as described in Section 3.2 and Appendix A. Details on how the sputtering yield is determined is presented in Section 4.3.

Additionally, emission spectra was acquired hourly at different axial positions from the sample face using a Horiba FHR100 spectrometer. The results, however, are not presented in this work due to issues with the spectrometer mis-aligning mulitple times during the experiment. Similarly, the sample surface was imaged every 5 minutes using in-situ cameras but results are not presented other than in the context of providing visual reference.

4.2.4 Plasma Material Interaction Experiments

The facility configuration for the PMI experiments of aluminum foams under xenon exposure is shown in Figure 4.12. The probes and QCM are both identified to provide physical reference on their positions. Aluminum is used as a surrogate for tungsten in the experiments due to its increased sputtering behavior which makes data acquisition and experiment time an order of magnitude fast (hours instead of tens of hours). However, tungsten is the material of ideal interest for PFC applications and is scaled to and compared in Chapter 5.

The four aluminum samples measured in the experiments are shown under xenon plasma in Figure 4.13. The flat aluminum sample was purchased and machined into a 2 inch diameter disc 0.125 inches thick. The 10, 20, and 40 PPI foams were all acquired from Duocel and are roughly cylindrical ligaments. The foams have a 4-6 % volume density and an aspect ratio of 5 [103]. The 10 and 40 PPI foams were tested using a ceramic custom-design sample mount as shown in Figure 4.13. The 10 and 40 PPI foams were 1.25 inches in diameter and 0.5 inches thick. The 20 PPI foam experiment was conducted prior to design of the mount and instead measured the 1 inch tall,

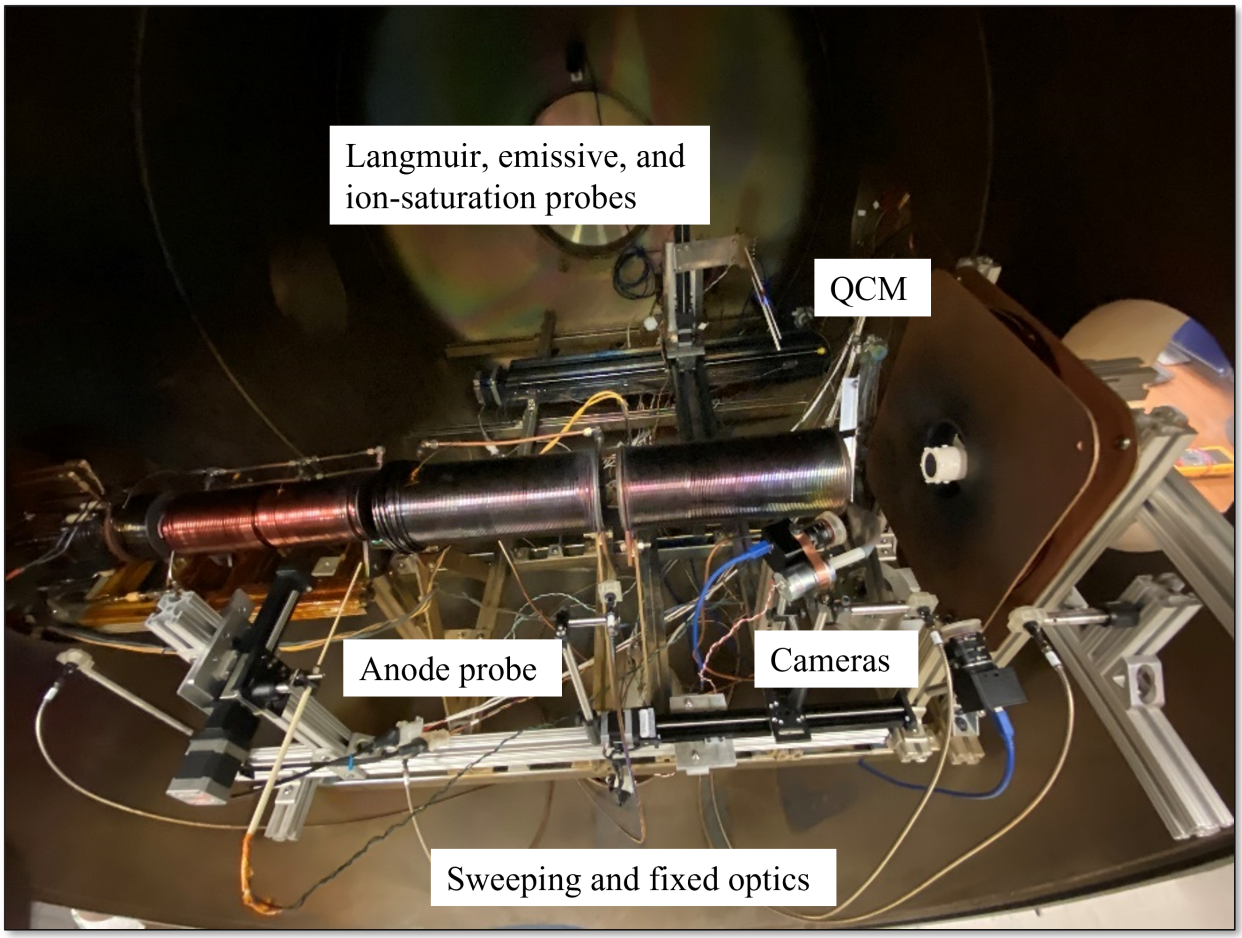

Figure 4.12: Image of Pi facility setup for PMI experiments descibed in this section with all relevant diagnostics indicated.

2 inches wide, and 0.5 inches thick. The size difference is considered to not be an issue as the spot size of the plasma was smaller than the sample in all cases and typically similar in size across experiments. All foam samples had a nickel backplate behind the sample. The nickel was chosen as it provided a different unique material composition that would be identifiable in ex-situ energy dispersive x-ray spectroscopy (EDS) to study particle transport within the foam.

The sample currents were monitored using a 5 Ohm shunt resistor on the sample bias circuit and monitored using a 300 V isolated DAQ channel. The currents are shown below in Figure 4.14 and are also used in the qcm analysis to determine sputtering yield. As seen in Figure 4.14, the sample currents for the different foams were similar and mostly constant over time. The flat sample

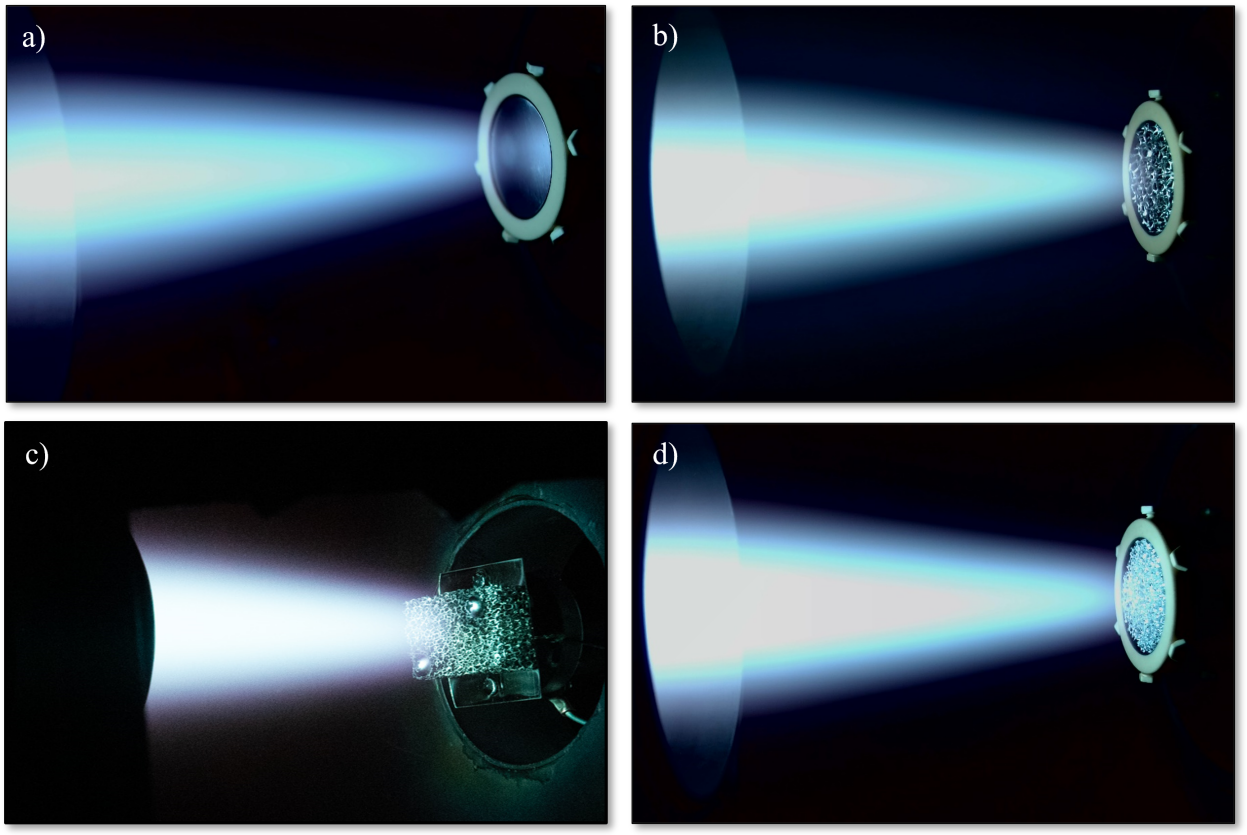

Figure 4.13: Aluminum flat and foam samples under xenon plasma exposure. (Top Left) Flat aluminum, (Top Right) 10 PPI aluminum foam, (Bottom Left) 20 PPI aluminum foam, and (Bottom Right) 40 PPI aluminum foam.

on the other hand was significantly higher and decreased with time. This difference is likely due to the flat sample being conducted first before significant contamination of the cathode resulting in an order of magnitude lower plasma density and reduced ion fluence.

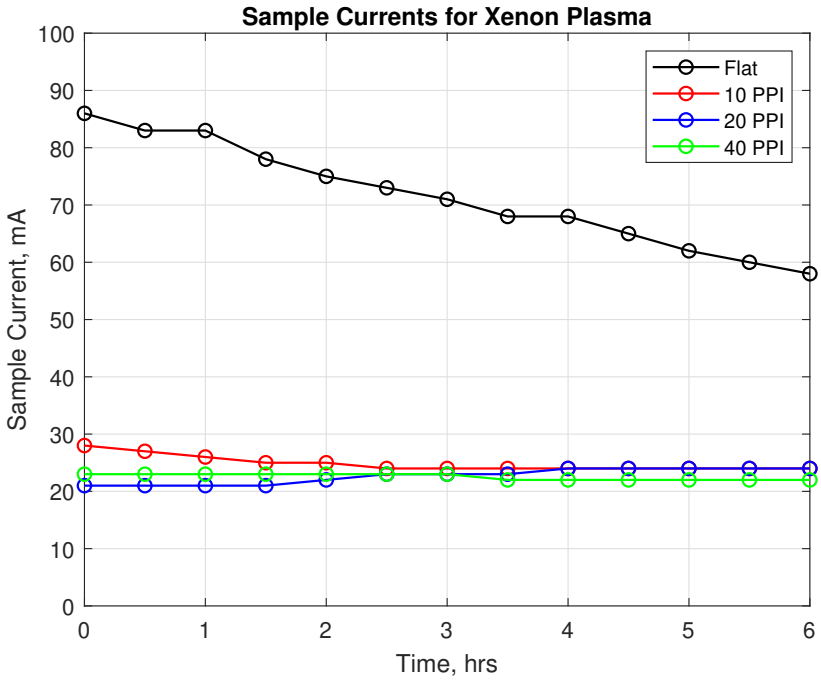

Figure 4.14: Sample currents for flat and foam aluminum samples under xenon plasma exposure during experiments discussed in analysis.

4.3 Material Sputtering and Erosion

Calculating the sputtering yield of a sample is a slightly intensive process that requires multiple assumptions. The process is illustrated in Figure 4.15 for the flat aluminum sample. The first step is determining the angular mass deposition rate, $R(\alpha)$, from the slope of the frequency at each angular location of a sweep during the appropriate measurement window (30 seconds into acquisition). The angular sputtering yield of the samples is determined using equation 4.9 from [26], where $dy(\alpha)/d\Omega$ is the angular differential yield, A_s is sample area, N_A is Avogadro's Number, m is the sputterant atom mass, J_i is the sample current, and r_{qcm} is radius of the QCM from the sample. The sample current is used to determine incident ion rate rather than a fluence measurement as it is more accurate and easier to accomplish.

$$\frac{dy(\alpha)}{d\Omega} = \left(R(\alpha)A_s\frac{N_A}{m}\right)\left(\frac{J_i}{e}\right)\left(\frac{A_s}{r_{qcm}^2}\right) \tag{4.9}$$

The center plot in Figure 4.15 shows the calculated angular sputtering profiles along with a background measurement to establish noise floor. The angular profiles are then integrated in hemispherical polar method to determine the total sputtering yield using equation 4.10.

$$Y = \int_0^{2\pi}\int_0^{\pi/2}\frac{dy(\alpha)}{d\Omega}sin(\alpha)d\alpha d\phi \tag{4.10}$$

It is significant to note that the measurements only extend to 30 degrees. This is due to the magnet coils and plasma column restricting access further towards to normal. To determine the yield, an approximation has to be made for that region, and the is the value from 0 to 30 is the value at 30 degrees. This is a reasonable approximation for flat surfaces [26], but as will be shown in Chapter 5 modeling indicates the shape will be slightly different.

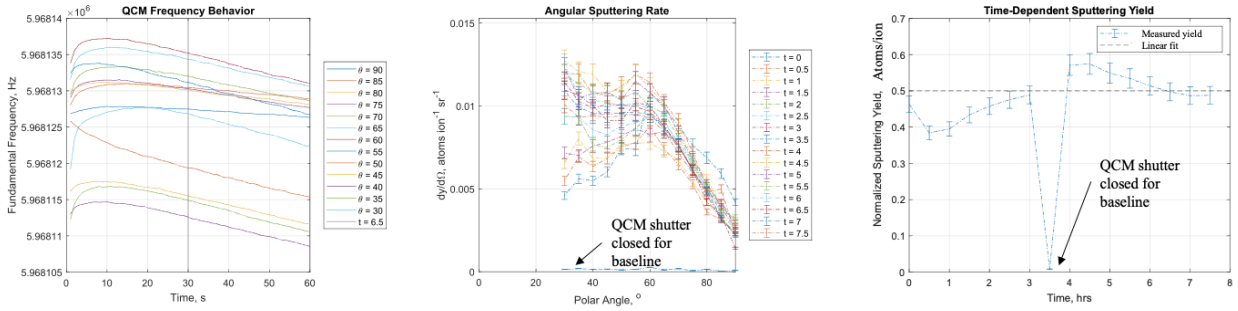

Figure 4.15: Sputtering yield acquisition of a flat aluminum sample. (Left) fundamental frequency behavior of QCM at different angular positions from which the mass flux is determined. (Center) Angular sputtering yield profiles determined along with baseline indicated. (Right) Total sputtering yield determined from integrating angular sputtering yield profiles.

The plot on the right in Figure 4.15 shows the sputtering yield over time for the flat surface. A linear fit is applied to determine a value (0.5 atoms/ion) as it can be approximated as constant over time. The value is slightly higher than the theoretical value of 0.45 atoms/ion, but within the error and possible mechanisms for the elevation discussed in Section 6.4.

Sputtering yield was measured at different sample bias energies for the 20 PPI foam and is shown in Figure 4.16. The results show the evolution of the profile shape with increasing energy, with the bump growing in significance. The foam reduces sputtering yield compared to a flat surface at all energies sampled, with the reduction decreasing with increasing energy. These trends are consistent with modeling results presented in Chapter 5 and discussed further there.

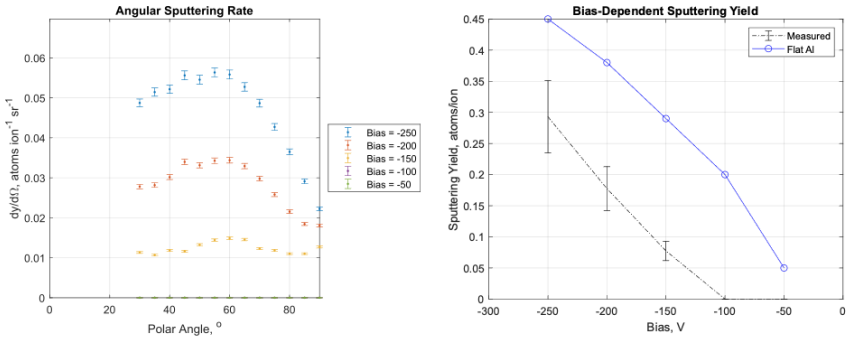

Bias	Sputtering Yield Reduction
-150 V	71 %
-200 V	53 %
-250 V	38 %

Figure 4.16: Sputtering yields of a 20 PPI aluminum foam at different bias. (Left) Angular sputtering yield profiles evolving with energy. (Center) Total sputtering yield demonstrating reduction at a range of energies. (Right) Tabulated sputtering yield reduction as a function of bias.

The same processes to calculate sputtering yield were carried out for the 10 and 40 PPI foams and shown in Figure 4.17. The yields are compared to the theoretical value for flat aluminum, and all show persistent reduction. More importantly, all the foams are of same aspect ratio, exposed to similar plasma conditions and sample currents, and demonstrate similar yields. This is interesting to note as it it supports the factor that the aspect ratio is the primary geometric factor that affects yield (especially in plasma facing). This point is further exemplified and validated in Chapter 5.

The same yields are shown in Figure 4.18 relative to the sputtering yield of flat aluminum. This form makes it easier to demonstrate the persistent reduction in comparison to a flat surface, here on the order of 40%. The reduction is the same for all the foam PPI as discussed in the paragraph above.

The foams are analyzed after exposure ex-situ using imaging, scanning electron microscopes (SEM), and EDS. Figure 4.19 shows images of the 10 PPI foam and nickel backplate before and

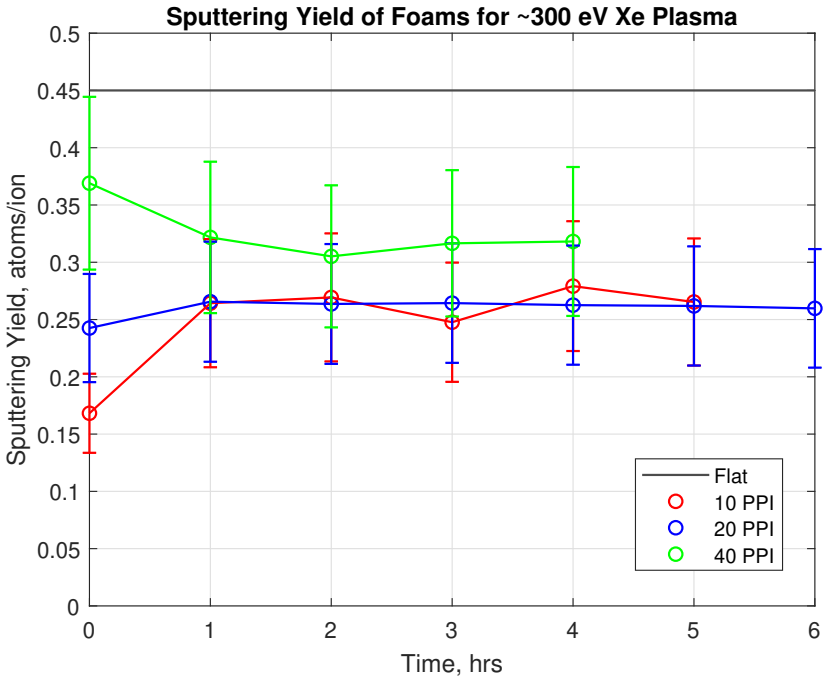

Figure 4.17: Measurements of sputtering yields of 10, 20, and 40 PPI aluminum foams under xenon plasma at -290 V bias.

after exposure. The pre-image shows a small amount of transparency that is harder to resolve in the post-image due to discoloration of the foam from the exposure. The transparency of these foams has been reported by Ottaviano and Wirz [103] and can be used for any quantative comparisons. Pre- and post- mass and dimension measurements were taken to compare mass loss to expected erosion. Unfortunately, due to the unexpected drop in facility density and fluence, the resolution of the measurements to 0.02 was not enough to provide substantial insight or comparison.

The 40 PPI foam was similarly analyzed and shown in Figure 4.20. The transparency is essentially 0% in this case as there are a substantial number of layers in a 0.5 inch thick sample. Interesting to note is the clear erosion dip of the beam profile visible in the sample due to the higher PPI nature. This confirms that the core interaction is in a spot near the center of the sample and mostly consistent with previously reported facility behavior in terms of spot size [46, 26].

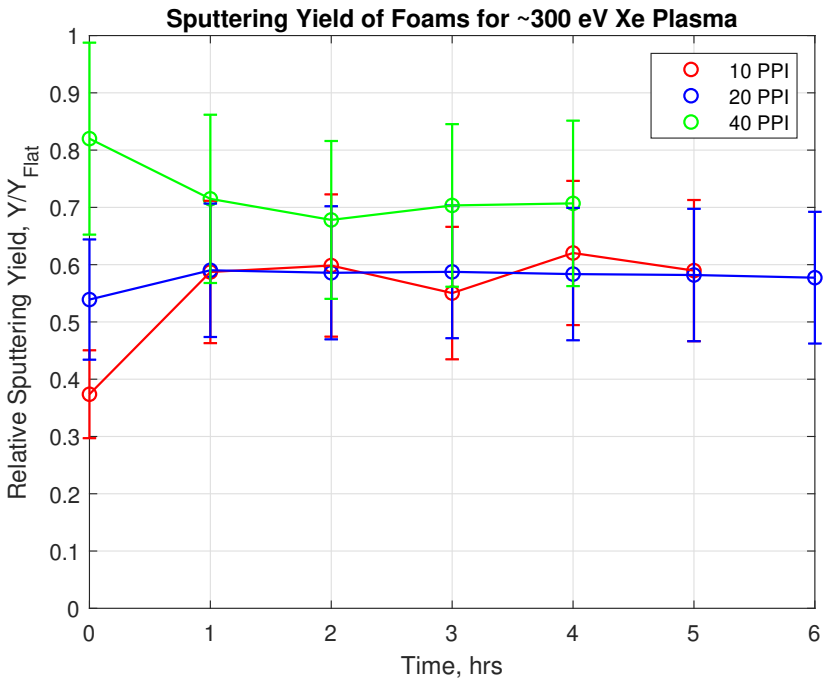

Figure 4.18: Sputtering yield reduction of 10, 20, and 40 PPI aluminum foams relative to a flat surface under xenon plasma at -290 V bias.

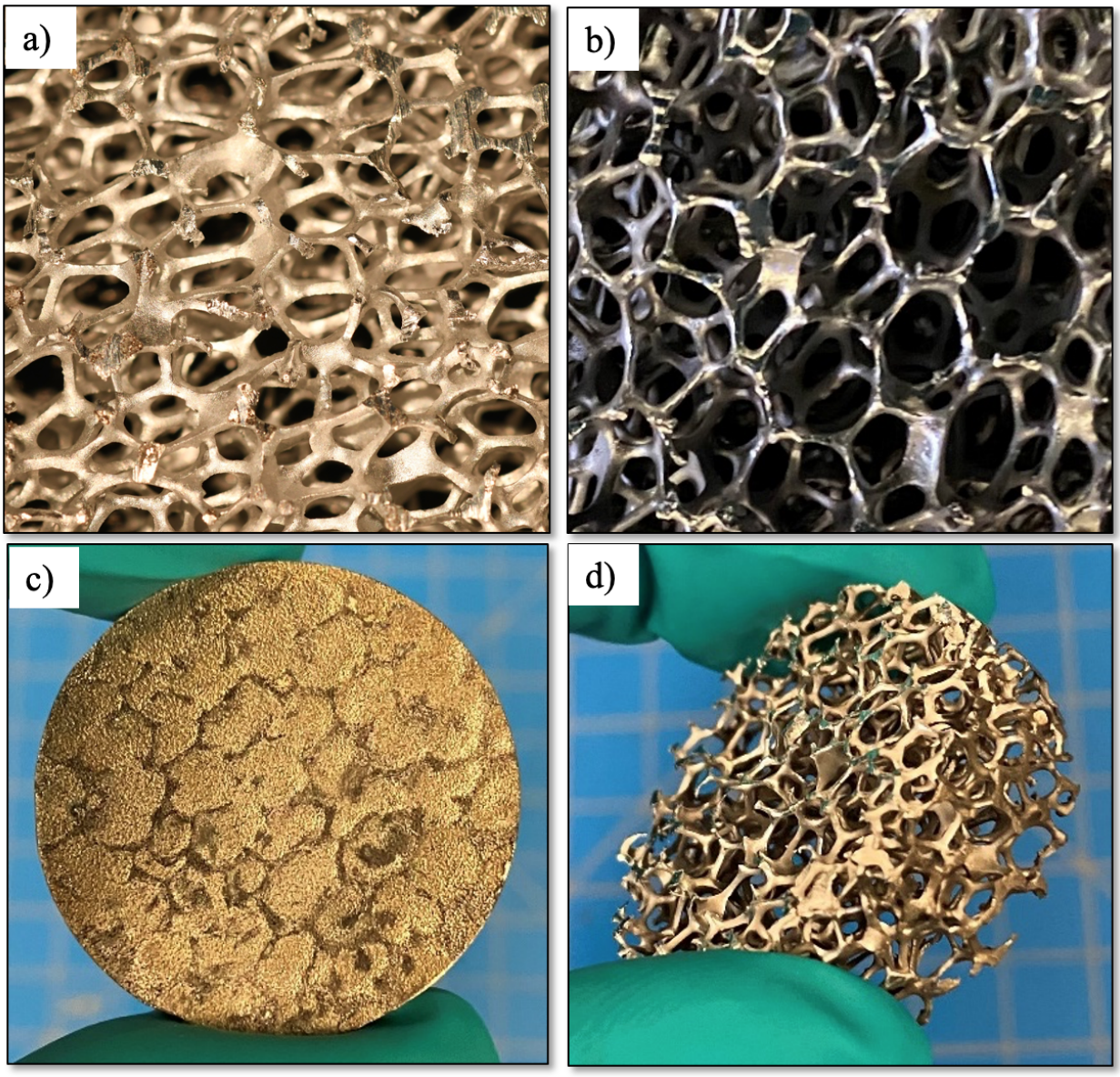

Figure 4.19: Images of 10 PPI aluminum foam and nickel backplate. (a) image from above of foam before exposure with black backing to demonstrate transparency, (b) image of foam after exposure, (c) 10 PPI foam after exposure, and (d) nickel backplate after exposure with marks where foam ligaments had press contact.

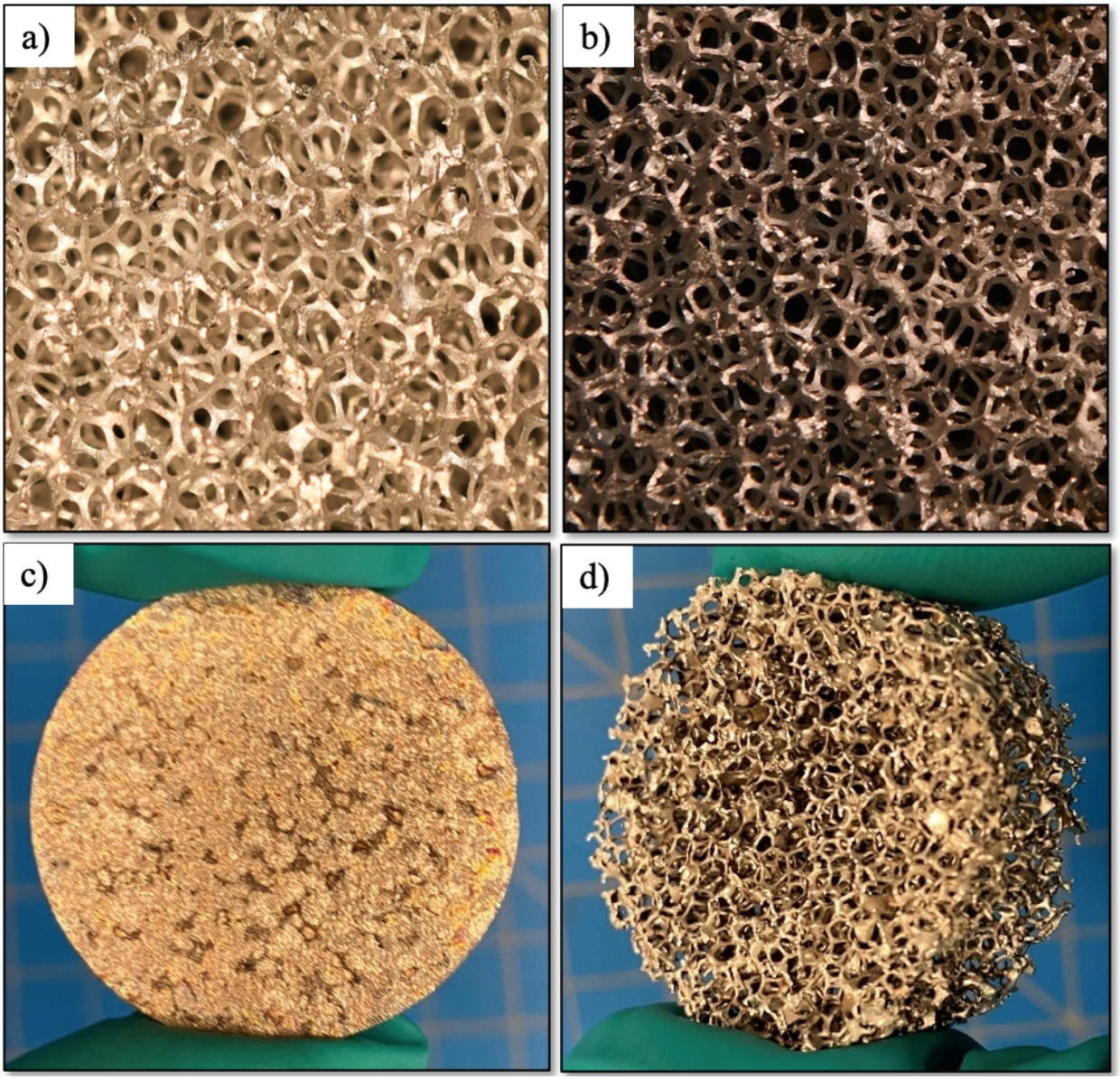

Figure 4.20: Images of 40 PPI aluminum foam and nickel backplate. (a) image from above of foam before exposure with black backing to demonstrate transparency, (b) image of foam after exposure, (c) 40 PPI foam after exposure, and (d) nickel backplate after exposure with marks where foam ligaments had press contact.

4.4 Plasma Behavior and Response

Probe measurements were acquired hourly during the 10 and 40 PPI foam experiments as described in Section 4.2. The sample region space was probed in a 10 x 10 cm 2-dimensional plane with each probe in 1 cm increments along the radial and axial directions. The resulting plasma density and potential contours for up to 5 hours are shown in Figure 4.21.

For simplicity, the case of the 40 PPI foam is first considered. The contours indicate relatively steady plasma behavior over the 5 hours. There is some modification of the potential far upstream of the sample that seems to be relatively insignificant. For easier comparison, radial plasma density and potential slices 2 cm from the sample surface are plotted in Figure 4.22. The plots more clearly illustrate the stability of the plasma behavior in the case of the 40 PPI foam, with the density and potential relatively steady. These results indicate that the foam is in the $\xi < 1$ range indicating a plasma-facing regime per Figure 4.4. Though the sheath is not measured here, the pre-sheath region is being probed and represented.

The 10 PPI foam on the other hand seems to present a dynamic plasma response. The potential structure beings quite conical and sharp as if following the magnetic cusp into the sample with a small sheath. The density structure is also more clearly visible. With time, the potential structure transforms to a shape similar to that of the 40 PPI and the density decreases. Similar radial slices are shown in Figure 4.23 for the 10 PPI foam. The plots show the drop in density and increase in potential more clearly. In the case of the 10 PPI foam, ξ 1 initially indicating that the plasma is partially-infusing the foam. This is consistent with the observed potential structure where it follows the cusp and the sheath seems much smaller in size based on inferring from the different behavior of the pre-sheath potential. However, as the density decreases with time (likely due to cathode contamination), $\xi < 1$ and the foam transitions into the plasma-facing regime with the plasma properties behaving similar to the 40 PPI foam behavior.

The is more complexity to the interaction to account for when considering longer timescales. If the foams were exposed for significantly longer duration or at higher fluence, ligament erosion

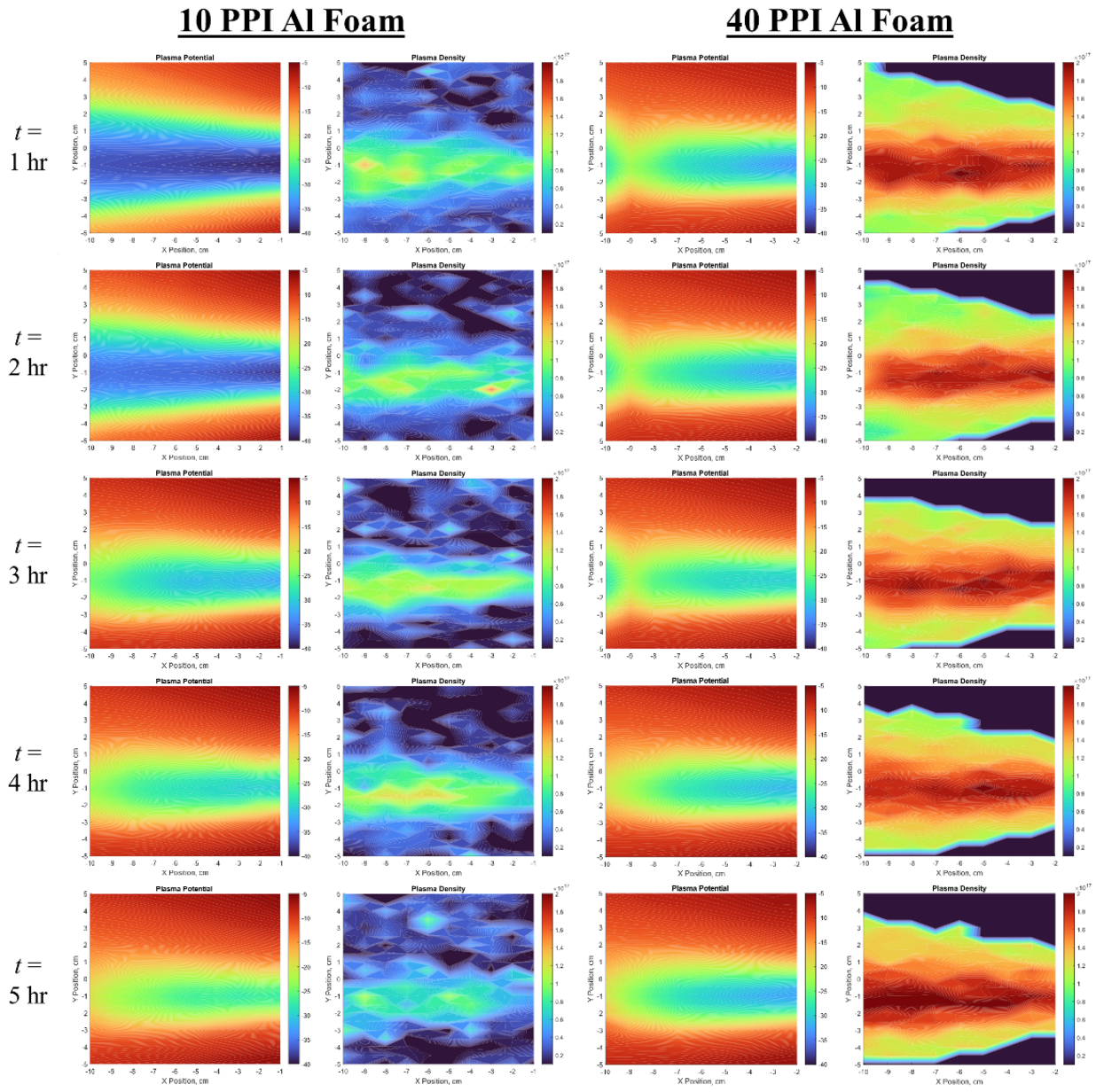

Figure 4.21: 2D contours of plasma potential (1st and 3rd columns) and density (2nd and 4th columns) near the 10 and 40 PPI samples over a 5 hour duration. The 10 PPI foam shows evolution of the potential structure towards the same form as the 40 PPI foam's structure.

would play a role in infusion. As the ligaments erode, the pore diameter increases thus affecting infusion of the plasma (makes ξ higher) and in turn causing more rapid erosion of the top layer. The benefit of VCMs is the repeating cycle of layers that allows this process to sustain and persistently

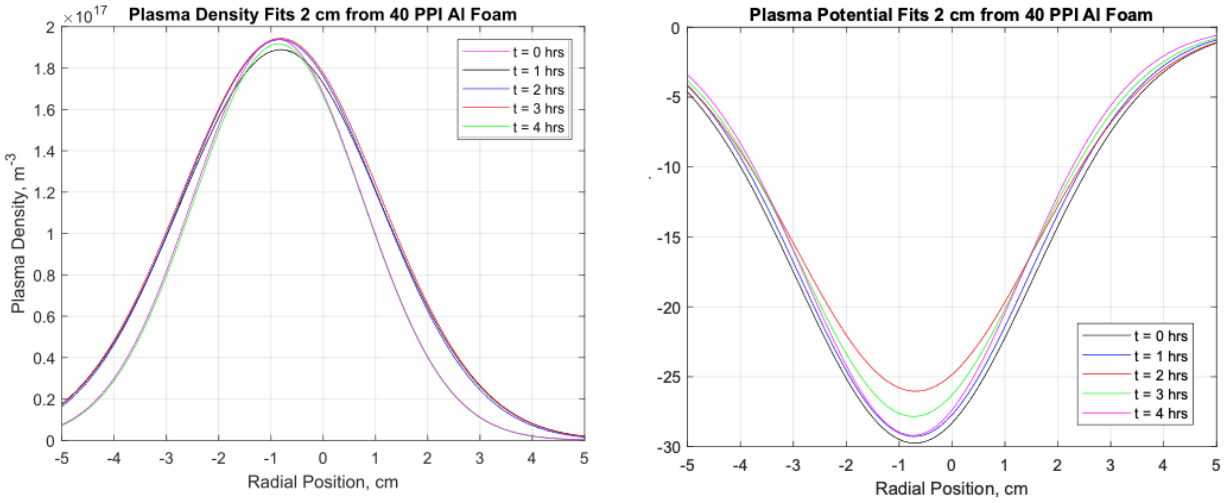

Figure 4.22: Radial slices of plasma (Left) density and (Right) potential 2 cm from surface of 40 PPI foam over 5 hours over plasma exposure.

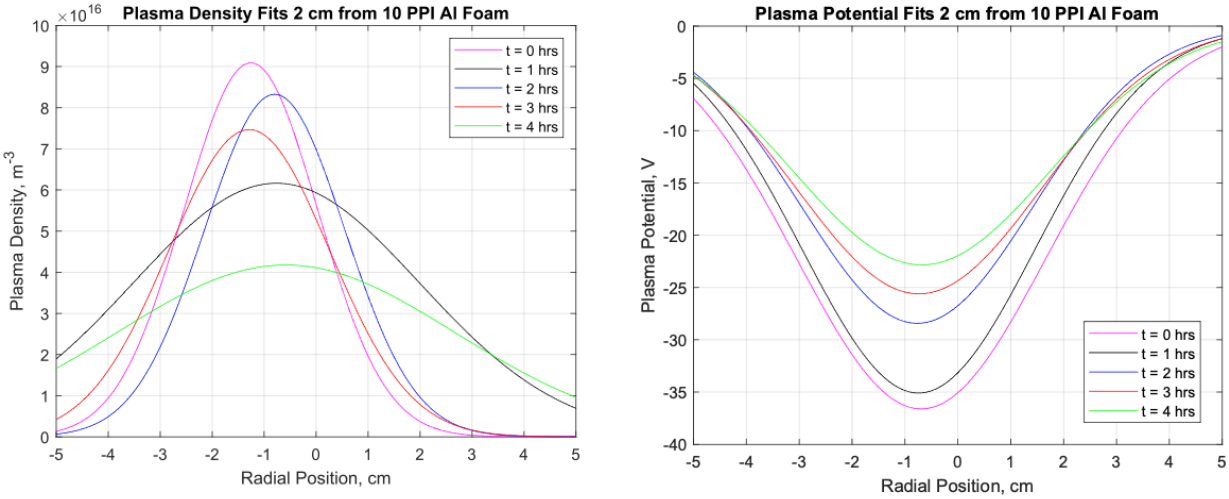

Figure 4.23: Radial slices of plasma (Left) density and (Right) potential 2 cm from surface of 10 PPI foam over 5 hours over plasma exposure.

trap sputterants to reduce total yield going back into bulk plasma.

4.5 PMI Experiment Takeaways

The fundamentals of plasma-infusion of VCMs were presented and expanded upon using considerations of collisionality for impact energy and demonstration of plasma infusion of a foam. An experimental setup and campaign involving multiple PPI aluminum foams and flat surface for comparison were conducted. The experiments consisted of precise and accurate measurements and analysis of sputtering behavior and plasma properties of foams. Sputtering measurements demonstrated persistent reduction in comparison to a flat surface and for a range of energies. More significantly, results show that the sputtering yield of foams in the plasma-facing regime are depending primarily on aspect ratio of the foam and not the PPI. Plasma measurements during the experiment demonstrate the successful measurements of a partially plasma-infused foam that transitions to a plasma-facing regime. Analysis reveals that the infusion is dependent on the plasma properties and PPI. This allows for an important takeaway in designing VCMs for plasma applications. The foam PPI is a design parameter for what plasma environment the foam is in, and the aspect ratio a toggle for the sputtering behavior as further demonstrated in Chapter 5.

CHAPTER 5

Sputtering of Volumetrically-Complex Materials

This chapter details an analytical model capturing sputtering behavior of foams. A random geometric approximation is created to develop a view-factor model. Based on calculated angles of shadowing of a ligament in a given layers to ligaments in layers above, sputtering distributions of individual ligaments are super-positioned to determine the angular sputtering distribution and total sputtering yield. The model is validated using measurements presented in Chapter 4 for plasma-facing regime. The parameter space of aspect ratio, energy, and material is then explore to determine the potential benefits VCMs can offer in PFC applications.

5.1 Ion Sputtering Background

Characterizing sputtering of foams is challenging due to the complex nature of the surface. The surface elements are not flat surfaces but rather ligaments with some cross-sectional shape (such as a circle or triangle) with incoming species coming at different angles of incidence based on the regime (plasma-facing vs plasma-infused). Furthermore, the 3-dimensional nature of VCMs and foams adds additional complexity as different layers are shadowed by layers above at certain angles resulting in trapping of species. Furthermore, there is a wide range of sputtering theories and models for describing sputtering off a material surface at a given incident species, energy, and angle of incidence. Commonly used is Yamamura [104, 105], including in the previous investigations and modeling of foams by Li and Wirz [96, 9]. However, recent modeling using different approaches including TRIM and TRI3DYN by Sabiston and Wirz [106] have shown shortcomings with the Yamamura empirical fits. As such, this effort expands on the previous modeling effort by Li and

Wirz by incorporating sputtering yield distributions from TRI3DYN and creating a view factor model of foam based on random geometry to obtain angular sputtering profiles and total sputtering yield. The objective was to create a semi-analytical model that accurately describes the sputtering behavior of foams and validate with experimental data.

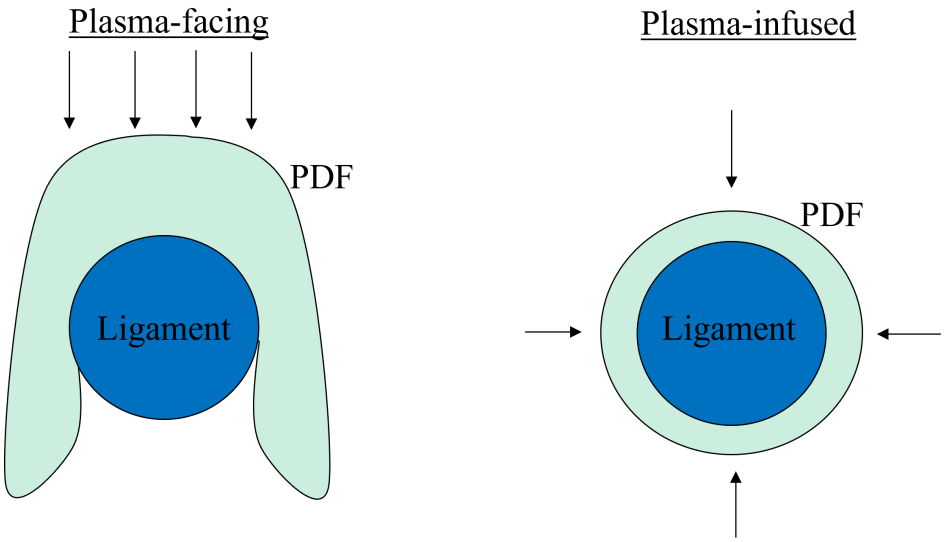

Figure 5.1: Pictorial representation of the sputtering probability distribution function for a single circular ligament in (left) plasma-facing and (right) plasma-infused scenarios.

This is accomplished by beginning on a ligament basis. Figure 5.1 shows expected probability distribution function (PDF) shapes for a plasma-facing ligament and a plasma-infused ligament. The plasma-infused ligament scenario is simple as the angle of incidence is always normal to the surface and of uniform energy, resulting in a uniform PDF all around the ligament. The plasma-facing scenario is more complex as it the ions are all incident at the same angle with respect to the centerline of the ligament, but varying angles with respect to the surface of the ligament. Ions incident toward the edges of the ligament impact with a steeper angle of incidence, resulting in a local PDF that is heavily skewed toward forward scattering (that is scattering into the foam in the same direction the ions are coming in for plasma-facing scenario). Summing each of the individual PDFs for angular locations along the ligament surface allows for the generation of a ligament PDF that describes the cumulative sputtering behavior of the ligament, and is visualized in Figure 5.1.

This distribution is plotted more accurately by Sabiston and Wirz in [106] including accounting for the reduced normal area of the edges of the ligament. This distribution is referred to as the Basset Distribution (due to the Basset Hound ear shape it forms around the ligament). These PDFs are generated for different materials and incident ion energies and serve as an input for the foam sputtering model described in this chapter. The distributions are scaled up input such that $pi * \int dy/d\Omega$ is equal to the total sputtering yield. Distributions for sputtering from a flat surface at the same energy are also input into the model to provide a comparison for reduction.

5.2 Sputtering Model Approach for Volumetrically-Complex Materials

Using a ligament PDF instead of individual angle PDFs allows for a view-factor approach where the ligaments in a foam geometry can be treated as points sputtering with view factors to subsequent layers calculated for geometric arguments. The challenge then is to create a mathematical construct for the layer geometry of a foam that successfully captures the somewhat random geometry while make the view factors derivable. This was accomplished using the same approach initially as Li and Wirz [9], shown in Figure 5.2. In this approach, the first layer is defined by a rectangular cell of inner size pore diameter D. Ligaments have a diameter and bisect the open space in each subsequent layer. This approach maintains the geometric definitions of PPI and aspect ratio for a foam while producing a very averaged geometric structure that a random geometries would ensemble average to. The only two geometric inputs to the model are PPI and aspect ratio (D/d). It will be evident soon that the PPI does not affect the geometry and sputtering as it scales both D and d equally, essentially maintaining the same are ratios of ligaments and view-factor angles. This is consistent with intuitive picture and findings in Chapter 4 that the PPI is the knob for controlling plasma parameters and infusion while maintaining independence from sputtering geometry.

Based on the geometric definition from Figure 5.2, the theoretical transparency as a function of layers can be calculated using equation 5.1. The transparency as a function of layers is shown in Figure 5.3 for different aspect ratios. For all aspect ratios shown, the transparency approaches

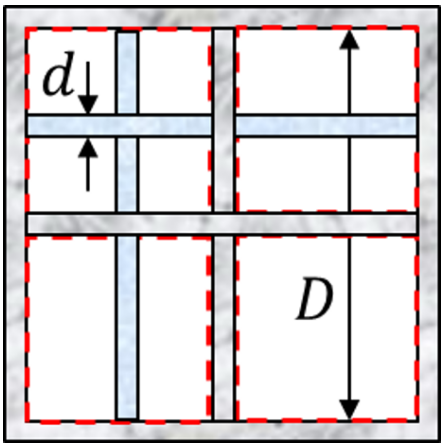

Figure 5.2: Top view of a geometric construction of a random foam from [9] where each sequential layer's ligament bisects the open pore area in half.

10% or lower by the fourth layer, indicating that capturing view factors thru the first four layers is sufficient for describing the bulk of sputtering behavior for plasma-facing foams as almost all of the unit cell area is captured.

$$T_n = \left(\frac{D-(n-1)d}{D+d} \right)^2 \tag{5.1}$$

A significant difference between this model and previous models is the construction of layers as shown in a cross-section view in Figure 5.4. The previous model by Li and Wirz nested every alternating layer directly below itself for the re-deposition calculations, which is not consistent with the construct shown in Figure 5.2. That was sufficient for the purpose of that model, but as this model's objective is to accurately capture the sputtering profile and yield, it must follow the proper construction. The top four layers are shown in Figure 5.4, with view factors a ligament in the 4th layer to all different layers indicated by different colors.

Each view factor can be defined as shown in Figure 5.5 using a combination of the angle with respect to the ligament normal, Ω, half-angle of the view-factor cone, Δ, and separation between the layers, h.

The view factor definitions for each layer combination thru the first four layers are listed below

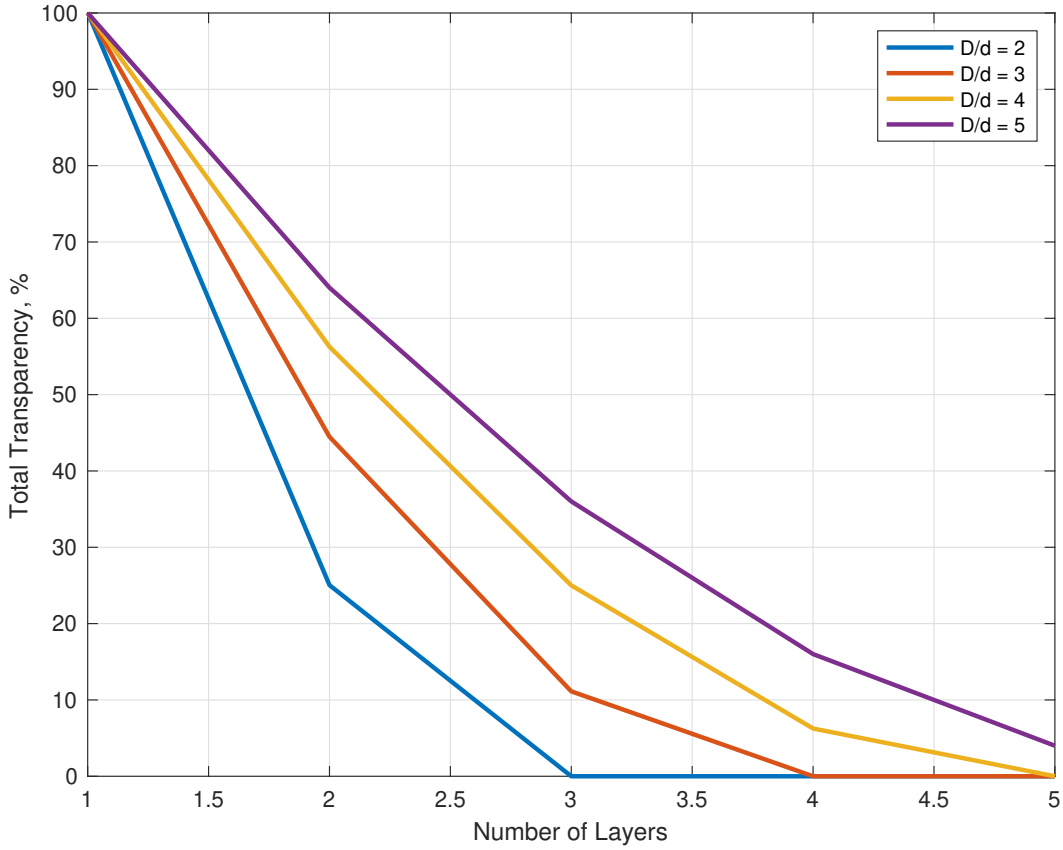

Figure 5.3: Transparency of foam geometry as a function of layers indicating the areas considered by depth.

in equations 5.2 to 5.14. The superscripts indicate the ligament combination being described (i.e. 32 is third layer ligament to second layer) and the subscript describes which sequential ligament in the layer above being described. In the model, each layers interaction is extended out to a total of 8 ligaments in each layer above (four on each side of the ligament) to capture interactions out to the far ranges. Additionally, view-factors to the neighboring ligament in the same layer is accounted for at -90 and 90 degrees.

$$h_y^{21} = h_y^{43} = \sqrt{1 + \frac{(2y-1)^2}{4}}(D+d) \tag{5.2}$$

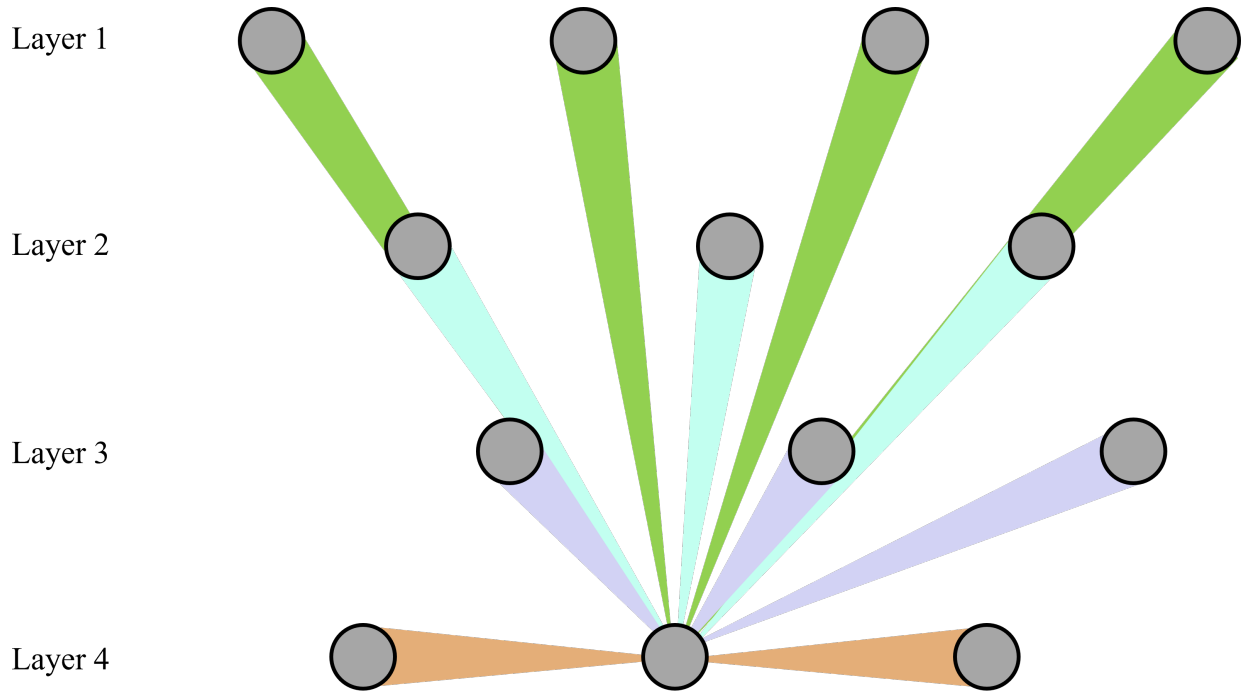

Figure 5.4: Cross-sectional view of foam geometry model based on Figure 5.2 with view-factors of a ligament in the 4th layer to all layers above indicated.

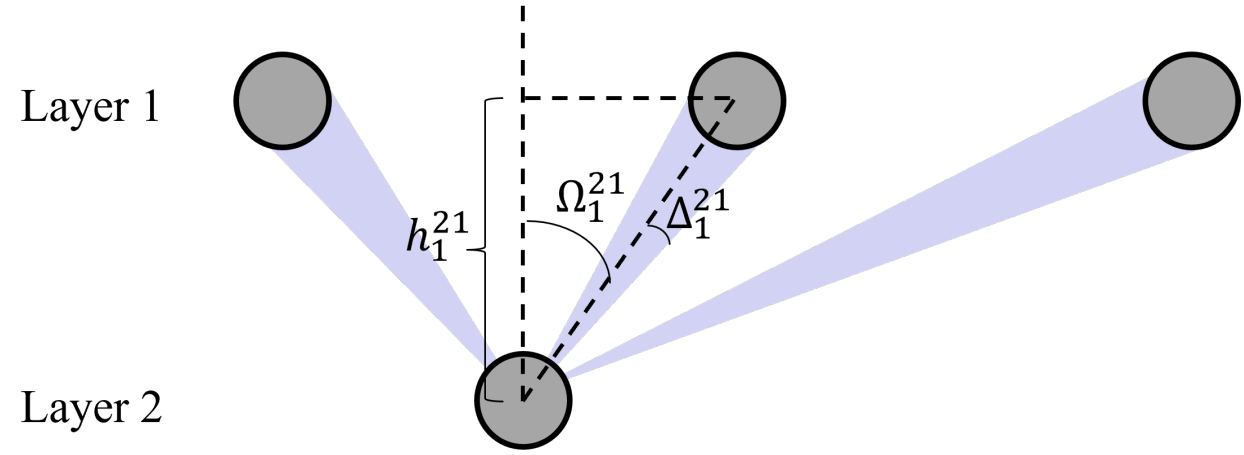

Figure 5.5: Geometric definitions of height separation, center angle, and half-angle between ligament layers used to define view factors.

$$tan\Omega_y^{21} = tan\Omega_y^{43} = \frac{2y-1}{2} \tag{5.3}$$

$$tan\Delta_y^{21} = tan\Delta_y^{43} = \frac{d}{2h_y^{21}} \tag{5.4}$$

$$h_y^{32} = \sqrt{(D+d)^2 + \left(\frac{yD + dF_R(y)}{2}\right)^2} \tag{5.5}$$

$$F_R(y) = 2round\left(\frac{y}{2}\right) - 3 \tag{5.6}$$

$$tan\Omega_y^{32} = (-1)^y \frac{yD + dF_R(y)}{2(D+d)} \tag{5.7}$$

$$tan\Delta_y^{32} = \frac{d}{2h_y^{32}} \tag{5.8}$$

$$h_y^{31} = h_y^{42} = (D+d)\sqrt{4 + \frac{(2y-1)^2}{16}} \tag{5.9}$$

$$tan\Omega_y^{31} = tan\Omega_y^{42} = (-1)^{y+1} \frac{2y-1}{8} \tag{5.10}$$

$$tan\Delta_y^{31} = tan\Delta_y^{42} = \frac{d}{2h_y^{31}} \tag{5.11}$$

$$h_y^{41} = (D+d)\sqrt{9 + \frac{(2y-1)^2}{4}} \tag{5.12}$$

$$tan\Omega_y^{41} = (-1)^y \frac{2y-1}{12} \tag{5.13}$$

$$tan\Delta_y^{41} = \frac{d}{2h_y^{41}} \tag{5.14}$$

These view factors of shading are essentially treated as a transfer function applied to the ligament PDF that reduces the PDF value to zero at those given angular locations. This then results in a ligament angular distribution function (ADF) for each layer. The primary different between plasma-facing and plasma-infused is the choice of the PDF to use for the ligament and an exponential drop applied to the fluence of each layer in plasma-infused to model the exponential drop in density with plasma-infusion [96]. The remainder of this chapter focuses on the plasma-facing case as that was shown to be the primary regime measured in Chapter 4. The transfer function corrected ADFs for each layer are then summed to create the total foam ADF. The horizontal offsets of different ligament units is accounted for in the area-normalized calculation process and the principle that as one gets further away from the source (foam), distributions superimpose to an averaged for which in this case is the unit ADF [78].

5.3 Geometry and Energy Dependence

The developed model is then tested using a comparison to measured data of foam angular sputtering yield. Figure 5.6 shows the measured profile for a 10 PPI aluminum foam plotted against the model profiles for foam, flat, and hemisphere (ligament) sputtering yields. The yields are all in atoms/ion with the measured yields values normalized to account for per steradian from the measurements. Comparing the shape of the the measured profiles versus the model profile shows very strong agreement in shape and behavior. This is promising in validating the model. An important aspect to note is the increase towards small angles in the model profile. This is consistent with intuition as those regions sputter at reasonably high probability with no view-factor prevent their escape. As discussed in Section 4.4, the experimental measurements cannot measure at those angles and therefore assume a horizontal profile shape from 0 to 30 degrees. The model results indicate that the assumption may underestimate the sputtering yield, but only by a small amount

as in determining the total yield, the polar angle must be corrected for by multiplying the who distribution by $sin(\alpha)$ per equation 4.10. The total yields from the model and experiments are compared later in this section and show good agreement. Additionally, the model profile shows reduction in comparison to the hemisphere, indicating the role geometric trapping plays in reducing the sputtering. Furthermore, a large difference is noticeable between flat and foams, exemplifying how the ligament shape and 3-dimension structure both play strong roles in reducing the sputtering yield.

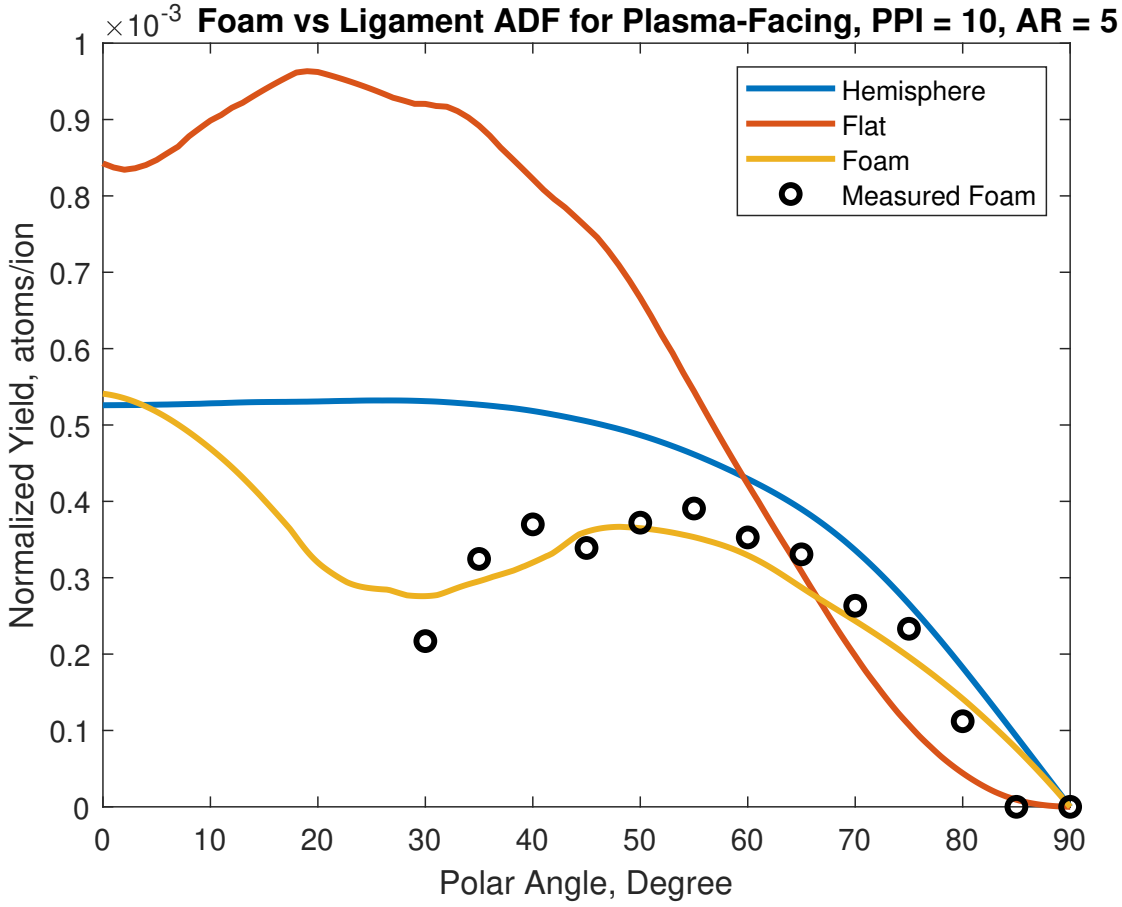

Figure 5.6: Model results of angular sputtering profiles of a foam compared to experiment measurements showing good agreement and reduction compared to flat.

Having validated the model, the parameter space is extend to cover a range of energies and aspect ratios for two different materials of interest, aluminum and tungsten. The energies are

chosen based on the data available from Sabiston's TRI3DYn simulations [106]. The angular sputtering profiles for aluminum as a function of energy and aspect ratio are shown in Figure 5.7. Note that the noisy behavior of the flat distributions at certain energies is due to computational noise from TRI3DYN simulations [106]. This occurs because of a fixed fluence being used for consistency cross the different energies in initially generating the PDFs. However, at low energy little sputterants are produced and so the results contain sampling noise. Sabiston notes that the noise can be reduced by re-running the simulations at lower energies with higher fluence, and that those results are similar to smoothing the noisy data curves. For the analysis in this foam sputtering model, the noisy PDFs for flat are used as the ligament PDFs themselves reduce the noise and the foam further smooths it out. As energy is increased, the trapping in the high angle region is increased due to a significant shift in the shape of the ligament PDF itself (demonstrated by the hemisphere).

The sputtering yields and relative yield in comparison to a flat surface for each distribution are calculated and shown in Figures 5.8 and 5.9 respectively. The results indicate that the foams perform better at higher energies, with small aspect ratio showing greater reduction due to increased trapping of underlying layers due to the large relative size of the ligaments in relation to their spacing. The yield values themselves agree well with measured values for the $AR = 5$ foams at higher energies but deviate at low energies. The foams show reduction steady to increased sputtering yield reduction in comparison to a flat surface with increasing, albeit over a narrow energy range. The $AR = 5$ foams indicate a 38% reduction at 300 eV regardless of PPI, which agrees with the measurements presented in Figure 4.18. This indicates the successful ability to model foam sputtering behavior that matches with experiments.

The model is then extended to tungsten, the material of interest for application for PFCs. The energies cover a wider range and higher magnitude as tungsten does not significantly sputter at lower energies. The angular profiles are shown in Figure 5.10. The flat and ligament sputtering behavior of tungsten across all energies different significantly from aluminum, with no peak towards the higher angle region. This is significant as the resulting foam profile shows significantly

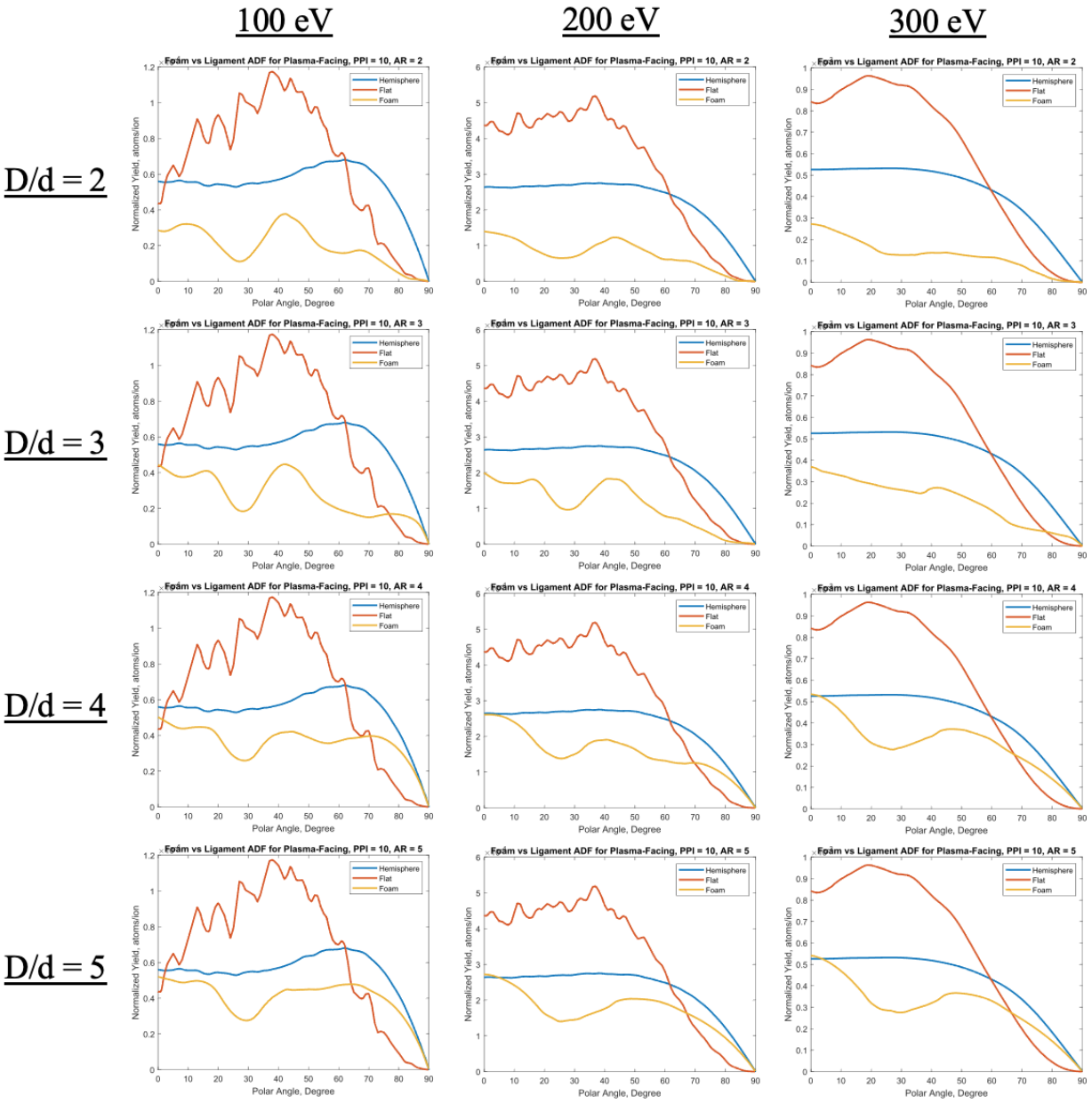

Figure 5.7: Angular sputtering distribution of aluminum foams and flat surfaces modeled at different energies (horizontally) and aspect ratios (vertically).

reduced sputtering as the there is effective trapping at the angles where most of the sputtering does occur. This is extremely promising as it shows that the material sputtering behavior of tungsten makes it ideal for coupling to the added benefits of reduction caused by VCMs.

The sputtering yields for each case and the relative sputtering are presented in Figures 5.11 and

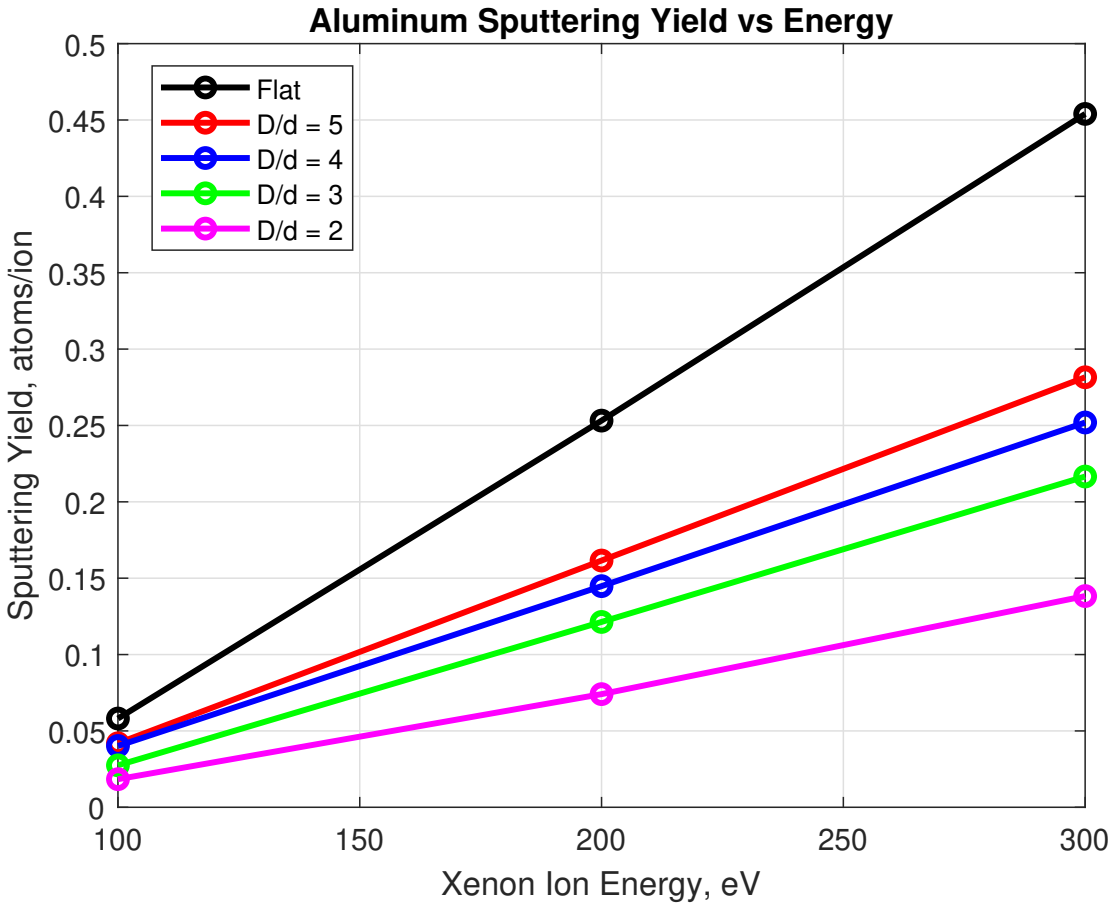

Figure 5.8: Sputtering yield and of aluminum foams as a function of energy for varying aspect ratios.

5.12 respectively. In general, tungsten shows better sputtering yield reduction by 15% on average than aluminum across all energies. This is due to the difference in material sputtering behavior described in the paragraph above. The reduction is relatively constant as a function of energy, with a very slight increase with increasing energy. These results indicate a very promising capability of VCMs to significantly reduce sputtering yield at high energies with geometric methods to produces materials that can reduce sputtering even further.

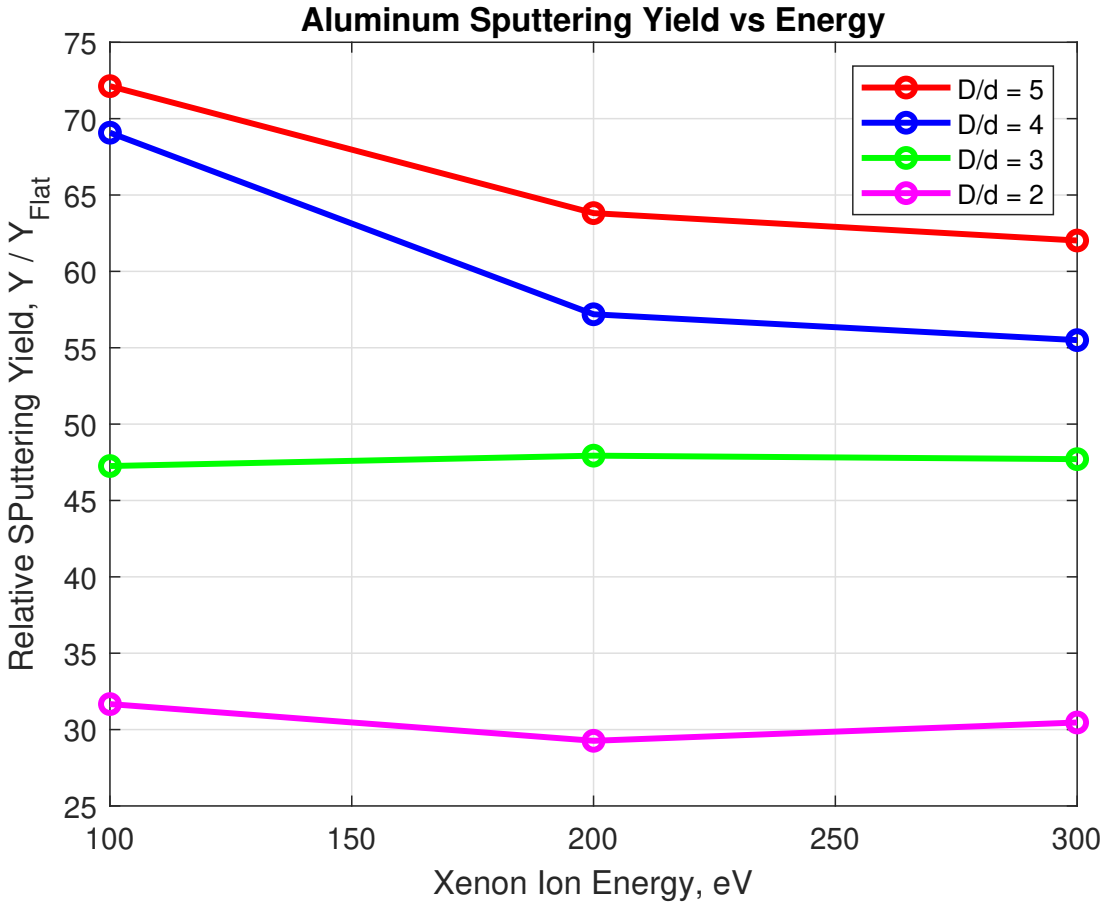

Figure 5.9: (Relative yields of aluminum foams as a function of energy for varying aspect ratios.

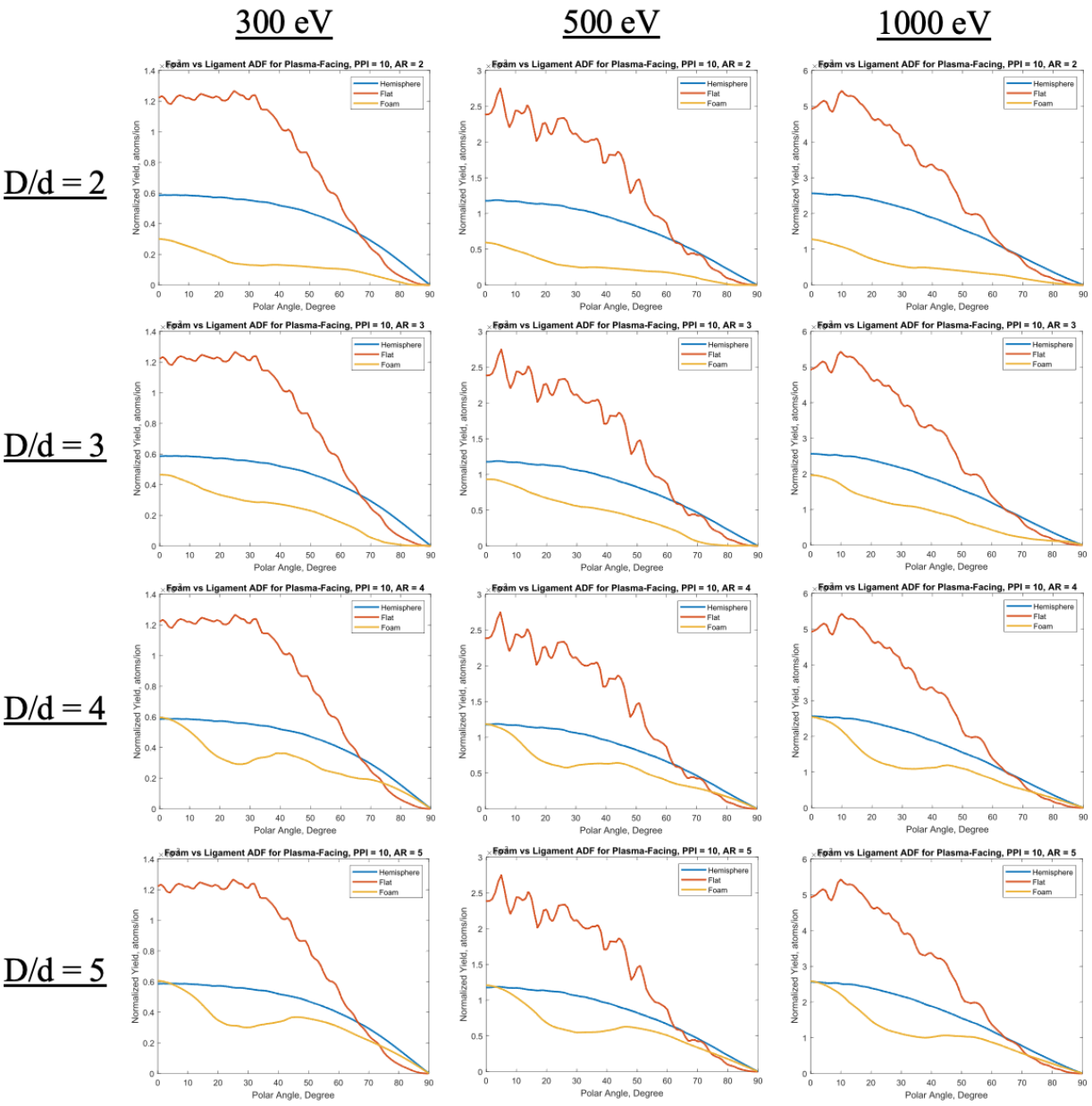

Figure 5.10: Angular sputtering distribution of tungsten foams and flat surfaces modeled at different energies (horizontally) and aspect ratios (vertically).

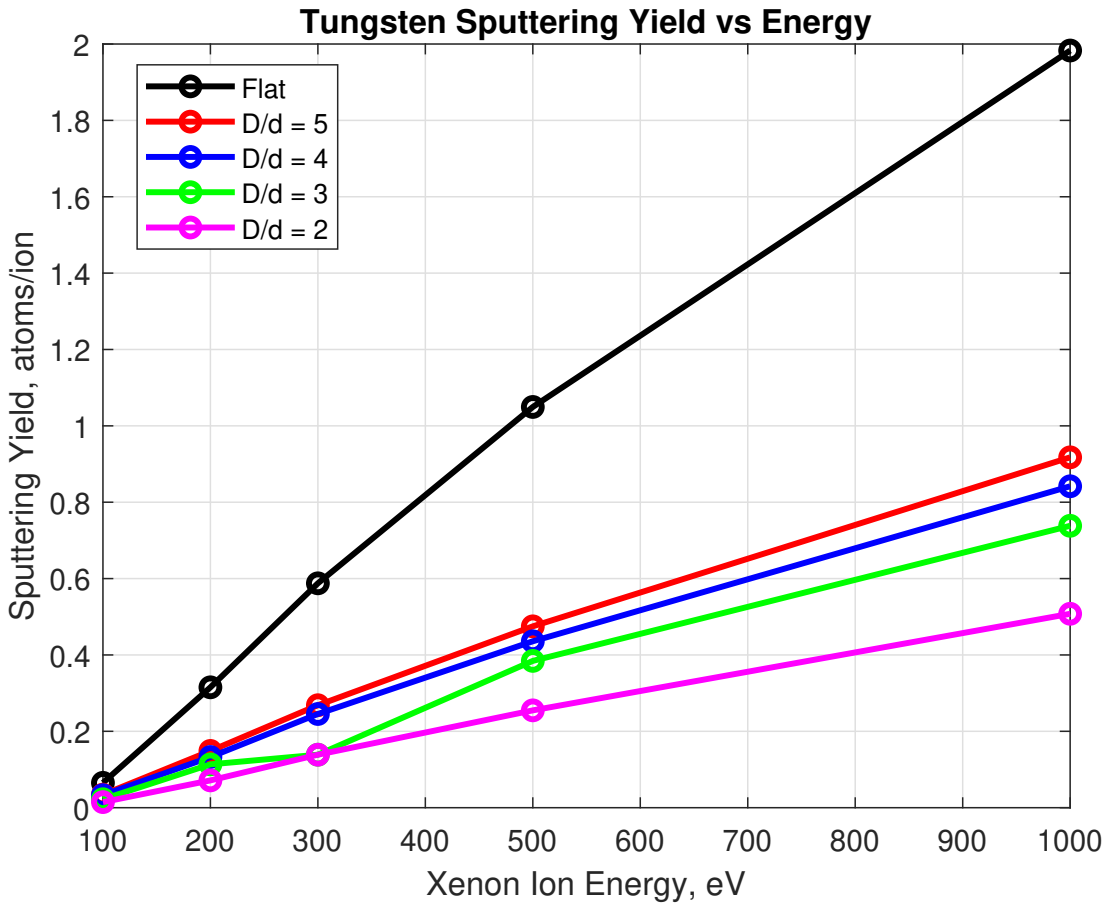

Figure 5.11: Sputtering yield and of tungsten foams as a function of energy for varying aspect ratios.

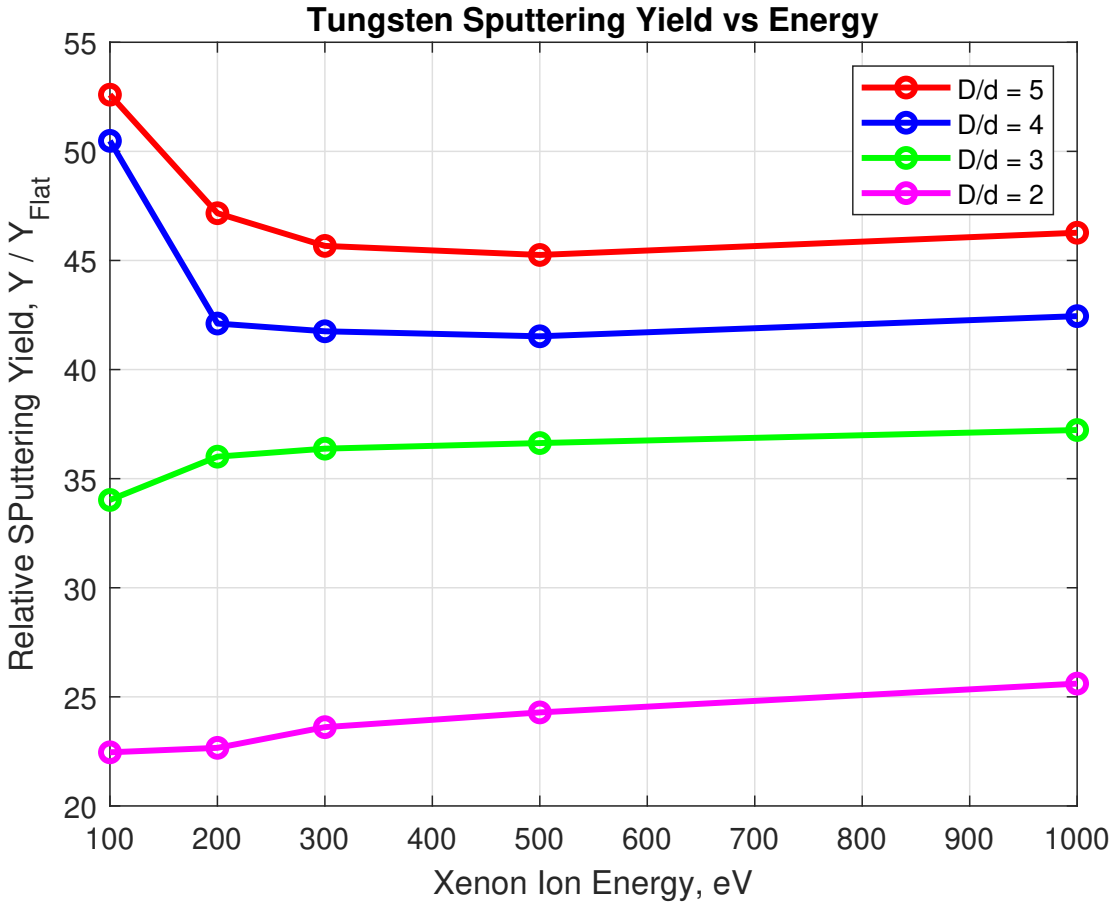

Figure 5.12: (Relative yields of tungsten foams as a function of energy for varying aspect ratios.

5.4 Sputtering Trapping Behavior

In addition to determining the sputtering yield distributions and total yield, the model is used to investigate the behavior within the foam to determine the transport mechanisms. The sputtering behavior of a ligament can be classified into three categories. The first is forward sputtering, where the sputterant is ejected at 0°-90° or 270°-360° with respect to the normal direction of the foam/ligament, and deposits further back into the foam or backing surface. The second is re-deposition, where the sputterant is ejected in the backward direction (90°-270°), but has a view-factor to a ligament in a layer above and therefore redeposits on that surface. The third is escape, where the sputterant is also ejected in the backward direction (90°-270°), but does not have a view-factor to a ligament and therefore escapes the foam as a sputterant. The sputterants that compose the sputtering yield distributions and sputtering yield of a foam as discussed in Section 5.3 are all from this portion of sputterants.

The different types of sputterants are normalized by the total sputterants to generate normalized fractions. The total sputterants produced by a ligament, N_{total}, is defined as the integral of the ligament PDF from 0°-360°. In the case plasma-facing foams of the aspect ratios presented in this chapter, the ligaments of different layers are all of equal size and see equal fluence, and therefore produce similar total sputterants that is dependent on just that specific PDF. The forward sputtering fraction , F_{fwd}, is determined by summing the integral of the ligament PDF from 0°-90° and 270°-360°, and then dividing by N_{total}. The escape fraction, F_{esc}, is determined by integrating the ligament PDF after convolving with the view-factor from 90°-270° and dividing by N_{total}. The re-deposition fraction, F_{redep}, is determined by subtracting the F_{back} and F_{esc} from 1.

The sputtering fractions are first analysed for different material and and energy behavior. The sputtering fraction behavior by layer for aspect ratio 5 aluminum foams is shown in Figure 5.13 for different ion energies. The forward sputtering fraction is dependent on the ligament PDF, which is not going to change with layer as discussed in the previous paragraph. As energy increases, the PDF begins to grow and less fractional portion sputters forward. This behavior is again inde-

pendent of layer, and therefore the total fraction sum of F_{esc} and F_{redep} will be a constant value of $1 - F_{fwd}$. In general, the re-deposition increases with layer as more trapping is present from increased view-factors. Therefore, the re-deposition fraction increases, and the escape fraction decreases equivalently. With increasing energy, the re-deposition fraction grows faster by layer due to the change in the shape of the ligament PDF with energy becoming more favorable for trapping based on the view-factors.

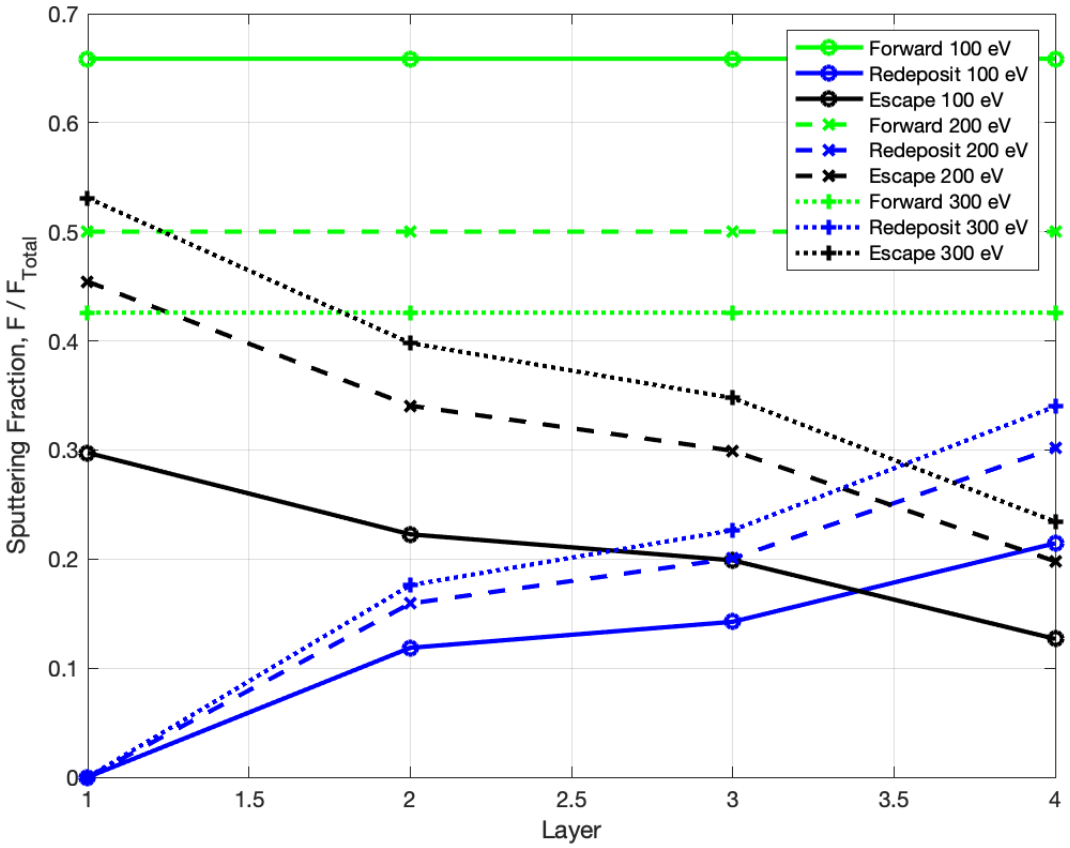

Figure 5.13: Sputtering fractions as a function of energy for aluminum foams of aspect ratio 5.

Similarly, Figure 5.14 shows sputtering fraction behavior by layer for tungsten foams of aspect ratio 5 for different ion energies. The general trends and behaviors described above for aluminum are again applicable here. At these higher energies the back-sputtering behavior of ligaments is general stronger, as indicated by F_{esc} being larger than F_{fwd} for the first few layers. However,

the ligaments begin trapping significantly and F_{esc} decreases rapidly by layer, with higher energy decreasing slightly faster proportionally.

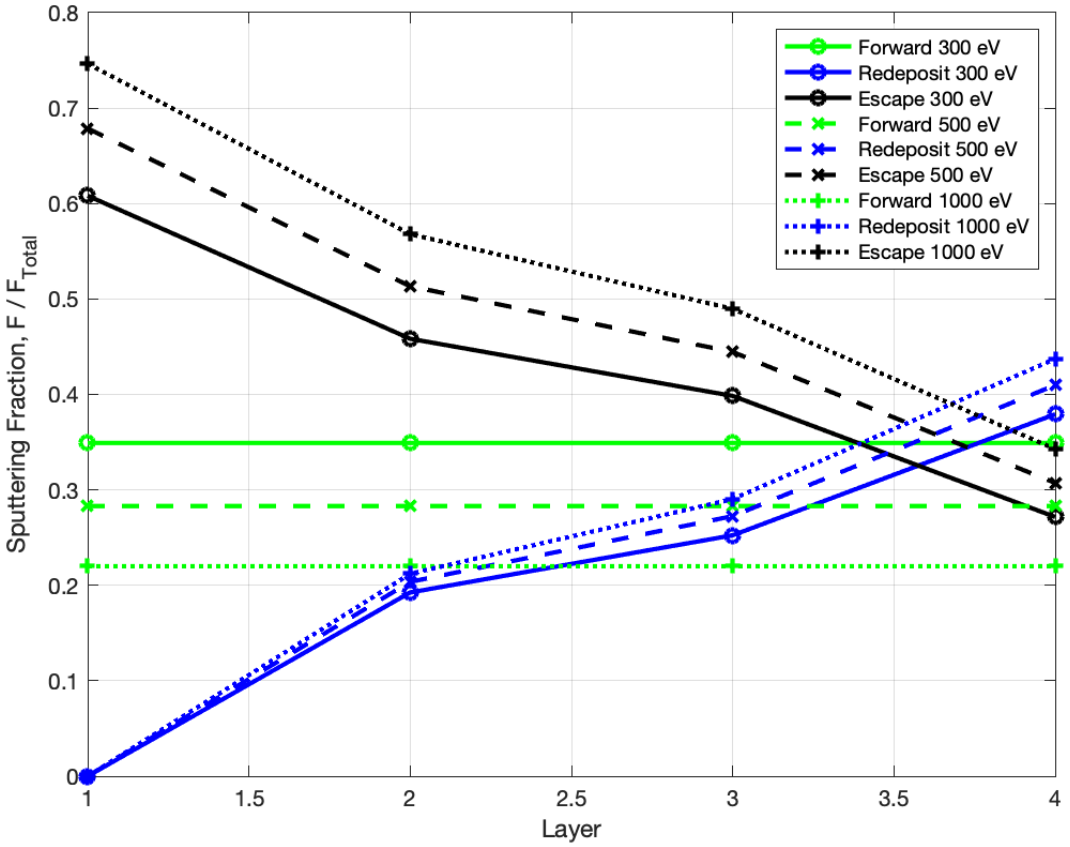

Figure 5.14: Sputtering fractions as a function of energy for tungsten foams of aspect ratio 5.

Next, the role of aspect ratio and how that affects the trapping and sputtering behavior was examined. Figure 5.15 shows the sputtering fractions for different aspect ratios and energies for aluminum and tungsten foams respectively. As the aspect ratio is decreased, the ligaments become larger in comparison to the pores and the view-factor sizes increase at each layer. Therefore, the trapping behavior is amplified and F_{redep} increases significantly at every layer with decreasing aspect ratio. Essentially, the first layer always produces the most sputtering relatively as there is no trapping mechanism to recapture. With each subsequent layer, the trapping increases somewhat asymptotically across all energies and aspect ratios.

Thought not presented in this chapter, the model is capable of analyzing the partially-infused regime and could provide significant insight on the capability of plasma-infused foams to dramatically reduce sputtering yield. For example, in a foam where the first layer is plasma infused, the second layer would be plasma-facing and sputter in a behavior similar to the first layer in Figure 5.15 with each subsequent layer following a similar pattern. The key difference is the first layer would have a ligament PDF uniform in all directions which would be different and smaller than a plasma-facing ligament PDF at higher energies. This would further reduce the sputtering yield of a foam as the first layer has the largest relative contribution of any layer of a plasma-facing foam. An additional benefit of plasma-infusion is the plasma density reduction by layer, which would decrease the fluence of ion underneath.

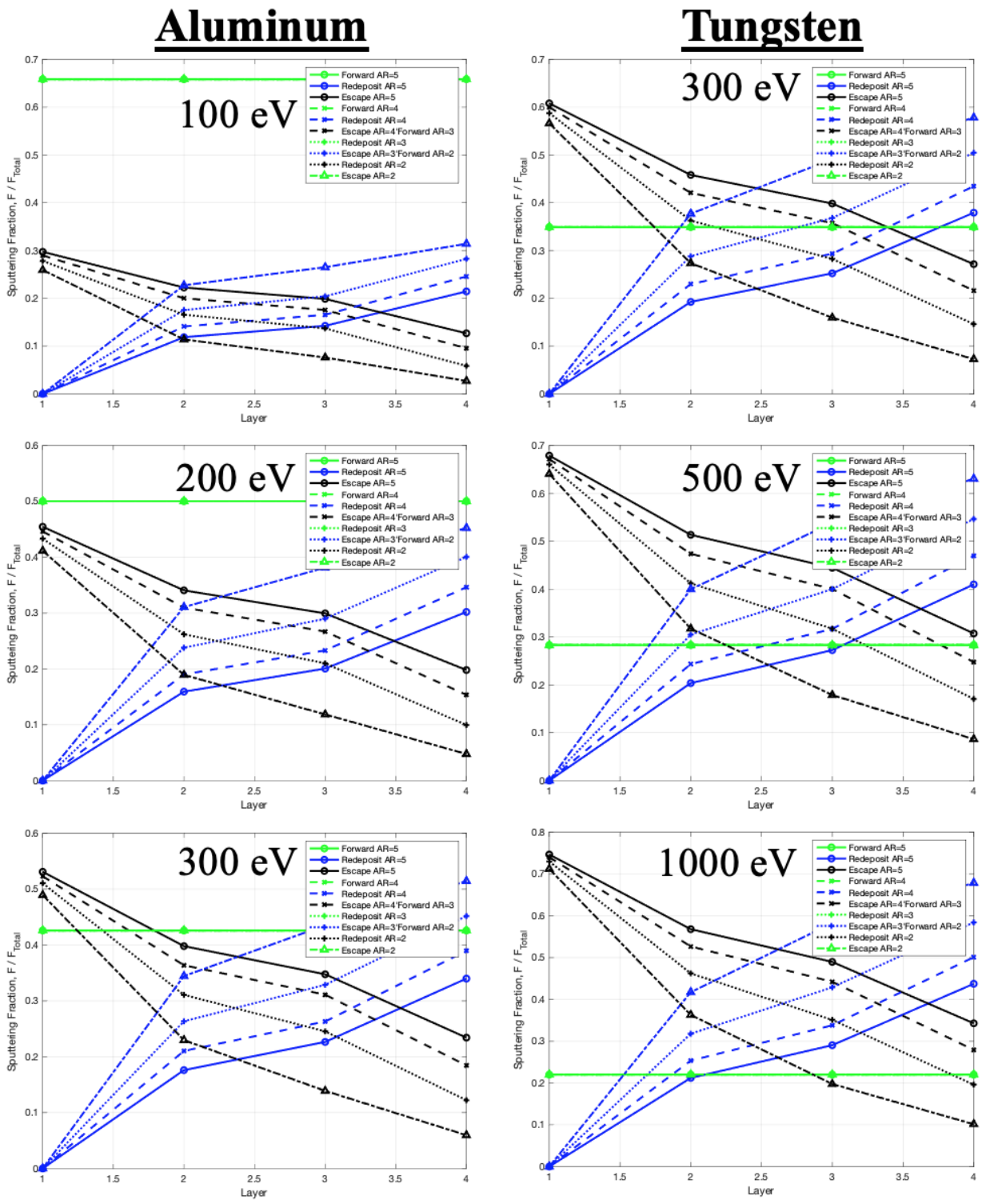

Figure 5.15: Sputtering fractions as a function of aspect ratio for (left) aluminum foams and (right) tungsten foams at different energies.

5.5 Foam Sputtering Model Takeaways

A semi-analytical model was successfully developed to accurately describe the angular profile and sputtering yield of foams. The model shows strong agreement with measurements presented in Chapter 4. Extension of the model to different energies and geometries demonstrates the remarkable capability of VCMs to significantly reduce sputtering yield by up to 55%-70% at high energies of 1 keV. Internal sputtering behavior analysis using the model provides significant insight on the forward sputtering and re-deposition behavior of foams as a function of aspect ratios and densities. Another important takeaway is the continued ability to separate design parameters of VCMs to adjust independently for plasma behavior and material sputtering properties. As discussed in Chapter 4, the PPI serves as the design parameter to control plasma infusion. This model demonstrates that the sputtering behavior in is strongly dependent on aspect ratio and weekly-dependent/independent of PPI. This allows for design of VCMs for plasma-facing applications where the geometry can be tailored as desired to reducing sputtering and erosion while the PPI can be independently tailored for the desired plasma conditions.

In this analysis, only the plasma-facing regime was explored. Exploring the plasma-infused regime and a partial-infusion scenario should demonstrate further significant reduction of sputtering achievable using a foam geometry. Furthermore, the sputtering fractions can supplement analysis efforts to understand transport within a foam using experimental measurement techniques. Additionally, using different ligament geometries instead of cylinders can be investigated using optimization techniques to determine what ligament PDF is most-favorable for decreasing sputtering and increasing re-deposition.

CHAPTER 6

E x B Plasma Instability

The following chapter discusses a low-frequency mode in the Pi facility and experimental efforts to characterize it. Mechanics of the low-frequency azimuthal mode in partially ionized plasmas with crossed field configurations are presented. Analytical derivations and computational modeling findings from key literature are presented along with a two-fluid plasma treatment to guide experimental measurements. Steady-state plasma properties are presented, along with a perspective on the implications on the mode. Additionally, correlation and fluctuation measurements of the mode at varying operating setpoints are presented and discussed. Finally, the impact of the mode on PMI experiment measurements and implications on the analysis are discussed.

6.1 Background and Analytical Framework

Previous efforts at UCLA conducted by Matlock, Dodson, Goebel, and Wirz have identified a modified Simon Hoh like instability in the Plasma interactions (Pi) facility [45, 46]. The mode has been characterized as a low frequency potential and density oscillations that have been experimentally resolved and shown to contribute to significant anomalous electron transport to the walls and boundaries [47, 12]. As discussed in detail in this chapter, the mode is believed to be driven by ion and neutral species and therefore can potentially impact plasma-material interaction investigations. Characterization of the plasma-material interaction process with volumetrically-complex materials in Chapters 4 and 5 requires and motivates further understanding of this mode in the PMI facility and it's implications.

6.1.1 Simon-Hoh Instability

The low-frequency instability in partially-ionized plasmas with crossed electric and magnetic fields was first investigated analytically by Simon and Hoh. Simon considered a slab geometry with crossed fields for a quasi-neutral plasma with no ionization and recombination [10]. Using a linearized small perturbation analysis of density and potential on the diffusion equations governing motion, Simon derived analytical expressions for stability conditions. Though the analysis isn't completely applicable to the conditions investigated in this work, the instability condition of $E_A dn_0/dx > 0$ is still relevant and must be satisfied in any geometry. Essentially, the instability is driven by the first-order drift and the density gradient occurring in the same direction, with the wavenumber in the fields cross-product direction proportional to the charge accumulation due to the separation.

Similar to Simon, Hoh analytically investigated the low-frequency instability in partially-ionized plasma column with axial magnetic field and radial electric field in a cylindrical geometry with an m=1 density perturbation about the central axis [33]. A linearized perturbation analysis of density and potential is introduced to analytically ascertain instability criterion. The ions drift slower azimuthally than the electrons due to neutral drag, resulting in a charge separation. The charge separation is shown to be the destabilizing term (and is $\propto m$) while the diffusional and conductional dissipation act as stabilizing terms (and are $\propto m^2$). As a result, the $m = 1$ mode is the most unstable, with a radial scale on the order of the plasma scale. As summarized in Figure 6.1, the charge separation amplifies that density perturbation and drives plasma out radially.

This instability is generally referred to as the Simon-Hoh Instability. The relevant plasma conditions for the instability is a partially-ionized, collisional, magnetized plasma with crossed magnetic and electric fields. The magnetized and collisional elements are critical as they introduce the charge separation in the cross-direction that sustains the instability. The case of a plasma with magnetized electrons and unmagnetized ions was addressed by Sakawa et. al [34] for an argon plasma. In this scenario, an modified form of the instability, called the Modified Simon-Hoh

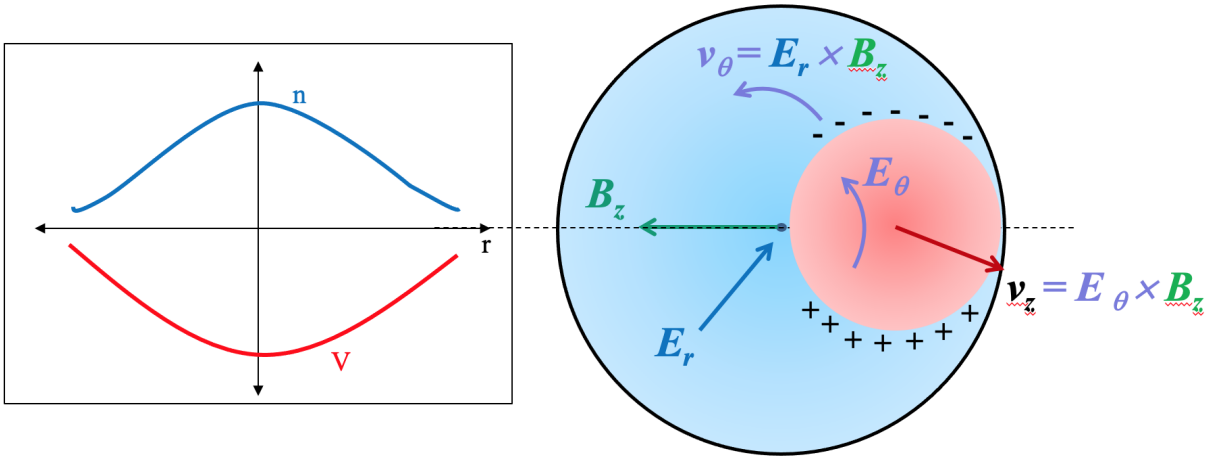

Figure 6.1: (Left) Steady-state density and potential distributions for Simon-Hoh Instability and (Right), resulting instability that drives plasma out radially. Adapted from [10].

Instability (MSHI), was still generated by similar mechanisms with a dispersion relation shown in equation 6.1, where ω^* is the electron diamagnetic frequency, ω_E is the electron E×B frequency, and $v_{\theta i}$ is the mean azimuthal ion drift speed.

$$\frac{\omega^*}{\omega - \omega_E} = \frac{k_\theta^2 c_s^2}{(\omega - k_\theta v_{\theta i})^2}, \tag{6.1}$$

In a later study, the larmor radius effect was found to cause the space charge separation between the electron and ion density perturbations [35], with the real and imaginary parts of the dispersion relation solution shown below in equations 6.2 and 6.3 respectively. The large ion dynamics thought to be significant to understanding the transition of the mode from coherent to turbulent.

$$\omega_R = k_\theta v_{\theta i} \tag{6.2}$$

$$\omega_I = \sqrt{\frac{k_\theta c_s (\omega_E - k_\theta v_{\theta i})}{\omega^*}} \tag{6.3}$$

The SHI and MSHI can be described in the context of this work as shown in Figures 6.2 and 6.3. The magnetized electrons exhibit a much faster $E \times B$ drift, $v_{e\theta} = \frac{E_r}{B_z}$, than the unmagnetized ions moving azimuthally, $v_{i\theta}$, as seen in Figure 6.2a. The resulting density fluctuations cause a charge separation in the azimuthal direction, causing a fluctuating potential and resultant E_θ as seen in Figures 6.2b, 6.3a-c. This in turns causes an $E_\theta \times B_z$ drift that points radially inward leading the potential oscillation and radially outward lagging the oscillation, shown in Figure 6.2c. This drift further amplifies the radial density gradient and azimuthal diamagnetic drift contribution to radial motion for electrons, $v_{dm} = \frac{Te}{eL_nB_z}$ where $L_n = n_e / \frac{dn_e}{dr}$, providing free energy to drive the instability and causing outward motion of the species across confining field lines as described in Figure 6.3d.

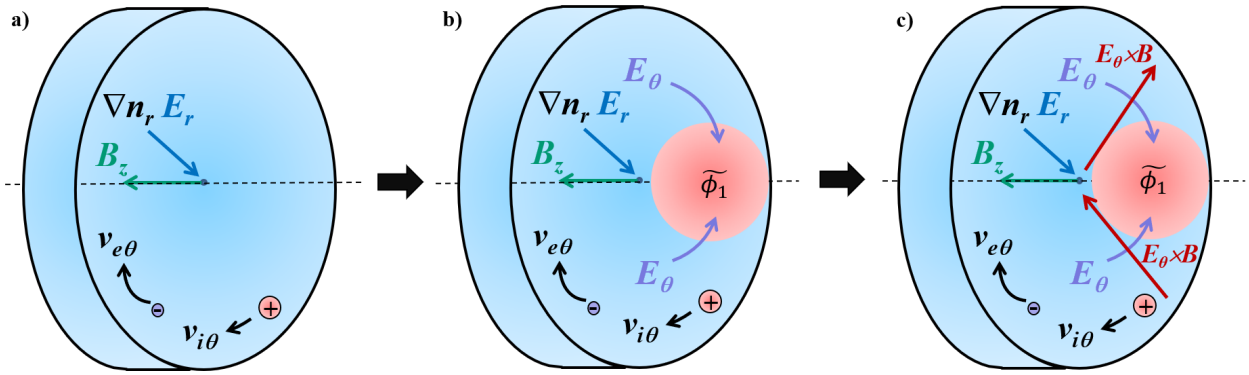

Figure 6.2: MSHI instability in a plasma column. a) Charge separation due to varying drift velocities of electrons and ions result in an azimuthally fluctuating potential. b) The resulting fluctuating potential causes an internal azimuthal electric field that follow the oscillation. c) The electric field results in an $E_\theta \times B_z$ force in the radial direction, conducting electrons across field lines and amplifying the radial density gradient.

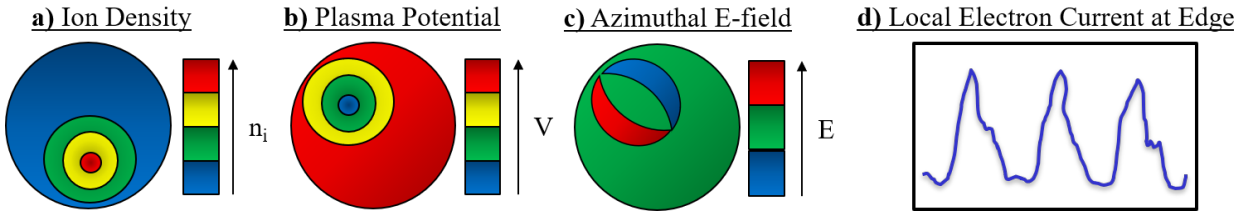

Figure 6.3: Fluctuating plasma property contour diagrams of a) ion density b) plasma potential and c) azimuthal electric field that occur as a result of the MSHI mechanism. d) The expected electron current at a location at the column boundary with peaks resulting from the oscillating mode conducting anomalous electron transport.

6.1.2 Models from Literature

Multiple fluid and kinetic models have been developed in the past few years investing modes and instabilities in similar plasma regimes to investigate anomalous heating and electron transport [42, 27, 43]. Particle-in-cell models using fluid treatment of ions and electrons to investigate anomalous electron mobility and turbulent oscillations have successfully shown instability similar to the Simon-Hoh Instability in a collisionless plasma with similar dispersion to equation 6.1 [43].

Beyond fluid models, hybrid kinetic models have been implemented due to the need for self-consistently capturing transport effects and spoke formation. These models often use a hybrid treatment where the electrons are treated as a fluid while the ions are treated kinetically [11, 107]. The effort by Powis et al. [11] specifically used one such model to investigate whether a spoke in Penning type discharge of comparable conditions to the effort at hand was driven by ionization wave or a MSHI. Results from their investigation, show the formation of a coherent potential structure that rotates around the domain and drives the radial transport of electrons. The model indicates that the structure rotates as turbulent fluctuations rather than as a rotor.

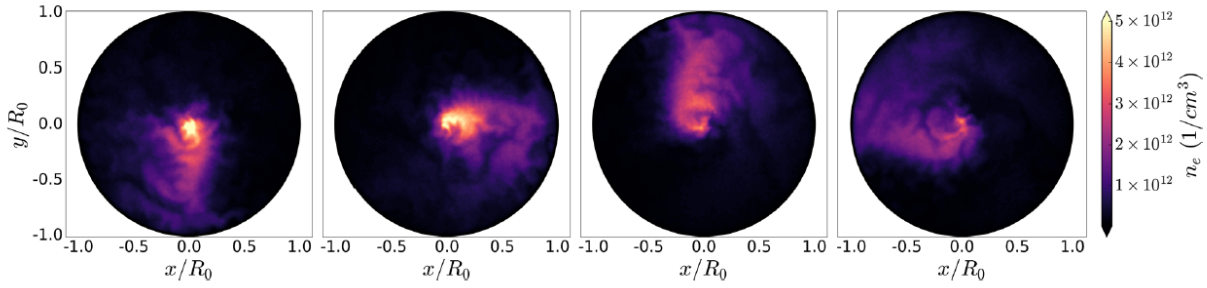

Figure 6.4: Electron density contours of rotating structure from a hybrid kinetic model, taken from [11].

The ion azimuthal rotation frequency, $\omega_{i\theta}$, is determined in [47] using fluid plasma theory and shown below in equation 6.4. The ions cyclotron frequency can be neglected due to the unmagnetized nature of the ions and ϕ_0 is the center potential of a parabolic potential well [108].

$$\omega_{i\theta} = \pm\sqrt{\frac{2e\phi_0}{m_i r_L^2}}\sqrt{1-\frac{T_e}{2T_e+e\phi_0}} - \frac{\omega_{ci}}{2} \approx \sqrt{\frac{2e\phi_0}{m_i r_L^2}} \tag{6.4}$$

The estimate for ion azimuthal motion, along with the instability criterion and physical picture of the mechanism serve to guide experimental efforts.

6.2 Steady-State Properties

Langmuir probe measurements were conducted in the chamber magnet coil gaps using the same probe and setup described in Section 4.4. The measurements were conducted at varying operating setpoints of different cathode flow rates, Q_C, discharge currents, I_D, cathode magnet currents, I_{CM}, anode magnet currents, I_{AM}, and chamber magnet currents, I_{ChM}, as shown in Figure 6.1. The sample magnet was always operated at 10 A and the downstream gas injection flow rate was always 7 sccm.

Setpoint	Q_C	I_D	I_{CM}	I_{AM}	I_{ChM}
1	5 sccm	65 A	0 A	25 A	4 A
2	5 sccm	65 A	14 A	19 A	4 A
3	5 sccm	65 A	7 A	22 A	4 A
4	5 sccm	65 A	7 A	22 A	7 A
5	7 sccm	65 A	7 A	22 A	4 A
6	5 sccm	45 A	7 A	22 A	7 A

Table 6.1: Table of Pi facility operating setpoints Langmuir probed for plasma properties.

The analysis of Langmuir probe data is dependent on the quality of fits to the different regions in the IV curve, making it a time consuming process. As such, only the centerline profiles are presented in this work as the axisymmetric nature of the profiles has been confirmed for the steady state measurements. The slight offset of the center of the profiles from the zero position is due to misalignment of the probe measurement position coupled with uncertainty of the finite length probe's position during a measurement. The offset is consistent with all the plasma property measurements, which indicates that it is indeed likely the probe's relative positioning and not an

off-axis plasma feature.

Measurements of the plasma density are shown below in Figure 6.5. The profiles peak on-axis in the inner beam as expected since energetic electrons from the cathode stream along the center. The radial drop off is Gaussian in nature and symmetric, establishing the clear presence of a radial density gradient in the plasma column across the range of operating setpoints. The radial density is a key criteria for the SHI and MSHI as detailed in Appendix F. The magnitude of the density is strongly dependent on the discharge current, as seen by the sharp drop off in magnitude at setpoint 6. Flow rate variation has similar magnitude of impact, as seen by comparing setpoints 3 and 6 where increasing the total flow rate increases the peak density. As expected, the highest densities occur when the strongest magnetic field is applied (setpoints 1 and 4) and decreases correspondingly. An interesting feature to note is that though the magnitudes change, the width of the profiles also varies to smooth out the change (ie. as magnitude decreases width increases).

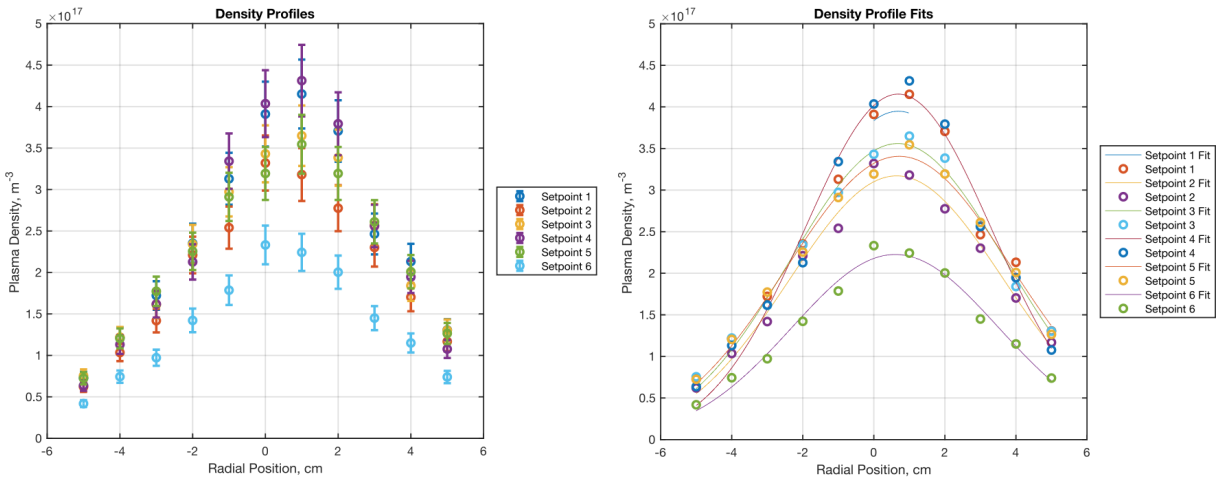

Figure 6.5: Plasma density Langmuir probe measurements at varying operating setpoints. (Left) Measured datapoints with uncertainty and (Right) parabolic fits to the measured data.

Measurements of the plasma potential are shown in Figure 6.6 with a Gaussian fit. The profiles indicate a triangular or Gaussian radial potential well, with a minimum at the centerline, that confines the plasma. The potential well is between 13 to 20 V deep, and exhibits similar general trends to the density profiles. This isn't surprising as the potential plays a strong role in shaping

the plasma structure and the resulting density gradient. A notable different from the behavior of the density, however, is the relative impact of discharge, flow rate, and magnetic field strength. The potential is not as significantly affected by discharge and flow rate variations, with smaller changes in peak magnitude. The magnetic field plays a more significant role, with clear separation evident between setpoints of comparable and varying magnetic field strengths.

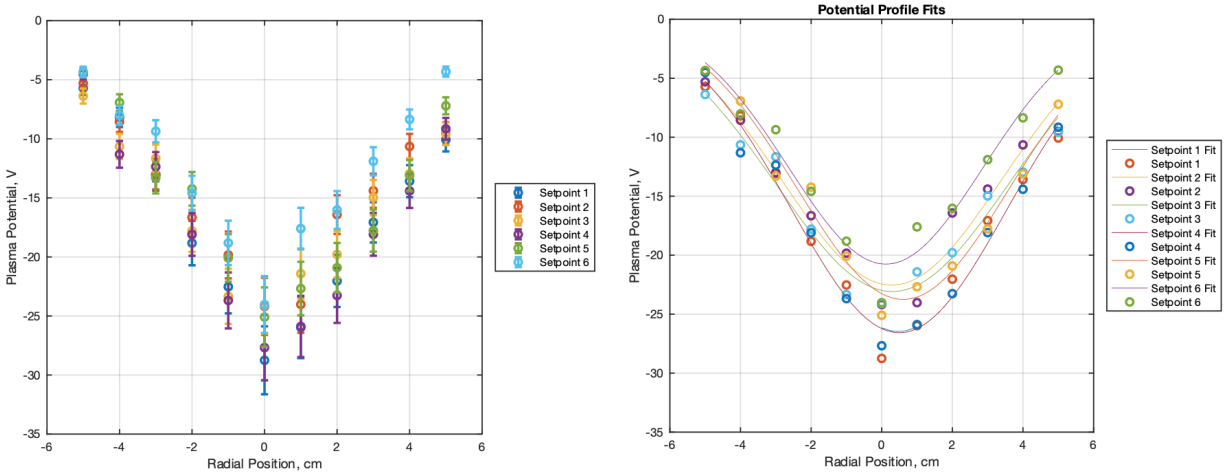

Figure 6.6: Plasma potential Langmuir probe measurements at varying operating setpoints. (Left) Measured datapoints with uncertainty and (Right) parabolic fits to the measured data.

The electron temperature profiles are shown in Figure 6.7 with Gaussian fits as well. The electron temperature is largely independent of the setpoint variations other than discharge current, with the range between peaks for the fits falling within the measurement uncertainties. The discharge current variation setpoint (setpoint 6) has measurement errors near the centerline as evidenced in the figure, however the measurements are still shown for full disclosure. The profile should still result in a relatively broad Gaussian or linear shape with drop off at the edges. The reduction in peak magnitude is due to the decreased energy of the energetic electrons produced by the cathode. The radial drop off in temperature in the profiles can be explained accordingly as well. The inner beam is composed of energetic electrons from the cathode streaming along the magnetic field lines. The electrons are radially pushed out due to collisions and other transport mechanisms that reduce their energy, hence the radial drop off in temperature.

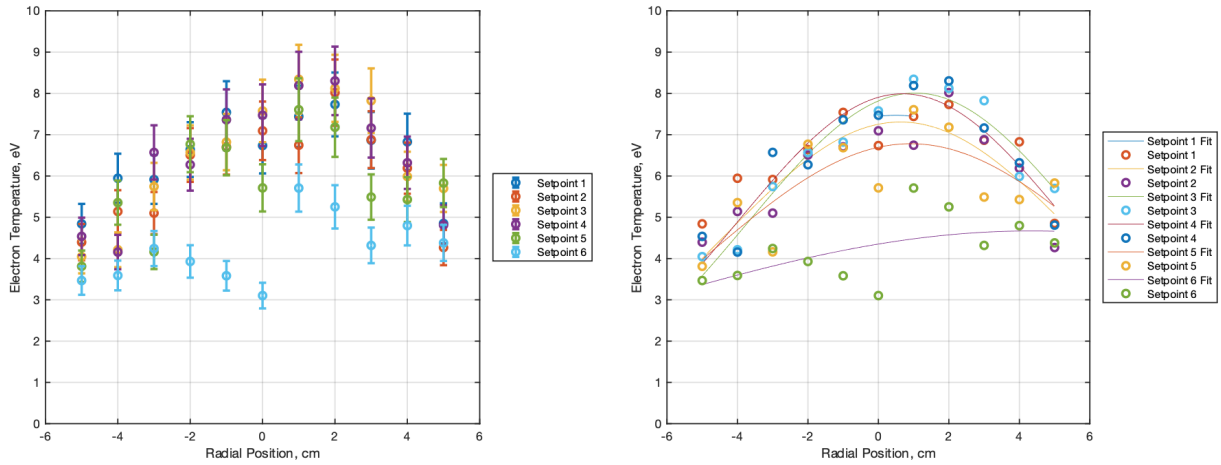

Figure 6.7: Electron temperature Langmuir probe measurements at varying operating setpoints. (Left) Measured datapoints with uncertainty and (Right) parabolic fits to the measured data.

The plasma properties presented in this section provide important insight on the structure of the plasma necessary to evaluate the nature of the low-frequency oscillation. Measurements of the plasma properties downstream of the anode were previously measured by Matlock et al. in [45, 46] for slightly different operating setpoints and cathode source performance, but can be used to supplement these measurements and generally show good agreement in geometric shapes and trends. Additionally, the quantitative values are necessary to estimate significant plasma parameters, as shown below in Figure 6.2, and develop simple models to assess experimental measurements.

Property	Range
Debye Length, λ_d	49 - 88 µm
Ion Sound Speed, C_s	2250 - 3300 km/s
Ion Cyclotron Frequency, Ω_i	290 - 580 Hz
Ion Neutral Collision Frequency	10 kHz [46]
MSHI Spoke, ω_r	8 - 24 kHz
Ion Rattle	30 kHz [47]
Ionization	400 kHz [46]
Lower Hybrid, ω_{LH}	357 - 713 kHz
Alfven Ion Azimuthal Frequency, ω_A	0.5 - 1 MHz
Electron ExB Frequency, $omega_{E\times B}$	0.7 - 2 MHz
Electron Diamagnetic Frequency, ω_{dia}	1 - 36 MHz
Ion Plasma Frequency, ω_{pi}	26 - 68 MHz
Electron Cyclotron Frequency, Ω_e	439 - 878 MHz
Electron Plasma Frequency, ω_{pe}	13 - 33 GHz

Table 6.2: Table of significant plasma phenomena frequency relevant to azimuthal instability calculated from probe measurements and supporting references.

6.3 Low Frequency Azimuthal Mode Measurements

6.3.1 Oscillation Measurements

With the steady-state properties known, the next step is to measure the nature of the oscillation itself and its response to system control parameters. The previous measurements of the fluctuation [12] serve as a guide to direct what frequency band to focus on and where to spatially perform the measurements. The objective of the correlation probes experiment discussed in this section is to experimentally measure and map the low-frequency mode behavior as a function of current system operation parameters and behaviors. The effort will provide a general picture of the mechanisms significant to the behavior of the mode.

The experiment consisted of two probes biased to ion saturation potential to measure density fluctuations and is shown in Figure 6.8. A fixed (reference) probe is inserted in vertically into the plasma column and placed 2.5 cm away radially from the center of the plasma. The probe design is similar to the Langmuir probe, however with a electrode diameter of 1.55 mm and a length of

4.9 mm. The Langmuir probe from Section 6.2 is used as the swept probe and is moved to three azimuthal positions corresponding to 90°, 135°, and 180° separation between the two probes (all 2.5 cm radially from the center of the plasma column).

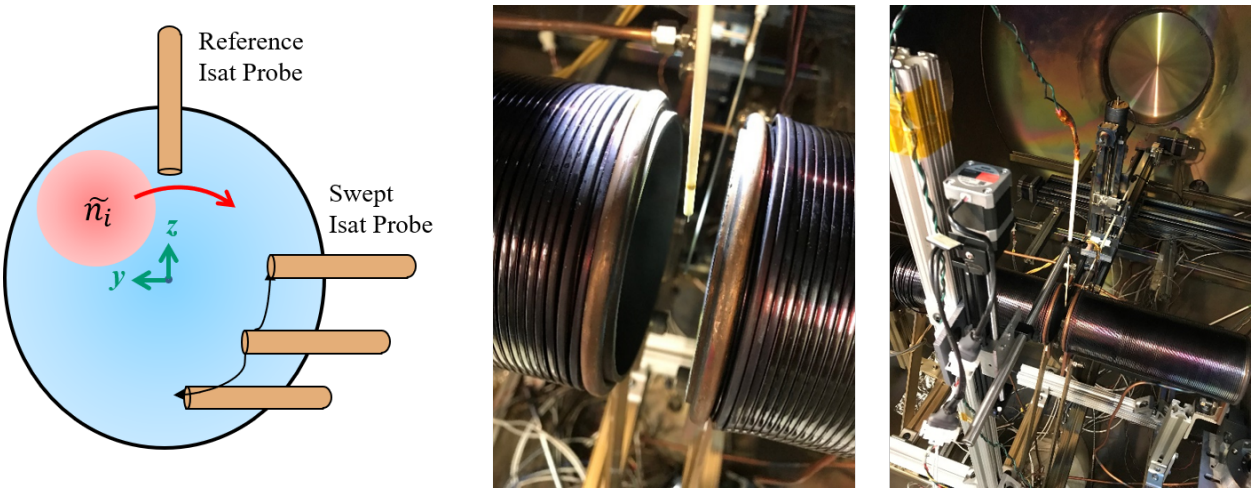

Figure 6.8: (Left) Positions of fixed and swept probes for correlation measurements. (Center) Image of probes in setup. (Right) Image of facility for experimental setup.

The probes are biased to -50 V using a constant voltage power supply and each have a 10 kΩ sense resistor in-line across which the differential voltage. The Tektronix oscilloscope is used to measure the differential voltages of both probes to determine the current, and samples at 12.5 MS/s for 5 s. The measurements are performed at a wide range of operating conditions for both argon and xenon plasmas, with the various operating parameters detailed in Figures 6.3 and 6.4. The flow rates, discharge current, and magnetic fields were all varied parameters. The sample magnet and boundary condition are not varied at any point in this investigation to narrow down the range of possible conditions. The purpose of the wide range and numerous setpoints is to characterize the mode in a wide parameter space and also capture different dynamics of the mode (coherent vs turbulent). Figure 6.9 shows visual images of the argon plasma at a few of the various setpoints to provide a sense of the range of the plasma conditions captured in the experiment. Additionally, background measurements without any discharge or magnetic fields are collected and used in the analysis to filter out the background.

Setpoint	Q_C	Q_A	I_D	I_{CM}	I_{AM}	I_{ChM}
1	5 sccm	7 sccm	65 A	7 A	22 A	4 A
2	5 sccm	7 sccm	65 A	7 A	22 A	7 A
3	5 sccm	7 sccm	65 A	7 A	22 A	10 A
4	5 sccm	7 sccm	65 A	7 A	22 A	0 A
5	5 sccm	7 sccm	65 A	0 A	25 A	4 A
6	5 sccm	7 sccm	65 A	0 A	25 A	0 A
7	5 sccm	7 sccm	65 A	0 A	22 A	4 A
8	5 sccm	7 sccm	65 A	0 A	19 A	4 A
9	5 sccm	7 sccm	65 A	7 A	19 A	4 A
10	5 sccm	7 sccm	65 A	14 A	19 A	4 A
11	5 sccm	7 sccm	65 A	14 A	19 A	7 A
12	5 sccm	7 sccm	65 A	0 A	25 A	7 A
13	5 sccm	7 sccm	65 A	0 A	25 A	10 A
14	7 sccm	7 sccm	65 A	0 A	25 A	7 A
15	7 sccm	7 sccm	65 A	0 A	25 A	4 A
16	7 sccm	7 sccm	65 A	7 A	22 A	4 A
17	7 sccm	7 sccm	65 A	7 A	22 A	7 A
18	7 sccm	7 sccm	65 A	14 A	19 A	7 A
19	7 sccm	7 sccm	65 A	14 A	19 A	4 A
20	7 sccm	5 sccm	65 A	14 A	19 A	7 A
21	7 sccm	5 sccm	65 A	14 A	19 A	4 A
22	7 sccm	5 sccm	65 A	7 A	22 A	4 A
23	7 sccm	5 sccm	65 A	7 A	22 A	7 A
24	7 sccm	5 sccm	65 A	0 A	25 A	7 A
25	7 sccm	5 sccm	65 A	0 A	25 A	4 A
26	5 sccm	7 sccm	55 A	0 A	25 A	4 A
27	5 sccm	7 sccm	55 A	7 A	22 A	4 A
28	5 sccm	7 sccm	55 A	14 A	19 A	4 A
29	5 sccm	7 sccm	45 A	7 A	22 A	4 A

Table 6.3: Table of Pi facility operating setpoints investigated for low-frequency azimuthal oscillations with a xenon discharge.

The FFTs of the probe current are obtained to investigate the frequency content. A disadvantage of this approach is the loss of time-local information as the FFT algorithm does not capture them. However, the process is still useful as the frequency content and PSD can be constructed and use to evaluate the presence of various modes. The process is carried out in MATLAB using the FFT algorithm and correcting necessary corrections. A resulting PSD of the fixed probe current

Setpoint	Q_C	Q_A	I_D	I_{CM}	I_{AM}	I_{ChM}
1	20 sccm	15 sccm	65 A	0 A	25 A	4 A
2	20 sccm	15 sccm	45 A	0 A	25 A	4 A
3	20 sccm	15 sccm	25 A	0 A	25 A	4 A
4	20 sccm	15 sccm	65 A	0 A	19 A	4 A
5	20 sccm	15 sccm	65 A	0 A	10 A	4 A
6	20 sccm	15 sccm	65 A	7 A	19 A	4 A
7	20 sccm	15 sccm	65 A	14 A	19 A	4 A
8	20 sccm	15 sccm	65 A	14 A	19 A	7 A
9	20 sccm	15 sccm	65 A	14 A	19 A	10 A
10	20 sccm	15 sccm	65 A	14 A	19 A	0 A
11	20 sccm	15 sccm	65 A	0 A	25 A	0 A
12	20 sccm	15 sccm	65 A	0 A	25 A	7 A
13	20 sccm	15 sccm	65 A	0 A	25 A	10 A
14	20 sccm	15 sccm	45 A	0 A	25 A	10 A
15	20 sccm	15 sccm	45 A	0 A	25 A	7 A
16	20 sccm	15 sccm	45 A	0 A	25 A	4 A
17	20 sccm	12 sccm	45 A	0 A	25 A	4 A
18	20 sccm	12 sccm	45 A	0 A	25 A	10 A
19	20 sccm	12 sccm	45 A	0 A	19 A	4 A
20	20 sccm	12 sccm	45 A	14 A	19 A	4 A
21	20 sccm	12 sccm	65 A	14 A	19 A	4 A
22	20 sccm	12 sccm	65 A	0 A	19 A	4 A
23	20 sccm	12 sccm	65 A	0 A	25 A	4 A
24	20 sccm	12 sccm	65 A	0 A	25 A	10 A
25	15 sccm	12 sccm	45 A	0 A	25 A	10 A
26	15 sccm	12 sccm	45 A	0 A	25 A	4 A
27	15 sccm	12 sccm	45 A	0 A	19 A	4 A
28	15 sccm	12 sccm	45 A	14 A	19 A	4 A
29	15 sccm	12 sccm	65 A	14 A	19 A	4 A
30	15 sccm	12 sccm	65 A	0 A	19 A	4 A

Table 6.4: Table of Pi facility operating setpoints investigated for low-frequency azimuthal oscillations with an argon discharge.

is shown in Figure 6.10. The FFT shows notable distinct peaks in the 20 and 60 kHz regions, with the 60 kHz having a broad spectral shape. Previous measurements indicate that the 20 kHz mode is the $m = 1$ azimuthal density fluctuation. The use of a spectrogram, also shown in Figure 6.10, demonstrates the time-evolution (or lack there-of) for the mode. The spectrogram applies a

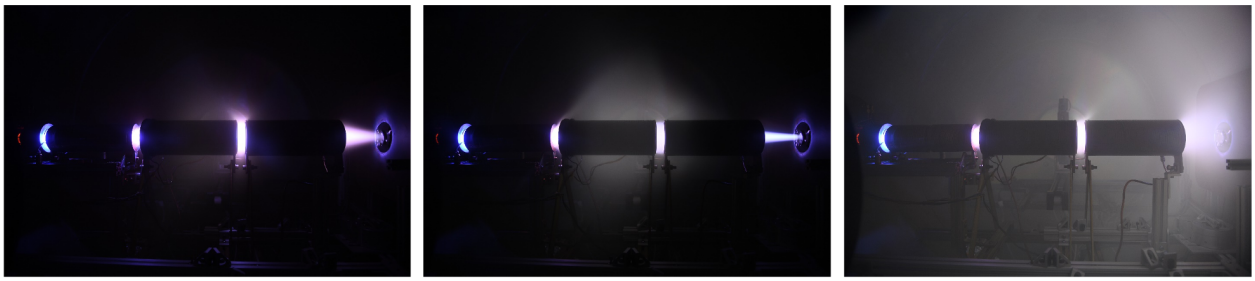

Figure 6.9: Images of the PI facility at a few of the setpoints to aid in visualizing the various plasma conditions investigated.

sliding FFT over a binned signal to obtain time-resolution at the trade off of frequency resolution. However, a better approach to evaluate time-evolution is Wavelet Transforms, which use a different basis of orthogonal functions to preserve time localization and decompose a signal into small oscillations localized in time. A Continuous Wavelet Transform (CWT), also shown in Figure 6.10, can be used to determine the evolution of a signal. In this analysis, CWTs generated using MATLAB are used to generally investigate the time-localized nature of the mode under study, but can be leveraged for much more rigorous analysis in the proposed work.

The last technique used in the analysis of these results are cross correlations, which measure how similar signals are by determining the effect of displacing one signal with respect to the other. The cross power spectral density (CPSD), obtained by taking the fourier transform of the cross correlation, describes the power associated with a given frequency of the correlation. The CPSD between the fixed and swept probe is used in the analysis to investigate the mode behavior as a function of operating parameters. The CPSD is chosen over the PSDs as the correlation should help reduce errors introduced by non-plasma phenomena. Other techniques such are transfer function signal reconstruction, wavelet coherence, and shadow manifold interpolation, were all utilized for exploratory research but are not presented in this discussion of the results.

The role of the discharge current on the low-frequency mode is shown in Figure 6.11. The low-frequency mode of interest in the xenon case is seen between 10-13 kHz. The nearby peaks seen at 20 kHz are shown to be a mode associated with the cathode magnetization in the discussion below. Though the power does not significantly change with discharge current over the range tested for

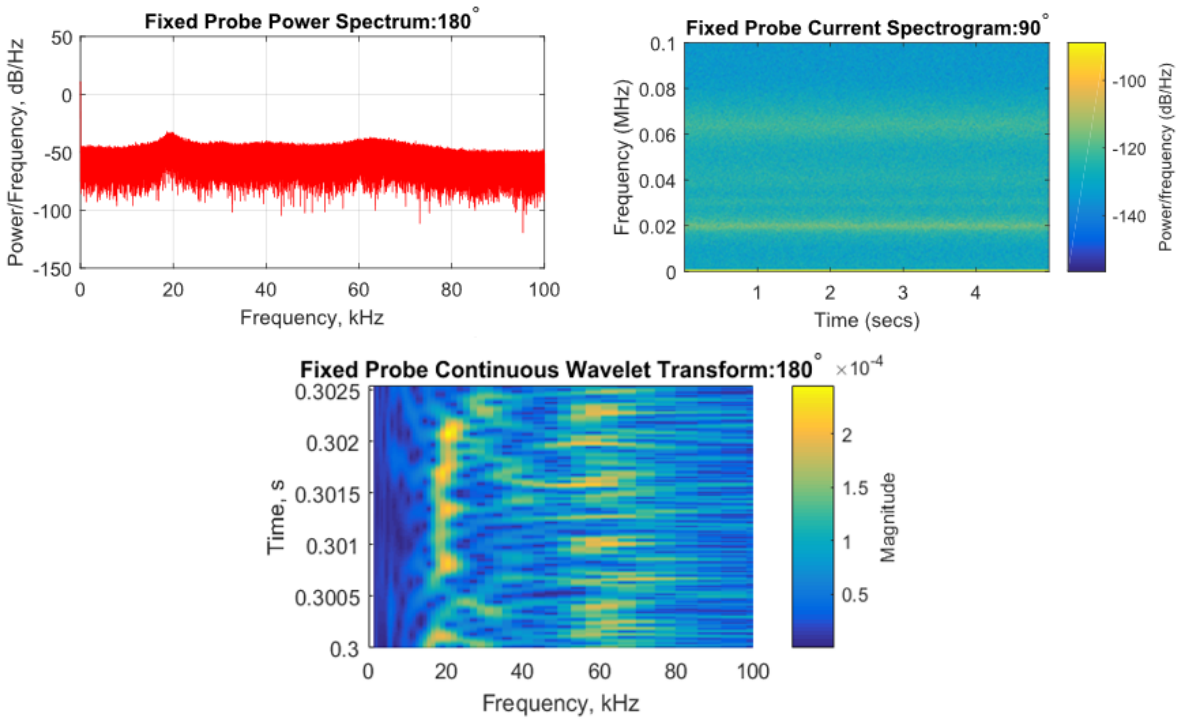

Figure 6.10: (Top-left) FFT of the fixed probe current from Setpoint 1 in the low-frequency band with modes of interest visible. (Top-right) Spectrogram of fixed probe current over sampling period from Setpoint 1, indicating steady presence of modes seen in FFT. (Bottom) Continuous wavelet transform of fixed probe current from Setpoint 1 using a Complex Morelet basis, demonstrating the periodic recurring coherent behavior of the low-frequency mode.

Xe, the peak frequency does increase with decreasing discharge current. In the case of argon, the mode of interest is seen around 20 kHz (the cathode magnetization mode is around 30 kHz in this case) with a clear power dependence on discharge current and an opposite trend for peak frequency in comparison to the xenon case. The contradicting nature of these measurements makes it difficult to draw any conclusions about the role onthe discharge current on the fundamental nature of this low-frequency oscillation.

Next, the role of flow rates is investigated as shown in Figure 6.12. For xenon, the frequency is dependent on the total flow rate rather than ratio of the two gas injection sites. The power does not significantly change but the peak frequency decreases with increased flow rate. A similar trend

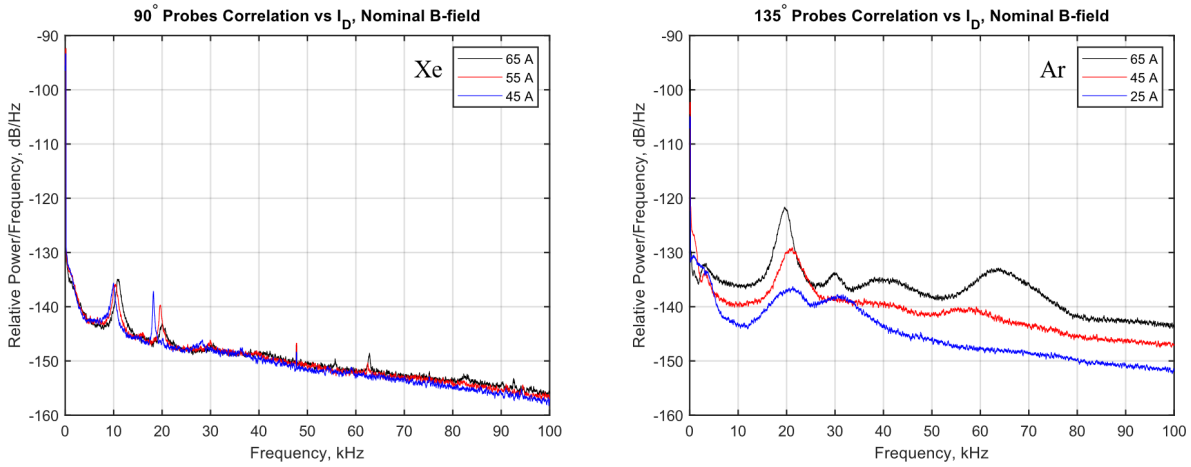

Figure 6.11: Probe correlation PSDs for varying discharge currents for (left) xenon at 12 sccm total flow rate and (right) argon at 35 sccm total flow rate.

is seen in the case of argon as well. This could possibly be explained by the increased quantity of neutrals and resulting collisions and drag on ions that would slow down the oscillation.

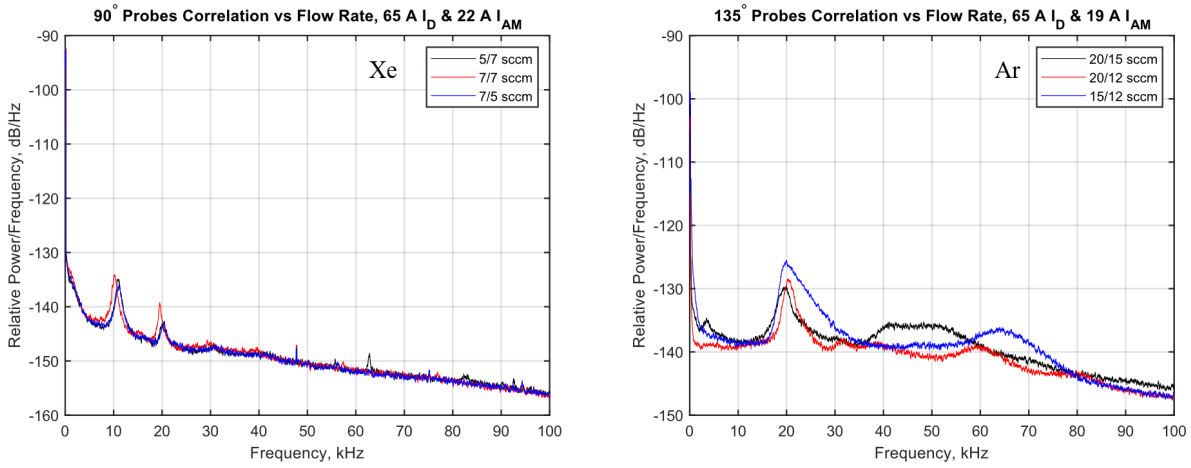

Figure 6.12: Probe correlation PSDs for varying flow rates for xenon (left) and argon (right) discharges.

One of the more interesting findings of this experiment is the role of the cathode magnet shown in Figure 6.13. The cathode magnet has almost no effect on the azimuthal mode of interest, but does have strong implications on the nearby observed mode at 20 kHz for xenon and 30-40 kHz for argon. The mode has very little power when the cathode magnet is not on. As the magnet current

is increased, the intensity of the mode significantly increases. The nature of the mode is not clear, though it is possibly an axial phenomena as previous azimuthal measurements of low-frequency density and potential did not indicate the presence of such behaviors [45, 47, 12].

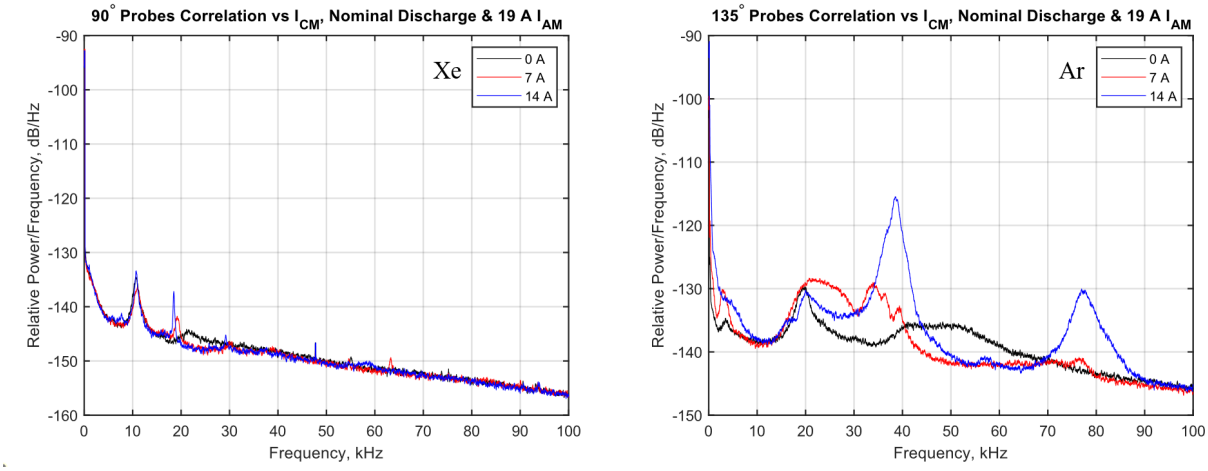

Figure 6.13: Probe correlation PSDs for varying cathode magnet currents for xenon (left) and argon (right) discharges.

Next, the role of the anode magnet is analyzed as shown in Figure 6.14. The xenon measurements did not encompass a large enough range of anode magnet currents and there for do not present any significant trends. The argon measurements were performed over a wider range and of anode magnet currents and provide valuable insight. It seems that the power associated with the mode increases with increasing magnet current. The case of the 10 A condition is difficult to evaluate due to the lack of a clear mode peak.

Analysis of the chamber magnet effects is shown in Figure 6.15. As expected, in the case of no magnetic field in the region, the plasma becomes unconfined in the region of the measurement and no mode is present. As the magnetic field is increased, the peak frequency of the mode is not impacted but the tail end of the peak is smeared. This is consistent for both the argon and xenon measurements. In the case of argon, significant power is shifted to into a slightly higher frequency band, demonstrated by the general broad lump in the 30-50 kHz region.

The xenon spectra in Figures 6.12, 6.11, and 6.13 provides notable insight on the dynamics of

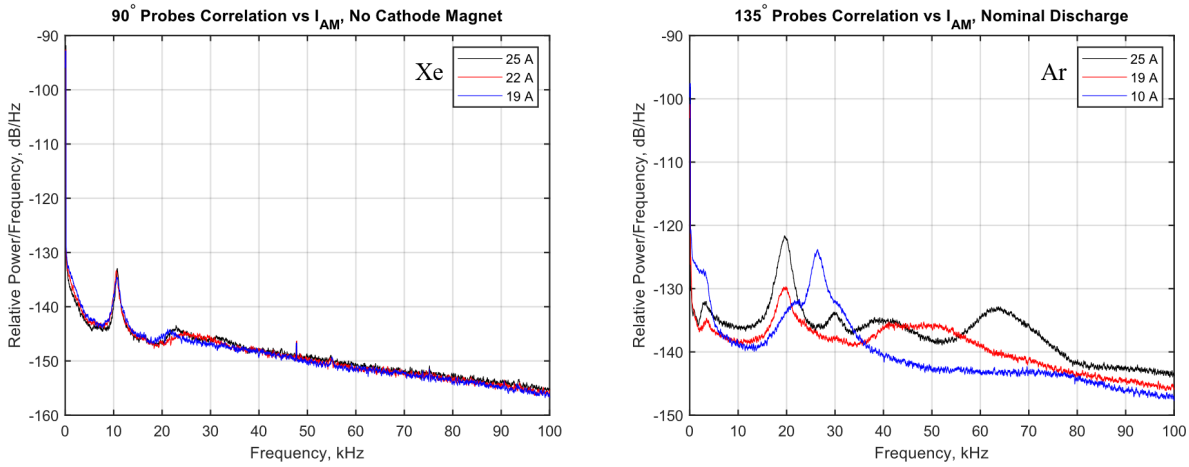

Figure 6.14: Probe correlation PSDs for varying anode magnet currents for xenon (left) and argon (right) discharges.

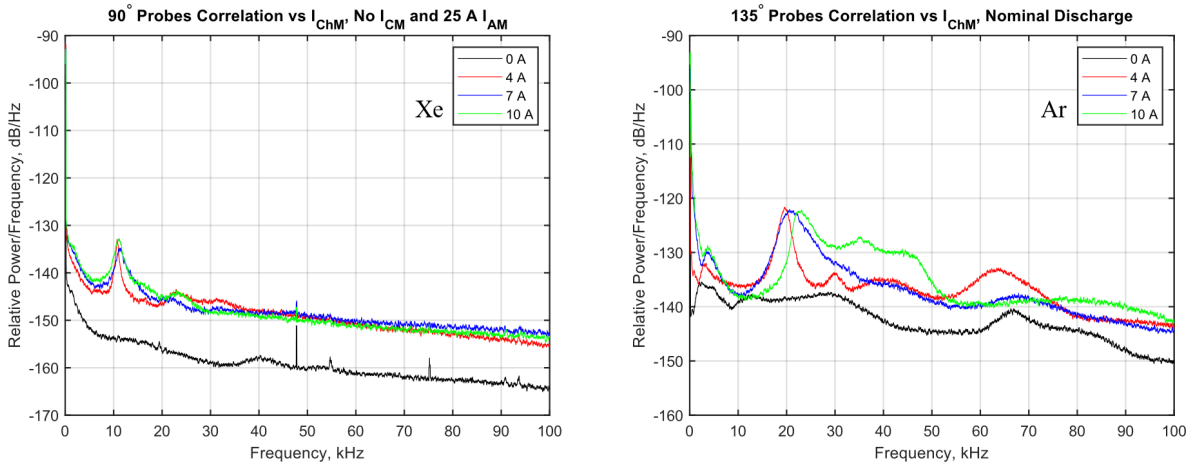

Figure 6.15: Probe correlation PSDs for varying chamber magnet currents for xenon (left) and argon (right) discharges.

the system. The spectra all show a clear exponential dependence between power and frequency. Maggs and Morales have shown that the clear exponential dependence is a signature of choatic dynamics [109, 110, 111]. The drift wave effects on the probe time series signals can be described as Lorentzian in shape, and uniquely result in the exponential behavior of the PSD. The exponential decrease is therefore an indicator of chaotic dynamics in this system, specifically deterministic chaos where large amplitude coherent modes induce trajectory effects in phase space [109] with turbulence-like implications.

6.3.2 Fluctuating Property Measurements

A crucial aspect of MSHI and SHI mechanisms are the fluctuating potentials and density. As described in Section 6.1, each plays a crucial role in the development of the coherent or turbulent mode. As such, measurements of each are critical to understanding the nature of the instability. These measurements were carried out in the past by Matlock et al. for the UCLA Pi facility [12]. A langmuir probe, floating emissive probe, and mach probe were each used to measure fluctuating ion density, plasma potential, and ion Mach number at various spatial locations. As shown in Figure 6.16, the measurements can all be referenced in time to each other using linear transfer functions. First, transfer functions, H_i, are determine for each spatial measurement using the probe signal and a reference probe signal measure at the same moment. A uniform reference signal for all the measurements is then chosen, and applied to each transfer function to recreated the probe signal in reference to the uniform reference signal. The remapped signals can then be used to create instantaneous contours, as performed previously by [12] and shown below in Figure 6.17.

The measurements, however, need to be repeated as the previous measurements were conducted at a different operating setpoint (and different cathode performance) than of interest to the current effort. The measurements will be conducted using floating emissive and ion-saturation probes. The use of a these probes for obtaining plasma properties has been discussed in Section 4.2. The simplified explanation of emissive probe utilization is explained in Section 4.2. More comprehensive details and considerations for emissive probe theory can be found in [102, 112, 113, 47].

The use of emissive probes in this scenario pose some challenges. As seen in equation 4.8, the temperature fluctuations are not accounted for. In this specific instance, it is not an issue, however it is worth noting. More problematic is the density fluctuation terms. Physically, this means that for the probe to float, the potential of the filament must respond to the density fluctuations in the plasma. Additionally, the large-amplitude nature of the potential fluctuations studied here pose a challenge as the probe response must be fast enough for the saturation condition to be met and the theory valid. These considerations serve to cast reasonable doubt on the accuracy of emissive

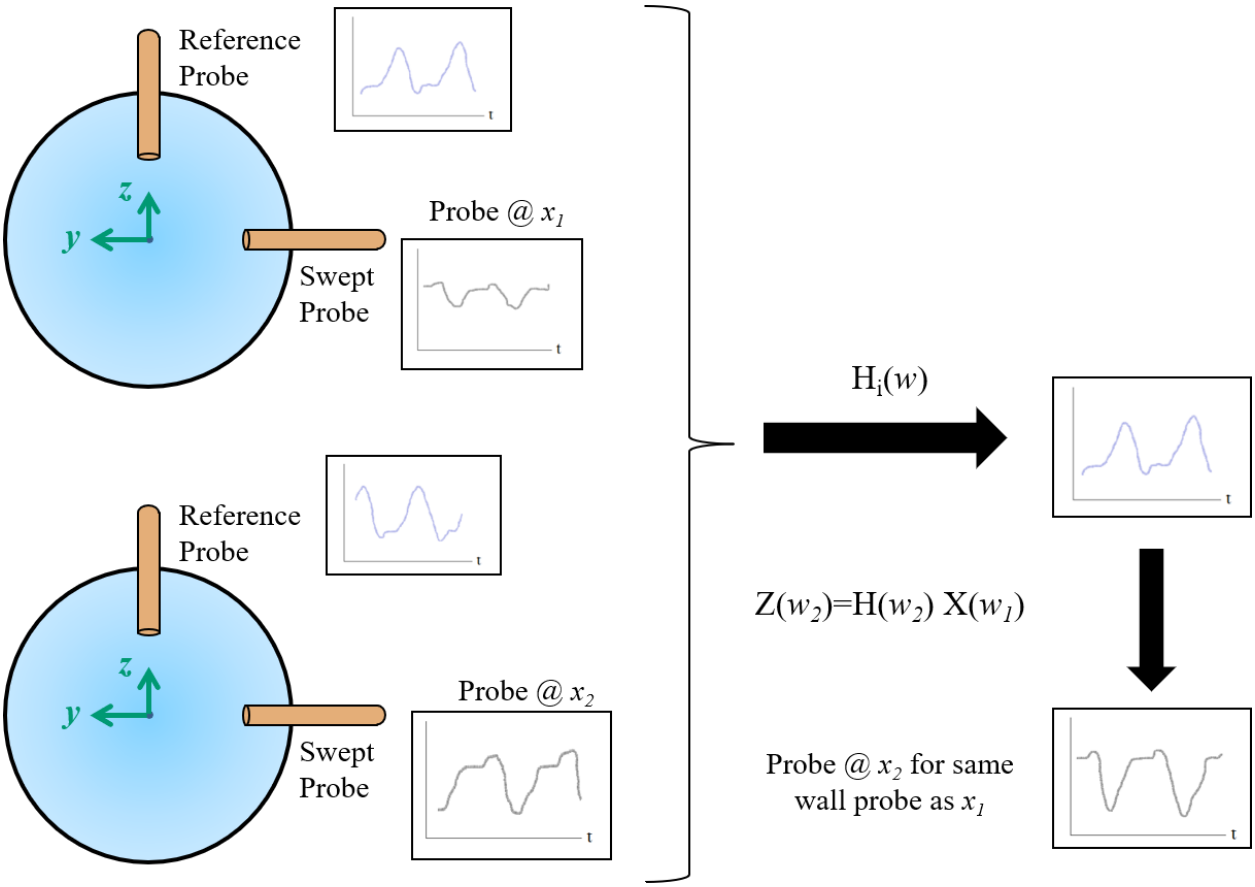

Figure 6.16: Reconstruction of time-matched data signals using a transfer function to synchronize the original time-series data to a uniform reference signal. The transfer function is applied in the frequency domain with resulting signals then transformed back to the time domain.

probe measurements for large-amplitude potential fluctuations.

An alternative approach to determine fluctuating potential is the possible use of a Langmuir probe instead. In this scenario, the cold probe bias is swept slowly (on the order of 0.1 Hz) with the current response measured at a much higher sampling frequency (250 kS/s). The fluctuating potential can be cleanly resolved for such large-amplitude fluctuations. The methods could provide measurements of the density and potential fluctuations that are crucial to understanding the fundamental mechanism of the instability and its coherent versus turbulent nature.

For the fluctating measurements, both probes were sampled at 100 kS/s to provide adequate

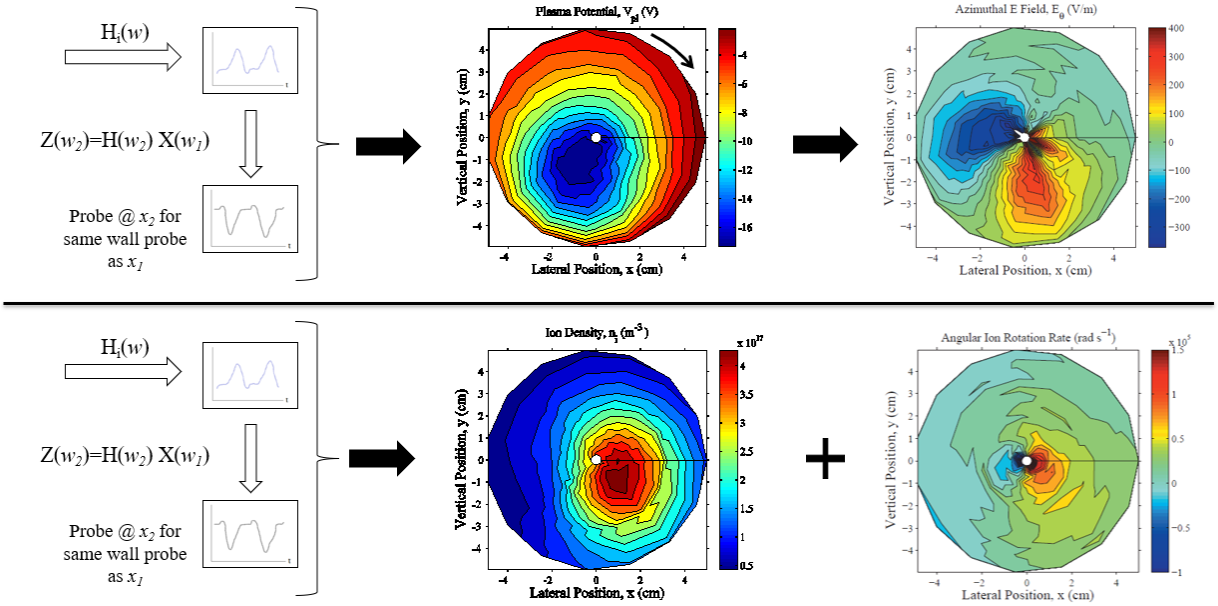

Figure 6.17: Instantaneous contours for plasma potential, azimuthal electric field, ion density, and angular ion rotation rate reconstructed from Langmuir, emissive, and Mach probe measurements using linear transfer functions, taken from [12].

resolution of the mode at 10-20 kHz. The probes were sampled in a 2-dimensional cross-section of the plasma column in-between the chamber magnets. The plane covered the entire plasma column with individual datapoints 5 mm apart. Measurements were conducted at 5 different system setpoints, but just two are presented here to illustrate the effect of increasing magnetic field in the region. It is again worth noting that these measurements were conducted with an underperforming cathode that seemed to result in an order of magnitude decrease in the density of the plasma, therefore significantly affecting the mode behavior in comparison to previous studies. The mode, however, was still noticeable and provided useful information on how magnetic field affects behavior.

2D power spectral density plots are shown in Figure 6.18 and 6.19 for setpoints 3 and 4 in Table 4.2 respectively. The plots make identification of the azimuthal clear as the power drops along the center and increases off-axis as expected of the $m = 1$ mode. The ion saturation probe plots indicate a strong global oscillation in the very low frequency range (<3 kHz). The fluctuation

has to be ion density in nature as it is not visible in the potential fluctuations. Comparison of the two setpoints indicate the presence of a second off-axis oscillation at higher magnetic field. The cause of the second oscillation is unclear, it does not occur at a harmonic or beat frequency.

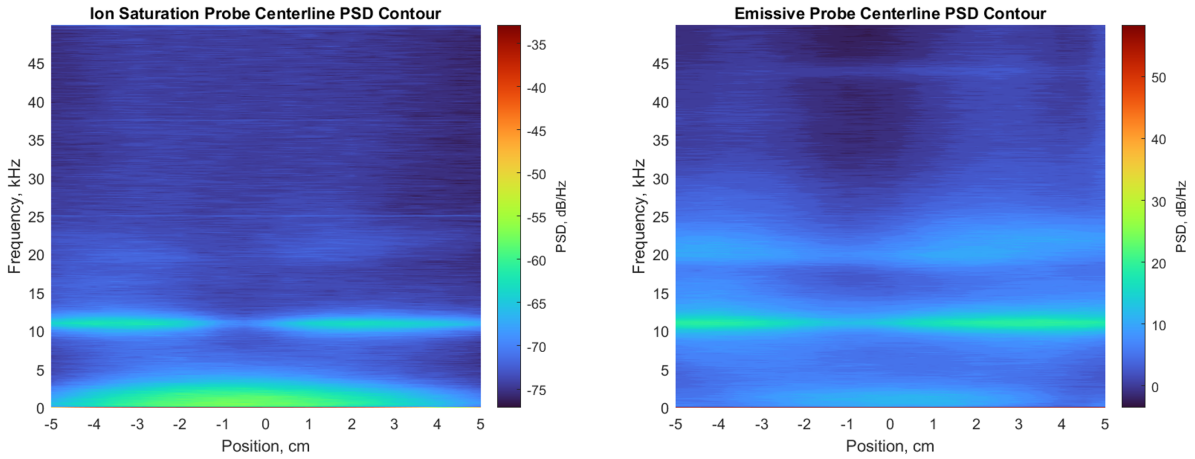

Figure 6.18: 2D PSDs of (left) ion density and (right) potential fluctuations along the centerline for setpoint 3 in Table 4.2.

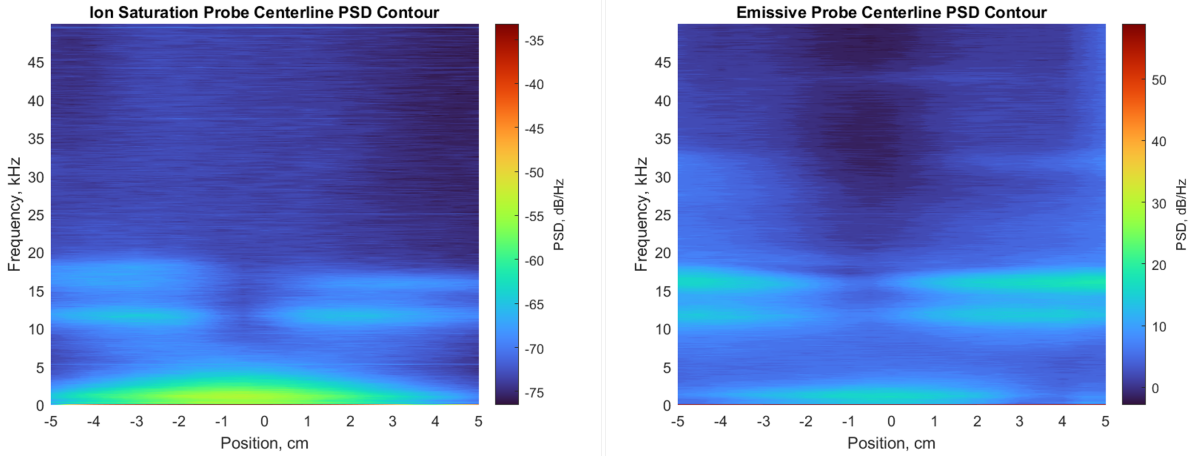

Figure 6.19: 2D PSDs of (left) ion density and (right) potential fluctuations along the centerline for setpoint 4 in Table 4.2.

The centerline probe data are used along with the transfer function approach described in Figure 6.16 to reconstruct the fluctuation. The oscillations are visualized below in spatial-temporal contour plots of density and potential in Figures 6.20 and 6.21 respectively. At Setpoint 3, a 2

kHz density fluctuation is visible along the centerline and disappears with increasing magnetic field. Additionally, the fluctuation behavior off-axis becomes more visible but not quite yet coherent. This is likely due to the lower density resulting in a weaker density gradient. The potential oscillation on the other hand appears a lot more clearly with increasing magnetic field.

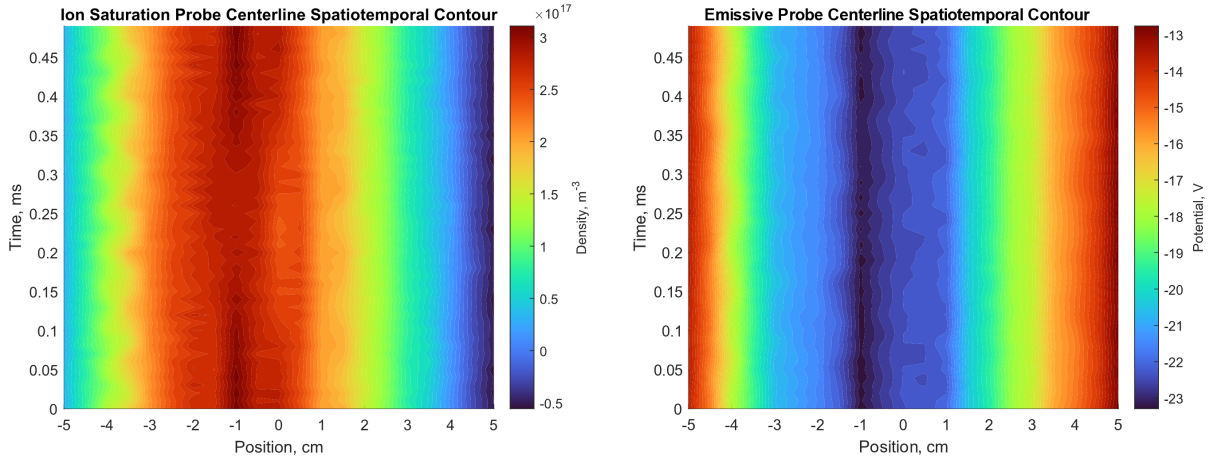

Figure 6.20: Spatial-temporal profiles of (left) ion density and (right) potential fluctuations along the centerline for setpoint 3 in Table 4.2.

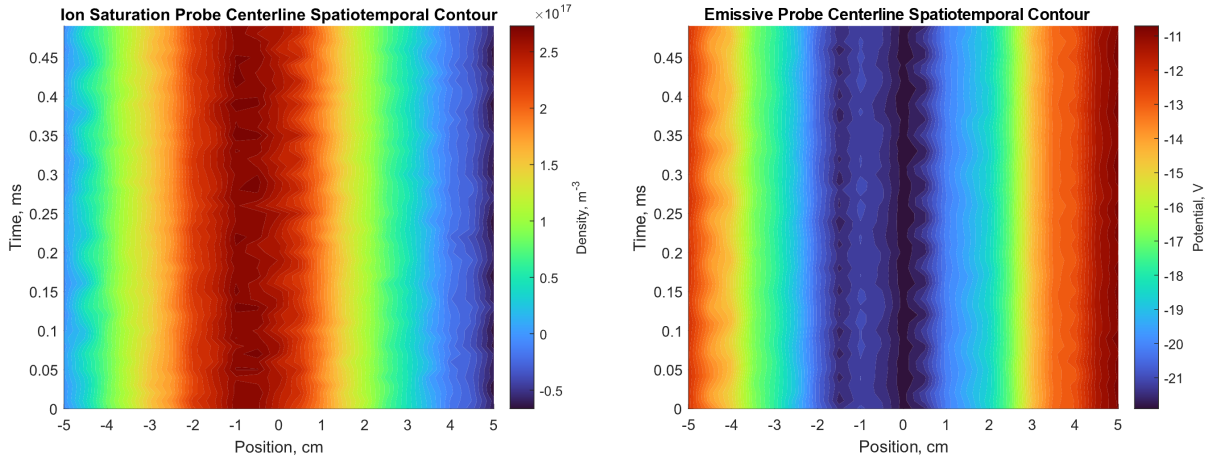

Figure 6.21: Spatial-temporal profiles of (left) ion density and (right) potential fluctuations along the centerline for setpoint 4 in Table 4.2.

These measurements confirm that the mode does exist at these setpoints and facility conditions relevant to PMI experiments and may impact ion behavior.

6.4 Azimuthal Mode Effects on Plasma Material Interaction

The behavior of the mode with increasing magnetic field is of significance as the same phenomena occurs near the sample. The sample magnet is run with a high current to cusp the plasma focus it onto the sample. This complicates the problem further as it creates a magnetic field gradient in the radial direction. Figure 6.22 shows 2D PSDs of emissive probe data at the face of a 10 PPI foam at two different times during the experiment. Both plots show clear presence of the mode at the sample face along with increased power in the high frequency with time.

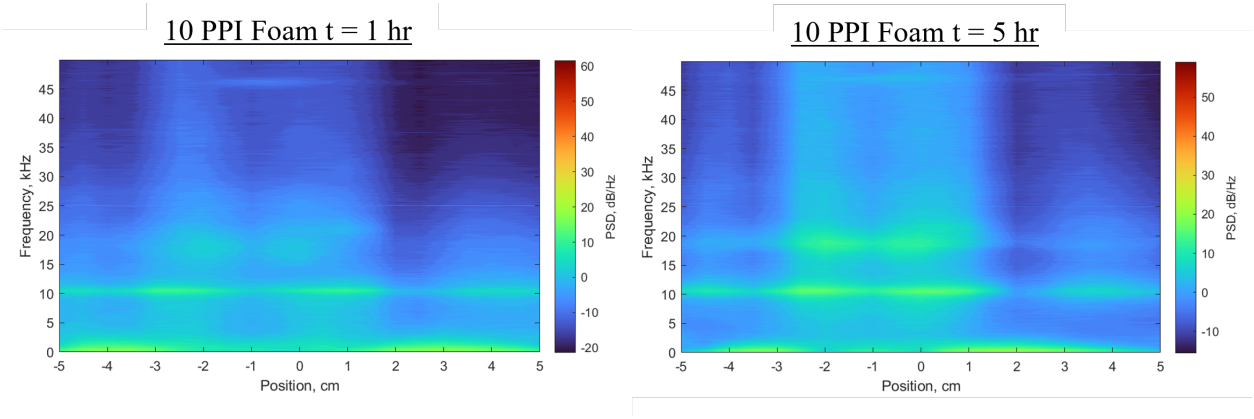

Figure 6.22: 2D PSDs of potential fluctuation 1 cm from the face of a 10 PPI foam (left) 1 hour and (right) 5 hours after starting biased exposure.

The primary implication from this measurement is that the mode exists at the sample face and therefore can affect ion motion due to the density oscillation. The concept is illustrated in Figure 6.23, where the foam surface plane is normal to the z-axis.

A plasma-facing sheath or sheath on a flat surface would form in that axis. Ions would be accelerated thru the sheath with the assumption that the impact energy is the gain from the sheath potential as described by equation6.5.

$$v_z = v_0 + \sqrt{\frac{2\varepsilon e \Delta\phi}{M_i}} \tag{6.5}$$

However, since the azimuthal oscillation creates a velocity component in the theta direction,

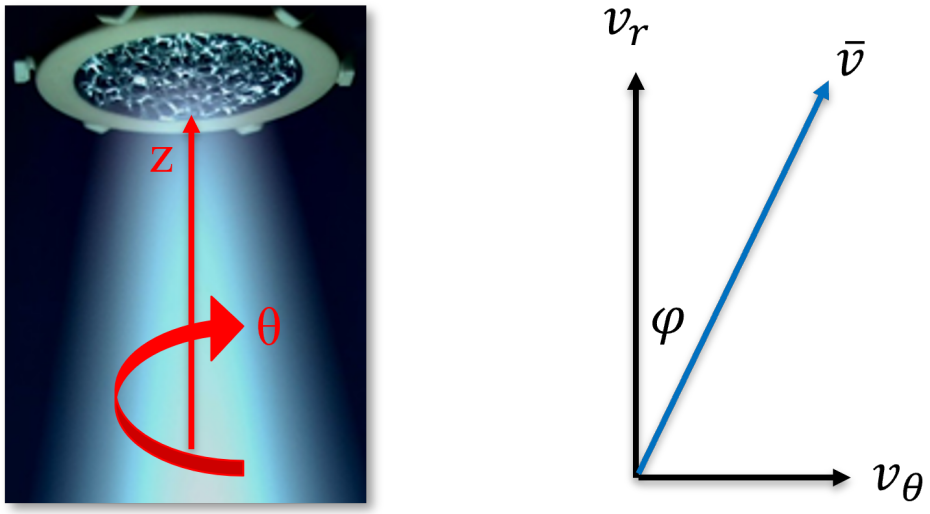

Figure 6.23: The azimuthal rotation causes xenon ions to drift in the azimuthal direction, introducing an additional velocity component and angle of incidence for the plasma-material interaction process.

the component would not be affected by the sheath and slightly increase the impact energy. More significant is the fact that the mode would create an angle of incidence for the incoming ions hitting the surface. Sputtering behavior is sensitive to impact energy and angle of incidence, both of which could case a slight increase in the actual sputtering yield.

The effect can be quantified using measurements made of the mode. In the case of a 300 eV ions, without accounting for the mode's effect on ions the assumption would be that the impact energy is 300 eV with 0 degree angle of incidence. Using the mode frequency, ω_θ, and radial position, r_θ, the azimuthal velocity component , v_θ, can be estimated using equation 6.6.

$$v_\theta = 2\pi r_\theta \omega_\theta \tag{6.6}$$

This component is vector summed to produce an impact energy of 303 eV, but an angle of incidence of 5 degrees. This angle of incidence is significant as according to sputtering simulations [106], it results in a 4.4% increase in sputtering yield. This is a notable increase and enough to explain the slightly elevated sputtering yield measured for flat aluminum in the experiments as

shown in Figure 4.15.

VCMs have the capability to be more robust against such phenomena. In the plasma-facing regime, the 3-dimentional structure and non-flat structure of ligaments allows for reduction of impact angle of incidence when particles come in with different velocity components. This is significant as sputtering yield can increase drastically with a few degrees of angle of incidence. Furthermore, in the plasma-infused scenario, the plasma infuses into the structure with sheaths formed normal to ligament surfaces. Therefore, the different velocity components can be neutralized as the angle of incidence is always normal to the surface if properly designed.

CHAPTER 7

Conclusions

7.1 Conclusion

Understanding and quantifying lifetime of electric propulsion and plasma-facing components requires physics-based approaches that capture key mechanisms, specifically plasma-material interaction. The first limiting factor for electrospray thrusters is propellant flux to and interaction with the grids, resulting in saturation and electrical failures. The first electrospray life model explicitly considering mass plume profile was developed in this work to inform the design of a high-thrust precision device. The model was used to study sensitivity of geometry, plume conditions, and electron backstreaming on device lifetime. The work identified the significance of the shape of the profiles and the fundamental requirement that mass and current distributions must deviate from each other. Super-Gaussian profiles for electrospray plumes were then discovered using novel mass-flux measurements. The measurements provided critical insight on open questions in the structure and understanding of electrospray plumes, and demonstrated the need for mass flux to be accurately accounted for in order to infer thruster performance and lifetime.

Similarly, plasma material interactions are a challenge for lifetime and performance of plasma devices for electric propulsion and fusion. Ion bombardment and sputtering degrades boundary materials and contaminants contaminates the plasma, reducing performance, limiting device lifetime, and increases component replacement costs. Plasma-infused volumetrically complex foams were characterized for persistent sputtering-yield reduction and plasma-favorability. Results demonstrated that foams that persistently reduce sputtering yield are capable of plasma infusion and

can be tailored for specific plasma applications. Experimental measurements of a foam under plasma exposure demonstrated the ability of the foam to partially-infused with plasma and subsequently transition to plasma-facing regime based on plasma properties. This provided insight on the plasma-infusion process dependence on plasma properties. PPI was shown to be the key design parameter to create VCMs for PFC or electrode applications tailored for specific plasma performance and infusion behavior. A novel sputtering model was developed for foams to accurately describe the sputtering distributions and trapping mechanisms. The model demonstrated the capability of tungsten foams to reduce sputtering yield up to 70%, a key milestone in the development of VCMs for PMI applications. Analysis showed that the aspect ratio is the primary driver for sputtering behavior in the plasma-infused region and can be used tailor a VCM for a specific application independent of PPI, which can be tailored for specific plasma properties.

Additionally, the role of azimuthal instabilities in ExB systems on the PMI process was characterized and shown to be non-negligible in certain scenarios. Investigation and characterization of the mode provide insight on the mode and potential underlying chaotic dynamics, with implications for Hall thrusters, low-temperature plasma devices, and plasma-material interaction characterization of volumetrically-complex materials. Azimuthal instabilities must be accounted for as they can significantly impact system dynamics via azimuthal velocity components, mode coupling, and cross-field transport.

7.2 Path Forward

7.2.1 Electrospray

Minor differences in the mass profile shape and emitted flow rate can have strong implications on lifetime [7, 2, 6, 78]. Therefore, the effects of temperature variation must be accounted for in modeling lifetime. Additionally, electrospray operating mode is not always steady, and can result in periods of pulsating emission [54, 55], especially during startup, shutdown, or changing operational setpoints. Understanding the frequency of unsteady emission events and avoiding unsteady

emission modes is a crucial factor in achieving long lifetimes. Furthermore, secondary electron emission, variations in charge-mass ratio, and possibility of backspray from the grids can affect lifetime. Future research should examine the extraction and plume evolution mechanisms that lead to the observed Super-Gaussian profiles and response.

A open question in electrospray is the plume formation and physics. The mass flux measurements indicate a gap in understand and modeling of these mechanisms. Better understanding of the mechanisms at play and the jet breakup and plume formation can provide significant information on the process and enable better modeling of lifetime and performance. This involves the investigation of neutral particles that are often neglected but can compose a non-trivial portion of the plume. Similarly, an analog of the life model and mass flux plume profiles can be explored for ion-mode electrosprays to gain better insight on the mechanics of those devices.

7.2.2 Plasma Material Interactions

Volumetrically-complex materials can greatly reduce plasma contamination while maintaining plasma-favorability. The sputtering model indicated potential performance of tungsten foam that would greatly benefit from experimental validation. Furthermore, experimental validation of small aspect ratio (higher volume density) foams would provide significant insight on the VCM design space. In addition, the experiments in this dissertation were performed at lower-than-ideal plasma densities. Similar experiments measuring VCM exposed to much higher density and temperature plasma would provide significant insight on the plasma response and material behavior in those regimes, as well as better validation of VCM performance in the plasma-infused regime. These experiments would also benefit from having better functioning spectroscopy and ex-situ mass loss characterization to validate erosion measurements.

The sputtering model was successful in capturing the angular sputtering behavior of the measured foams. The analysis can be expanded to consider plasma-infused scenario using the same framework. Additionally, the exponential density drop in plasma-infusion can possibly be better

approximated by treating the ligaments using probe theory and enforcing current saturation. This could provide a more accurate description of plasma-infused VCMs and insights on the plasma physics of plasma-infusion of VCMs. Furthermore, the sputtering analysis can be complemented with a similar analysis of secondary electron emission (SEE).

7.2.3 E x B

Perhaps the most significant measurement necessary is resolving the motion of the ions as it is crucial to the instability mechanism. Specifically, measuring the ion motion will provide insight on the cause of azimuthal drift of the ions, as discussed in Section 6.1. The measurements could validate the MSHI instability mechanism in this discharge configuration, provide drift velocity distributions for transport estimates, and shed light on the coherent nature of the mode. More details and some preliminary thoughts and analysis can be found in Appendix E. Additionally, a core motivation for this effort is the role the mode plays in enhancing cross-field electron transport. The electron transport to the walls and the mode behavior can be measured using ring probes located at varying axial locations in the plasma column. The ring probes were previously used by Matlock et al. [12] and the results can be used to infer the total anomalous electron transport conducted by the azimuthal instability and compared to theoretical predictions of current based on classical transport. The results from the proposed measurement will provide clarity on the quantity of electron current transported across field lines in relation to the phase of the rotating oscillation, as measured in [12, 30]. Additionally, measurements at varying setpoints can quantitatively examine the role of a coherent vs turbulent mode on electron transport and provide further clarity on the debate over what the cause(s) of anomalous electron transport are and how to mitigate it. Azimuthal measurements from all three ring probes can be used to evaluate the axial nature of the fluctuations. Similar analysis will provide the relative phase difference axially to inform on whether the mode is a rigid rotor that's uniform axially or flute-like mode.

Additionally, the ring probe measurements can be instrumental for dynamical system analysis techniques [114, 115] that can provide significant insight on the nature of the low-frequency

oscillation. Shadow Manifold Interpolation can be used to quantify the effect of a measured quantity, such as the low-frequency azimuthal mode, on another measured quantity, such as cross-field electron transport. The analysis can be extended to the correlation probes data and for evaluating the ring probes measurements with the probe inserted into the plasma and other key system components, including the cathode and boundaries, to provide valuable insight on the dominant mechanisms causing the observed phenomena. An attempt at using such analysis techniques for mode classification and prediction can be found in Appendix D. Another element of this effort that can benefit from advances in dynamical systems analysis is the coherent vs turbulent classification of the mode. DMD provides modal decomposition where each mode consists of oscillations at a given frequency with growth or decay, in essence providing both dimensional reduction in terms of modes and their time evolution [116, 117, 114]. DMD can be used along with high speed imaging of the azimuthal mode to provide insight on the coherent nature of the mode. High speed imaging can be used to look axially down the plasma column from the target region during the ring probes experiment. Additionally, SMI can be used to evaluate specific coherent content in the videos (such as the visual density fluctuation) along with time-series data from the ring and Langmuir probes or cathode signal. The combination of spatial and temporal data provided by the probes and Fastcam along with the dynamical system analysis techniques can provide valuable insight on the fundamental dynamics of the mode.

Bibliography

[1] Wirz R E, Collins A L, Thuppul A, Wright P L, Uchizono N M, Huh H, Davis M J, Ziemer J K and Demmons N K 2019 Electrospray thruster performance and lifetime investigation for the lisa mission *AIAA Propulsion and Energy 2019 Forum, Indianapolis, IN* p 3816

[2] Thuppul A, Wright P L, Collins A L, Ziemer J K and Wirz R E 2020 *Aerospace* **7** 108

[3] Wirz R 2022 *Nuclear and Plasma Sciences Society* **1** 1–4

[4] Adamovich I, Baalrud S D, Bogaerts A, Bruggeman P, Cappelli M, Colombo V, Czarnetzki U, Ebert U, Eden J G, Favia P *et al.* 2017 *Journal of Physics D: Applied Physics* **50** 323001

[5] Parker J, Raitses Y and Fisch N 2010 *Applied Physics Letters* **97** 091501

[6] Thuppul A, Collins A L, Wright P L, Uchizono N M and Wirz R E 2021 *Journal of Applied Physics* **130** 103301

[7] Thuppul A, Collins A L, Wright P L, Uchizono N M and Wirz R E 2019 Spatially-resolved mass flux and current measurements of electrospray plumes *36th International Electric Propulsion Conference* (Vienna, Austria) pp 1–10

[8] Ottaviano A, Thuppul A, Hayes J, Dodson C, Li G Z, Chen Z and Wirz R E 2021 *Review of Scientific Instruments* **92** 073701

[9] Li G Z and Wirz R E 2021 *Physical Review Letters* **126** 035001

[10] Simon A 1963 *The physics of fluids* **6** 382–388

[11] Powis A T, Carlsson J A, Kaganovich I D, Raitses Y and Smolyakov A 2018 *Physics of Plasmas* **25** 072110

[12] Matlock T, Dodson C, Goebel D and Wirz R 2015 Measurements of transport due to low frequency *30th International Electric Propulsion Conference, Hyogo-Kobe, Japan, IEPC-2015-137* pp 4–10

[13] Ziemer J, Marrese-Reading C, Dunn C, Romero-Wolf A, Cutler C, Javidnia S, Li T, Li I, Franklin G, Barela P, Hsu O, Maghami P, O'Donnell J, Slutsky J, Thorpe J, Demmons N, Hruby V and Team L P 2017 Colloid microthruster flight performance results from space technology 7 disturbance reduction system *35th International Electric Propulsion Conference* (Atlanta, GA, USA) pp 1–17

[14] Blandino J J, Martinez-Baquero N, Demetriou M A, Gatsonis N A and Paschalidis N 2016 *Journal of Spacecraft and Rockets* **53** 864–875

[15] NASA 2015 Nasa technology roadmaps, ta 2: In-space propulsion technologies Tech. rep. National Aeronautics and Space Administration 2.2.1.5 Electrospray Propulsion

[16] Marrese-Reading C, Anderson J R, Jung-Kubiak C, Greer F, Rouhi N, Wilson D, White V, Dickie M, Mueller R, Singh V, Mackie W, Wirz R and Gamero-Castano M 2016 Silicon emitter needle and array design for indium electrospray arrays for spacecraft propulsion *52nd AIAA/SAE/ASEE Joint Propulsion Conference* (Salt Lake City, UT, USA) pp 1–14

[17] Marrese-Reading C, Anderson J R, Jung-Kubiak C, Polk J, Singh V, Yee K, White V, Wilson D, Bruneau P, Rouhi N, Greer F, Borgonia J, Dickie M, Muller R, Swindlehurst R, Niblett N, Ziemer J, Gray A, Mueller J, Wirz R and Gamero-Castano M 2016 Microfluidic electrospray propulsion (mep) thruster performance with microfabricated emitter arrays for indium propellant *52nd AIAA/SAE/ASEE Joint Propulsion Conference* (Salt Lake City, UT, USA) pp 1–15

[18] Tajmar M, Genovese A and Steiger W 2004 *Journal of propulsion and power* **20** 211–218

[19] Hruby V, Spence D, Demmons N, Roy T, Ehrbar E v Zwahlen J, Martin R, Ziemer J, Connolly W, Rhodes S *et al.* 2008 St7-drs colloid thruster system development and performance summary *44th AIAA/ASME/SAE/ASEE Joint Propulsion Conference & Exhibit* (Hartford, CT, USA) pp 1–32

[20] Demmons N R, Lamarre N, Ziemer J K, Parker M and Spence D 2016 Electrospray thruster propellant feedsystem for a gravity wave observatory missions *52nd AIAA/SAE/ASEE Joint Propulsion Conference* (Salt Lake City, UT, USA) pp 1–16

[21] Ziemer J K 2009 Performance of electrospray thrusters *31st International Electric Propulsion Conference* (Ann Arbor, MI, USA) pp 1–13

[22] Amaro-Seoane P, Audley H, Babak S, Baker J, Barausse E, Bender P, Berti E, Binetruy P, Born M and Bortoluzzi D 2017 *arXiv preprint arXiv:1702.00786*

[23] Ziemer J K, Randolph T M, Gamero-Castaño M, Hruby V, Connolly W, Demmons N, Ehrbar E, Martin R, Roy T, Spence D and Zwahlen J 2007 Flight hardware development of colloid microthruster technology for the space technology 7 and lisa missions *30th International Electric Propulsion Conference* (Florence, Italy) pp 1–13

[24] Ziemer J K, Randolph T, Hruby V, Spence D, Demmons N, Roy T, Connolly W, Ehrbar E, Zwahlen J and Martin R 2006 Colloid microthrust propulsion for the space technology 7 (ST7) and LISA missions *AIP Conference Proceedings* vol 873 (American Institute of Physics) pp 548–555

[25] Linke J, Du J, Loewenhoff T, Pintsuk G, Spilker B, Steudel I and Wirtz M 2019 *Matter and Radiation at Extremes* **4** 056201

[26] Li G Z, Matlock T S, Goebel D M, Dodson C A, Matthes C S, Ghoniem N M and Wirz R E 2017 *Plasma Sources Science and Technology* **26** 065002

[27] Boeuf J P 2014 *Frontiers in Physics* **2** 74

[28] Hargus Jr W A and Charles C S 2008 *Journal of Propulsion and Power* **24** 127–133

[29] Koshkarov O, Smolyakov A, Kapulkin A, Raitses Y and Kaganovich I 2018 *Physics of Plasmas* **25** 061209

[30] Ellison C, Raitses Y and Fisch N J 2012 *Physics of Plasmas* **19** 013503

[31] Koshkarov O, Smolyakov A, Raitses Y and Kaganovich I 2019 *Physical review letters* **122** 185001

[32] Sigmund P 1973 *Journal of Materials Science* **8** 1545–1553

[33] Hoh F 1963 *The Physics of Fluids* **6** 1184–1191

[34] Sakawa Y, Joshi C, Kaw P, Jain V, Johnston T, Chen F and Dawson J 1992 *Physical review letters* **69** 85

[35] Sakawa Y and Joshi C 2000 *Physics of Plasmas* **7** 1774–1780

[36] Lafleur T, Baalrud S and Chabert P 2016 *Physics of Plasmas* **23** 053502

[37] Lafleur T, Baalrud S and Chabert P 2016 *Physics of Plasmas* **23** 053503

[38] Lafleur T, Martorelli R, Chabert P and Bourdon A 2018 *Physics of Plasmas* **25** 061202

[39] Croes V, Lafleur T, Bonaventura Z, Bourdon A and Chabert P 2017 *Plasma Sources Science and Technology* **26** 034001

[40] Hara K 2018 *Physics of Plasmas* **25** 123508

[41] Hara K and Treece C 2019 *Plasma Sources Science and Technology* **28** 055013

[42] Smolyakov A, Frias W, Kaganovich I and Raitses Y 2013 *Physical review letters* **111** 115002

[43] Smolyakov A, Koshkarov O, Romadanov I, Janhunen S, Chapurin O, Raitses Y, Kaganovich I and Sydorenko D 2017 Fluid and kinetic modelling of instabilities and transport in exb plasma discharges *Proc. Int. Electr. Propuls. Conf.(IEPC)* p 411

[44] Janhunen S, Smolyakov A, Chapurin O, Sydorenko D, Kaganovich I and Raitses Y 2018 *Physics of Plasmas* **25** 011608

[45] Matlock T S, Goebel D M and Wirz R E 2013 Near anode plasma in the plasma interaction facility at ucla *33rd International Electric Propulsion Conference*

[46] Matlock T, Goebel D, Conversano R and Wirz R 2014 *Plasma Sources Science and Technology* **23** 025014

[47] Matlock T S, Goebel D M and Wirz R E 2014 An investigation of low frequency plasma instabilities in a cylindrical hollow cathode discharge *50th AIAA/ASME/SAE/ASEE Joint Propulsion Conference* p 3508

[48] Thuppul A, Wright P and Wirz R E 2018 Lifetime considerations and estimation for electrospray thrusters *2018 Joint Propulsion Conference* p 4652

[49] Demmons N, Martin R, Hruby V, Roy T, Spence D, Ehrbar E and J Z 2011 Electrospray device uS Patent 7,932,492

[50] Courtney D G and Shea H 2015 *Applied Physics Letters* **107** 103504

[51] Terhune K J, King L B, He K and Cumings J 2016 *Nanotechnology* **27** 375701

[52] Brikner N and Lozano P C 2012 *Applied Physics Letters* **101** 193504

[53] Lozano P and Martínez-Sánchez M 2004 *Journal of colloid and interface science* **280** 149–154

[54] Wright P L, Thuppul A and Wirz R E 2018 Life-limiting emission modes for electrospray thrusters *54th AIAA/ASME/SAE/ASEE Joint Propulsion Conference & Exhibit* (Cincinnati, OH, USA) pp 1–9

[55] Rosell-Llompart J, Grifoll J and Loscertales I G 2018 *Journal of Aerosol Science*

[56] Barrios-Collado C, Vidal-de Miguel G and Sinues P M L 2016 *Sensors and Actuators B: Chemical* **223** 217–225

[57] Lozano P and Martínez-Sánchez M 2003 *Studies on the ion-droplet mixed regime in colloid thrusters* Ph.D. thesis Massachusetts Institute of Technology, Department of Aeronautics and Astronautics

[58] Konermann L, Metwally H, McAllister R G and Popa V 2018 *Methods* **144** 104–112

[59] Borner A, Li Z and Levin D A 2013 *The Journal of Physical Chemistry B* **117** 6768–6781

[60] Mehta N A and Levin D A 2019 *Physical Review E* **99** 033302

[61] Daily J W and Micci M M 2009 *The Journal of chemical physics* **131** 094501

[62] Kim D Y and Micci M M 2013 *Journal of Propulsion and Power* **29** 899–905

[63] Gamero-Castano M and Fernandez De La Mora J 2000 *The Journal of Chemical Physics* **113** 815–832

[64] Gamero-Castaño M 2008 *Journal of Fluid Mechanics* **604** 339

[65] Grifoll J and Rosell-Llompart J 2014 *Journal of Electrostatics* **72** 357–364

[66] Davis M, Collins A L and Wirz R E 2019 Electrospray plume evolution via discrete simulations *The 36th International Electric Propulsion Conference, IEPC-2019* vol 590

[67] Gamero-Castaño M 2008 *Physics of Fluids* **20** 032103

[68] Demmons N, Hruby V, Spence D, Roy T, Ehrbar E, Zwahlen J, Martin R, Ziemer J and Randolph T 2008 St7-drs mission colloid thruster development *44th AIAA/ASME/SAE/ASEE Joint Propulsion Conference & Exhibit* (Hartford, CT, USA) pp 1–18

[69] De La Mora J F and Loscertales I G 1994 *Journal of Fluid Mechanics* **260** 155–184

[70] Fernández de La Mora J 2007 *Annual Review of Fluid Mechanics* **39** 217–243

[71] Demmons N R, Hruby V J, Courtney D, Ziemer J K and Marrese-Reading C 2018 Ground and on-orbit thruster performance comparison for the lisa pathfinder colloid MicroNewton thrusters *2018 Joint Propulsion Conference* (Cincinnati, OH, USA: American Institute of Aeronautics and Astronautics) pp 1–15

[72] Courtney D G, Dandavino S and Shea H 2015 *Journal of Propulsion and Power* **32** 392–407

[73] Wirz R E, Katz I, Goebel D M and Anderson J R 2011 *Journal of Propulsion and Power* **27** 206–210

[74] Ryan C, Daykin-Iliopoulos A, Stark J, Salaverri A, Vargas E, Rangsten P, Dandavino S, Ataman C, Chakraborty S, Courtney D and Shea H 2013 Experimental progress towards the microthrust mems electrospray electric propulsion system *33rd International Electric Propulstion Conference* URL `http://infoscience.epfl.ch/record/197810`

[75] Prince B D, Fritz B A and Chiu Y H 2012 Ionic liquids in electrospray propulsion systems *Ionic Liquids: Science and Applications* (ACS Publications) pp 27–49 (*Preprint* `https://pubs.acs.org/doi/pdf/10.1021/bk-2012-1117.ch002`) URL `https://pubs.acs.org/doi/abs/10.1021/bk-2012-1117.ch002`

[76] Miller S W, Prince B D, Bemish R J and Rovey J L 2014 *Journal of Propulsion and Power* **30** 1701–1710

[77] Ma C and Ryan C N 2018 The design and characterization of a porous-emitter electrospray thruster (pet-100) for interplanetary cubesats *7th Interplanetary CubeSat Workshop*

[78] Collins A L, Thuppul A, Wright P L, Uchizono N M, Huh H, Davis M J, Ziemer J K, Demmons N R and Wirz R E 2019 Assessment of grid impingement for electrospray thruster lifetime *36th International Electric Propulsion Conference* (Vienna, Austria) pp 1–17

[79] Thompson J W, Eschelbach J W, Wilburn R T and Jorgenson J W 2005 *Journal of the American Society for Mass Spectrometry* **16** 312–323

[80] Chandrupatla T R 2009 *Quality and reliability in engineering* vol 2 (Cambridge University Press New York, NY)

[81] Smith K, Alexander M and Stark J 2006 *Journal of applied physics* **99** 064909

[82] Choi H K, Park J U, Park O O, Ferreira P M, Georgiadis J G and Rogers J A 2008 *Applied Physics Letters* **92** 123109

[83] Smith D P 1986 *IEEE Transactions on Industry Applications* 527–535

[84] De La Mora J F and Loscertales I G 1994 *Journal of Fluid Mechanics* **260** 155–184

[85] Uchizono N M, Collins A L, Thuppul A, Wright P L, Eckhardt D Q, Ziemer J and Wirz R E 2020 *Aerospace* **7** 141

[86] Miller S W, Prince B D, Bemish R J and Rovey J L 2014 *Journal of Propulsion and Power* **30** 1701–1710

[87] Gamero-Castaño M and Cisquella-Serra A 2021 *Phys. Rev. Fluids* **6**(1) 013701 URL `https://link.aps.org/doi/10.1103/PhysRevFluids.6.013701`

[88] Davis M J, Collins A L and Wirz R E 2019 Electrospray plume evolution via discrete simulations *36th International Electric Propulsion Conference, Vienna, Austria, IEPC-2019-590*

[89] Rosell-Llompart J, Grifoll J and Loscertales I G 2018 *Journal of Aerosol Science* **125** 2–31

[90] Hartman R, Borra J P, Brunner D, Marijnissen J and Scarlett B 1999 *Journal of Electrostatics* **47** 143–170

[91] Gañán Calvo A M 1997 *Phys. Rev. Lett.* **79**(2) 217–220 URL `https://link.aps.org/doi/10.1103/PhysRevLett.79.217`

[92] Higuera F J 2003 *Journal of Fluid Mechanics* **484** 303–327

[93] Collins A L, Thuppul A, Wright P L, Uchizono N M, Huh H, Davis M J, Demmons N K, Ziemer J K and Wirz R E 2019 Assessment of grid impingement for electrospray thruster lifetime *36th International Electric Propulsion Conference, Vienna, Austria, IEPC-2019-213*

[94] Ganan-Calvo A, Lasheras J, Dávila J and Barrero A 1994 *Journal of Aerosol Science* **25** 1121–1142

[95] Wright P, Thuppul A and Wirz R E 2018 Life-limiting emission modes for electrospray thrusters *54th AIAA/ASME/SAE/ASEE Joint Propulsion Conference & Exhibit, Cincinnati, OH* p 4726

[96] Li G Z 2020 *Plasma sputtering behavior of structured materials* (University of California, Los Angeles)

[97] Sheridan T and Goree J 1991 *Physics of Fluids B: Plasma Physics* **3** 2796–2804

[98] Konopliv M, Johnson L K, Chaplin V H, Lobbia R B, Thuppul A, Simka T and Wirz R E 2021 Collisional-radiative models of neutral and singly-ionized xenon in hall thrusters: Experimental validation and model investigations *AIAA Propulsion and Energy 2021 Forum* p 3390

[99] Chaplin V H, Johnson L K, Lobbia R B, Konopliv M F, Simka T and Wirz R E 2022 *Journal of Propulsion and Power* 1–14

[100] Bose S, Kaur M, Chattopadhyay P, Ghosh J, Saxena Y and Pal R 2017 *Journal of Plasma Physics* **83**

[101] Lobbia R B and Beal B E 2017 *Journal of Propulsion and Power* **33** 566–581

[102] Kemp R F and Sellen Jr J 1966 *Review of Scientific Instruments* **37** 455–461

[103] Ottaviano A and Wirz R 2022 *Journal of Applied Physics, D (in submission)*

[104] Yamamura Y, Matsunami N and Itoh N 1982 *Radiation Effects* **68** 83–87

[105] Yamamura Y and Shindo S 1984 *Radiation effects* **80** 57–72

[106] Sabiston G and Wirz R 2022 Volumetrically-complex materials for reducing electric propulsion facility effects *International Electric Propulsion Conference*

[107] Powis A T, Carlsson J A, Kaganovich I D, Rodriguez E, Raitses Y and Smolyakov A 2019 Scaling of spoke rotation frequency within a penning discharge & code development updates (IEPC-2019-816, the 36th International Electric Propulsion Conference ...)

[108] Emmert G, Wieland R, Mense A and Davidson J 1980 *The Physics of Fluids* **23** 803–812

[109] Maggs J and Morales G 2011 *Physical Review Letters* **107** 185003

[110] Maggs J and Morales G 2012 *Plasma Physics and Controlled Fusion* **54** 124041

[111] Maggs J and Morales G 2012 *Physical Review E* **86** 015401

[112] Sheehan J, Raitses Y, Hershkowitz N, Kaganovich I and Fisch N J 2011 *Physics of Plasmas* **18** 073501

[113] Sheehan J, Raitses Y, Hershkowitz N and McDonald M 2017 *Journal of Propulsion and Power* **33** 614–637

[114] Brunton S L and Kutz J N 2019 *Data-driven science and engineering: Machine learning, dynamical systems, and control* (Cambridge University Press)

[115] Eckhardt D, Koo J, Martin R, Holmes M and Hara K 2019 *Plasma Sources Science and Technology* **28** 045005

[116] Schmid P J 2010 *Journal of fluid mechanics* **656** 5–28

[117] Kutz J N, Brunton S L, Brunton B W and Proctor J L 2016 *Dynamic mode decomposition: data-driven modeling of complex systems* (SIAM)

[118] Goebel D M, Watkins R M and Jameson K K 2007 *Journal of Propulsion and Power* **23** 552–558

[119] Goebel D M and Katz I 2008 *Fundamentals of electric propulsion: ion and Hall thrusters* (John Wiley & Sons)

[120] Guerrero Vela P P 2019 *Plasma Surface Interactions in LaB6 Hollow Cathodes with Internal Xe Gas Discharge* Ph.D. thesis California Institute of Technology

[121] Guerrero P, Mikellides I G, Polk J E, Carmina Monreal R and Meiron D I 2021 *Journal of Applied Physics* **130** 043306

[122] Guerrero Vela P P, Polk J E, Richter M H and Lopez Ortega A 2021 *Journal of Applied Physics* **130** 083303

[123] Goebel D M, Becatti G, Mikellides I G and Lopez Ortega A 2021 *Journal of Applied Physics* **130** 050902

[124] Becatti G and Goebel D M 2022 *Vacuum* 110895

[125] Hutchinson I H 2002 *Plasma Physics and Controlled Fusion* **44** 2603

[126] Chung K S 2012 *Plasma Sources Science and Technology* **21** 063001

[127] Dodson C A, Perez-Grande D, Jorns B A, Goebel D M and Wirz R E 2018 *Journal of Propulsion and Power* **34** 1225–1234

[128] Dodson C, Jorns B and Wirz R 2019 *Plasma Sources Science and Technology* **28** 065009

[129] Svarnas P, Romadanov I, Diallo A and Raitses Y 2018 *IEEE Transactions on Plasma Science* **46** 3998–4009

[130] Manzella D 1994 Stationary plasma thruster ion velocity distribution *30th Joint Propulsion Conference and Exhibit* p 3141

[131] Chaplin V H, Conversano R W, Lobbia R B, Ortega A L, Mikellides I G, Hofer R R and Jorns B A 2017 Laser-induced fluorescence measurements of the acceleration zone in the 12.5 kw hermes hall thruster *35th International Electric Propulsion Conference* vol 229 pp 8–12

[132] Huang W, Gallimore A D and Hofer R R 2011 *Journal of Propulsion and Power* **27** 553–563

Appendix A

Quartz Crystal Microbalance

This appendix provides details on the use of a quartz crystal microbalance (QCM) in the context of this dissertation for mass flux measurements. The emphasis is on the considerations for electrospray applications, specifically the measurements presented Chapter 3. However, the measurement principles and considerations are also relevant for material sputtering presented in Chapter 4.

A quartz crystal microbalance measures the measured mass deposited on a crystal using the Sauerbrey equation, shown in Equation A.1 and also in Chapter 3. The change in the fundamental frequency of a crystal is proportional to it's change in mass, where $\frac{dm}{dt}$ is the mass flux, ρ_q is the density of the quartz crystal, μ_q is the shear modulus of the quartz crystal, f_0 is the initial resonant frequency, and $\frac{df}{dt}$ is the rate of change of the measured frequency.

$$\frac{dm}{dt} = -\frac{\sqrt{\rho_q \mu_q}}{2f_0^2}\frac{df}{dt} \tag{A.1}$$

The QCM systems in this dissertation are acquired using an Inficon IC6 Mass Deposition Controller that is capable of internal rate calculations. However, due to the unique applications in this work the system is used to directly output the natural frequency from which the mass flux is computed by the author using Equation A.1 where a linear fit of the frequency is used for $\frac{df}{dt}$. This is done to properly account for additional background and calibration corrections. The first correction considered is the natural behavior of the crystal in the vacuum environment. To determine this, the crystal is exposed with shutter open at different angular positions and the fundamental frequency is measured over a time persiod significantly larger ($10\times$) than the measurement duration. The frequency traces are shown in Figure A.1. The fundamental frequency decreases over time

naturally, indicating some small mass flux rate as a result. This natural drift varies slightly at different angles, and is subtracted as background from the measurements presented in Chapter 3. It is worth noting that the resulting mass flux magnitude due to the drift is orders of magnitude smaller than the measured flux rates while spraying, indicating the correction can be negligible. However, at lower flow rate setpoints or higher half-angles, where the magnitude of the actual spray can be low, these corrections can become significant and must be considered.

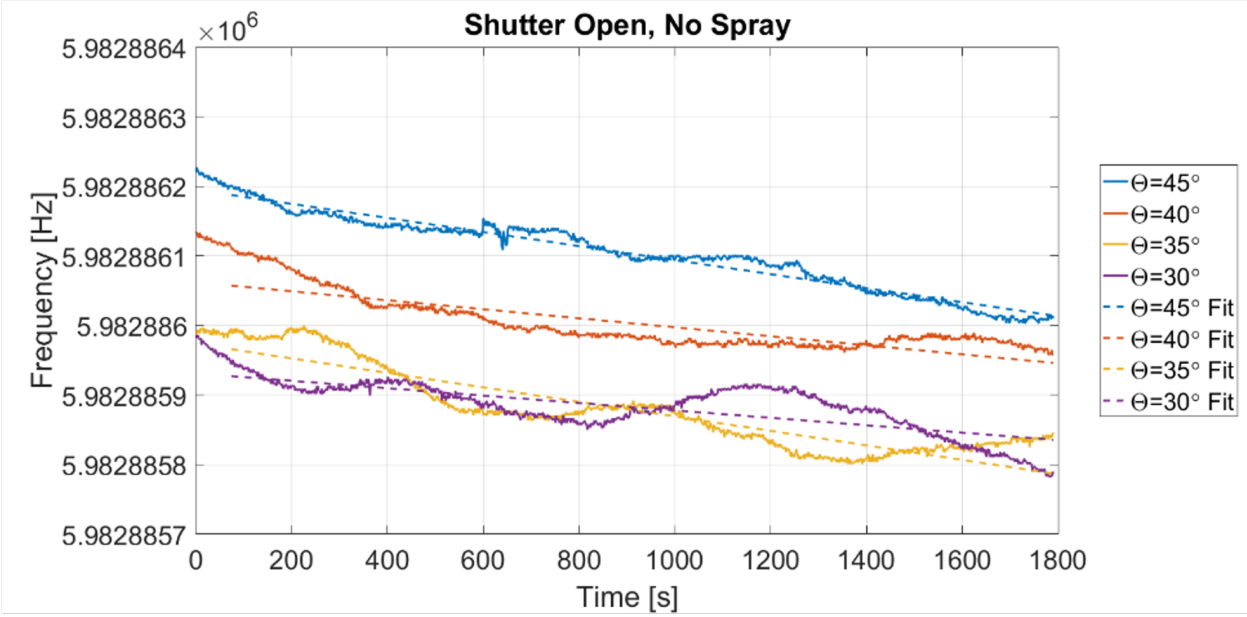

Figure A.1: QCM fundamental frequency traces and linear fits at different angular positions with shutter open but no active mass deposition process to determine natural drift and background effects for measurement calibration.

Since the measurement at it's core is based on frequency, vibration effects must be considered. One of the significant factors that was discovered in the development and use of this diagnostic for this application is the role the shutter plays on the measurement. The crystal has a shutter in front to prevent mass from depositing on it during operation to prevent the crystal from being overloaded with propellant and reaching end of its life. The shutter is pneumatically actuated as necessary when ready to perform measurements. However, as shown in Figure A.2, when the shutter is opened the fundamental frequency initially increases and asymptotically levels off over the course of a minute. Therefore, only the data after 45 seconds of opening the shutter onward at

each physical datapoint are used for the frequency fit and analysis. Additionally, another 30 second delay at each physical datapoint is added initially to allow for the vibrational effects of the motion stages to wear off.

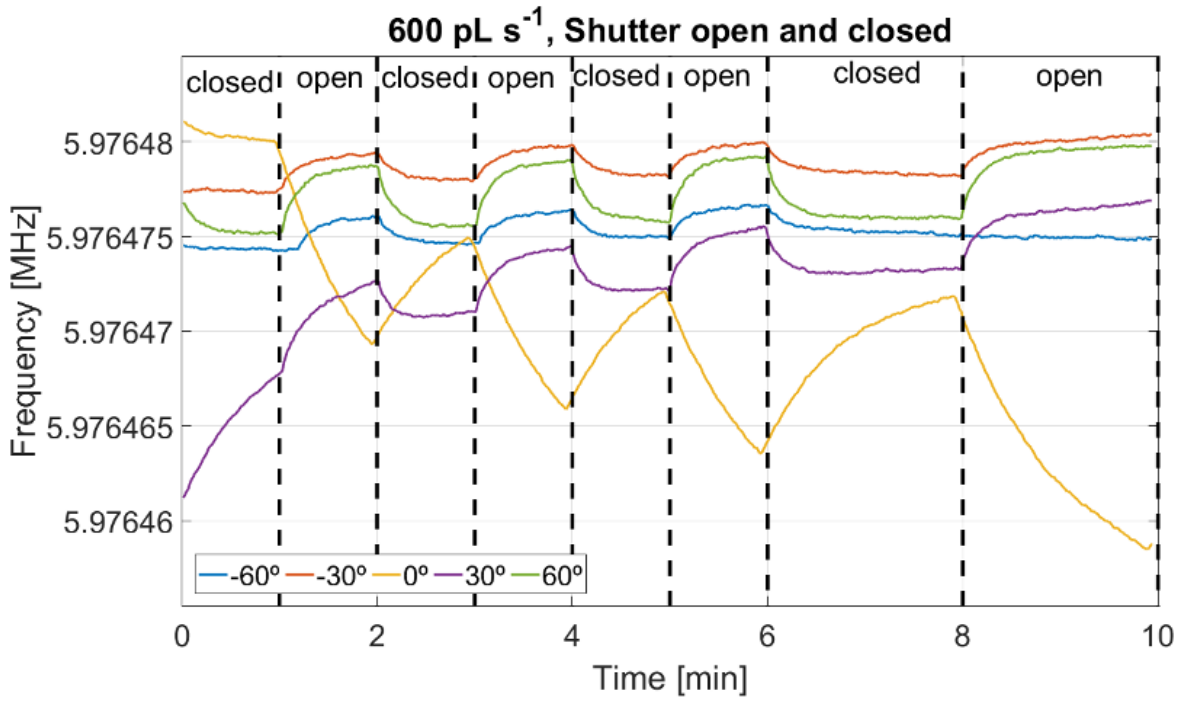

Figure A.2: QCM fundamental frequency traces at different half-angles showing the dynamic response when opening and closing the shutter. The asymptotic increase in the frequency when the shutter opens indicates the need to wait after opening to perform measurements.

The total dwell time at a physical location therefore must me long enough for the vibrational effects from the motion and shutter to wear off, and for enough sampling to occur to collect enough reliable frequency data to form a fit. In the case of electrospray plume measurements presented in Chapter 3, this dwell time ranged from 300 s at high half angles (where signal is low and 180 s of data is needed to fit frequency) to 120 s in the center (where 30 s is sufficient for a reliable fit). The shutter is closed at each angular point to prevent the crystal from saturating prematurely before the experiment ends. For the sputtering measurements in Chapter 4, the mass flux to the crystal is significantly lower in comparison to the center regions of an electrospray plume and as a result, the crystal shutter can be left open through the angular sweep and closed at the end to reduce dwell time

at each angular point in the sweep. Typically, the QCM is parked at each angular location for 60 s which the last 30 s of frequency data used for the linear fit. The uncertainty of the measurement can be determined by propagating the root-mean-square (rms) error of the frequency linear fit appropriately in through the calculation and adding in other factors pertaining to the measurement. For example, in the case of sputtering yield the fit rms is carried through the Sauerbrey Equation, and then the sample current measurement uncertainty, error, and QCM dimension measurement uncertainty are all combined together using square-sums appropriately to determine total error on the measurements.

Another factor considered in these measurements is the potential effects of crystal surface damage from bombardment and propellant wetting/beading. SEM imaging of the crystal surfaces pre- and post- measurements indicated little evidence of significant surface damage; therefore those concerns were considered negligible. Additionally, the imaging indicated relatively even distribution of deposition from the propellant and sputterants. Accounting for all these effects and considerations provides higher confidence in the quality of the measurements in capturing true behavior and the significance of the results presented in Chapters 3 and 4.

Appendix B

Cathode Design

This appendix provides a brief summary of the hollow cathode used for plasma generation in the Pi facility for experiments in Chapter 4 and 6. The cathode suffered from contamination issues briefly shown below that affected facility performance. As a result, the design was modified based on literature and advice from experts in the field to hopefully mitigate the contamination issues.

The hollow cathode in the Pi facility was built by Wirz, Matlock, and Goebel [46] based on the hollow cathode design by Goebel et al. [118]. The general design considerations and principles of hollow cathodes are extensively described in literature and not the focus of this appendix. Rather, the focus is specifically on the issues with this specific cathode that may provide potential insight for readers experiencing similar problems. The cathode assembly and a CAD drawing recreation of the geometry are shown below in Figures B.1 and B.2 respectively. The key component is the insert, composed of Lanthanum hexaboride (LaB6). The insert has a low work function on the order of 2.7 eV that allows for thermionic electron emission to ignite and sustain the plasma discharge. The purpose of the components in the cathode are to achieve this and are discussed in better detail in [119].

The work function and performance of the insert is paramount as it sustains the plasma discharge and affects the plasma properties. However, the extreme thermal environment of the hollow cathode due to the thermionic nature results in components undergoing chemical and materials effects that can contaminate the insert [120]. Examples of this contamination in the hollow cathode in the Pi facility is shown in Figure B.3. The insert is coated in carbon from the pusher tube and and other graphite components that are not ideally outgassed and treated for high tempera-

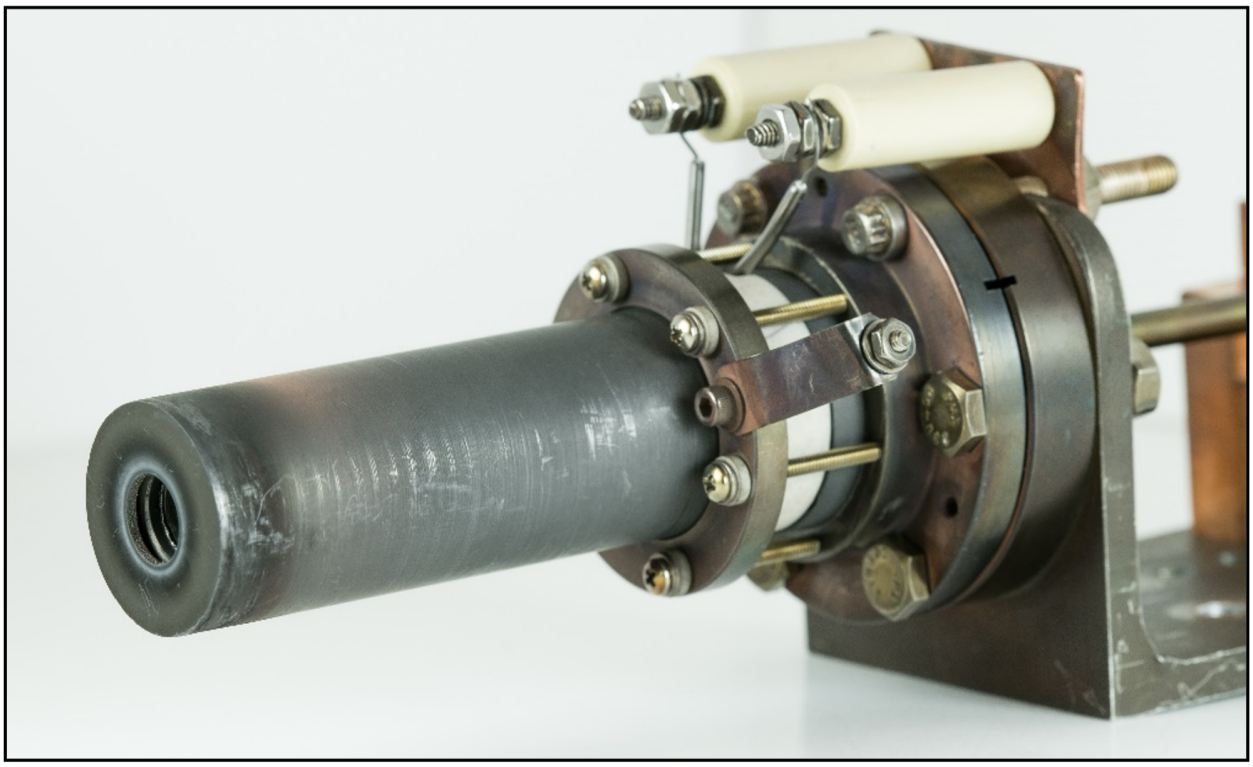

Figure B.1: Photo of the 250 A LaB6 Hollow Cathode and supporting assembly used in the Pi Facility.

ture operation. As a result, the insert's effective work function is elevated and higher operating temperatures are required for achieving a set discharge current. This higher temperature leads to an unfavorable feedback cycle as at higher temperatures, the components contaminate the insert more and lead to significant decreases in plasma density [121, 120]. It additionally leads to higher degrees of thermal expansion and thermal effects such as the bonding of the LaB6 insert and the cathode tube that makes it difficult to disassemble the cathode for cleaning and maintenance.

The contamination of the inserts in the Pi facility hollow cathode resulted in significant decreases in facility plasma density by 1-2 orders of magnitude. As a result, experiments described in Chapters 4 and 6 were performed at these lower densities rather than the planned intention of higher density regimes. The density drop affected the plasma-infusion process, the ion fluence for sputtering, and the behavior of the low frequency azimuthal mode. In an attempt to prevent this issue and perform the studies in the desired regimes, a new cathode was designed with input from

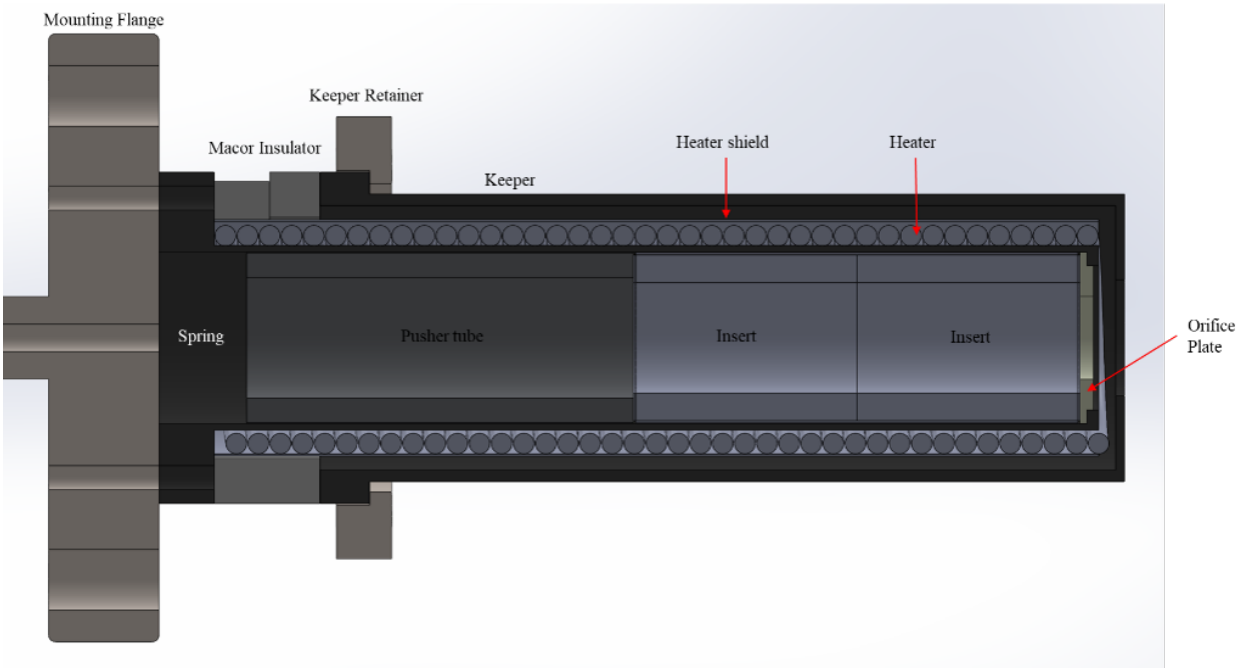

Figure B.2: CAD drawing of the cathode design with significant components indicated.

Guerrero, Goebel, and Becatti [122, 123, 124] to mitigate these contamination issues. The design changes should hopefully prevent graphite contamination of the insert and allow for nominal performance of the hollow cathode and Pi facility for higher density and ion fluence PMI experiments as well as hollow cathode investigations.

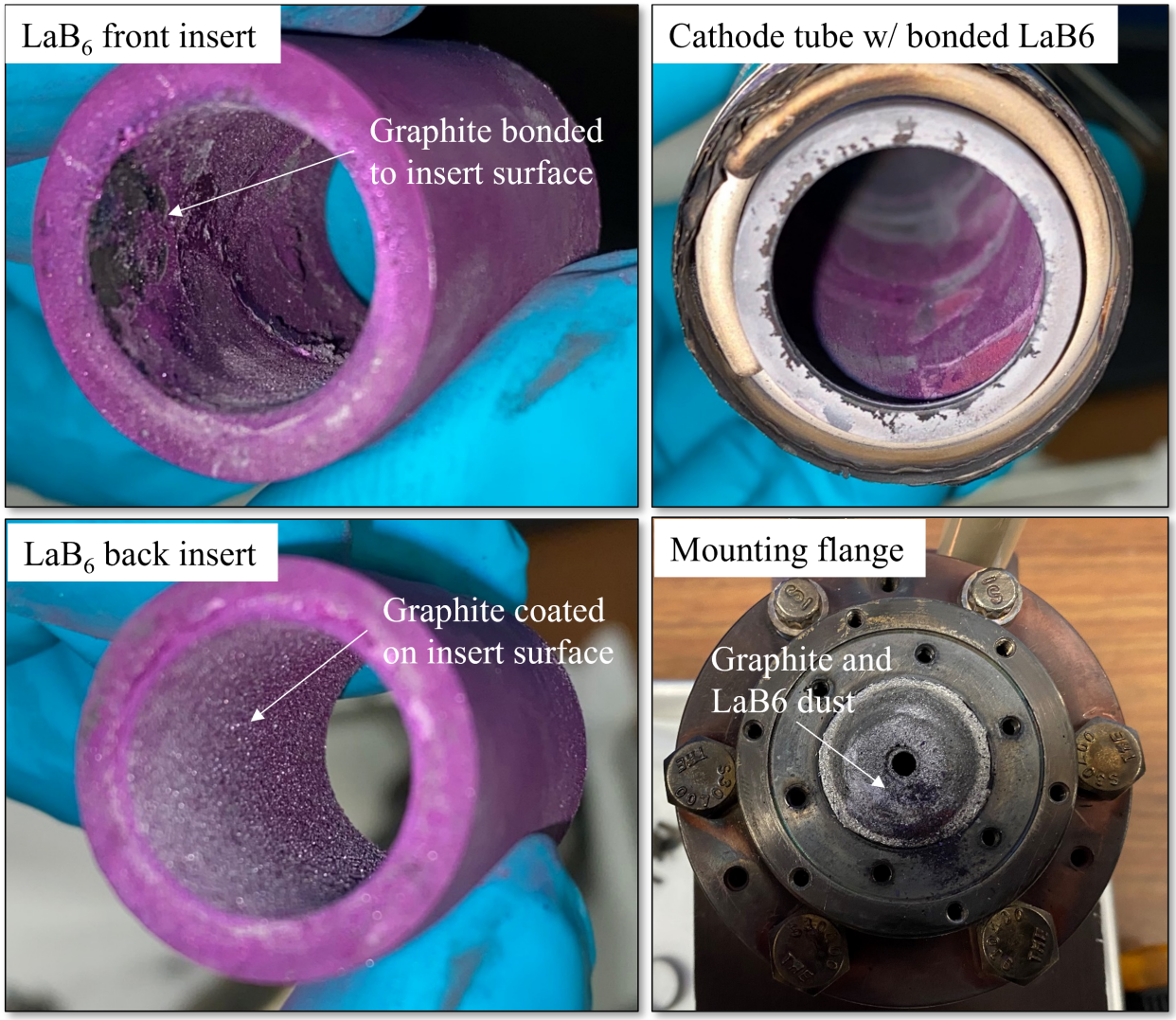

Figure B.3: Photos of cathode components after hundreds of hours of operation showing contamination of the insert and bonding to the cathode tube.

Appendix C

Langmuir Probing

This appendix presents example data from the Langmuir probing experiment to provide some more details on how the plasma properties were determined from the measurements. The analysis detailed here was performed using a general laboratory-use Langmuir probing setup and MATLAB analysis script developed by the author. The data acquisition and general setup is discussed in Section 6.2. The measured and voltage from a datapoint are shown below in Figure C.1. The voltage was swept at 50 Hz for the experiment and sampled for over 1 s such that a reliable 50 traces are measured. The measurements are then snipped to contain an even set of cycles and average over the cycles to produce a current-voltage (IV) curve as shown in Figure C.2.

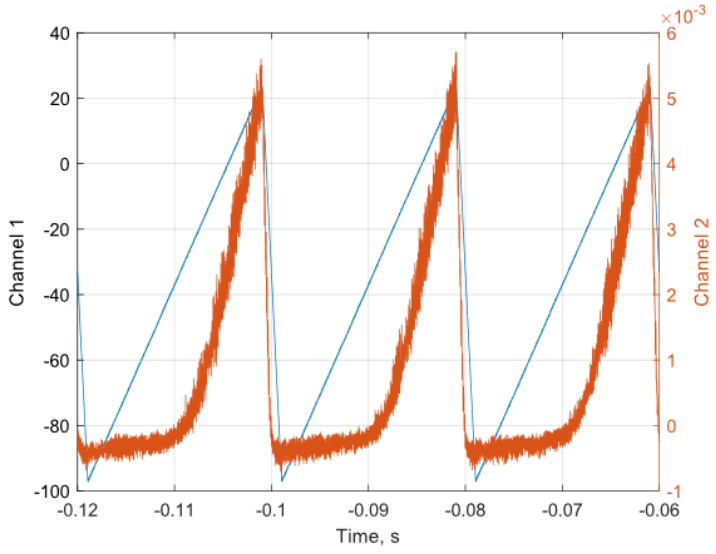

Figure C.1: The raw voltage (blue) and current (orange) measurements by the Langmuir probe for a datapoint. Only thee periods of the voltage sweep are shown for visual clarity.

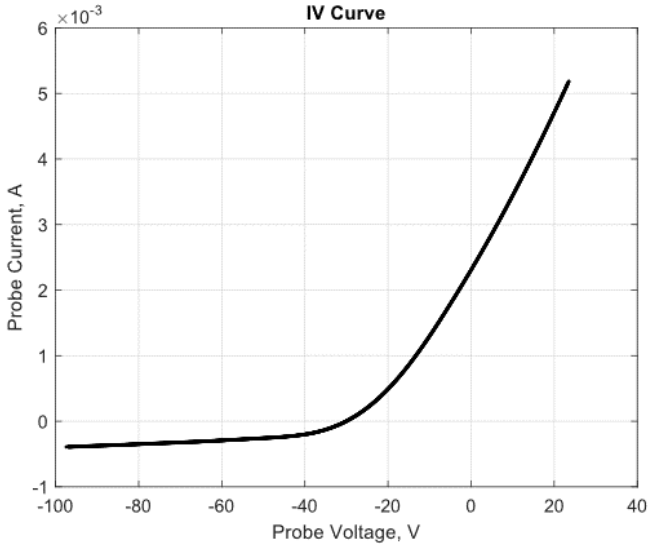

Figure C.2: The voltage current (IV) curve obtained from averaging the voltage sweeps shown in Figure C.1.

IV curves have three general regions corresponding to physical behaviors: the ion-saturan region, the transition region, and the electron transition region. The general principle of Langmuir probing is to use each region along with plasma theory to discern plasma parameters. As briefly discussed in Section 6.2, a variety of probe theories exist. This analysis uses orbit motion limited (OML) and Laframboise (BRL) theories, further described with more details in [101]. Langmuir analysis is strong dependent on fits made to the regions of the IV curve, with an example shown in Figure C.3. In the ion saturation region, the probe sheath is ion saturated and thus any changes to probe bias should not change the current in theory. As a result, region is described with a linear fit, with the slope dependent on the density and temperature. Using BRL, the density serves as an iteration condition with iterations on temperature until the density converges. In the transition region, electrons can reach the probe based on the energy they possess in relation to the probe bias. This region, in summary, is described by an exponential behavior with the exponent linearly dependent on the electron temperature. The electron saturation region is the region in which the probe sheath is saturated and cannot collect any more correct, though the current rarely rolls over experimentally as evidenced by Figure C.2. Typically, the curve rolls over and is treated as the

plasma potential, found by taking the derivative of the current and finding the maximum. The electron-saturation region is fit with an exponential shape as well, with the plasma potential also estimated by the intersection with the transition region fit. In this analysis, both values for potential are calculated and usually found to be with 5 V of each other. The measurements presented in Section 6.2 are the intersection method values.

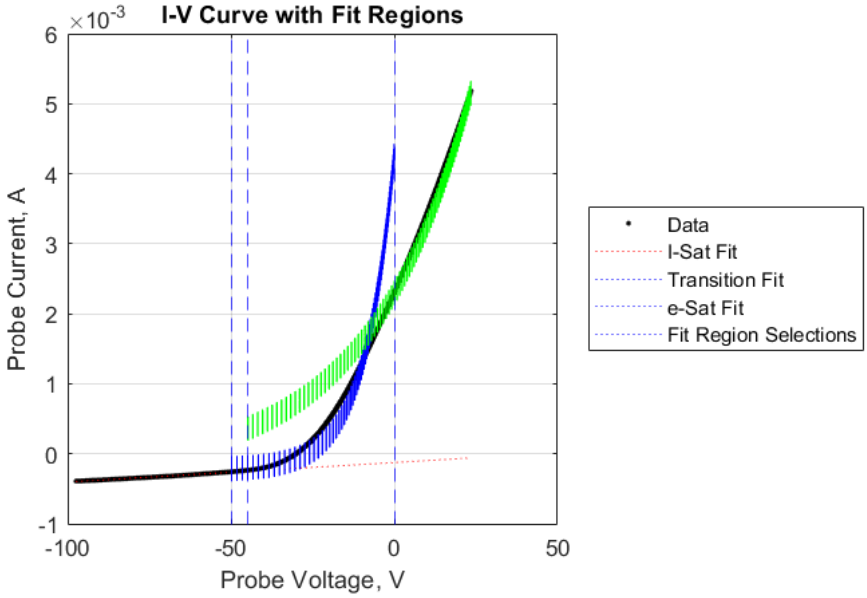

Figure C.3: The IV curve along with fits to the different regions used to estimate the plasma properties.

Appendix D

Machine Learning for Mode Classification

The effort described in this appendix was conducted as part of a course Project for Atmospheric & Oceanic Sciences 204: Machine Learning for the Physical Sciences course at UCLA and available on Medium.com.

The goal of this effort is to use classification and regression algorithms to understand how simplified control parameters which affect key plasma properties of density, electron temperature, magnetic fields, and electric fields affect the nature of the instability that is fundamentally dependent on those properties in a non-linear relationship. The data consists of 58 setpoints (i.e. datapoints) that the facility was tested at by varying different control parameters (i.e. features) such gas flow rates, magnetic field settings, and discharge currents. At each system setpoint, multiple ion-saturation probes sampled at high resolution (30–300 MHz) for 1–5 seconds were used to measure ion current from which Fourier and correlation analysis was used to determine azimuthal mode frequencies, amplitude, and number of low-frequency modes in the plasma. The data was then processed and summarized into a csv file by the author for easy access and utilization with Jupyter Notebooks for analysis, as summarized below in Figure D.1.

Parameters that are dependent on other features were removed in the preprocessing, such as magnet voltages and facility pressure(dependent on flow rates). The resulting final dataset is composed of 7 features that differentiate 59 setpoints for 3 target parameters. Finally, all data was normalized by feature or parameter using the normalize function found in the sklearn preprocessing package.

A K-means classification was initially used to classify the data to see how well it could be

	Mass (amu)	MF_C (sccm)	MF_A (sccm)	I_D (A)	I_CM (A)	I_AM (A)	I_ChM (A)	Mode Peak (kHz)	Mode Amplitude (dB/Hz)	Other Modes
count	59.000000	59.000000	59.000000	59.000000	59.000000	59.000000	59.000000	59.000000	59.000000	59.000000
mean	86.271186	12.525424	10.152542	59.406780	4.983051	21.847458	5.152542	15.205085	-133.711864	0.576271
std	45.883973	6.831358	3.740798	9.517894	5.963948	3.122850	2.565108	7.712606	5.884084	0.498390
min	40.000000	5.000000	5.000000	25.000000	0.000000	10.000000	0.000000	0.000000	-145.000000	0.000000
25%	40.000000	5.000000	7.000000	55.000000	0.000000	19.000000	4.000000	10.500000	-136.500000	0.000000
50%	131.000000	15.000000	12.000000	65.000000	0.000000	22.000000	4.000000	11.200000	-134.000000	1.000000
75%	131.000000	20.000000	15.000000	65.000000	10.500000	25.000000	7.000000	20.500000	-130.000000	1.000000
max	131.000000	20.000000	15.000000	65.000000	14.000000	25.000000	10.000000	30.000000	-120.000000	1.000000

Figure D.1: Simplified Data Table Description for Regressor Inputs.

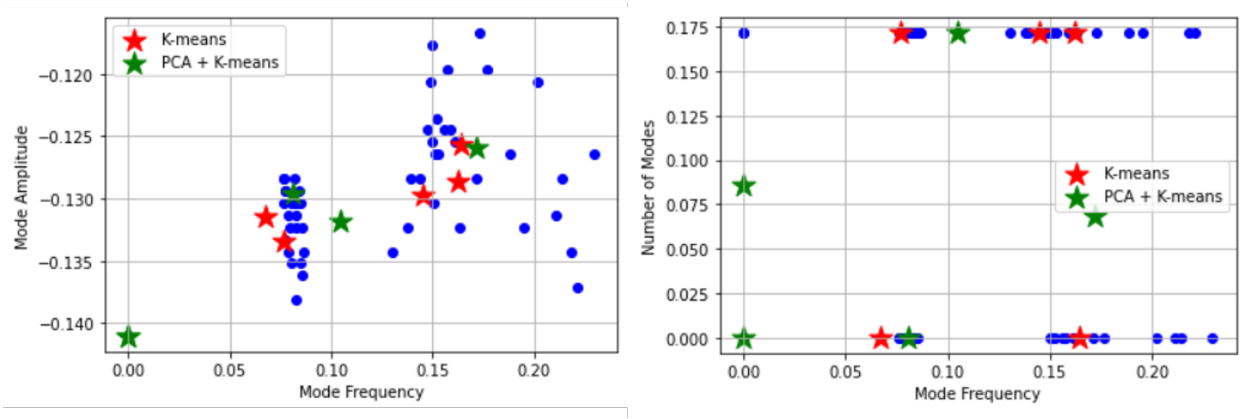

Figure D.2: Classification centroids from K-means and K-means and PCA for mode amplitude and number of modes.

grouped. Two target parameters were evaluated, the mode amplitude and the number of low-frequency modes, as shown in Figure D.2 with data indicated as blue scatter. The kmeans function from the sklearn.cluster package was used, with 5 target clusters ultimately chosen after testing a range between 3–6 clusters. The centroids are indicated by red stars in Figure D.2, and in the case of the amplitude tend to find the mid-range frequency clusters well but do not capture the low end at all and over-classify in the high end. When evaluating the number of modes, the k-means centroids and clustering again fail to classify the low-frequency range but otherwise do well in the binary classification.

Next, principle component analysis (PCA) was used to enhance to classification by reducing the parameter space and creating an initial weighting for the k-means analysis. The PCA function

from the sklearn.decomposition package was used decompose the data into 5 principle components (based on the ideal number of clusters from k-means). This was then used with the k-means algorithm in the reduced-dimensionality model to determine classification of the mode amplitudes and number of modes. As seen in Figure D.5, the PCA reduced model performs better in the case of mode amplitude by successfully locating a centroid at 0 for the cluster there and locating 2 centroids each in the medium and higher frequency ranges. However, in the case of classifying number of modes the PCA reduced model struggles and classifies the gap between the split. The binary nature of this data and the possibility of using this model with a wider spread is discussed in the conclusion.

Regression models were used to attempt to predict the mode behavior to better understand it's behavior and characteristics. Different regressors were used to predict the mode frequency and number of modes based on the system features. A support vector regression (SVR) model was built for each using the SVR function from the sklearn.svm packing. The models after trial and error were chosen to be polynomial kernel of 5th order, with RMSE of 0.07 and 0.09 respectively. The SVR appears to not be very effective at predicting the mode frequency. Different kernels and variations within the kernel were attempted, but the percent of correct prediction still remained poor, as seen in Figure 3. This might be due to the relatively small set of datapoints that cover a wide spread.

A neural network regression model was then built to for each target parameter. A multi-layer preceptron (MLP) regressor was built using the sklearn.neural-network package, using an lbfgs solver over a maximum of 500 iterations. The models were slightly more successful than SVR as seen in Figure D.3, with RMSE of 0.07 and 0.08.

Lastly, random forest regression models of depth 8 were used to see how well it performs and if better, use feature-ranking to determine what parameters matter most. A visualization of the prediction against the data is shown in Figure D.3 for the mode frequency, along with the REC curve comparisons showing the best performance. The model provides further information in the form of feature ranking, indicating that the cathode flow rate and chamber magnet strength play a

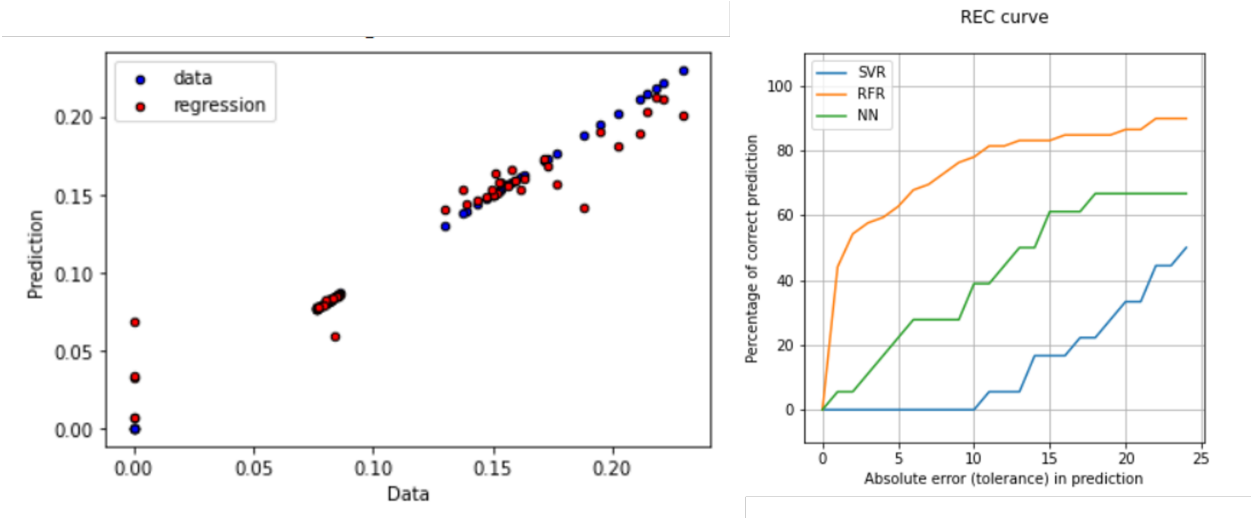

Figure D.3: (Left) Data and Random Forest Regressor prediction of mode frequency. (Right) REC curve for support vector regressor, random forest regressor, and Neural network regressor.

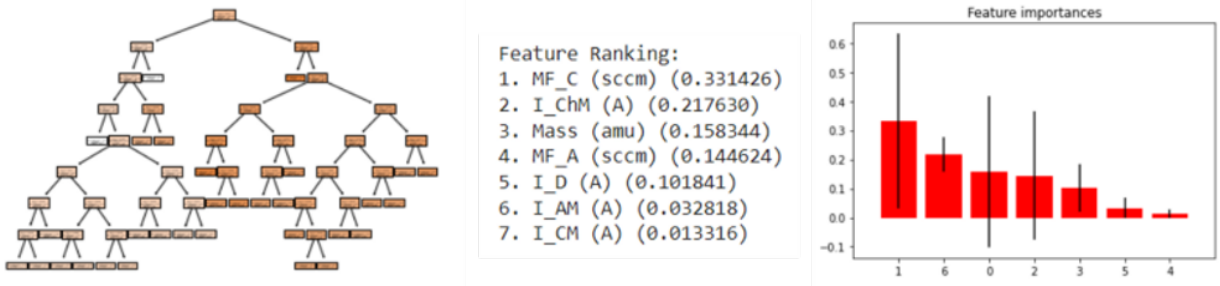

Figure D.4: (Left) Decision Tree example from random forest regressor for mode frequency. Feature ranking values listed (Center) and in histogram form (Right).

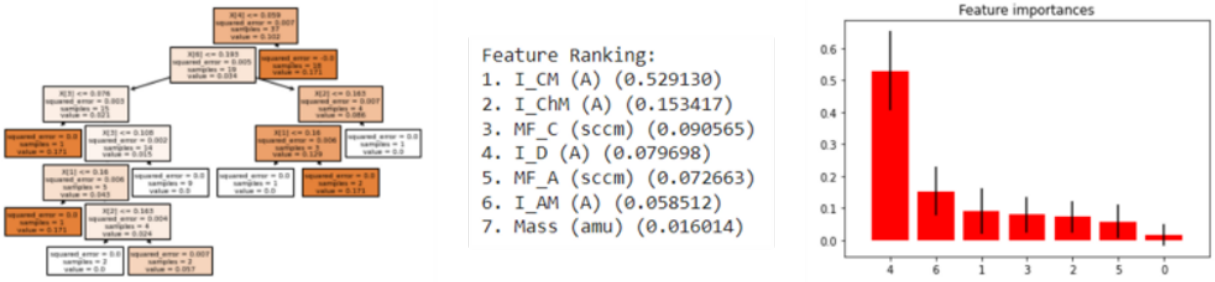

Figure D.5: (Left) Decision Tree example from random forest regressor for number of modes. Feature ranking values listed (Center) and in histogram form (Right).

strong role on the mode frequency behavior. The other features contribute less accordingly.

The feature ranking for random forest regression model for the number of modes is seen in Figure D.5. It's worth noting the behavior is strongly dependent on the cathode magnet strength and substantially less on other features. This is significant insight as the trend is the opposite of the mode frequency that depends least on the cathode magnet.

In summary, classification analysis was applied to low-frequency mode data scatter to classify the mode amplitude and number of modes occurring. Principle component analysis was then used to decompose the feature space and provide a better initial basis and performed slightly better than the initial model. Regression models were then used to attempt to predict the mode frequency and number of modes. SVR, NN MLP, and RF regressors were each built with varying success. The RF regressor is shown to be the most accurate and provided insight on what features have the most impact using feature ranking.

This analysis was all conducted with a relatively small dataset and feature space, but did demonstrate the applicability of these analysis to the problem. This provides a basis and incentive for further data collection across a wider range of feature space so that the models can be of better use. For example, modes outside the narrow band considered here can be included in the analysis, especially for number of modes, to better inform the problem. With more data, the models can potentially provide insight on how specifically physical parameters given the behavior of this mode and interaction with other modes.

Appendix E

Using LIF for E x B Mode Ion Behavior

Previous measurements of ion rotation rate were performed by Matlock et al. [12], and shown in Figure 6.17c. The measurements were taken using a Mach probe [125], which will again be used in this effort to validate laser-induced fluorescence (LIF) measurements. The challenge with using Mach probes for this effort is the lack of a consensus theory for cylindrical Mach probes in a partially-ionized plasma with unmagnetized ions [12]. The probes are composed electrodes (tungsten) exposed from an isolating holder (alumina) with semi-circular surfaces pointing in opposite directions. The electrodes are biased to ion saturation potential. The ratio of ion currents to each electrode, I_s, face allows for an estimate of the ion Mach number as shown in equation E.1, where K is a calibration constant based on ion and electron temperatures [126]. However, the use of a calibration factor with a range of fits introduces large uncertainty to the measurements (up to 25% in [12]). An additional challenge with Mach probes is the time-dependence, with large variations based on whether a instantaneous current or averaged current is used. These factors collectively pose doubts on the validity of Mach probe results for measurements of faster time-scale.

$$M = \frac{v_i}{c_s} = K\ln\left(\frac{I_1}{I_2}\right) \tag{E.1}$$

LIF is a more-precise non-intrusive technique that measures the Doppler shift of an absorption line to determine the velocity distribution function (VDF) of a species. The technique offers multiple advantages in comparison to probes, specifically the non-perturbative nature of the technique and the increase spatial resolution. The relationship can be described by equation E.2, where v_s is the species velocity, f_0 is the absorption frequency in the rest frame, Δf is the difference between

the laser frequency and f_0, and c is the speed of light.

$$v_i = c\frac{\Delta f}{f_0} \tag{E.2}$$

For xenon ions, a XeII $5d^2F_{7/2} \rightarrow 6d_2^{5/2}$ transition will be used due to it's high transition probability and previous applications in similar efforts [127, 128, 129, 130, 28]. The transition is excited by 834.953 nm (vacuum) and results in a fluorescence at 542.066 nm (vacuum). A tunable single-frequency titanium sapphire laser pumped by a Nd:YAG solid state laser will be used to excite the transition. The laser wavelength is swept with the range and frequency increments defined by the user. The wavelength is measured using a High Finesse WS7 wavelength meter with 60 MHz resolution. The input power is monitored using a ThorLabs PM100D power meter measuring power from a split-off beam path that has been calibrated against downstream beam power at injection. As the background intensity of the plasma is much higher than the fluoresced signal, a modulated signal that can be measured using phase-sensitive detection is necessary. A ThorLabs MC2000 optical chopper is used to modulate the injection beam at 2 kHz. A Stanford Research Systems SR830 lock-in amplifier uses the optical chopper as an input to filter the fluoresced signal at the chopper frequency with a specified bandwidth to de-noise the signal and recover the true fluoresced response. The injection beam is carried to the vacuum chamber using 200 μn fibers, adapters, and feedthroughs (with a power budget developed to account for all losses in the system).

Inside the chamber, 25 mm injection optics focus the beam down to a 2.5 mm spot size at a 30 cm working distance. 50 mm collection optics focuses on a 1.5 mm spot size at a working distance of 30 cm. The collection optics are placed on motorized stages to enable alignment corrections conducted in vacuum before the experiment. The collections optics are connected to a ThorLabs photo-multiplier tube (PMT) located outside the vacuum chamber using 600 μn fibers, feedthroughs, and a 543 nm bandpass filter with a 10 nm FWHM. A current amplifier passes the current response of the PMT as a voltage signal to the lock-in amplifier. The lock-in amplifier time constant, τ_{lia} is on the order of 100s of ms to 1 s based on previous LIF experiments on plasmas of

similar density and temperature [128]. The integration time is $\approx 5\tau_{lia}$.

The proposed experimental plan is to measure IVDFs in radial chord profiles. The injection and collection optics will be positioned radially outside the plasma column focusing on the measurement plane in-between the chamber magnets. Both optics are swept radially completely through the plasma column in the y and z directions in 5 mm increments. The z-direction (vertical) sweep will contain Doppler shifts along the purely azimuthal direction as it's parallel to the injection optics, which means the measured distributions should be time-averaged IVDFs of the azimuthal velocity. The y-direction (horizontal) sweep will contain Doppler shifts along the purely radial direction as it's parallel to the injection optics, which means the measured distributions should be the time-averaged IVDFs of the radial velocity.

Interpretation of the resulting line-shapes requires knowledge of the plasma dynamics. The scope of this knowledge varies from simple analytical models all the way to a full-kinetic simulation with IVDFs to compare the experiments with. As the task of developing a comprehensive kinetic model is beyond the timeline of this proposed work, priority will be placed instead on leveraging models and findings from literature [11, 107], and developing simpler models to predict expected IVDFs for a few different conditions. In lieu of these quantitative results to date, a brief qualitative discussion of expected results is presented below.

First, the case of just the steady-state plasma properties (see Section 6.2) in a collisionless scenario is considered for time-averaged measurements. The plasma has a potential well that confines the ions. Therefore, the plasma slowly rattles around the well and processes azimuthally. In this scenario, the azimuthal IVDFs would be thermalized in nature (thus Maxwellian in shape) with a small drift due to the azimuthal procession. The FWHMs of the azimuthal IVDFs should be independent of radial location of the measurement, while the drift velocities should change signs about the centerline. The radial IVDFs should be double-peaked with each peak Maxwellian in shape due to the trapped motion of the ions in the potential well (going up and down the well resulting in forward and backward streaming). The FWHMs of the radial Maxwellians should be similar in an IVDF and not change significantly with radial position. The absolute value of the

magnitude of the drift velocities of the populations should be nearly identical and decrease with increasing radial position as the potential well slows and reflects the trapped ions.

Next, the scenario previously considered is modified with the additional of an $m = 1$ potential fluctuation as shown in Figure 6.17. The time-averaged nature of the IVDF measurements means that the fluctuations would be smeared out. Therefore, the fluctuations can be imagined as an annular potential rings. The addition should not have any measurable changes to the azimuthal IVDFs. The radial IVDFs however, will be influenced and the drift velocity will have a maximum located off-center at the radial position corresponding to the bottom of the oscillating potential well. In these scenarios, the role of collisions have been neglected. It is suspected that the ion collisons with neutrals will effectively drag the ions and broaden their distributions. The qualitative analysis provides a pathway to develop simpler models to obtain quantitative distribution functions that can guide the analysis of experimental measurements.

In addition to physical mechanisms, broadening mechanisms that affect the line shape must be carefully considered and accounted for to ensure accuracy of the results obtained. A few effects will be considered and are briefly summarized below. Saturation broadening is the response of the fluorescence to the incident laser power and causes a broadening of the measured line-shape. The saturation intensity for a transition can be estimated using equation E.3, with degeneracy, g, and rate, γ, found in NIST databases. This estimate can help guide limits for intensity used during the experiment and how significant saturation broadening could be. For a thermalized species population, the line-shape of the velocity profile is a Gaussian distribution. The broadening lineshape can be described by a lorentzian distribution, with the convolution of the two resulting in a Voight distribution for the measured line-shape [127]. As fitting a Voight profile to the measured result and deconvolving can be rather difficult for noisy and complex profiles, the estimated saturation broadening can instead be treated as the temperature uncertainty [127, 131].

$$I_{sat} = \left(\frac{g_1}{g_1 + g_2}\right)\left(\frac{2\pi\gamma h\nu_0^3}{c^2}\right) \tag{E.3}$$

Zeeman splitting is the interaction of a magnetic field and atomic energy levels, leading to line broadening. The broadening can be described using a semi-empirical model [132], $\Delta\nu = \alpha B$, where $\alpha = 2.7$ MHz/G and B is the magnetic field (discussed in Section 4.2). Hyperfine splitting is the interaction of the nuclear electric and magnetic moments interacting with the electronic angular momentum, causing multiple absorption lines of varying strength. The effects of Hyperfine splitting were to be less than 10% on a 1 eV population and thus negligible [132, 127].

Appendix F

Fluid Derivation for Modified Simon-Hoh Instability

This appendix provides details on the framework for a fluid model of the modified Simon-Hoh instability. The continuity and momentum equations are expanded out and the incorporation of the energy equation is described to determine azimuthal frequency estimates derived in literature.

A fluid model for the modified Simon-Hoh stability has used in numerous past works [34, 43, 47] and is re-derived to some detail below to provide readers for potential future work applications. It can be developed by assuming a cold quasi-neutral plasma treatment with ionization collision, ν_{ion}, and neutral collisions, ν_{sn}. The electrons and ions are treated separately with each governed by their continuity and momentum equations shown in equations F.1 and F.2 respectively.

$$\frac{dn_s}{dt} + \nabla \cdot (n_s u_s) = n_s \nu_{ion} \tag{F.1}$$

$$\frac{d\mathbf{u_s}}{dt} + \mathbf{u_s} \cdot (\nabla \mathbf{u_s}) = -\frac{1}{m_s n_s} \nabla \cdot \mathbf{P_s} + \frac{q_s}{m_s}(\mathbf{E} + \mathbf{u_s} \times \mathbf{B}) - \nu_s \mathbf{u_s} \tag{F.2}$$

A perturbation to the density and potential of the form shown in equations F.3 and F.4 is used linearize the governing equations.

$$\widetilde{\phi} = \phi(r) e^{i(m\theta + k_z z - \omega t)} \tag{F.3}$$

$$\widetilde{n} = n(r) e^{i(m\theta + k_z z - \omega t)} \tag{F.4}$$

Equation F.1 for each species is linearized as described previously and separated into steady-state and fluctuating equations. The steady-state continuity equations for the electron fluid and ion fluid are shown below in equations F.5 and F.6, with simplifications made assuming quasi-neutrality.

$$\frac{dn}{dt} + u_{ir} + n\frac{du_{ir}}{dr} + \frac{nu_{ir}}{r} = n\nu_i \tag{F.5}$$

$$\frac{dn}{dt} + u_{er} + n\frac{du_{er}}{dr} + \frac{nu_{er}}{r} = n\nu_e \tag{F.6}$$

Similarly, the fluctuating continuity equations for each fluid are shown below in equations F.7 and F.8.

$$\frac{d\widetilde{n}}{dt} + n\left(\frac{d\widetilde{u}_{ir}}{dr} + \widetilde{u}_{ir}r + \frac{1}{r}d\widetilde{u}_{i\theta}d\theta + d\widetilde{u}_{iz}dz\right) + u_{ir}\frac{d\widetilde{n}}{dr} + u_{iz}\frac{d\widetilde{n}}{dz} + \widetilde{u}_{ir}\frac{dn}{dr} + \widetilde{n}\left(\frac{u_{ir}}{r} + \frac{du_{ir}}{dr}\right) = n\widetilde{\nu}_i + \widetilde{n}\nu_i \tag{F.7}$$

$$\frac{d\widetilde{n}}{dt} + n\left(\frac{d\widetilde{u}_{er}}{dr} + \widetilde{u}_{er}r + \frac{1}{r}d\widetilde{u}_{e\theta}d\theta + d\widetilde{u}_{ez}dz\right) + u_e \cdot \nabla\widetilde{n} + \widetilde{u}_{er}\frac{dn}{dr} + \widetilde{n}\left(\frac{u_{er}}{r} + \frac{du_{er}}{dr}\right) = n\widetilde{\nu}_e + \widetilde{n}\nu_e \tag{F.8}$$

Assuming that the pressure tensor is diagonal, the momentum equations for each fluid along component directions are also separated into steady-state and fluctuating components. The steady-state ion momentum equations are shown below in equations F.9, F.10, and F.11.

$$u_{ir}\frac{du_{ir}}{dr} - \frac{u_{i\theta}^2}{r} = -\frac{e}{m_i}\frac{d\phi}{dr} - \frac{1}{m_i n}\left[\frac{dP_{rr}}{dr} + \frac{1}{r}\left(P_{rr} - P_{\theta\theta}\right)\right] - u_{ir}\nu_i \tag{F.9}$$

$$u_{ir}\frac{du_{i\theta}}{dr} + \frac{u_{i\theta}u_{ir}}{r} = -\frac{1}{m_i nr}\frac{dP_{\theta\theta}}{d\theta} - u_{i\theta}\nu_i \tag{F.10}$$

$$\frac{1}{m_i n}\frac{dP_{zz}}{dz} = -u_{iz}\nu_i \tag{F.11}$$

The steady-state electron momentum equations are shown below in equations F.12, F.13, and F.14.

$$\frac{u_{e\theta}^2}{r} = \frac{e}{m_e}\left(-\frac{d\phi}{dr} + u_{e\theta}B_z\right) + \frac{1}{m_e n}\left[\frac{dP_{rr}}{dr} + \frac{1}{r}\left(P_{rr} - P_{\theta\theta}\right)\right] - u_{er}\nu_e \tag{F.12}$$

$$u_{er}\frac{du_{e\theta}}{dr} + \frac{u_{e\theta}u_{er}}{r} = \frac{eu_{er}B_z}{m_e} - \frac{1}{m_e nr}\frac{dP_{\theta\theta}}{d\theta} - u_{e\theta}\nu_e \tag{F.13}$$

$$\frac{1}{m_e n}\frac{dP_{zz}}{dz} = -u_{ez}\nu_e \tag{F.14}$$

Similarly, the fluctuating momentum equations are expressed below in equations F.15 thru F.20. The pressure term is left in so that the fluctuating can be re-introduced in a substitution later on.

$$\frac{d\widetilde{u}_{ir}}{dt} + u_{ir}\frac{d\widetilde{u}_{ir}}{dr} + \widetilde{u}_{ir}\frac{du_{ir}}{dr} + \frac{u_{i\theta}}{r}\frac{d\widetilde{u}_{ir}}{d\theta} - \frac{2u_{i\theta}\widetilde{u}_{i\theta}}{r} = -\frac{e}{m_i}\frac{d\widetilde{\phi}}{dr} - \frac{1}{m_i n}\frac{dP_{rr}}{dr} - \widetilde{u}_{ir}\nu_i \tag{F.15}$$

$$\frac{d\widetilde{u}_{i\theta}}{dt} + u_{ir}\frac{d\widetilde{u}_{i\theta}}{dr} + \widetilde{u}_{i\theta}\frac{du_{i\theta}}{dr} + \frac{u_{i\theta}}{r}\frac{d\widetilde{u}_{i\theta}}{d\theta} + \frac{u_{i\theta}\widetilde{u}_{ir}}{r} + \frac{u_{ir}\widetilde{u}_{i\theta}}{r} = -\frac{e}{m_i r}\frac{d\widetilde{\phi}}{d\theta} - \frac{1}{m_i nr}\frac{dP_{\theta\theta}}{d\theta} - \widetilde{u}_{i\theta}\nu_i \tag{F.16}$$

$$\frac{d\widetilde{u}_{iz}}{dt} + u_{ir}\frac{d\widetilde{u}_{iz}}{dr} + \frac{u_{i\theta}}{r}\frac{d\widetilde{u}_{iz}}{d\theta} + u_{iz}\frac{d\widetilde{u}_{iz}}{dz} = -\frac{e}{m_i}\frac{d\widetilde{\phi}}{dz} - \frac{1}{m_i n}\frac{dP_{zz}}{dz} - \widetilde{u}_{iz}\nu_i \tag{F.17}$$

$$\frac{d\widetilde{u}_{er}}{dt}+u_{er}\frac{d\widetilde{u}_{er}}{dr}+\widetilde{u}_{er}\frac{du_{er}}{dr}+\frac{u_{e\theta}}{r}\frac{d\widetilde{u}_{er}}{d\theta}-\frac{2u_{e\theta}\widetilde{u}_{e\theta}}{r}=\frac{e}{m_e}\left(\frac{d\widetilde{\phi}}{dr}-\widetilde{u}_{e\theta}B_z\right)-\frac{1}{m_e n}\frac{dP_{rr}}{dr}-\widetilde{u}_{er}\nu_e \quad \text{(F.18)}$$

$$\frac{d\widetilde{u}_{e\theta}}{dt}+u_{er}\frac{d\widetilde{u}_{e\theta}}{dr}+\widetilde{u}_{e\theta}\frac{du_{e\theta}}{dr}+\frac{u_{e\theta}}{r}\frac{d\widetilde{u}_{e\theta}}{d\theta}+\frac{u_{e\theta}\widetilde{u}_{er}}{r}+\frac{u_{er}\widetilde{u}_{e\theta}}{r}=\frac{e}{m_e}\left(\frac{1}{r}\frac{d\widetilde{\phi}}{d\theta}+\widetilde{u}_{er}B_z\right)-\frac{1}{m_e nr}\frac{dP_{\theta\theta}}{d\theta}-\widetilde{u}_{e\theta}\nu_e \quad \text{(F.19)}$$

$$\frac{d\widetilde{u}_{ez}}{dt}+u_{er}\frac{d\widetilde{u}_{ez}}{dr}+\frac{u_{e\theta}}{r}\frac{d\widetilde{u}_{ez}}{d\theta}+u_{ez}\frac{d\widetilde{u}_{ez}}{dz}=\frac{e}{m_e}\frac{d\widetilde{\phi}}{dz}-\frac{1}{m_e n}\frac{dP_{zz}}{dz}-\widetilde{u}_{ez}\nu_e \quad \text{(F.20)}$$

The diagonal pressure can be expressed in terms of pressure and temperature using $P = nkT$. Additionally, with knowledge of the geometry and general plasma structure discussed in Sections 4.2 and 6.2, expressions for the steady-state velocities can be determined. The geometry and plasma structure inform what drifts occur, namely an E×B drift and diamagnetic drift in the azimuthal direction and Hall transport in the radial direction. The component terms for the steady-state velocities for both ions and electrons are shown below in equations F.21 thru F.23, with the ions assumed to be confined by the potential structure. The remaining velocity components can be determined by substituting into the momentum equations and solving.

$$u_{ir} = 0 \quad \text{(F.21)}$$

$$u_{er} = \frac{\nu_e}{\omega_{ce}} v_{e\theta} \quad \text{(F.22)}$$

$$u_{e\theta} = -\frac{E_r}{B_z} - \frac{T_e}{enB}\frac{dn}{dr} \quad \text{(F.23)}$$

As shown by Matlock et al. [47], the energy equation can be used in a simplified form to relate

the temperature, density, and potential. By solving for the fluctuating velocities and substituting into the continuity equation for both species, the ion azimuthal rotation frequency, $\omega_{i\theta}$, is determined in [47] and shown below in equation F.24. The ions cyclotron frequency can be neglected due to the unmagnetized nature of the ions and ϕ_0 is the center potential of a parabolic potential well [108].

$$\omega_{i\theta} = \pm\sqrt{\frac{2e\phi_0}{m_i r_L^2}}\sqrt{1-\frac{T_e}{2T_e+e\phi_0}} - \frac{\omega_{ci}}{2} \approx \sqrt{\frac{2e\phi_0}{m_i r_L^2}} \tag{F.24}$$